Estimating and Mitigating Effects of Space Radiation Damage in Single-Photon Avalanche Diodes

by

Joanna Krynski

A thesis
presented to the University of Waterloo
in fulfillment of the
thesis requirement for the degree of
Master of Science
in
Physics (Quantum Information)

Waterloo, Ontario, Canada, 2022

Author's Declaration

I hereby declare that I am the sole author of this thesis. This is a true copy of the thesis, including any required final revisions, as accepted by my examiners.

I understand that my thesis may be made electronically available to the public.

Abstract

Satellite-based quantum key distribution (QKD) necessitates practical and robust detectors capable of withstanding the harsh environment of space. Single-photon avalanche diodes (SPADs) have been shown to fulfill the required criteria, especially with their excellent detection characteristics and easy of integration. However, these detection characteristic can be degraded when exposed to space radiation. While there is a significant number of studies on the radiation hardness of Silicon based SPADs, there is little information available for such detectors with an Indium-Gallium-Arsenide (InGaAs) substrate.

This thesis presents results of a ground radiation test of commercial-off-the-shelf InGaAs SPADs in the context of their viability in future satellite-based QKD applications. The expected radiation over the lifetime of such a satellite was modelled using the open-source European Space Agency Space Environment Information System (SPENVIS). Orbit altitudes, solar cycle period and detector substrates were varied to model the expected damage equivalent to 100 MeV protons. We found that in the absence of large solar events, low-Earth orbit incurs more radiation exposure than further orbits. This is probably due to the ever-present trapped particle radiation field near the Earth's atmosphere. The results of the modelling were used to draw a ground radiation testing plan with target fluences calibrated to a 100 MeV proton beam. In preparation for ground testing, eight InGaAs SPADs were procured and electronics circuits were designed for them. Six of devices were gated, necessitating a modified passive-quenching circuit, while the remaining two were negative-feed back avalanche diodes. The devices were mounted to a metal bracket and were cooled to $-50°$C within a closed chamber using solid CO_2. The devices were exposed to 10-years equivalent of radiation in eight steps with characterization of the detector's current-voltage (IV) curve and dark count rate (DCR) occurring before radiation and after each radiation exposure.

The IV curve of the devices did not change significantly, nor did their breakdown voltage. Although there is a general trend of DCR increasing with increasing radiation, the data is quite variable, even between devices of the same model and making. This result provides some evidence that radiation effects are dependent of the manufacturing of the substrate with respect to the active area volume and substrate defect profile. Investigation into the influence of the detector manufacturing was outside the scope of this thesis, but it is a recommended next step into the understanding of radiation effects in InGaAs SPADs. Additionally, we estimate the device's photon detection efficiency using a correlated single-photon source and two methods of calculation. We find that the efficiency dropped significantly as compared with the manufacturer datasheet, but it is difficult to

attribute this difference to the radiation exposure since a different measurement method is used.

This thesis also investigated using laser annealing as method of healing radiation damage which manifest itself in elevated DCR. The Cool-Annealing Payload Satellite (CAPSat) mission, which is currently orbiting Earth, aims to use a high-power laser to reduce dark count rates in Si-based SPADs exposed to space radiation in real-time. Here, we present results of a ground-test of annealing the CAPSat prototype detector module within a space-like environment in a vacuum chamber. We exposed previously irradiated detectors to various annealing powers ranging from 50 mW to 2.3 W, as well as at various annealing duration, from 10 s to 16 min. We found that no significant DCR reduction occured below 1 W, and employment of higher annealing power lead to steeper decreases in DCR. Annealing duration played a smaller role in DCR, with exposures as short as 10 s able to incur some alleviation of DCR when coupled with a high annealing power. Using the results of this experiment, as well as other function testing of the flight-version of CAPSat detector module, a suggested measurement methodology for the CAPSat mission is described.

Acknowledgements

I would like to firstly acknowledge my supervisor, Dr. Thomas Jennewein, who conceived the concepts for my Master's project and guided me through a steep learning curve during an unusual time. I have learned so much from him during these two years and appreciate the opportunities to work on interesting projects while I have been given in his group. I would like to thank my commitee members, Dr. Kevin Resch and Dr. Michael Reimer, for providing valuable discussion and guidance during our meetings.

I especially would like to thank Dr. Nigar Sultana, who was my day-to-day advisor and from whom I have learned practically everything on electronics and the design of readout circuits. We collaborated closely throughout my Master's and I am grateful to have such a role model to inspire my future research goals.

From my lab group, the Quantum Photonics Laboratory, I thank in particular Dr. Paul Godin and Paul Oh, who traveled with me to TRIUMF for the radiation testing and assisted me with the set-up, measurements and troubleshooting of the experiment. While such a small group, I think we accomplished much during that time.

I would like to acknowledge the support of our collaborators at Politecnico di Milano led by Dr. Alberto Tosi. Dr. Tosi and Fabio Signorelli responded zealously to our proposal to conjoin our radiation tests together, produced fresh devices and readout circuits to test and provided insight into the fundamentals of single-photon avalanche detectors.

Similarly, I acknowledge our collaboration with Dr. Paul Kwiat's and Dr. Michael Lembeck's groups at the University of Illinois at Urbana-Champagne, with whom I have become quiet familiar through the projects described in the Thesis. Through this collaboration, I have learned so much about building, integrating and launching small satellites.

I extend my gratitude to my research group at the Quantum Photonics Laboratory, especially to Ramy Tannous, Wilson Wu and Kimia Mohammedi, who took time to read and edit my Thesis, as well as a former group member Dr. Youn Seok-Lee, who helped immensely with the laser annealing experiment. My lab group has been stellar and I am extremely grateful for their knowledge-sharing and camaraderie, even if we were not always

able to meet in person. Our weekly group meetings, albeit sometimes long, provided me with varied perspectives and opinions on how to approach some of my research problems. Thank you all for your support during this degree.

Thank you also to my friends at IQC and abroad: Mike, Twesh, Sandra, Alex and Elsie. Without you guys, I would not have enjoyed my time here nearly as much as I did. I would like to especially mention Toly for supporting me through and through and believing in my skills to finish this degree.

Finally, I would like to thank my family for their love and constant support.

Dedication

I dedicate this Thesis to my parents, who have been full of wonder at the science we get to do in lab and in space on a daily basis.

Table of Contents

List of Figures

List of Tables

Chapter 1

Introduction

1.1 Background in quantum communication

The history of quantum communication can be described as brief, with the term first appearing in literature in the latter half of the 20th century [5]. Before delving into the earliest days of quantum communication, it is good to understand how it relates to the more prominent topic of quantum computing.

In 1982, Richard Feynman posed the question of how computers can simulate physics. Since the world is of a quantum mechanical nature, he suggested that computers which truly reflect real world physics must also abide by quantum mechanics [43]. Classical computers store information in the form of a high (1) or low (0) electronic state known as a logical bit. It is not an over-exaggeration to say that strings of these bits form the fabric of modern life: classical computers are present in every home, in people's pockets and even in their wristwatches. While these classical machines seem to become more sophisticated every year, their use has limits, such as when it comes to modelling quantum systems. A quantum computer, in comparison, uses the quantum mechanical principle of superposition to encode information in two states at once, meaning that the quantum bit, or qubit, can exist in both the 1 or 0 state simultaneously. Two-level quantum systems which can be harnessed for use in a quantum computer include photons, trapped ions

and superconducting circuits, though there are many more platforms being investigated [55, 36, 37]. Each of the quantum computing platforms has been researched and developed in the race towards quantum supremacy, which is the point at which quantum computers demonstrate a computing advantage over the most-powerful classical supercomputers [72].

Quantum supremacy will be an important step towards what Feynman alluded to: modelling the most complicated and inherent quantum systems we know like protein folding or elementary particle reactions, which even now with our current state-of-the-art classical computers can take millions of years [51, 62]. However, quantum supremacy also promises an advantage for nefarious purposes, like cracking classical encryption. Classical encryption schemes are ubiquitous in our daily lives: from accessing your emails to submitting sensitive government documents online. Classical encryption methods such as Advanced Encryption Standard (AES) or the Rivest–Shamir–Adleman (RSA) algorithm rely on complex mathematical problems to suppress adversaries [75, 76]. For example, RSA algorithm uses the product of prime numbers to encrypt information; factoring the product to re-gain the original prime number is much more difficult, with 829-bit keys requiring thousands of CPU years to crack with current classical computers [32]. Prime factorization, however, becomes much more tractable in the hands of an adversary with a quantum computer. In 1994, Peter Shor presented an algorithm which could efficiently factor any large number into its primes if the information could be encoded in quantum states on a quantum computer [79]. Shortly after, Lov Grover discovered a method by which a quantum computer could defeat AES, foreboding yet another blow to the long-used classical encryption schemes [44].

The answer to this apparent problem lies in two general solutions. One can create classical algorithms which are secure against quantum computers – this is known as post-quantum cryptography [31]. Otherwise, one can create security protocols which encrypt information in a quantum system; this is known as quantum key distribution (QKD) [78]. The former follows a similar methodology as previous classical encryption methods in that it relies on using mathematical problems which are yet to be proven solvable by a quantum computer. This runs a risk that sometime in the future someone will indeed find a way of cracking the algorithm. QKD, on the other hand, is grounded in the laws of

quantum physics and has provable limits to how much an adversary, known as Eve, can extract from the communication channel. Additionally, the no-cloning theorem prevents Eve from intercepting information and re-sending it without knowledge of the true recipient [96]. Significant development has been made in QKD systems to make them commercially viable, successful and above all secure.

1.2 Quantum Key Distribution (QKD)

Charles Bennett and Gilles Brassard first proposed a quantum mechanically secure method of encrypting information in 1984, later coined as the BB84 protocol to immortalize the creators and the year [28]. In BB84, Alice (the sender) encodes her bits of information in the polarization of single photons. Her bits can be 1 or 0, and are encoded in two photon polarization bases: Horizontal-Vertical polarization basis (HV) or Diagonal-Antidiagonal (DA) polarization basis. The 0 bits are randomly encoded in the H or D polarization while the 1 bits are randomly encoded in the V or A polarization. The photons are then sent to Bob (the receiver) who randomly sets his detectors to measure in either HV or DA basis. If Bob randomly chooses the correct basis, then he detects Alice's photon correctly 100% of the time. However, if he chooses the incorrect basis then 50% of the time he will detect the wrong photon polarization. After measurements, Bob is left with a string of encoded bits, although he doesn't know which ones were measured correctly. As such, Alice and Bob communicate on a public channel and compare in which basis she encoded and in which basis Bob measured, then discard the bits where there is basis mismatch. Alice and Bob are then left with matching strings of bits (if there was no eavesdropper) which are their secure keys to be used for future communication.

There is a chance that an eavesdropper, Eve, inserts herself between Alice and Bob in an effort to perturb the key distribution. However, even if Eve measures Alice's photons, she has only a 50% chance of measuring in the correct polarization basis, and if she attempts to send another state to Bob, then she has at most a 50% chance of relaying the correct state since he once again randomly chooses his measurement basis. The presence of an

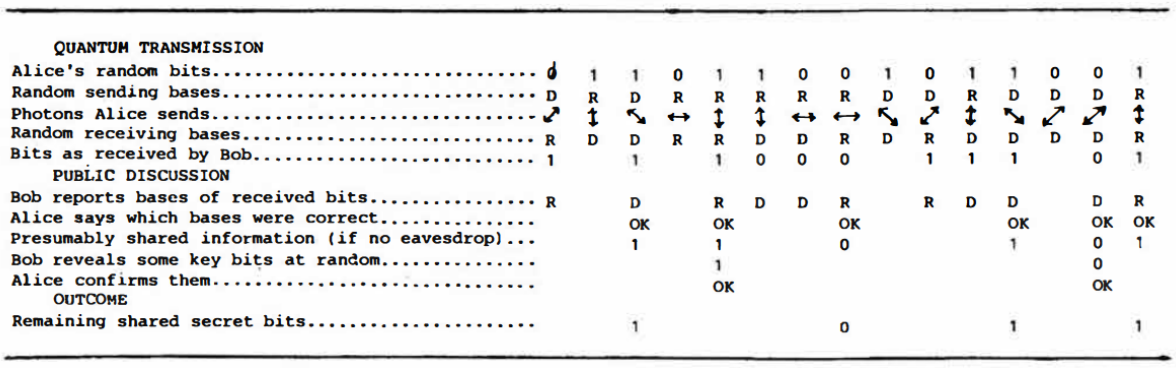

Figure 1.1: Original illustration of BB84 protocol from the seminal paper, reprinted from [28].

eavesdropper can be revealed if Alice and Bob sacrifice a portion of their sifted key by comparing actual sent and received bits. If all the bits in the shared subset are the same, then Alice and Bob conclude that there was little-to-no eavesdropping. However, if a set threshold of errors is reached, Alice and Bob conclude that channel is not secure and no key is distributed.

A competing QKD scheme was developed shortly after. Ekert came forwards with a protocol in which Alice and Bob share an entangled pair of particles and make use of a version of Bell's inequality to test that the communication channel was not eavesdropped, as the eavesdropping hacker would appear to invoke local hidden information [42]. A year later, Bennett, Brassard and Mermin rebutted Ekert with an adjusted version of BB84 known as BBM92 which showed that entangled pairs could be used to constitute a secure channel withot Bell's theorem [30]. Further protocols as well as proofs of their security or investigations into possible eavesdropper loopholes continued to be developed in tandem to physical realizations of QKD schemes [71].

The first demonstration of BB84 occurred in 1992 by the inventors themselves (along with a few other colleagues) and showed a successful distillation of a 659-bit secret key between a 30-cm separated Alice and Bob [29]. Within the same decade, various experimental groups extended QKD channel distances to even hundreds of kilometers with either line-of-sight free-space or fiber optically connected end-nodes. With each demonstration,

QKD appeared to become a more tenable solution to the impending doom of classical encryption methods. However, it became apparent in the early 2000s that such line-of-sight or fiber-based links would not be viable for QKD on a global scale: obstacles in the channel path, severe weather and eventually the Earth's curvature could all prevent the feasibility of secret key generation. Similarly, severe attenuation of photons in fiber coupled with the lack of a quantum analog to optical repeaters limits to long-distance fiber networks more than few hundred kilometers. As a response to this limit, early proposals and feasibility studies of satellite interlinks between Alice and Bob appeared from several groups [20, 73, 69].

Less than 15 years later, a satellite-to-Earth QKD link was demonstrated by Liao et al. via the low-Earth orbit satellite *Micius*. The group reported a key rate of 1.1 kbit/s over a 1200 km link and later, in 2021, a key rate of 47.8kbit/s after modifications to the ground station were made. The launching of *Micius* constituted as the first quantum communication satellite, however, many more have been proposed for launch in the near future (see Figure 1.2 for summary of current proposed missions).

1.3 Satellite QKD Receiver Considerations

The satellite-Earth quantum link between QKD transmitters and receivers is susceptible to various types of degradation including beam diffraction and atmospheric turbulence [34]. While the optimization of optics is the primary method of limiting these link losses, another important consideration for maximizing the collected quantum signal is the choice of single-photon detector used in the QKD receiver.

There are many types of detectors capable of resolving single photons: photomultiplier tubes (PMTs), single-photon avalanche diodes (SPADs), transition-edge sensors (TES) and superconducting nanowire single-photon detectors (SNSPD), to name a few [65]. Several options can be excluded from space-based QKD based on the operation and maintenance requirements. If a downlink configuration is adopted– where the quantum signal originates from the satellite and is sent to a terrestrial ground station– limiting the size and operation

Initiative	Goal	Vehicle	Status/Results
QUESS[20]	LEO-to-ground trusted-node satellite QKD, uplink quantum teleportation and double-downlink entanglement distribution.	Micius 631 kg satellite.	Entanglement distribution of 1203 km[47], teleportation up to 1400 km[43] and BB84 QKD up to 1200 km with QBER ~1% and sifted key 14 kbps.[42]
Toyoshima et al.[121]	LEO-to-ground polarization measurement.	OICETS 570 kg satellite.	Polarization preserved within system rms error of 28 mrad.
Takenaka et al.[90, 122]	LEO-to ground polarization measurements from a small optical transponder (SOTA).	SOCRATES 48 kg satellite.	Effectively no depolarization was observed (100% Degree-of-polarization) and QBER of < 5%.
Günthner et al.[103]	GEO-to-ground test of quantum state used in coherent communication.	Alphasat I-XL 6649 kg satellite.	Quantum-limited states arrive on the ground after transmission from satellite.
Vallone et al.[46]	Test of polarization state for weak coherent pulses using retro-reflectors on LEO satellites.	Jason-2 510 kg, Larets 21 kg and Starlette/Stella 48 kg satellites.	Average QBER of 6.5% achieved.
Yin et al.[122]	Test of polarization state for weak coherent pulses using retro-reflectors in a LEO satellite.	CHAMP 500 kg satellite.	Signal to noise ratio of 16:1 observed for polarization measurements.
Dequal et al.[124]	Test of weak coherent pulse transmission from retro-reflectors on a MEO satellite.	LAGEOS-2 411 kg satellite.	Peak signal-to-noise ratio of 1.5 with 3 counts per second.
Tang et al.[19]	In-orbit observation of polarization correlations from a photon-pair source on a nano-satellite.	Galassia 2 kg 2U CubeSat.	97% contrast in polarization correlation measurements. Pathfinder for SpooQySats (below).
Nauerth et al.[125]	QKD between the ground and a aircraft moving at similar angular velocities to a LEO satellite.	Dornier 228 utility aircraft.	Sifted key rate of 145 bps, QBER of 4.8% from range of 20 km at angular speed of 4mrad per second.
Bourgoin et al.[18]	QKD with a moving receiver similar to the angular speed of satellite at 600 km altitude.	Pick-up truck.	Key rate of 40 bps with QBER of 6.5 to 8% with receiver at a range of 650 m moving at angular speed of 13 mrad per second.
Wang et al.[126]	Verification of pointing, acquisition and tracking.	Hot-air balloon.	Key rate of 48 bps and QBER of ~4% over a range of 96 km.
SpooQySats[127]	Demonstrate polarization-entangled photon-pair sources in space.	3U CubeSats.	Funded mission. Launches planned from 2018.
QEYSSat[43]	Trusted-node receiver for uplink QKD.	Microsatellite.	Funded mission.
CAPSat[94]	Laser annealing of radiation-damaged APDs.	3U CubeSat.	Funded mission.
NanoBob[128]	Trusted-node receiver for uplink QKD.	CubeSat.	Proposal.
SpaceQUEST (2008)[41]	Double LEO-to-ground downlinks QKD using polarization-entangled photon-pairs.	International Space Station.	Proposal (since updated as a mission exclusively investigating decoherence due to gravity[111]).
Scheidl et al.[86]	Entanglement-based QKD and Bell tests, ground-to-LEO.	International Space Station.	Proposal.
NanoQEY[109]	QKD and Bell tests ground-to-LEO with a trusted-node satellite.	Based on NEMO nanosatellite bus, 16 kg.	Proposal.
Zeitler et al.[85]	Superdense teleportation, LEO-to-ground.	International Space Station.	Proposal.
QuCHAP-IDQuantique	Establish QKD networks based on high altitude platforms.	High-altitude platform.	Proposal.
CQuCom[53]	LEO-to-ground QKD downlinks.	6U CubeSat.	Proposal.

Figure 1.2: Current and proposed quantum long-distance free-space experiments [27].

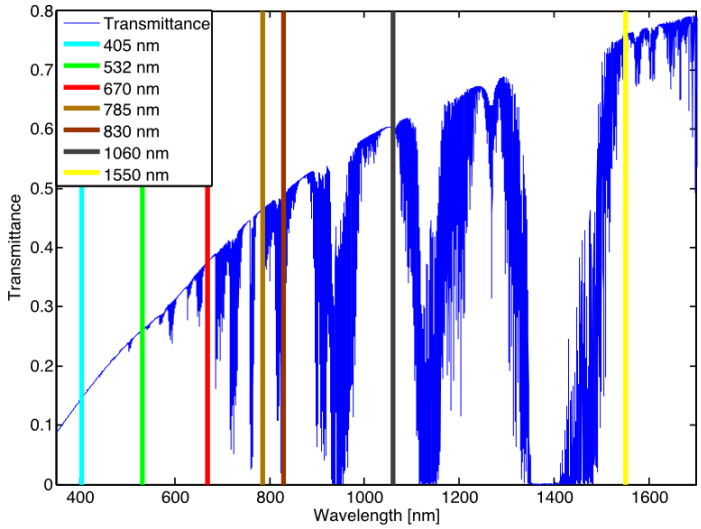

Figure 1.3: Modelled vertical transmittance through Earth's atmosphere. Coloured vertical lines represent wavelengths of commercially available lasers. Reprinted from [34].

maintenance of the receiver detectors is not critical. However, in the event that an uplink configuration is chosen, there are strict limitations to the weight and complexity of the receiver detectors and their readout circuits. Cryogenically cooled detectors such as TES and SNSPD are not currently viable for an uplink QKD scheme with detectors mounted in the orbiting satellite, although there is significant movement towards developing these technologies for space [102, 99]. PMTs, on the other hand, do not require sophisticated temperature control and have been proven successful with regards to their easy integration in scores of satellite missions. Furthermore, they appear to show very little radiation damage in a 2017 study by Anisimova et al. [17]. However, PMTs have been avoided broadly from QKD applications due to their poor sensitivity to signal wavelengths of interest [46]. Modelling by Bourgoin et al. found that the Earth's atmosphere was most transparent to wavelengths in the near-infrared to infrared wavelengths (750 nm to 1550 nm), with nearly 80% transmittance for the highest wavelengths in that bandwidth (Figure 1.3).

As such, the choice of quantum receiver should be limited to detectors which are sensitive in the regions of high atmosphere transmittance. This discourages the use of PMTs due to their lower detection efficiency at wavelengths above 500 nm (at which their peak

efficiency is about 40%). Therefore, the most feasible choice of detectors to use in quantum receivers are SPADs, which do not require complicated maintenance, and have higher efficiencies at both near-infrared (up to 70%) and infrared wavelengths (up to 40%), depending on the semiconductor within them. The structure and operating characteristics of SPADs will be further discussed in Chapter 2.

Another positive attribute of these single-photon detectors is their low dark count rate (∼10 counts per second (cps) when new and cooled to a low operating temperature). Detector dark count rate (DCR) is one of the parameters considered when calculating the achievable secret key generation rate or quantum-bit error rate (QBER), and it can ultimately limit the maximum link distance [34, 35]. As such, QKD-suitable SPADs should be manufactured in conditions leading to minimum impurities (which can lead to higher dark count rate), and should also be operated such that the dark count rate is minimized. This latter constraint is a non-trivial concern for uplink QKD missions where space-borne SPADs are exposed to the harsh radiation environment. Research spanning the second half of the 20th century has cemented the fact that radiation in space can be fatal to all types of semiconductor components, from logic gates to light sensors, through introductions of defects in the sensitive lattice structures [87, 33]. SPADs are likewise affected by space radiation, with the dominant effect of damage being elevated dark count rate. The latter half of Chapter 3 explains the mechanisms by which SPADs are damaged by space radiation and the effect of this damage on SPAD operation.

While there is a bulk of studies on the topic of radiation damage of silicon-based SPADs, there is much less available on this topic for Indium-Gallium-Arsenide (InGaAs)-based SPADs (Chapter 3 outlines the few studies available). These InGaAs SPADs have been considered less suitable for free space QKD purposes in the past due to their historically poorer operating characteristics as compared with silicon SPADs (lower efficiencies, higher rate of false counts correlated with detection in free running operation). However, significant advances are being made to improve the production process of this type of SPAD so they can be applied for highly sensitive applications like QKD, albeit at a longer wavelength of 1550 nm [80]. Figure 1.3 shows that 1550 nm light transmits readily through the Earth's atmosphere. Also, background light, such as from light pollution and sunlight

during the day, will be lower due to reduced scattering at this longer wavelength [21]. Additionally, any fiber-based QKD also requires 1550 nm wavelength quantum signals, thereby limiting the choice of SPAD to InGaAs or other Group III-V semiconductors platforms. 1550 nm wavelength light is extensively utilized in classical telecommunications, so existing fiber infrastructure can be repurposed for quantum communication, with one improvement being the installation of InGaAs SPADs in turn of classical light detectors. Choosing 1550 nm as the single operational wavelength for both the space-borne and fiber channels will simplify the eventual linking of these two networks to create a truly global and locally accessible quantum internet. As such, better understanding of the challenges of using 1550 nm-sensitive InGaAs SPADs in the space environment is necessary to work towards this future goal. With few prior published results on radiation damage in InGaAs SPADs, Chapter 4 focuses on estimating the expected effects in such devices through modeling the expected radiation environment at various satellite orbits, as well as through experimental characterization of three models of commercially available SPADs and two models of experimental SPADs which were exposed to proton radiation.

In conjunction with classifying the tolerable level of radiation damage SPADs can endure while still remaining useful for QKD purposes, efforts have been made to create active damage mitigation methods. Chapter 5 outlines the process of using a high power ($\sim$W) laser to anneal radiation-damaged SPADs in an effort to combat elevated dark count rates. Examples of this technique have been shown in bench-top lab environments [59]. Here we present results of laser annealing Silicon SPADs irradiated to a 10-year equivalent dose in a space-like environment inside a thermal vacuum chamber (TVAC). These results are extremely relevant as they provide a direct comparison to the data from the recently launched Cool Annealing Payload Satellite (CAPSat) where radiation exposed SPADs will be annealed while in orbit.

I conclude this thesis in Chapter 6, with a brief summary of the results of the two major experiments undertaken during my Master's, as well as with an outlook towards what future steps should be taken to continue improving our understanding of using single-photon avalanche diodes in space applications.

Chapter 2

Single-Photon Avalanche Diodes

2.1 Introduction

Single-photon avalanche diodes are widely used in both fiber and free-space quantum communications because of their favourable operating characteristics and easy integration into set-ups. As a mature technology, they are commercially available in many forms with various substrate types and sizes for numerous applications. Their operation as a single-photon detector will be explained in the following section, followed by discussion of their key characteristics. Since these detectors require specially designed readout circuits to function usefully, two popular circuits are presented.

2.2 Principles of Operation

In the simplest terms, a single-photon avalanche diode is a PN junction operated in reverse bias at a voltage (V_A) greater than the diode breakdown voltage (V_{Br}), known as the excess voltage (V_{Ex}). A PN junction is a semiconductor with one side doped positively (*p side* with an excess of holes) and with the other side doped negatively (*n side* with an excess of electrons). To neutralize the charge mismatch, holes migrate towards the negative

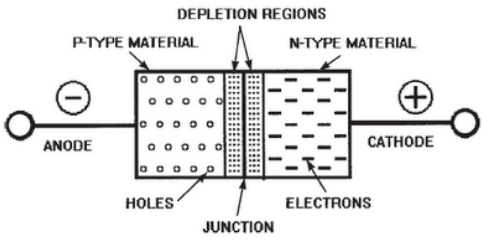

(a) Biasing PN junctions in reverse (negative terminal to positive side and vice versa for other side) leads to the formation of carrier-deprived depletion region [2]

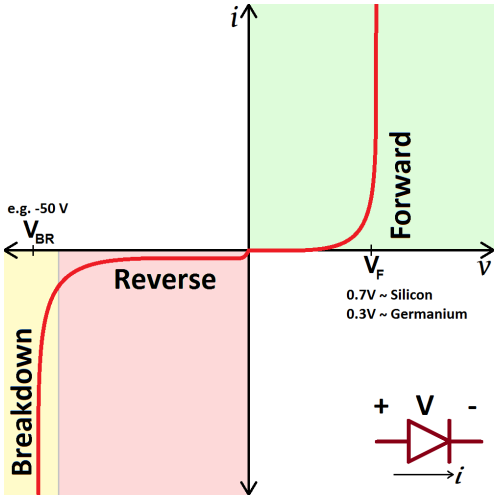

(b) Current (i) versus voltage (V) curve of a diode [9].

Figure 2.1: Characteristics of SPADs

side of the material, while electrons will migrate the opposite way. When a negative lead is attached to the *p side* of the material and a positive lead to the *n side* of the material, then the junction is reverse-biased (Figure 2.1a). The result is that holes are now attracted the opposite way, that is, towards the negative lead rather than towards the *n side* of the junction. Similarly, the electrons are attracted away from the *p side* and towards the positive lead. This creates a region void of mobile charge carriers known as the *depletion region*. As the bias voltage is increased, the depletion region extends, carrier migration is further suppressed, and only a very small leakage current is able to pass. If a beam of photons of sufficient energy manages to excite electrons within the PN junction, a *photocurrent* will start to flow. The magnitude of the current is proportional to the intensity of the incident light, giving this mode of SPAD operation the name of linear mode [49]. Linear mode operation extends to the point of junction breakdown, when the electric field strength is so great that it is able to liberate the previously suppressed electrons to the conduction band, creating a current larger than the leakage current (Figure 2.1b) [63]. Operation of SPADs above breakdown is known as Geiger-mode operation and is necessary in order to detect single photons [49, 39, 65]. In Geiger-mode, the electric field

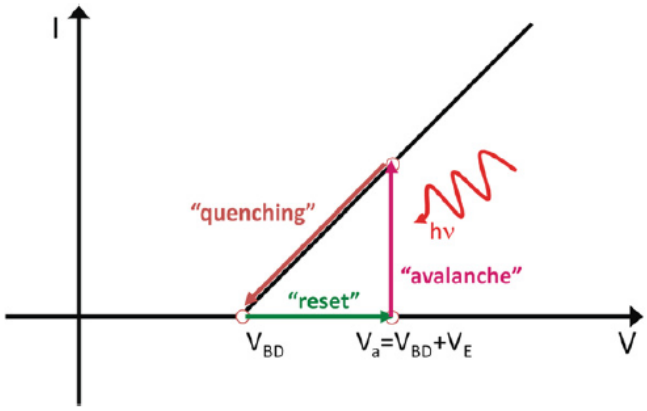

Figure 2.2: Cycle of SPAD operation: At $V_A > V_{Br}$ a single photon will spur a large current, after which a quenching circuit will reduce the voltage down to breakdown and reset to the appropriate V_{Ex}. Reprinted from [65].

strength is so high that the injection of a single photon into the depletion region can excite a photoelectron which which can in turn excite other electrons in a multiplicative fashion. The result of this multiplication of single carriers is a macroscopic current called an avalanche. The leakage current prior to photon detection is in the nA range, while the post-photon-detection avalanche current can reach the mA range. The avalanche is self-sustaining: the large current will continue to flow until it is quenched by lowering the applied voltage to V_{Br} or below. Quenching of avalanches requires a circuit which can sense the onset of an avalanche, generate an output pulse to indicate this onset, quench the avalanche by lowering the bias appropriately low and finally restore the bias to above breakdown so the SPAD is ready to sense the next photon (see Figure 2.2) [39, 65]. Several methods of quenching circuits will be highlighted later in the chapter.

The type of semiconductor used in the SPAD will dictate the photosensitivity range of the photodiode. Silicon-based SPADs are sensitive in the visible to near-infrared wavelengths (400 nm - 1000 nm), while longer wavelengths are better detected by semiconductors in the III-V semiconductor compound group, such as those made with Indium-Gallium-Arsenide/Indium-Phosphorus (InGaAs/InP) (Figure 2.3) [46, 39]. The semiconductor's sensitivity is determined by the its lattice energy bandgap. A larger energy bandgap requires a more energetic photon to initiate excitation of an electron from the conduction to the valence band, and since photon energy is inversely proportional to wavelength, a shorter wavelength photon is needed. For the two semiconductors mentioned, silicon has

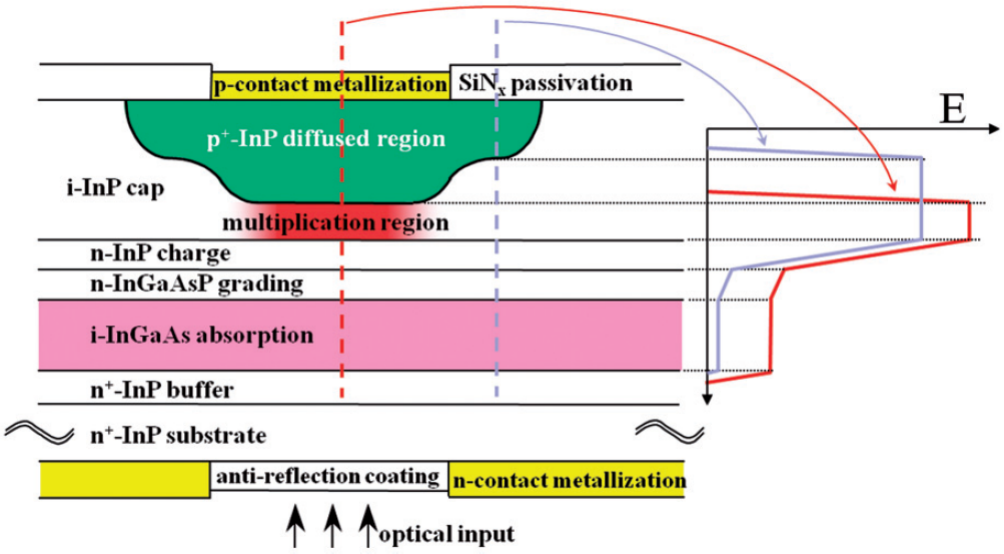

Figure 2.3: Typical layer structure of a separate absorption and multiplication type of InGaAs/InP photodiode with electric field magnitude for each layer. Reprinted from [49].

a bandgap of >1 eV at room temperature, corresponding to photons of at most 1000 nm, while InGaAs has a bandgap of 0.7 eV, corresponding to photons of at most 1700 nm[1][53, 3].

Although the semiconductor bandgap energy indicates which photons can induce excitation within the diode material, it does not ensure that every photon impinging on the active area of the detector will be absorbed to create an avalanche. This type of conversion efficiency, as well as other specific characteristic of SPADs, will now be explored.

[1]The InGaAs bandgap energy is dependent on the fraction of Indium. For this example the ratio of Indium to Gallium 0.53:0.47, which enables a lattice-matching with the InP substrate. More about this will be discussed later in the Chapter4.

2.3 Typical parameters of SPAD characterization

2.3.1 Photon Detection Efficiency

The probability of an incident photon triggering an avalanche is not unity. The photon detection efficiency is the probability the detector will output an electronic pulse upon photon arrival, and this depends on several efficiencies both within and outside the SPAD structure:

- Coupling efficiency (η_{coupl}): In both a fiber-based and free-space setting, not all photons will be incident on the active area of the SPAD due to to misalignment of the beam on the active area or reflections on the SPAD's glass window.
- Absorption efficiency (η_{abs}): A photon must not only transmit through the glass window of the SPAD, but also through several layers of the semiconductor material. The absorption coefficient α of a material characterizes how easily photons can penetrate it. The efficiency of getting through to the absorptive region of the SPAD is given by $\eta_{abs} = 1 - e^{-\alpha d}$, where d is the depth of the absorption layer.
- Injection efficiency (η_{inj}): After photon absorption and subsequent excitation of a carrier, the carrier must be accelerated to the multiplication layer to excite additional carriers. This efficiency is dependent on the applied bias voltage since the magnitude of the electric field scales proportional to bias voltage.
- Avalanche probability (η_{ava}): This is the probability that the carrier multiplication process will generate a macroscopic current. This parameter is also dependent on the magnitude of the electric field and therefore on the applied bias.

Once considering these individual efficiencies, photon detection efficiency is $PDE = \eta_{coupl} \times \eta_{abs} \times \eta_{inj} \times \eta_{ava}$ [39, 101]. The only variable parameters contributing to PDE are the last two which depend on V_{ex} (since the optical set-up is assumed to be fixed and the absorption coefficient and SPAD structure is constant). Therefore, PDE increases approximately linearly with V_{ex} until a point of saturation [65].

2.3.2 Dark Count Rate (DCR)

Avalanches can be triggered by carriers in the absence of photon illumination due to thermally excited carriers from defects. The probability of these false counts, or dark counts, follows a Poissonian fluctuation and is temperature-dependent, with greater temperatures capable of thermally exciting more carriers [39]. V_{ex} also plays a vital role: as the magnitude of the electric field increases with applied bias, more carriers are generated from deeper levels of the band gap [65]. The density of these deep energy levels must be minimized during the SPAD fabrication.

While non-Geiger-mode avalanche photodiodes also experience similar shot noise such as thermally generated dark counts mentioned above, SPADs' DCRs in Geiger-mode are not correlated to the dark current measured in linear mode [101]. This distinction is important when comparing avalanche photodiodes with Geiger-mode SPADs, particularly when dark current and dark count rates are used as tools to measure changes within the devices' structures.

2.3.3 Afterpulsing

Afterpulsing is another type of false count which differs from the Poissionian thermally generated dark counts as it is strongly correlated with the occurrence of a genuine photo-generated avalanche (Figure 2.4). Carriers from a true avalanche can get trapped within deep levels located in the mid-gap of the material and may cause another avalanche not related to a photon detection upon release from the trap at a later time. The trapped carrier release time is characteristic of the trap energy level [65]. Afterpulsing can be minimized by reducing the avalanche charge or total number of generated carriers, since fewer generated carriers translates to fewer trapped carriers. Additionally, external circuit electronics may be used to quench and hold the SPAD below breakdown long enough so that trapped carriers are released while the detector is unable to generate avalanches [39, 65]. Increasing SPAD temperature can also aid in reducing the trap lifetime [101].

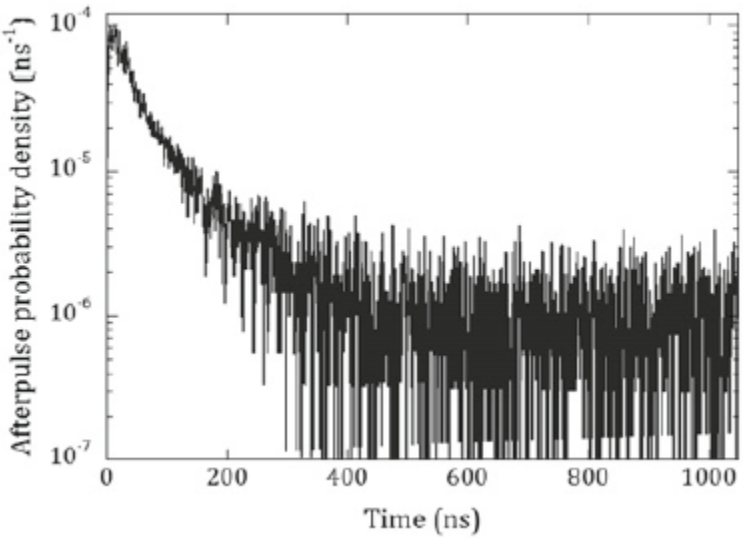

Figure 2.4: Probability density of an afterpulse generation. A true avalanche occurs at the starting of counting. The elevated probability of avalanches in the first few hundred nanoseconds after the start of counting indicates afterpulsing. Uncorrelated thermal dark counts begin appearing after 350 ns after the true avalanche when all the trapped carriers have been released. Reprinted from [65].

2.3.4 Timing Jitter

After a photon is absorbed and an avalanche is generated, there is an unavoidable delay of the sensing of the avalanche by the readout electronics. The timing resolution or timing jitter of a detector system is the sum of all delays in the detection system (SPAD and quenching circuitry). Timing jitter is quoted as the full-width half max of the distribution of detected photon arrival times (Figure 2.5) [40]. On the side of SPAD operation, increasing V_{ex} will decrease the uncertainty of photon arrival since photogenerated carriers will quickly be accelerated by the strong electric field. This results in a sharp peak on a photon arrival time distribution, while the tail of the distribution is due to carriers which diffused into the depletion layer and were eventually accelerated [65].

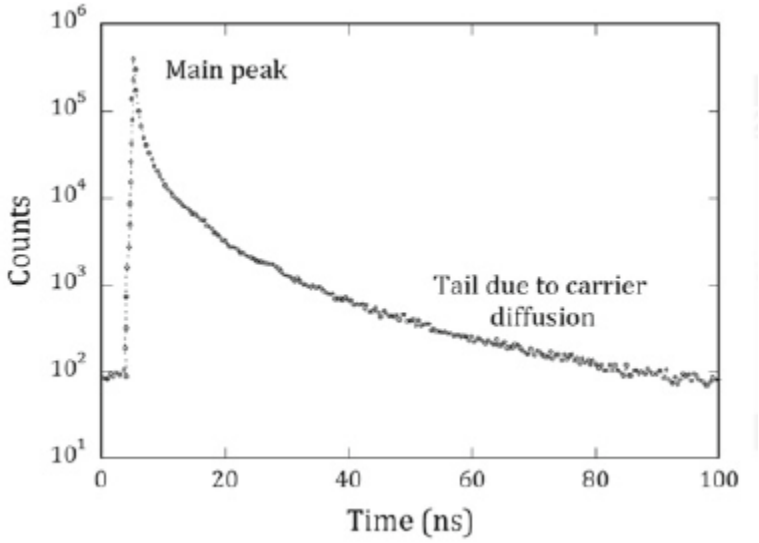

Figure 2.5: Photon arrival time distribution with main peak created by carriers generated by photoexcitation in the depletion region of the SPAD and the slow tail created by distant carriers diffusing into the depletion region. Reprinted from [65].

2.4 Quenching Circuits

2.4.1 Passive Quenching

The simplest method of curtailing a self-sustaining avalanche and reducing the bias voltage below breakdown is through developing a voltage drop on a large ballast resistor R_L (Figure 2.7a). The process is as follows: the SPAD is reverse-biased via the large resistor at its cathode (typically >100 kΩ), while a small resistor (R_s) at the anode (usually on the order of 50 - 1000 Ω) is used to observe the the current pulse. When a photon triggers an avalanche, it amounts to closing a switch in the diode equivalent circuit and a current begins to flow with magnitude described by:

$$I_d(t) = \frac{V_A - V_{Br}}{R_s} = \frac{V_{ex}(t)}{R_s} \tag{2.1}$$

The avalanche discharges the total capacitance of the diode, and the voltage across the diode begins to decrease back towards V_{Br}. The steady state current reached is $\frac{V_{ex}}{R_L}$. R_L must be large enough such that the current is reduced to a certain cutoff current, typically between 50 μA to 100 μA . At this point that avalanche is no longer self-sustaining and is ultimately quenched [65, 39].

After quenching the avalanche, the bias voltage begins to recover towards V_A during the period known as the reset transition. As long as $V_A > V_{Br}$, the SPAD is able to generate avalanches albeit at a lower detection efficiency and lowered photon-timing resolution [65]. It is not until the SPAD fully restores the excess voltage level that it can accurately detect the next photon. The full recovery time is determined by a few things: (a) T_d is the time delay between avalanche onset and the beginning of the quenching transition, (b) T_q is the quenching transition and is dependent on the time constant $R_D(C_D + C_S)$, where R_D is the diode resistance, C_D is the diode capacitance and C_S is the stray capacitance, (c) The time to reset the bias voltage above breakdown is dependent on the time constant $R_L(C_D + C_S)$. The reset process limits the maximum count rate the SPAD can handle. While recovery times are usually in the tens of nanoseconds, this may still be too long for some high count rate cases and active quenching may be used.

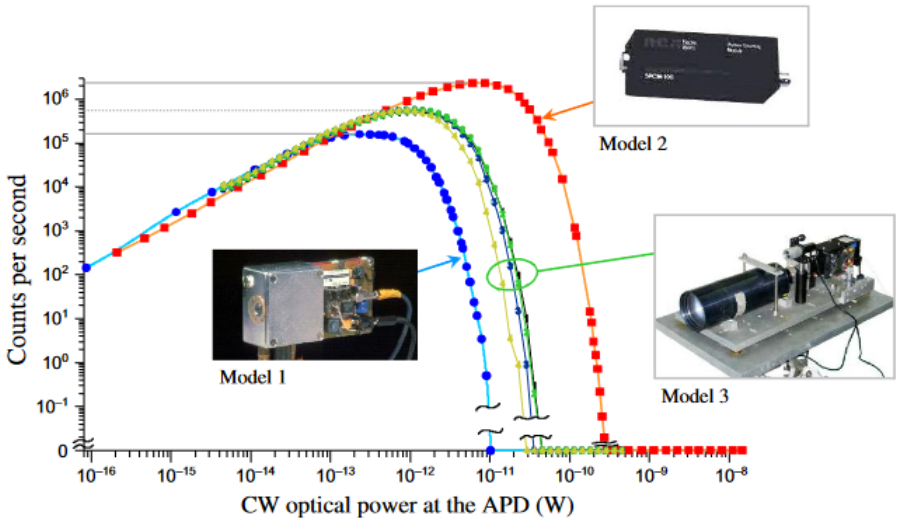

Figure 2.6: Detector saturation curve for three SPAD models. Reprinted from [60].

When count rates are too high, the passive quenching circuitry is unable to reset fast enough to report the high number of dark counts accurately. This can happen when the light source is too intense (near nW level) or when V_{ex} is too high and the count rate is dominated by thermally generated false counts . One can spot SPAD saturation by adjusting the intensity of the photon source and observing decreasing counts with increasing intensity, or by adjusting the excess bias and observing decreasing dark count rate with increasing bias (see Figure 2.6). Operation below the saturation point is necessary to obtain an accurate measurement of count rates [60].

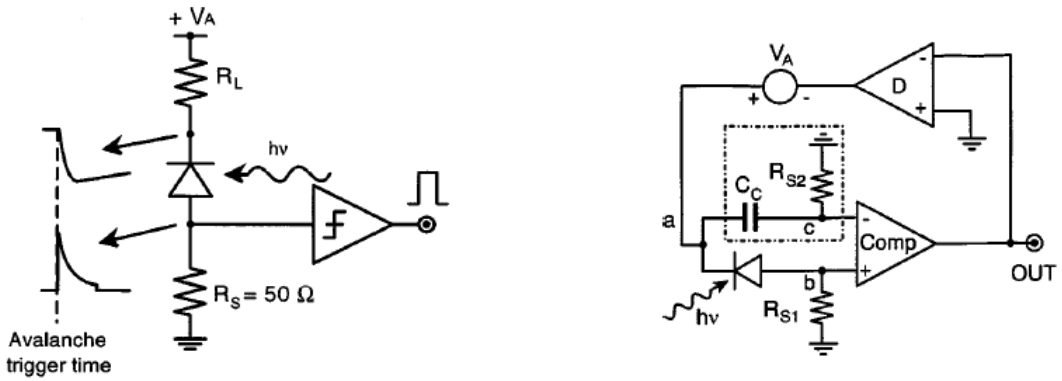

(a) (b)

Figure 2.7: Passive (a) and active (b) quenching circuit schematics [39].

2.4.2 Active Quenching

The principle of active quenching is based on a feedback loop which senses the rise of the avalanche pulse and adjusts the SPAD bias voltage accordingly (Figure 2.7b). This reduces the quenching and reset transition duration. This circuit type is active because a voltage driver switches the bias voltage down to V_{Br} or below in real time, then the switches back to V_{ex} after a controlled hold-off time. The advantage of active quenching is a fast transition time which makes it a better circuit for high count rate applications [39].

2.4.3 Gated Operation

Similar to active quenching, gated operation of SPADs forces the bias voltage below V_{Br} for a fixed hold-off time. However, this forced transition is periodic and independent of avalanche timing. Figure 2.8a shows a typical schematic for gated passive quenching. The SPAD is operated at $V_A < V_{Br}$. With the use of a function generator set to output a pulse of voltage height of V_g, the SPAD is biased to $V_{ex} = V_A + V_g > V_{Br}$ at the frequency of the pulse waveform. The periodic overbiasing takes the SPAD from the gate `off` state to the gate `on` state when it can sense photons [39].

Gated operation of SPADs is useful in applications when the photon arrival time is approximately known [74, 38]. It is also commonly employed when using SPADs which suffer large afterpulsing effects, such those fabricated with InGaAs/InP. This is because the gate `off` state of the SPAD can be useful for detrapping carriers which could potentially add to false avalanche counts upon release. The gate duty cycle must be chosen so that it allows for most trapped carriers to be released between gate `on` states. However, too long of a gate `off` time (or hold-off time) limits the maximum count rate which the SPAD can accept. Therefore, there is a careful balance that must be fulfilled so that the SPAD is able to sufficiently account for incoming photons, but also is quenching for enough time to release any trapped carriers [39, 74, 38, 67]. Another difficulty with gating is the suppression of derivative signals created due to the capacitative response of the SPAD [101]. Clever circuit design must be employed to combat this issue, such as the use of band elimination filters [67]. Using passive quenching, high tens of MHz gating has been achieved, and faster gating is possible with additional active quenching electronics [101, 38].

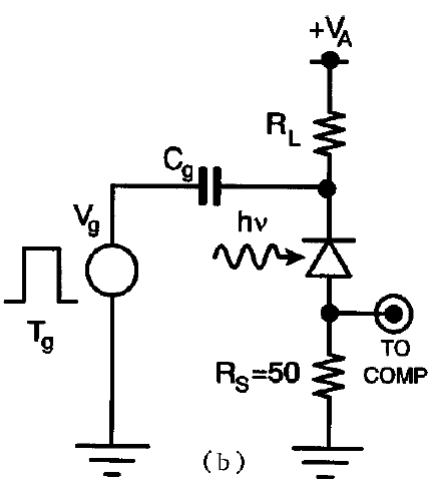

(a) Gating circuit schematic [39].

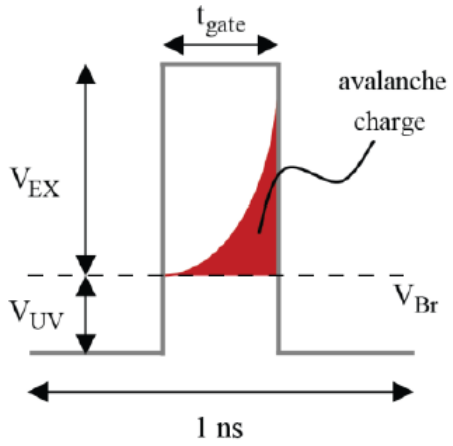

(b) Avalanche current occurring within in the gate on state of the SPAD. Reprinted from [38].

Figure 2.8: Gating circuit with passive quenching

As detectors capable of detecting a single quanta of light, SPADs are a natural choice for applications in quantum communication. However, other single-photon detecting technologies exist, as mentioned in Chapter 1. SPADs have a large advantage over the named technologies when operating in space. For one, they do not need cryogenic cooling but rather can solely use compact thermoelectric coolers to fine-tune the operating temperature. SPADs are much smaller in general when compared to PMTs and other detectors, and their readout circuits are relatively simple. Minimizing payload weight and size is critical from a engineering an well as cost standpoint. SPADs have been historically chosen as the detectors used for quantum measurements and their security in quantum communication schemes has been well-studied. Early demonstrations of the feasibility of SPAD use in space quantum communication are preceded by years of testing semiconductors and non-avalanche detectors in space or at least in space-like environment on Earth. A major consideration of sending SPADs into space is the effect of radiation on the single-photon detection ability of the detector. This topic will now be examined more closely, both from a historic and current state-of-the-art standing perspective.

Chapter 3

SPADs in Space Radiation

3.1 Introduction

There are several types of harmful radiation which must be considered while designing electronics destined for space. As on Earth, there are two overarching types of radiation: non-ionizing and ionizing. The former comes in the form of photons, such as radio waves and visible light, or particles. Non-ionizing particles can cause displacement damage through displacing atoms in the lattice through transfer of energy and momentum. Ionizing radiation from photons or particles has enough energy to ionize electrons from atoms thereby increasing the population of charge carries [83]. Energetic photons such as gamma rays are more problematic for biological materials and their effects are considered predominately for putting humans in space. In comparison to particulate radiation, photons contribute a negligible amount of damage to electronics in space. Particulate radiation, however, can wreak havoc on electronics through the mechanism of displacement damage, which will be discussed shortly. Therefore, it is important to study, understand and model the space radiation environment when planning missions involving sensitive electronics like single-photon avalanche diodes and their readout electronics.

Table 3.1: Classification of mission hazards expected at various altitudes. Adapted from [81].

Feature	LEO ($< 2000km$)	MEO	GEO ($> 35000km$)
Van Allen Belt	At worst, may reduce missions effectiveness.	At best, may reduce effectiveness. At worst,will shorten mission.	May cause upset to mission transiently.
Solar flare particle	May cause upsets.	May cause upsets.	May reduce mission effectiveness.
Galactic Cosmic Rays	May cause upsets	May cause upsets.	May reduce mission effectiveness.

3.2 Space radiation environment

The immediate space radiation environment around Earth is well-known and can be modelled effectively, although it is quite dynamic. Table 3.1 summarizes the three types of particulate radiation and the threats they pose to missions.

Trapped Particle

Energetic particles trapped in the Earth's magnetosphere create the Van Allen Belt (Figure 3.1). This region extends from the geomagnetic equator to approximately $\pm 50^o$ geomagnetic latitude [81]. The shape of the Belt follows the geomagnetic field, except at the South Atlantic Anomaly, where the Belt extends almost to the atmosphere ($\sim$ 500 km altitude) due to an ever-changing offset[1]of the geomagnetic field from the Earth's axis of rotation. This extension of the trapped particles makes the South Atlantic Anomaly the area of most radiation damage accumulation (Figure 3.2). .

The Van Allen Belt can be subdivided in to electron-dominated and proton-dominated areas, and the electron-dominated areas can be further divided into an inner and an outer zone. The inner zone begins at the geomagnetic equator and extends to 15 000 km, while the outer zone extends until almost 80 000 km [87]. Within these two electron zones, the electrons are distributed according to their energies and flux (number of particles per unit area). Although electrons have a large presence in the Van Allen Belt, their effects on electronics can be eliminated through moderate shielding, since the dominant energies are

[1]The location of the magnetic poles drifts every day due to the dynamic nature of the Earth's molten core [23]

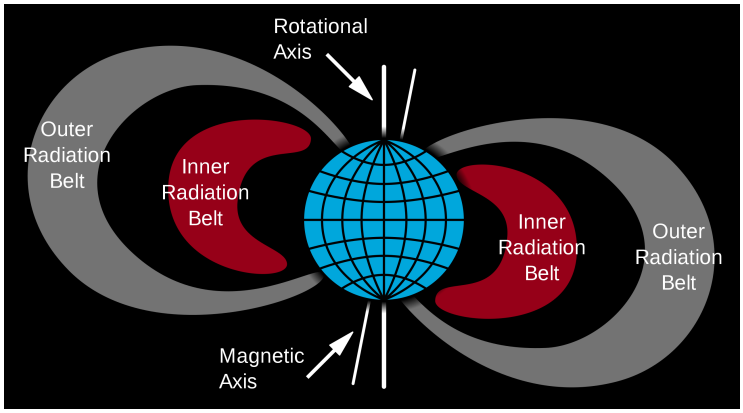

Figure 3.1: Schematic of shape of inner and outer radiation belts which make up the Van Allen Belt of trapped particles [14].

in the keV range [81]. Protons in the Van Allen belt do not occupy zones, but rather inhabit a continuous area extending to geosynchronous altitudes. Protons can reach much higher energies than electrons, with a peak of >30 MeV protons at 2500 km altitude, and therefore shielding against them must be considered more seriously.

Although electrons, protons and other charged particles are trapped in the Earth's magnetic field, it is does not mean they are static. Charged particles gyrate along the magnetic field lines and reflect at "mirror points", which are regions of maximum magnetic field strength (Figure 3.3) [87]. The distribution of the Van Allen Belt varies with solar activity. During solar maximum, the Earth's atmosphere extends further out and the Van Allen belt is compressed [81]. This would result in fewer potentially harmful radiation interactions for satellite transiting through the belt. Additionally, it is believed that during solar maximum there is an increase in the removal rate of trapped protons from the belt [77]. The trapped particle flux is greater, therefore, at solar minimum.

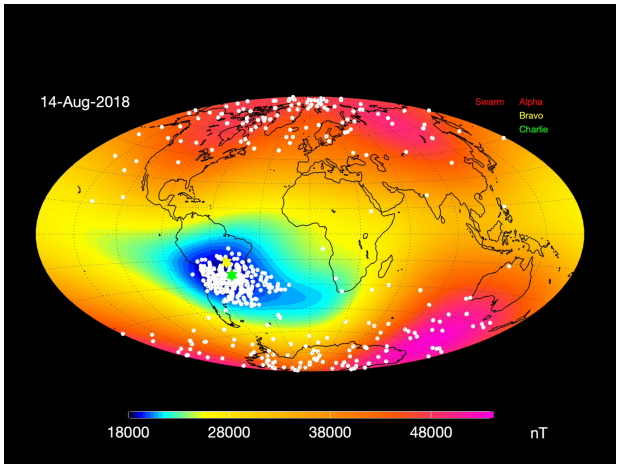

Figure 3.2: Heat map of Earth's magnetic field with dark blue section showing the weakening of the field which causes the South Atlantic Anomaly (SAA). White dots show areas where ESA Swarm instruments register radiation impact, showing visibly more occurrences near the SAA and geomagnetic poles [13].

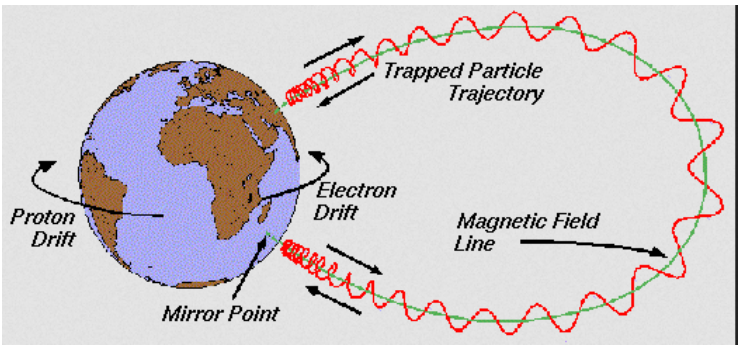

Figure 3.3: Illustration of trapped particle motion [10].

Galactic Cosmic Rays

Galactic Cosmic Rays (GCR) is a general term for an atomic nucleus or electrons incoming isotropically from deep space. Their energies vary immensely from 10 MeV per particle to 10^{16} MeV [81]. Despite their huge energies, GCRs are complications mostly for GEO missions, since the Earth's magnetic field and solar winds tamp down the effect of GCRs

close to the Earth. There are two caveats to this protection: firstly, there is limited protection against GCRs at the magnetic poles, since the field is weaker there. As such, polar orbits will likely incur more radiation due to this; secondly, like trapped protons in the Van Allen Belt, GCR flux varies inversely with solar activity so that the maximal occurrence of GCR interaction will be during solar minimum. This is solely because during solar maximum there is more contribution to dose from interaction with solar-created particles, like protons and other charged nuclei. There is a factor of three or more difference in GCR radiation dose at GEO compared to LEO and, due to their possibly high energy, shielding may not be sufficient to protect electronics [81]. Therefore, careful design of electronics must be made when sending them into GEO regions.

Solar Particles

This category of particulate radiation consists mostly of protons but can include other nuclei generated by the Sun in regular solar activity as well during periods of increased activity such as during coronal mass ejections (solar flares). Although solar cycle tracking is possible, solar flares or storms are still difficult to predict. As such, Solar Particle Events (SPE) are the most variable component of space radiation [81]. The energies of particles in these events can range from 10 to 1000 MeV and, while the magnetosphere will trap these particles from reaching the atmosphere, a solar flare can hugely increase the amount of trapped particles in the Van Allen Belt, as well as reach critically low altitudes at the magnetic poles. Beyond the Earth's protective magnetosphere, SPEs can be especially detrimental to electronics since they are essentially random and can be very energetic. Anomalously large events ($\sim$1000 MeV) render shielding useless, can cause displacement damage and other upsets and can severely reduce mission lengths. The most promising choice to mitigate issues due to SPEs would be operate at solar minima, however, as discussed earlier, this comes with increased interaction with potentially highly energetic GCRs and trapped protons [81].

Deep-space radiation

With increasing interest of sending manned missions and performing experiments beyond LEO, observing and modelling deep-space radiation is critical. GCRs and SPEs will both contribute to the radiation effects experienced by electronics (and humans alike), but one must not forget the interaction with energetic particles while traversing through the Van Allen Belts. The geometry and trajectory of the spacecraft will affect the exposure and dose rates while attaining the terminal altitude (Figure 3.4) [22].

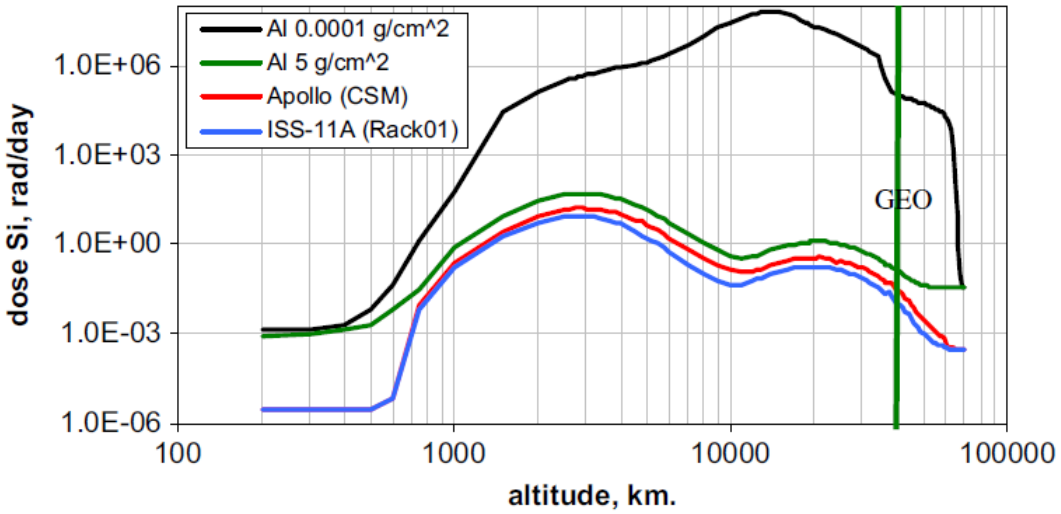

Figure 3.4: Modelled total ionizing dose rate in silicon while traversing through LEO to GEO. The black and green curve represent two thicknesses of Al shells, while the red and blue curve represent structures from an Apollo-era mission and from the ISS. The humps in the curve show the peak densities of trapped particles. Reprinted from [22].

Beyond the Earth's magnetosphere, spacecraft are still susceptible to interactions with charged particles. Even a relatively close and familiar object to us, our Moon, hardly receives any radiation protection from its proximity. Modelling charged particles arriving isotropically towards the Earth, thus simulating GCRs, showed that these particles' fluxes did not change significantly inside a distance equal to 100 times the Earth's radius (R_E) (638 000 km; Moon is at around 400 000 km), and remained unchanged until 7.8 R_E where

the magnetic field finally deflected the lower energy particles. Therefore, the Moon is shown to be outside of the protective influence of the magnetosphere [48]. Conversely, the Moon in fact may contribute to radiation effects through "albedo" particles, which are particles like protons and neutrons released into the near Moon area through nuclear interactions between incoming GCRs and the lunar surface. Since the Moon's surface position relative to the Earth is constant, it actually provides a shadow for the Earth from GCRs and SPEs, and the surface facing away from Earth is bombarded with GCRs. Measurements from the Cosmic Ray Telescope for the Effects of Radiation (CRaTER) aboard the Lunar Reconnaissance Orbiter (LRO) found that the composition of particles 50 km above the Moon's surface consisted 91.35% of GCRs and 8.62% of albedo particles (Figure 3.5) [82]. Albedo particles are mostly an issue for spacecraft on the surface of or closely orbiting objects without an atmosphere, and even then GCRs and SPEs will make up the bulk of the radiation hazards.

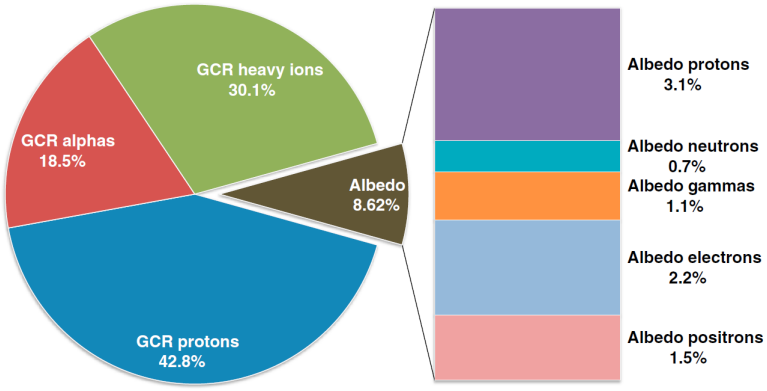

Figure 3.5: Proportion of GCR and albedo particles measured by CRaTER orbiting Moon. Reprinted from [82].

Other measurements from deep space that we posses include those from the Mars Odyssey mission, of which a portion of the hardware aboard were solely devoted to measuring GCRs and solar particles [100]. Ironically, one of the measurement apparatus suffered immense radiation damage during a huge solar event and went offline for a large portion

of the mission. However, the other devices aboard had sufficient precision to estimate the magnitude of the random solar event which lead to the demise of its co-inhabitant. The mission determined that GCRs near Mars are continuous and variable with protons consisting of up to 90% of the particle population, followed by helium, electrons and other heavy ions. SPEs were defined by their relatively larger flux as compared to concurrent GCRs in units of $cm^{-2}sr^{-1}s^{-1}$ which they dubbed particle flux units (pfu). The mission experienced on the order of 0.1-0.2 pfu of GCR on a constant basis but during SPEs the distribution of events was 12 events at less than 1 pfu, 7 events between 1 and 6.1 pfu, 2 between 50 and 100 pfu and 1 above 100 pfu. Measurements on the same days at Earth showed that the scaling of SPEs from Earth to Mars is a greater drop than R^{-3}, however, the Earth's magnetic field shields most satellites and humans from these bursts of high flux [100].

3.3 Radiation processes in semiconductors

Radiation particles deposit energy into semiconductor materials via two means: ionizing or non-ionizing processes. An ionizing process has enough energy to strip electrons from the semiconductor atoms, thereby creating electron-hole pairs. This can lead to damage as it introduces excess charges which may be trapped at interface region between the semiconductor and neighbouring insulator regions [50]. Non-ionizing process, as the name suggests, do not ionize atomic electrons, but rather have enough energy to displace an atom from the semiconductor lattice via Coloumbic, nuclear inelastic or elastic scattering[84]. If the first displaced atom (known as the primary knock-on atom) has sufficient energy to displace other atoms, the displacement process will continue (Figure 3.6). The damage resulting from this energy deposition process is known as displacement damage and has broad consequences on the semiconductor operation and behaviour. While ionization damage is expected in space, displacement damage is the dominant issue for operating semiconductors in space. As such, this damage mechanism will now be discussed more in depth.

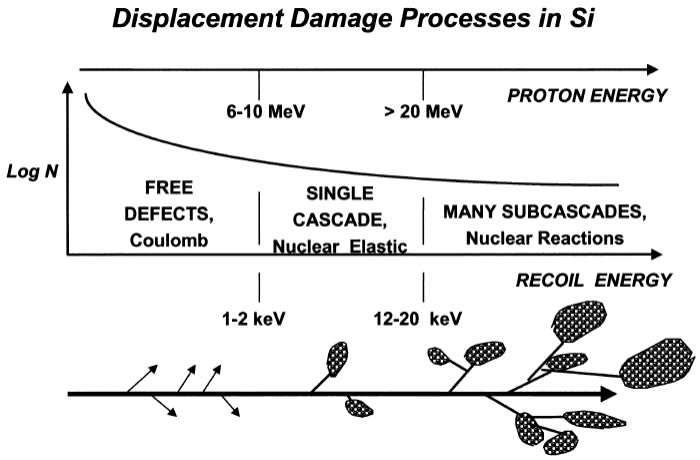

Figure 3.6: The size and concentrations of defects is a direct result of the incident particle energy and the number of interactions which can take place before the displacement damage process is complete. The above schematic relates the number of interactions (N) with the particle energy and the resulting types of defects, from point defects to large clusters caused by cascading displacement processes. Reprinted from [86]

Displacement of atoms from the semiconductor lattice creates absences in the lattice pattern known as vacancies and, in conjunction, introduces atoms in non-lattice positions, known as interstitials [86]. Vacancies and interstitial atoms are considered to be defects in the semiconductor and can exist as isolated entities (point defects) or appear in larger groups (clusters). Both point defects and clusters can result from non-ionizing processes with highly energetic particles ($>$ 10 MeV). The fundamental result of introducing these defects in the lattice is a change in the energy levels of the semiconductor bandgap, therefore inducing changes in the characteristic parameters of the semiconductor [86, 84]. To be more specific, the major effects resulting from displacement damage induced defects are :

a) Increased thermal generation of carriers (electrons and holes)

b) Increased recombination of electron-hole pairs leading to shorter recombination lifetimes

c) Temporary trapping and subsequent emission of carriers

d) Increased carrier tunnelling events

Figure 3.7 illustrates this in a neat schematic of the effects of new energy levels in the lattice bandgap. Introduction of the energy level E_G, shown in part (a), allows for more thermal generation of carriers since movement from the valence (E_V) to conduction (E_C) band requires two steps of lesser energy input compared to when the energy level is absent. Similarly, introduction of the energy level E_R, shown in part (b), enhances recombination of carrier pairs by requiring a lower threshold energy. Part (c) demonstrates a carrier getting trapped at newly formed energy level E_T and its subsequent release back to the conduction band. Finally, part (d) demonstrates an overall reduction in carriers due to the presence of increase donor and carrier energy levels (E_D and E_{CR}, respectively). Tunnelling events will also decrease carrier concentration [84]. All these microscopic effects will contribute to an overall increase in noise or false events in semiconductor devices, including SPADs.

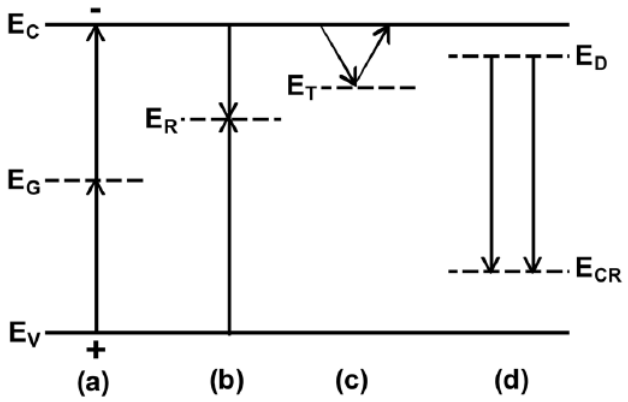

Figure 3.7: Schematic of major effects in energy bandgap due to displacement damage.E_G, E_R, E_T here represent energy levels which can lead to thermal generation, carrier recombination and carrier trapping, respectively. Reprinted from [84].

The changing of materials' characteristic parameters with radiation must be described with respect to the amount of radiation the material is exposed to and the amount of energy that is absorbed. This is encompassed in the concept of Non-Ionizing Energy Loss (NIEL), which calculates the rate of energy loss due to atomic displacements as radiation

particle traverses through the material. Essentially this is $-(dE/dx)$, meaning it is the rate of energy loss per unit length. In nuclear physics this concept is known as stopping power. The negative sign indicates that energy is being lost by the incident particle to the absorbing medium. NIEL can be calculated by the following integral:

$$NIEL = \frac{N}{A} \int_{E_{thresh}}^{E_R^{max}} E_R L[E_R] \frac{d\sigma(E, E_R)}{dE_R} dE_R \tag{3.1}$$

The integral can be explained through the atomic scattering picture. The incoming particle has energy E. Upon scattering, the target atom will have recoil energy E_R. The integral is a summation of all possible target atom recoil energies from the minimum threshold energy that may be imparted onto the target nuclear E_{thresh} up to maximum recoil energy E_R^{max}. Additionally, $\frac{d\sigma(E,E_R)}{dE_R}$ is the differential cross section of incident particle with energy E to transfer recoil energy E_R onto the target atom. This can be phrased in terms of a probability of that amount of energy being transferred. Finally, $L[E_r]$ is the Lindhard Partition Function which estimates the amount of energy lost via ionization processes, N is Avogadro's number and A is the atomic mass of target atom. NIEL, therefore, takes into account the incident particle type, energy and target material. Tabulation of NIEL values has been undertaken many times in the past and NIEL versus incident particle energy plots can be easily generated using open-source web-based calculators such as the Screened Relativistic Nuclear and Electronic Stopping Power Calculator [12]. NIEL can be calculated for a range of particle energies, depending on the expected radiation environment, thereby yielding a NIEL curve. Figure 3.8 shows a typical NIEL curve. We see that the highest loss of energy occurs for lower incident particle energies, just above the threshold energy of the target atom. This can be interpreted as the following: when a particle of energy $E >> E_{thresh}$ interacts with the atom, it imparts recoil energy $E_R \geq E_{thresh}$. The original incident particle now has a lower energy than before the first interaction, but if it still has energy greater than the displacement threshold energy of the material (that is, $E' < E$ but $E' > E_{thresh}$), it will continue to displace further atoms. A greater proportion of its energy is transferred with each interaction, such that when the incident particle has energy just greater than that of the threshold energy, it is finally completely transferring

all its energy to a target atom. Similar curves can be generated for compound materials such as InGaAs, although now one must consider than each atom in the compound has a separate displacement threshold energy, so the stoichiometric balance of the compound is also inputted into the calculation.

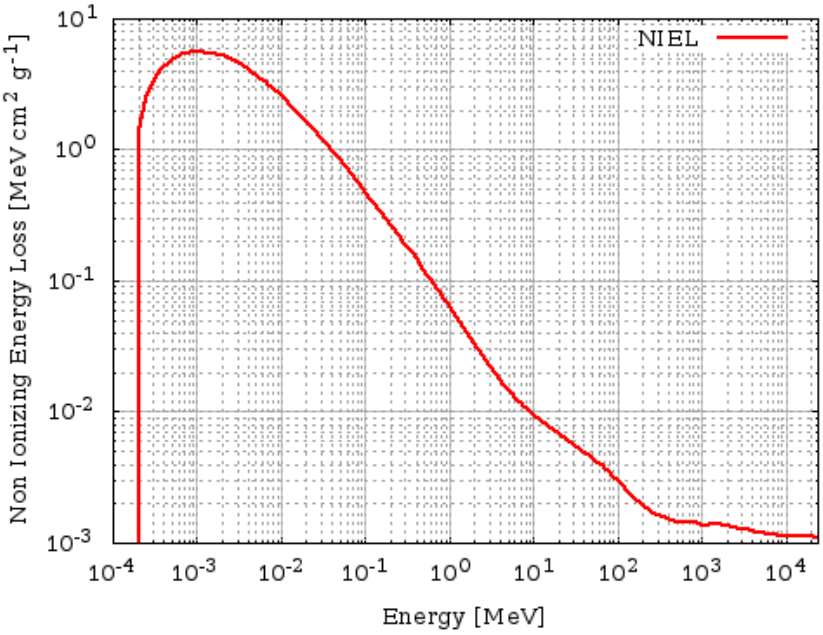

Figure 3.8: NIEL curve for protons incident onto Silicon with a threshold energy of 21 eV [12].

NIEL is the displacement process analogue to linear energy transfer which is the energy transferred in an ionization process. As such, other similarities have been made between displacement and ionization processes, namely with respect to the concept of absorbed dose. Like NIEL, linear energy transfer takes the incident particle and material into consideration and maps out the amount of energy loss due to ionization; then, the absorbed dose is the energy transferred to the material per particle, so it is the product of the linear energy transfer with the ionzing particle fluence. This framework can be utilized with respect to non-ionizing processes as well: the product of NIEL with fluence gives the displacement damage dose [89]:

$$D_d = \Phi \times NIEL \tag{3.2}$$

An interesting result of this relationship between NIEL and D_d is the so-called "NIEL scaling" phenomenon, where the damage inccured by the material is observed to be invariant with NIEL for any incident particle type and energy [84]. This can be seen in Figure 3.9a and Figure 3.9b. The top plot shows the normalized power degradation in GaAs solar cells when exposed to several energies of protons. The ordinate axis is particle fluence. Though difficult to see in this printing of the plot, the order of the curves from bottom to top (from maximum power degradation to least) is 0.5 MeV, 1.0 MeV, 3.0 MeV and finally 9.5 MeV. We see that the highest proton energy, 9.5 MeV, required a much higher fluence in order to inflict the same amount of power degradation in the solar cell. If one multiplies the NIEL of each particle by the required fluence, then the data can be replotted such that the ordinate axis shows the absorbed (displacement damage) dose (bottom plot). Critically, we see that all the points lie on the same curve. Therefore, regardless of the particle energy and simply due to the particle fluence, the same power degradation was achieved after the same absorbed dose.

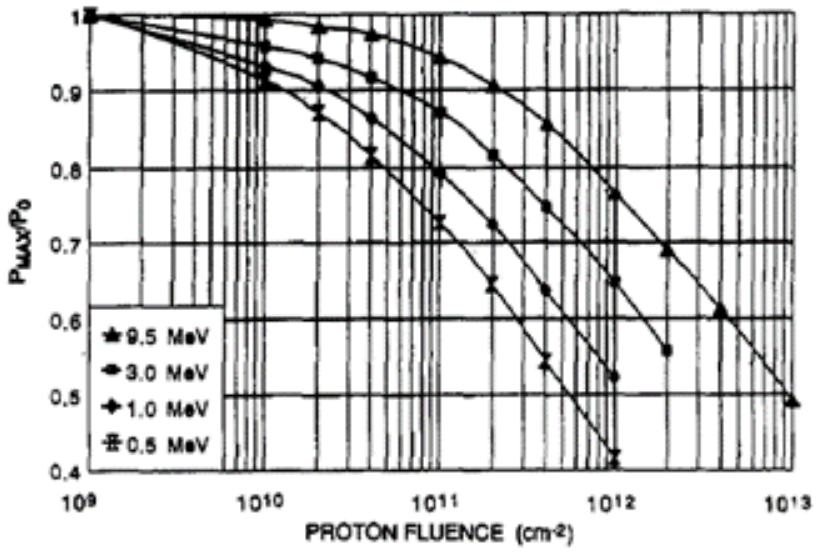

(a)

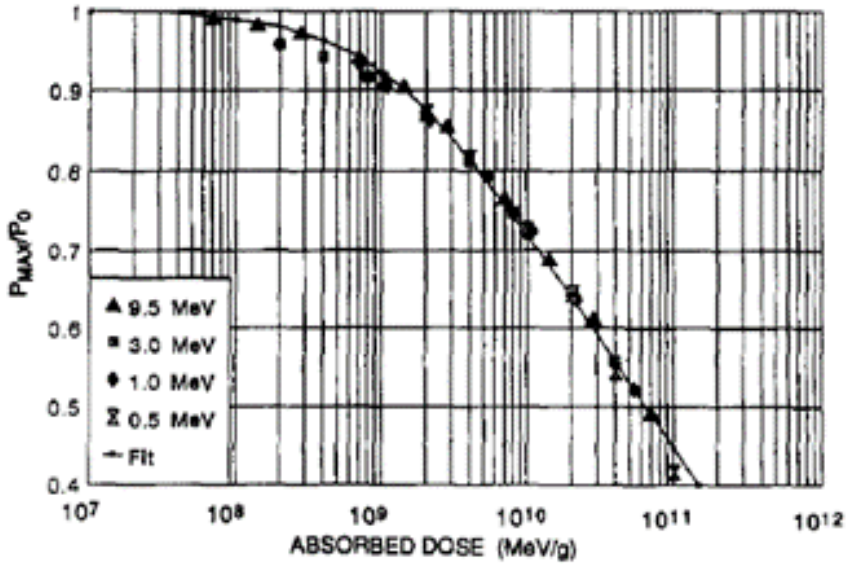

(b)

Figure 3.9: Normalized power degradation of GaAs solar cells after exposure to protons of various energies, plotted as function of particle fluence (a) and absorbed dose (b). Reprinted from [89].

One possible explanation for NIEL scaling is that absorbed dose and the observed radiation effects in the materials result from the type and concentration of defects created by the radiation. Low NIEL particles produce small, isolated defects while high NIEL particle can produce both isolated and cluster defects [86]. NIEL scaling is an essential phenomenon for ground testing of materials prior to sending them to space because it allows for correlating one particle and energy type to another through the concept of equivalency. Space radiation is composed of a large spectrum of particle types and energies, but on the ground, one can usually only shoot a single beam of one type of particle and energy. NIEL scaling ensures that the same amount of damage will occur in the material as long as the corresponding displacement damage dose is achieved, and that dose can be achieved with any particle type or energy. Therefore, we can take the expected displacement damage dose in space due to many particle types and energies and simulate it using a single equivalent fluence of one particle type and energy on the ground, such as 100 MeV protons. NIEL scaling is well-documented and discussed, though its application limits are still under investigation [86, 84, 18, 19].

The final step to describing radiation effects quantitatively is the relate the displacement damage dose to the observed change in the material. The damage factors can be generated for any characteristic parameter of a semiconductor so long as it measurably affected by the radiation [85]. For example, the typical damage factor quoted for semiconductors with a depletion region is the change in a dark-current damage factor which establishes the change in dark current per unit displacement damage dose. This damage factor can be extracted from a plot of particle displacement damage dose versus $\frac{1}{\tau_g} - \frac{1}{\tau_{g_0}}$, where τ_{g_0} and τ_g are the pre- and post-irradiation thermal generation lifetimes in the depletion region [85]. Such damage factors make is easier to quantitatively compare radiation effects for various radiation fields and materials.

3.4 Current understanding of radiation effects in non-single-photon sensitive InGaAs detectors

Research into the manifestation of radiation damage in semiconductor materials is spurred by the application of those materials, whether it is being used in a microelectronic component such as metal-oxide-semiconductor (MOS) gates or as part of a solar cell. Silicon has been a typical choice for many studies since it is pervasively used in multiple industries, though InGaAs studies are not necessarily underrepresented. The primary application of InGaAs experiments' results are for the telecommunications and remote-sensing industries which do not necessarily require single-photon sensitivity. Therefore, radiation effects for such classical signal detectors are typically described by differences in dark current (ΔJ) between radiation exposures. This is contrast with measuring differences in DCR between radiation exposures, which is the characteristic shot noise of single-photon sensitive SPADs and is not directly correlated to the dark current measured in SPADs' linear mode operation [101]. Due to the structural and operation differences between SPADs and less sensitive photon detectors, results from InGaAs non-SPAD radiation testing (like those presented in Table 3.2) can provide a preliminary insight into expected radiation effects, but should be interpreted with consideration.

Table 3.2: Selected results of proton radiation ground testing InGaAs detectors.

Max Proton Energy [MeV]	Maximum Fluence $[p^+/cm^2]$	Photodiode Type	Active Area Size [μm]	ΔJ [orders of magnitude]	Reference
63	2×10^{12}	avalanche avalanche	30 80	2 4	[26]
105	2×10^{11}	PIN	1000	1	[16]
170	6.3×10^{11}	PIN Unknown	350 1000	1.5 1.5	[70]
3.5	1×10^{13}	PN	500	3.5	[68]

Previous non-SPAD studies have reliably shown that dark current increases linearly with increasing particle fluence (or with displacement damage dose). When extracting a

dark current damage factor, that is, the rate of dark current increase per unit fluence, Becker et al., found that despite normalizing results by the detector active volume, a sample with a large active volume still had a much large damage factor (>6) [26]. They concluded that displacement damage is likely more dependent on the semiconductor's doping profile rather than the detector active area size: higher doped depletion regions suffer more carrier generation and greater dark current. This result was contradicted by Nuns et al., who argued that larger active volumes should incur more defects and present a larger post-radiation dark current. The relationship between change in dark current, or other semiconductor characteristic parameters, and displacement damage dose is still unclear and more analysis is required [70].

In addition to proton testing, a comprehensive list of electron, neutron and gamma ray testing has also been conducted by Nuns et al. In general, neutrons and protons caused the largest increase in dark current, and above 1.5 MeV displacement damage effects dominate over ionization effects. Additionally, biasing the detectors during irradiation was found to be slightly less dark current increase, though this was only evident with exposure to low electron and gammas. As such, biasing conditions during irradiation likely do not result in additional changes in dark current [70].

In-orbit observation of macroscopic effects of displacement damage were also reported for non-SPAD InGaAs detector arrays aboard two satellites, SPOT 4 and ENVISAT [24], [54]. These arrays were multiplexed photodiodes where each photodiode acted as a pixel. Both of the satellites' instruments reported pixels with dark current spikes (10 to 1000 times increase) or pixel fatality, as well as unstable dark current levels which periodically switch between discrete levels. In the case of array on the ENVISAT, pixels were found to stop functioning almost exclusively around the area of the South Atlantic Anomaly (Figure 3.10).

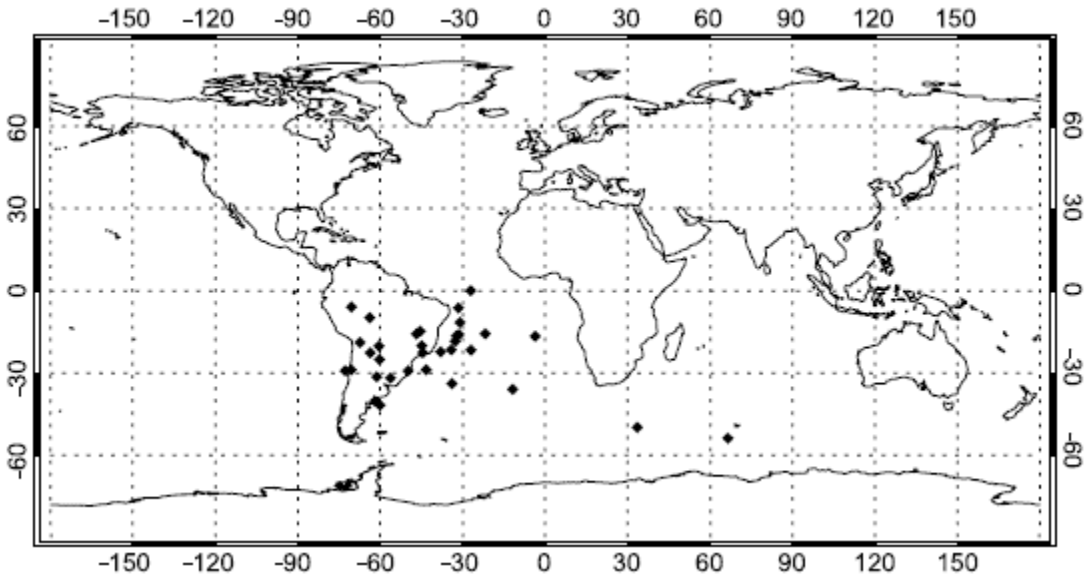

Figure 3.10: Geolocation of pixel degredation aboard ENVISAT corresponds to high radiation field of South Atlantic Anomaly. Reprinted from [54].

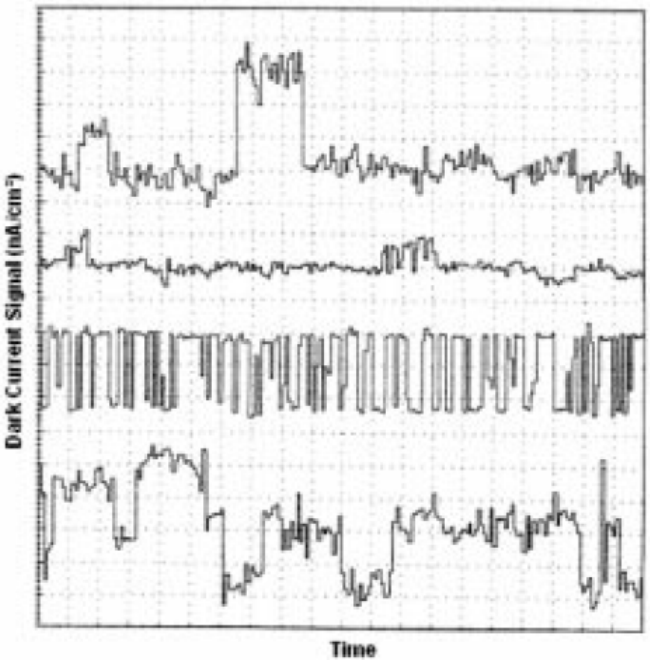

Figure 3.11: Dark current signal over time after 38.5 MeV irradiation of InGaAs detectors similar to those on SPOT 4. The dark current fluctuates over long periods of time between distinct levels. Reprinted from [24].

These are the first reports of dark current spikes (known as hot pixels) and dark current level switching (known as random telegraph signal, Figure 3.11) in in-orbit InGaAs detectors. These effects were previously well-documented in ground testing of silicon electronics and detectors, but this is the first occurrence of likely radiation-induced InGaAs pixel failure. After discovering this behaviour in in-orbit, the SPOT 4 researchers conducted ground testing of similar InGaAs diodes, exposing them to a range of proton energies from 9.1 to 300 MeV with a maximum fluence of $10^{10} p^{+}/cm^{2}$. They found that dark current spikes were found as large as 37 times greater than the average dark current value and 3% of pixels had a dark current ten times larger than the mean, confirming the in-orbit detector array's behaviour [24].

In-orbit measurements aboard the ENVISAT revealed an interesting deviation in measurements of the InGaAs detector arrays aboard which could be divided into subsets classified by the lattice matching of the semiconductor (InGaAs) to the substrate (InP). A stoichometric proportion of 0.53 Indium to 0.47 Gallium produces a *lattice-matched* material, while a a higher proportion of Indium leads to *lattice-mismatch* with the InP substrate. The substrate lattice-matching was chosen to tune the detector wavelength sensitivity, with a larger Indium fraction allowing for better responsitivity to longer wavelengths [54]. The in-orbit data showed that lattice-matched detector channels did not suffer nearly as much dark current increase or pixel failure as the lattice-mismatched channels. After gathering in-orbit measurements, Kleipool et al. conducted ground testing of lattice-mismatched InGaAs with 2.5 MeV electrons and 15 MeV protons to a final dose similar to that of the ENVISAT detectors in-orbit, in the hope of confirming that lattice-mismatched InGaAs detectors suffer radiation effects more than lattice-matched detectors. However, no significant increase in dark current was found during this ground testing. Despite this, real macroscopic effects were reported for the in-orbit detectors, leading the authors to suggest that a combination of device properties, operating conditions and known high radiation field lead to pixel fatalities and the random telegraph signals. They also concluded that the lattice-mismatched detectors suffered greater damage due to inherently more defects in the lattice structure than lattice-matched detectors. As such, lattice-matching the semiconductor and substrate was recommended to reduce the sensitivity to displacement damage

[54].

3.5 Current understanding of radiation effects in SPADs

As discussed previously, the difference in operating conditions and sensitivity between non-SPAD and SPAD devices prevents a direct translation of results between the two detection platforms. For good understanding of radiation effects in SPADs, one must focus on studies which directly test Geiger-mode avalanche diodes. While there is an abundance of such studies for silicon-based SPADs (some of which are presented discussed below and summarized Table 3.3), there is a deficiency of studies on InGaAs-based SPADs (Table 3.4).

3.5.1 Silicon SPAD studies

A large portion of early work in silicon SPAD radiation testing was undertaken by Xiaoli Sun and colleagues at NASA in preparation for and during the deployment of the Geoscience Laser Altimeter System (GLAS) aboard the Ice, Cloud and land Elevation Satellite (ICESat) [93, 90, 92, 91, 57]. Ground-testing was conducted to explore the feasibility of using such sensitive instruments in satellite-based remote sensing programs. A proton beam was chosen to simulate the space radiation environment since the proposed ICESat would be at LEO and cross through the South Atlantic Anomaly which is dominated by trapped protons. Fluences were chosen to reflect expected doses during the mission. Dark count rates were found to increase significantly with as little as 50 rad of exposure (corresponding to a fluence of $1.31\times10^{8}p^{+}/cm^{2}$). Dark count rate increased linearly initially but then began to decrease as the ultimate dose of 30 krad was approached. This was attributed to detector saturation, since at this point DCR $>$ 500 kHz. The next round of studies using the same type of silicon SPADs resulted in similar outcomes of linearly increasing dark count rate with fluence, up to an increase of 4 orders of magnitude, as well as a random telegraph signal behaviour over a long-term dark count rate measurement [90]. The increase in dark count rates observed in both studies from the Sun group, as well through additional simulation and modeling, was determined to be within the GLAS

ICESat mission allowances. Observed saturation was to be combatted by employing eight single-photon counting modules (SPCM, consisting of SPADs and readout electronics), so that while one SPCM was insensitive during its dead time, another SPCM would be ready for detection. The estimated increase in dark count rate per year per device was 50 kcps, which was determined to be acceptable sine it was still lower compared to the background photon rate of the sunlit Earth [92]. Radiation ground testing of identical SPCMs along with other typical pre-flight testing of fresh, non-irradiated SPCMs were fairly successful[2]and the ICESat was launched January 12, 2003.

The SPCMs were first biased on September 28, 2003 and initial dark count measurements showed a large increase in dark counts after the nine-month operational delay. Pre-launch DCR was ∼200 cps while the first in-orbit measurements indicated a DCR of 11 kcps per SPCM. Shortly after the first operation, a monumental solar storm occurred, peaking around October 31, 2003, and provided a unique insight of a clearly harsher radiation field (Figure 3.12) [92]. Prior to the storm, the DCR increased by approximately 30 cps per day per SPCM; during the three day storm, DCR increased by about 3800 cps per day per SPCM. Despite the large increase in dark counts during the storm, the average observed radiation damage in terms of an increase of DCR per year per SPCM for the mission from September 28 to November 18, 2003 was found to only be 15 kcps, about 30% of the predicted level of damage of 50 kcps per year per SPCM [92].

The GLAS ICESat mission published mid-mission results after approximately four years in orbit (2007) and after mission completion in 2010. DCR was found to increase linearly with mission length at a rate of about 60 cps per day per SPCM between 2003 and 2007, after which DCR increased to a rate of 200 cps per day per SPCM (Figure 3.13). The change in rate of DCR increase is not discussed in the most recent study and the authors simply state that the radiation damage was apparent but did not have major effect on the intended altimetry measurements of the mission [57].

[2]Four devices malfunctioned during ground testing and were not operated during the satellite mission [57].

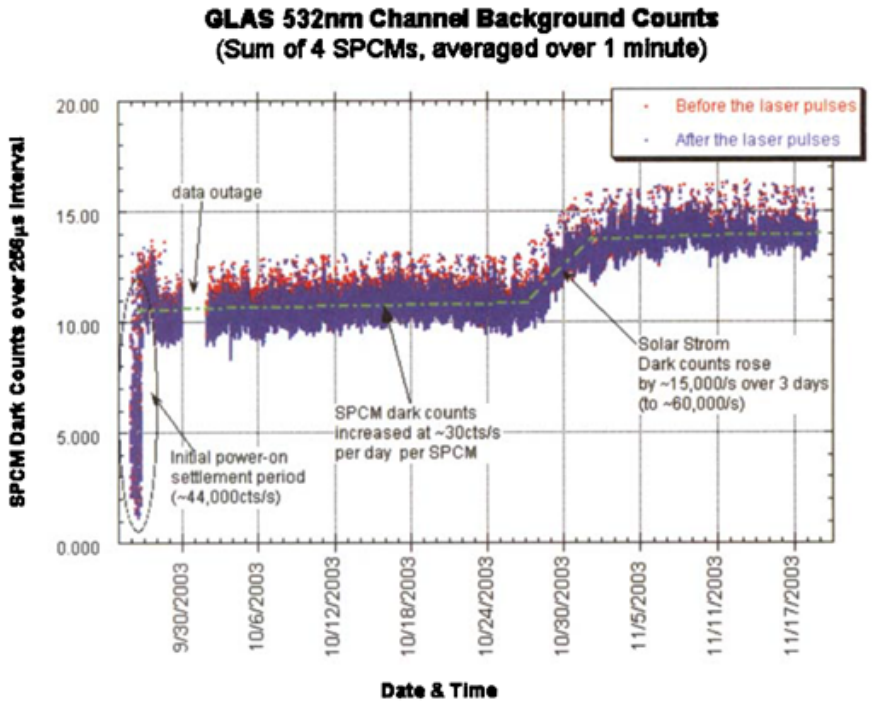

Figure 3.12: Observed dark count rate (purple) of all four GLAS SPCMs over first two month period of ICESat mission. Initial spike in DCR is due to nine-month delay in booting the SPCMs. The Great Halloween Solar Storm of October 28 - 31 2003 increased the DCR by 3800 cps per day per SPCM, and DCR remained permanently higher after the storm. Reprinted from [92].

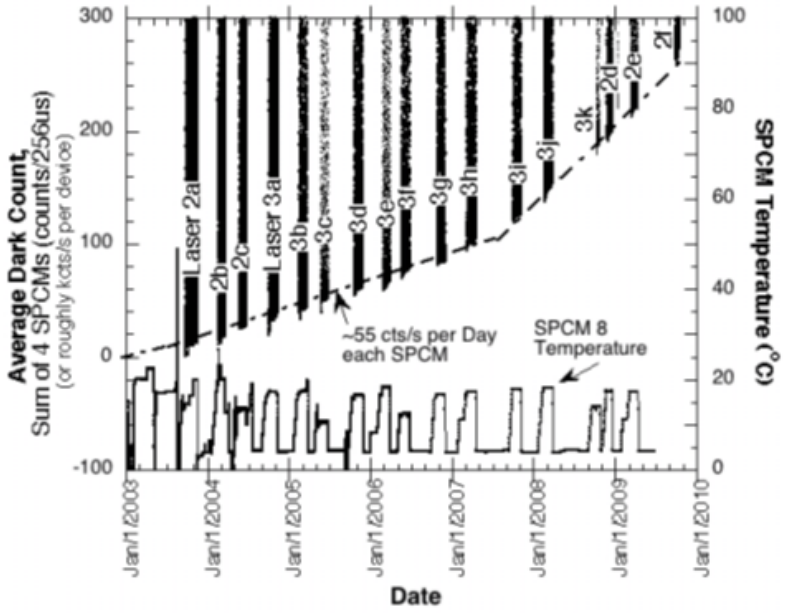

Figure 3.13: Average dark count rate measured throughout ICESat mission duration. The initial DCR increase from 2003 to 2007 was about 60 counts per day; this rose to 200 counts per day after 2007, even after device operating temperature was lowered. Reprinted from [57].

The GLAS ICESat publications were the first in-orbit Si SPAD measurements. Ground testing of various sizes of Si SPADs has occurred with several studies summarized in Table 3.3. In general, at least an order of magnitude difference in post-radiation dark count rate is reported. Other major results of the presented papers include limited evidence of significant ionization damage [94, 61, 66], cases of RTS [66], and detector saturation [94, 56]. In the Italian study, [66], one interesting result was the variability in outcome between devices of identical size and manufacturing quality. For example, of two 50 μm devices irradiated with 31.8 MeV protons, one device showed a four order of magnitude increase in DCR, while the other only showed a factor of 3 increase (Figure 3.14). They ascribe this to a difference in the formation of cluster defects within the semiconductor: if the clusters are formed in the high-electric flied depletion region then the dark count rate should increase [66]. While the location of cluster formation is not controllable, manufacturers of SPADs should attempt

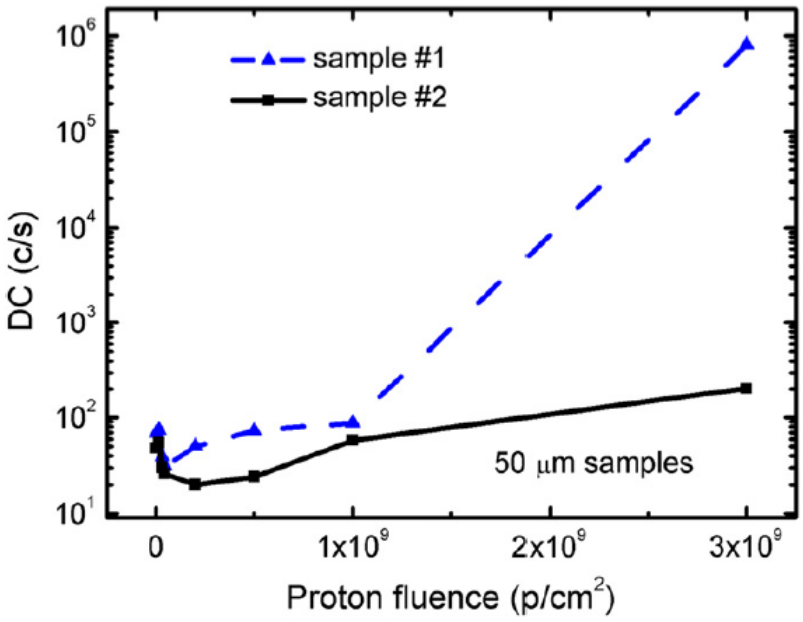

Figure 3.14: Post-irradiation dark count rate (DCR) measurement of two Si SPADs show huge variation despite fabrication process.

to create as similar doping profiles and defect concentrations between devices in order to minimize variation in the response to radiation.

Of the selected studied in Table 3.3, only the last two conducted by members in our group tested SPADs intended for quantum communication (the others were for remote-sensing or high-energy physics purposes)[3][17, 41]. As per Bourgoin et al., successful ground-to-satellite quantum communication requires DCR to be below 200 cps and Anisimova and colleagues point out that at the initial DCR increase of 30 cps per day found by the GLAS ICESat mission a quantum communication receiver would be unusable in a matter of mere months in LEO [34, 17]. This study used identical SPADs to the GLAS ICESat mission (180 μm with on-board thermoelectric coolers), as well as other Si SPADs with larger diameter, irradiated them with 100 MeV protons to a total fluence expected after two years in LEO. After 2 year equivalent irradiation of protons, the DCR of the 180μm

[3]Actually, no other study was found to specifically conduct radiation tests on SPADs for quantum communication.

Table 3.3: Selected silicon SPAD ground radiation testing conditions and change in DCR in number of orders of magnitude. If fluence values were not given, they were calculated using the following equation: $Dose(rad(Si)) = NIEL \times \Phi \times 1.6 \times 10^{-8} \frac{rad(Si)}{gMeV}$ [93]. If Δ DCR was not given in terms of orders of magnitude, it was estimated using the data provided in the study.

Proton Energy [MeV]	Max Fluence $[p^+/cm^2]$	Active Area [μm]	ΔDCR [orders of magnitude]	Ref
14.8 22 28	7.85×10^{10}	500	>1	[93]
53 75 123 151 189	5×10^9	200	4 4 3 4 2	[90]
5 25 50	7.48×10^8 6.92×10^8 5.88×10^8	500	<2	[94]
27	2×10^{10}	50 200	4 3	[66]
31.8	3×10^9	50 350 500	3 >1 >2	
27	2×10^{10}	200	>3	[61]
105	4×10^9	500 500 180	3 2.5 3	[17]
105	4×10^9 2×10^{10}	180 180	2 3	[41]
53	6.7×10^9	100	2	[56]

devices was on the order of 10^5 cps, a scale clearly exceeding the parameters required for successful quantum communication (Figure 3.15) [17]. To counteract the increase in dark count, the group then thermally annealed the irradiated samples using deep cooling and subsequently a hot flow oven. Such thermal annealing was shown to reduce dark counts below to 200 cps threshold [17]. A related more recent study from our group, conducted by a former Master's student Ian D'Souza, showed that repeated annealing (as opposed to annealing after the full dose of proton radiation) managed to sustain the DCR below 200 cps, despite high pre-annealing DCRs [41]. Thermal annealing, as well as other annealing techniques, of SPADs will be discussed later in the thesis. Both studies from our group focused on Si SPADs for satellite-based quantum communication and showed that these sensitive instruments can be employed in space with the appropriate radiation damage control.

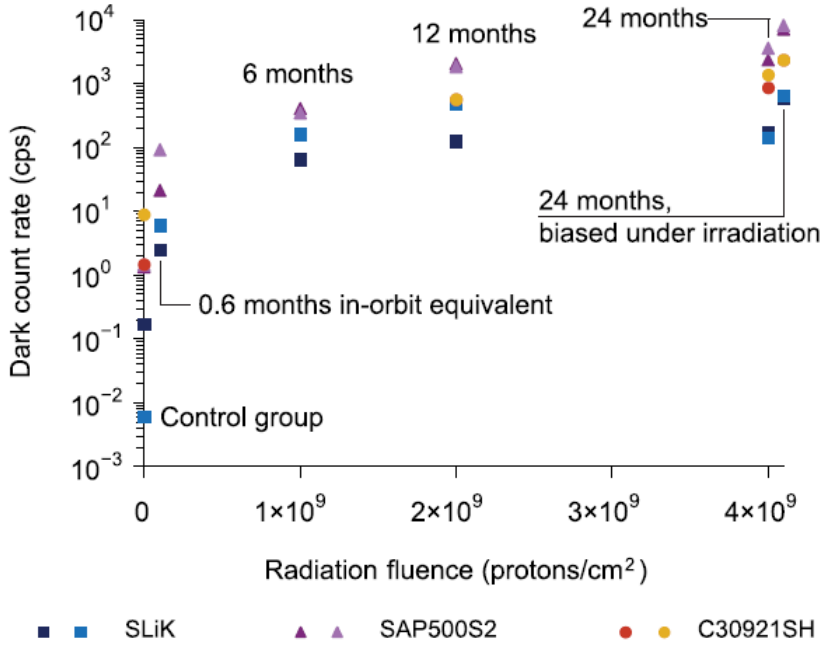

Figure 3.15: Observed dark count rates of 100 MeV proton irradiation of three Si-based SPADs. Reprinted from [17].

3.5.2 InGaAs SPAD studies

In contrast to the previous section, only two publications were found which specifically tested Geiger-mode InGaAs/InP avalanche photodiodes suitable for single-photon detection purposes (Table 3.4).

Table 3.4: Testing conditions and results from previous studies with proton-irradiated InGaAs SPADs.

Proton Energy [MeV]	Max Fluence $[p^+/cm^2]$	Active Area [μm]	ΔDCR [orders of magnitude]	Ref
51	1.25×10^{11}	200	$\leq$2	[25]
51	8.1×10^{10}	25	3	[47]

The two studies come from the same group at NASA testing with the same proton source, but the earlier tests InGaAs/InAlAs Geiger-mode photodiodes while the latter tests InGaAs/InP SPADs. The choice of substrate was likely motivated by the eventual application of these photon detectors, though this was not discussed explicitly in either study. The main result of the two studies is again a linear increase in dark count rate with increasing proton fluence; the later study of the InP substrate detectors found the DCR was very high after a relatively low fluence of $7.5\times10^9 p^+/cm^2$ such that they concluded it would quickly be unusable in space. Neither study found that other characteristics of the detectors such as breakdown voltage and efficiency changed significantly. However, an interesting result of the earlier InAlAs substrate detectors was that the IV curve changed subtly. The section of the IV curve near breakdown where the current begins to rise then plateaus and finally shoots up at breakdown, typically called the "shoulder" or "knee", was found to become less pronounced or to be less sharp after radiation (Figure 3.16). The overall increase in dark current coupled with the displacement-damage-induced additional recombination centers causing a decreased photocurrent likely explains this softening of the IV curve near the breakdown region [25].

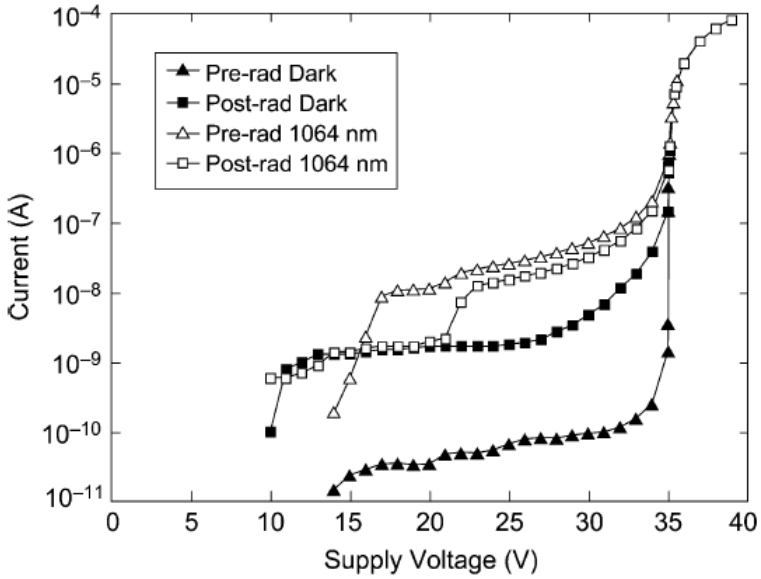

Figure 3.16: Changing IV curve for 200μm InGaAs/InAlAs SPAD after 51 MeV proton irradiation. Reprinted from [25].

3.6 Conclusion

Repetition of SPAD radiation testing and publication of results is necessary to better understand the limits of these sensitive instruments in harsh environments like space. While the effects of radiation have been well-documented in devices that are commonly employed in missions, such as microelectronics components and avalanche photodiodes, there is a much smaller array of studies specifically on avalanche detectors capable of detecting single photons. Additionally, there is an even smaller proportion of SPAD radiation testing studies dedicated to near-infrared SPADs such as InGaAs-based devices. Radiation test design is highly dependent on the proposed purpose of the devices to be tested. As the development of a viable global satellite-based quantum network continues, performing radiation testing on single-photon avalanche detectors, which will constitute a fundamental part of node receivers, as well as limiting their incurred damage, will continue to be crucial task to undertake. InGaAs/InP SPADs will surely play a part in the future quantum net-

work since they are sensitive in the infrared wavelength range used in classical and quantum fiber-based telecommunication networks. Coupling of the fiber system with satellite links necessitates understanding the limits of InGaAs/InP SPADs in space. The next chapter works towards building this understanding and contributing to the small repertoire of studies on the subject.

Chapter 4

Assessing radiation effects in InGaAs/InP SPADs

4.1 Introduction

Past studies with silicon SPADs provided a firm foundation that radiation effects manifest in SPADs predominantly through an increase in dark count rate. This behaviour was also witnessed in the two studies which irradiated InGaAs SPADs, with a measurable 2-3 order of magnitude difference in dark count rate before and after irradiation. Given this support from literature, we expect that our radiation test of InGaAs SPADs suitable for quantum communication purposes will also yield a measurable increase in dark count rate. The magnitude of increase is difficult to predict since it is believed to depend on active area size and the concentration of the semiconductor defects [70]. As such, we formed a hypothesis that dark count rates should rise with exposure to radiation, but the magnitude of the increase is likely to be smaller than that seen in larger Silicon SPADs. This chapter describes the experiment which tested this hypothesis, outlining the choice of radiation fluences, design of hardware, actual radiation exposures and measurements, and finally the analysis.

4.2 Space Radiation Modelling

In conjunction with actual observations in space, much of the knowledge on space radiation is modelled using complex simulations which modelling particle transport and interactions. The European Space Agency's **SP**ace **ENV**ironment **I**nformation **S**ystem (SPENVIS) is an open-source compilation of current standard space radiation simulations [58]. The user inputs details on the satellite trajectory and timing, and chooses environments to model such as trapped particles or solar protons. SPENVIS can then can simulate the expected displacement damage dose based on the input material.

Three orbits were explored: LEO, GEO and a deep space orbits represented by an orbit around Mars. The altitude of the LEO was 600 km, with the angle of orbit at 90° with respect to the equator (ie, passing over the poles). This represents a worst-case scenario, since more GCR interactions are expected in the polar regions. GEO orbit altitude was fixed to 35 786 km above the equator and is of particular interest for near-future quantum communication missions for developing a full-scale global quantum internet. A GEO satellite period is the same as the rotational period of the Earth (23 hours and 56 minutes), therefore it appears stationary to an observer and an uninterrupted link is theoretically possible. Mars was chosen as the representative deep space environment because there is a wealth of data for Mars from former and current missions sent to the planet and dedicated code to simulate its immediate environment (Earth-Moon-Mars Radiation Model or EMMREM). The next parameter explored was solar activity. Launching and operating during solar maximum or solar minimum comes with both advantages and disadvantages, as laid out in the previous chapter. Two missions were simulated, one starting in August 2009, the beginning of the Solar Cycle 24 minimum, and the other on April 2014, marking the beginning of the Solar Cycle 24 maximum. Since the mission was simulated to last ten years, regardless of launch the satellite would experience the effects of either one of the solar stages since it takes approximately 5 years to go from solar maximum to minimum. Finally, two semiconductor materials were compared. Accurate data exists for both Silicon and InGaAs, since these are ubiquitous semiconductors used for microelectronics. While our group has previously radiation-tested Si-based SPADs, this project solely focuses on

testing InGaAs SPADs. We expect there will be differenes between the effects seen in Si SPADs versus InGaAs SPADs, not only because of the subtrate difference, but also the active area size and readout circuit type.

4.2.1 Orbit Altitude

SPENVIS takes into account incident particle type, energy and flux when computing the expected radiation fluence. However, ground testing makes uses of monoenergetic, single particle beam sources such as those found at particle accelerators where we eventually hoped to conduct an experiment. As such, all the radiation fluences outputted from SPENVIS are stated in units of 100 MeV proton effective radiation fluence (p^+/cm^2). 100 MeV is chosen as a representative fluence because the planned ground testing experiment will use a 100 MeV beam of protons. The code used in SPENVIS first calculates the expected fluence of all incoming particle energies and then uses the principle of NIEL scaling to to simulate as if only 100 MeV protons are impinging on the chosen material. In all cases, a 10 mm thick aluminum shielding is assumed, since this would be a typical choice of shielding in a satellite. The results of such modelling provided us with a way to set target particle fluences for our ground experiments.

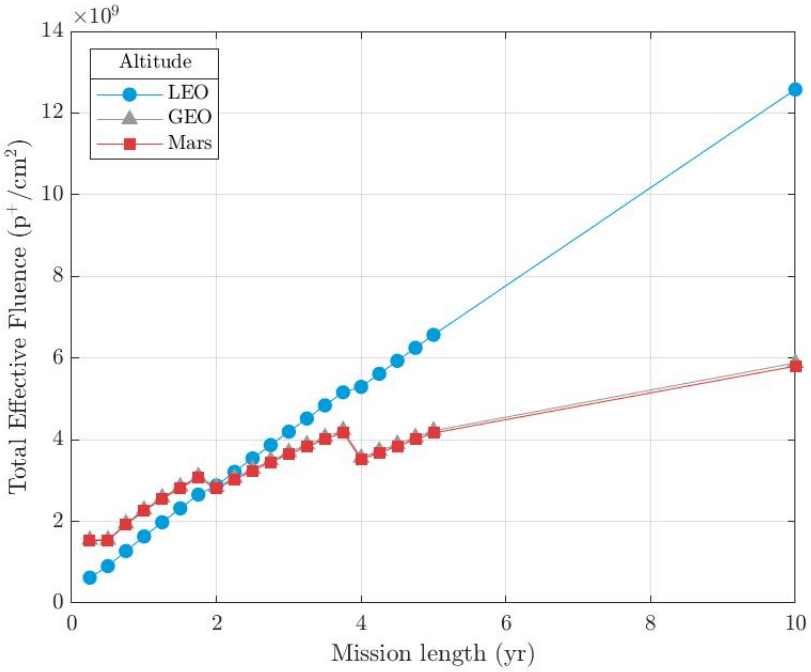

Figure 4.1: Total effective 100 MeV proton fluence for three orbit altitudes over 10 years. GEO markers are not visible as they are almost exactly underneath the Mars markers. The saw-tooth trend in the GEO and Mars data is a result of choosing different confidence intervals for the different parts of the mission, as suggested by Tranquille and Daly [15]. Changing confidence intervals are a consequence of sporadic occurrence of large proton events leading to limited predictive power.

Plotting total effective fluence as a function of mission length yielded the surprising result that LEO satellite (blue curve) would experience a much greater exposure to radiation than GEO (grey curve) or Mars-orbiting satellite (red curve) for mission lengths greater than two years (Figure 4.1). This is likely due to the fact that there are no trapped particles beyond the Earth's magnetosphere and large solar proton events are not exactly predictable. A LEO satellite is spared from harmful solar storms by the magnetic field but is exposed to a constant population of trapped protons, electrons and other heavy ions. The dips in the GEO and Mars fluences at 2 and 4 years in space are due to a change in the model's confidence intervals, which becomes smaller as the mission duration increases [15].

One must also remember that in order to get to GEO or Mars, a satellite must first traverse LEO territory and thus will also accumulate radiation damage from trapped particles (Figure 3.4). The real fluence would most likely be some sort of convolution of the LEO and GEO curves. Figure 4.1 gives us the best case scenario for a 10-year mission, since it does not include any large solar proton events. We see that we can bound our experimental target fluences according to the LEO model since it predicts the largest effective fluence out of the three satellite orbits.

4.2.2 Solar Cycle

The same orbit altitudes were modelled for missions beginning during solar cycle 24 minimum (Aug 1, 2009) or maximum (April 1,2014) (Figure 4.2). Again, LEO mission is expected to accrue more fluence over the 10 year period, however, it appears that starting the mission at solar minimum increases the predicted fluence. This is likely due to the increased presence of GCRs, whose maximum population varies inversely with the solar cycle and whose high energies can permeate the magnetic field and interact with LEO objects. At further orbits, launching during a solar maximum yields poorer results in the long term. Since GEO and Mars-orbiting satellites lack the protection of a magnetic field, an active solar cycle increases the likelihood of large and harmful solar proton events. Though these models factor in a particular start date and particular solar cycle phase, a 10 year mission would extend from one phase into the next, so one must consider the radiation characteristics of both solar phase cycles when planning appropriate mitigation tactics.

The trends in Figure 4.2 raise some concerns. During parameter setting in SPENVIS, the mission start date was set to either solar cycle 24 minimum or maximum. Additionally, as the mission length was extended, the offset from solar maximum was manually adjusted within the SPENVIS's solar proton model package Solar Accumulated and Peak Proton and Heavy Ion Radiation Environment (SAPPHIRE, for short) which produces the data seen in Figures 4.1 and 4.2. As discussed in Chapter 3, there is significant modulation in solar particle fluence during the 11-year solar cycle. This is not reflected accurately, however, in the results of SPENVIS modelling, since we would expect to see some fluctuations or

sinusoidal behaviour during the span of the cycle. A possible reason for this could be that the historical data from solar cycle 24 did not produce huge differences in particle fluence throughout the cycle. However, given the dominant linear trend seen here, it is likely that when calculating the effective fluence of 100 MeV protons, the SPENVIS model does not take solar cycle data into consideration. While unfortunate, Figure 4.3 still provides an upper bound of the expected radiation fluence if the whole mission duration were in solar minimum or solar maximum conditions. In terms of expected damage to SPADs, the solar minimum LEO orbit would expose InGaAs devices to more radiation. Therefore, this curve (dark blue dotted curve) is used to set the target fluences for the planned ground experiment experiment. Choosing a worst case scenario allows for observing and preparing for the extreme cases expected during a mission.

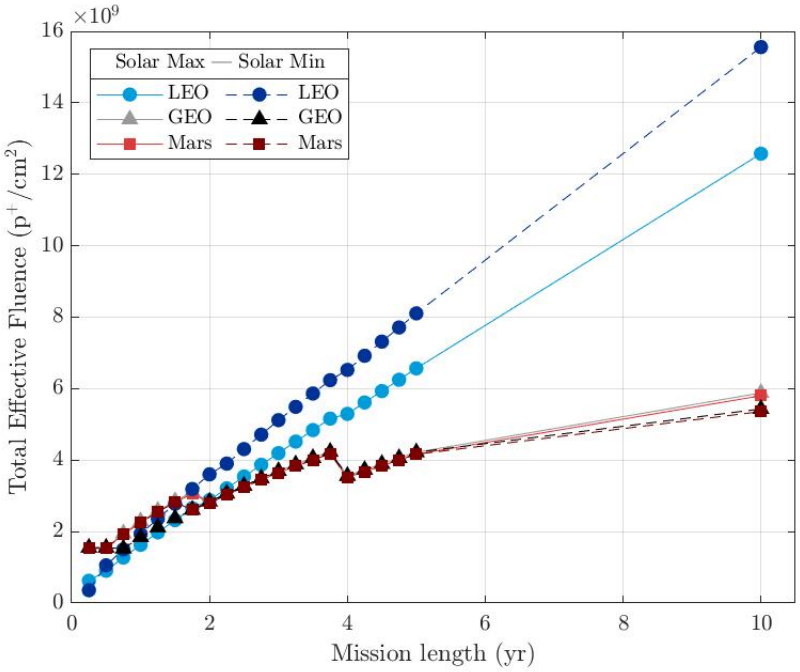

Figure 4.2: Comparison of total effective 100 MeV proton fluence for missions launched in solar maximum or solar minimum.The saw-tooth trend in the GEO and Mars data is a result of choosing different confidence intervals for the different parts of the mission, as suggested by Tranquille and Daly [15].

4.2.3 Semiconductor Type

Given that previous radiation campaigns in our group were focused on observing radiation effects in Silicon-based devices, a final model based on the dam was created to compare predicted fluences in InGaAs versus Silicon devices. The results of this model can be seen in Figure 4.3. Total effective fluence should be interpreted here as the 100 MeV proton fluence required to yield the same damage in differing materials. The damage curves for Si and InGaAs used to model calculated in Summer et al. ([89]), we see that over the 10-year mission duration, a higher 100 MeV equivalent fluence is required to provide the same damage effect in InGaAs devices as in Si devices at LEO. At GEO and Mars, however, a smaller fluence is required to create the same damage in InGaAs as in Si devices. It is hypothesized that this change is due to the difference in particle energy and types at LEO versus at GEO or Mars: there are higher fluences of low energy particles trapped in the Van Allen belt and these types of particles contribute to more interactions in Si than in InGaAs. Outside of LEO there are more contributions of high energy GCRs which interact more readily with InGaAs than with Si. In summary, the SPENVIS model based on the Summers et al., damage curves does not predict a large variation in the response of InGaAs devices compared to Si devices.

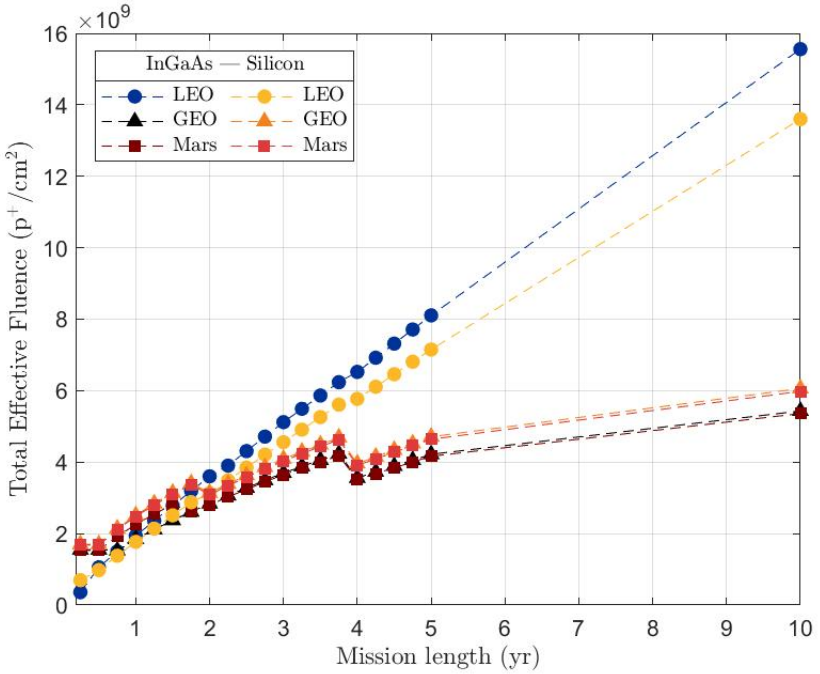

Figure 4.3: Comparision of total effective 100 MeV fluence for two semiconductor materials: InGaAs and Silicon. The data represents a mission beginning at solar minimum. The saw-tooth trend in the GEO and Mars data is a result of choosing different confidence intervals for the different parts of the mission, as suggested by Tranquille and Daly [15].

4.2.4 Radiation testing plan

As a result of the simulations generated using SPENVIS, an 8 step radiation ground test of InGaAs devices using a 100 MeV proton source was planed and can be found in Table 4.1. Radiation exposure steps are divided into equivalent LEO mission duration, beginning with 3 months and ending with 10 years in space; total radiation fluence is cumulative, therefore, the amount of radiation exposure per step is given by the difference between subsequent cumulative fluences. The cumulative fluence values were calculated using the previously discussed SPENVIS results.

Table 4.1: InGaAs device radiation ground testing schedule.

Step	Step Fluence (p^+/cm^2)	Cumulative Fluence (p^+/cm^2)	Equivalent LEO Mission Duration (Yr)
0	0	0	0
1	3.60×10^8	3.60×10^8	0.25
2	7.0×10^8	1.06×10^9	0.5
3	8.8×10^8	1.94×10^9	1
4	1.66×10^9	3.6×10^9	2
5	1.52×10^9	5.19×10^9	4
6	1.41×10^9	6.53×10^9	5
7	9.07×10^9	1.56×10^{10}	10

4.2.5 Outlook for ground testing

Results from modeling in SPENVIS (Section 4.2) as well as information gathered during literature review (Chapter 3) helped form a more concrete outlook for the proposed ground radiation testing. It is expected the dark count rate is InGaAs SPADs will increase, although the magnitude of this effect is highly dependent on SPAD active area size. We expect that smaller active areas will yield a smaller response to radiation. Additionally, SPENVIS modelling im Section 4.2.3 indicated that a higher 100 MeV equivalent fluence would be required to produce the same damage in InGaAs devices as in Si devices; therefore, we believe that the final target fluence of 1.56 $\times 10^{10} p^+/cm^2$ impinging on InGaAs devices will result in a higher dark count rate than a similar target fluence on similarly sized Si devices.

4.3 Radiation Test Hardware Design

Although radiation tests with SPADs have been conducted in our group, there was limited experience in the group with commerical-off-the-shelf InGaAs/InP SPADs and the necessary readout. Therefore, this round of radiation testing required a survey of current available InGaAs SPADs and a new design of readout electronics. This study did, however, retain the thermal management system and overall measurement methodology of the previous studies [17, 41].

4.3.1 SPAD Procurement

SPADs were chosen based on their characteristics that are favourable for quantum communication applications. The characteristics considered were: dark counts rate, detection efficiency and afterpulsing probability. As outlined in the previous section on quantum communication, the maximum dark count rate that would be suitable for LEO satellite QKD is 250 Hz [34]. The detection efficiency should be as high as possible, keeping in mind that higher detection efficiency means higher dark count rate. Afterpulsing probability should be small, since it contributes to the dark count rate, but it is possible to minimize this effect by employing gating.

Table 4.2: Single-photon detector technical specifications at -40°C as provided by manufacturer datasheet

Manufacturer	Model	Active Area (μm)	Detector Efficiency (%)	DCR (kHz)	Afterpulsing probability (%
Princeton Lightwave Ltd.	PGA-300-U	16	20	4.5	4×10^{-5}
RMY Electronics Ltd.	PGA-314	16	20	100	2.5×10^{-4}
	PNA-300	32	10	75	
Wooriro	SPAD without TEC	16	20	0.5	1×10^{-1}
Politechnico di Milano	Custom SPAD	–	–	–	–

The chosen SPAD models can be found in the Table 4.2; two of each commercially available SPAD models were procured, as well as eight SPADs from a collaborating group led by Dr. Alberto Tosi from Politechnico di Milano. The dark count rate of the commercially available SPADs, is elevated much over the suggested DCR limit, however, the combination of lower operating temperature, gating operation and low excess bias should limit the dark counts further. The detector efficiencies are typical for InGaAs/InP SPADs and besides increasing the bias (and risking high dark count rates), there is little that can be done to maximize it. Afterpulsing probabilities are not too high of a concern with the appropriate gating settings. It appears that the Wooriro detectors could present higher dark count rates in comparison to the other three detectors, possibly due to their larger afterpulsing probability.

The RMY PNA-300 detectors are NFAD (negative-feedback avalanche detectors) SPADs which integrates a resistor within the package. The advantages of this, rather than placing the resistor in the readout circuit, is that it diminishes the avalanche pulses quicker than the conventional passive quenching circuit, thereby limiting the likelihood of afterpulse generation.

The Milano SPADs arrived already characterized from the collaborators, so the exact parameters of the devices were not characterized due to the quick timeline of the project.

4.3.2 Readout Circuit Design

Two readout circuits were designed were a gated passive quenching circuit and a free-running NFAD circuit, following guidance from [67] and [97], respectively.

Gated Passive Quenching Circuit

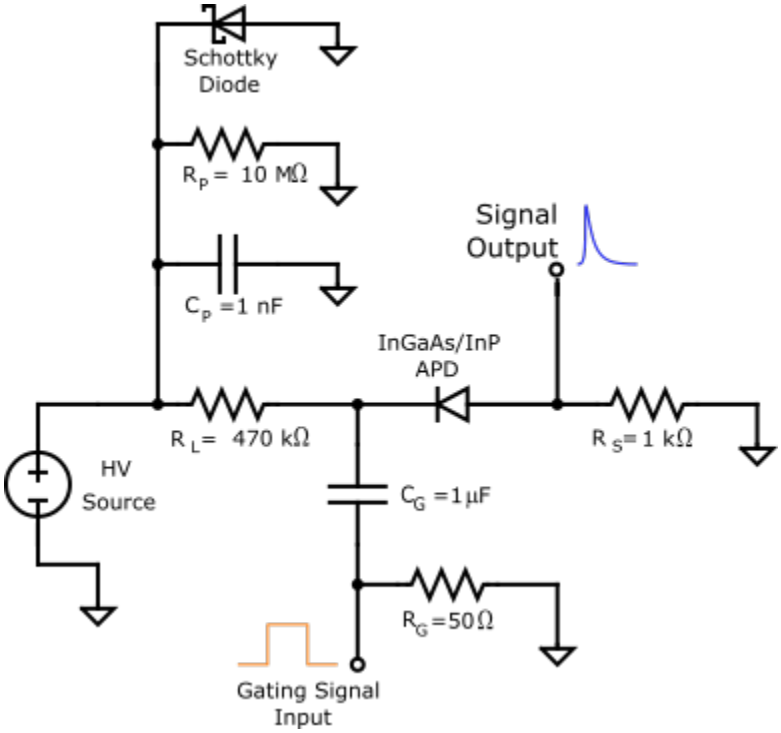

Figure 4.4: Gated readout circuit schematic.

The gated passive quenching circuit can be examined in three parts, shown in Figure 4.4. First, there is the passive quenching line which consists of a high ballast resistor R_L of 470 kΩ followed by the reverse-biased APD and a lower value resistor R_S of 1 kΩ. The function of R_L is to dissipate the large voltage created by an avalanche, while the output pulse can be read across R_S. The next part of the circuit is the gate signal which consists of an external input from the function generator providing the gate signal, a 50 Ω termination resistor and a capacitor. The value of C_G was chosen to be fairly large so that the gate pulse amplitude was not attenuated much by the effective voltage divider created by the circuit capacitances (C_G, diode and stray capacitances) [39]. The output signal is the voltage across R_S, which is directly proportional to the current across the diode. The final part of the circuit is a circuit protection line which consists of capacitor C_P, very high

value resistor R_P and a Schottky diode. In the event of the passive quenching line shorting or left floating at the negative terminal of R_L, the current would be forced by the Schottky diode to be dissipated by the 10 MΩ resistor.

Free-running NFAD Circuit

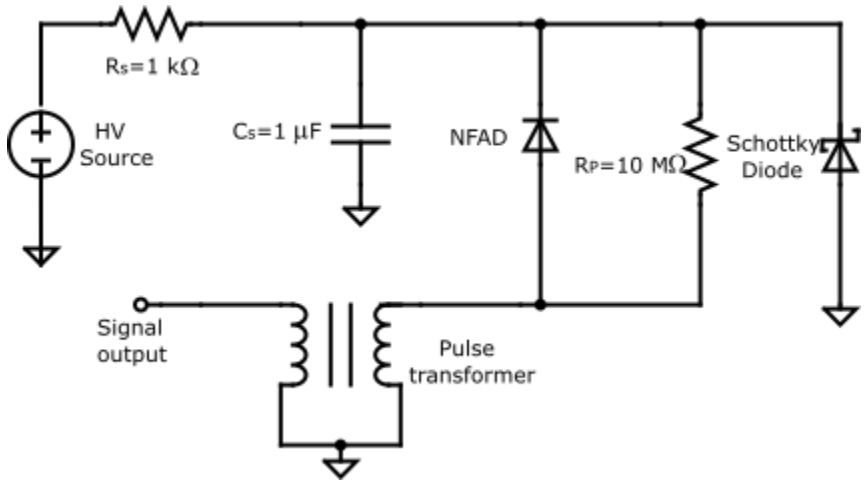

Figure 4.5: Free-running readout circuit schematic

In the NFAD readout circuit above (Figure 4.5), there is no external ballast resistor to quench the circuit; the resistor is integrated within the diode package. The primary coil of the pulse transformer is connected to the NFAD anode and the secondary coil is coupled to a transmission line to the output. Like the gating circuit, there is a 10 MΩ resistor and Schottky diode to provide protection from voltage surges.

PCB Design

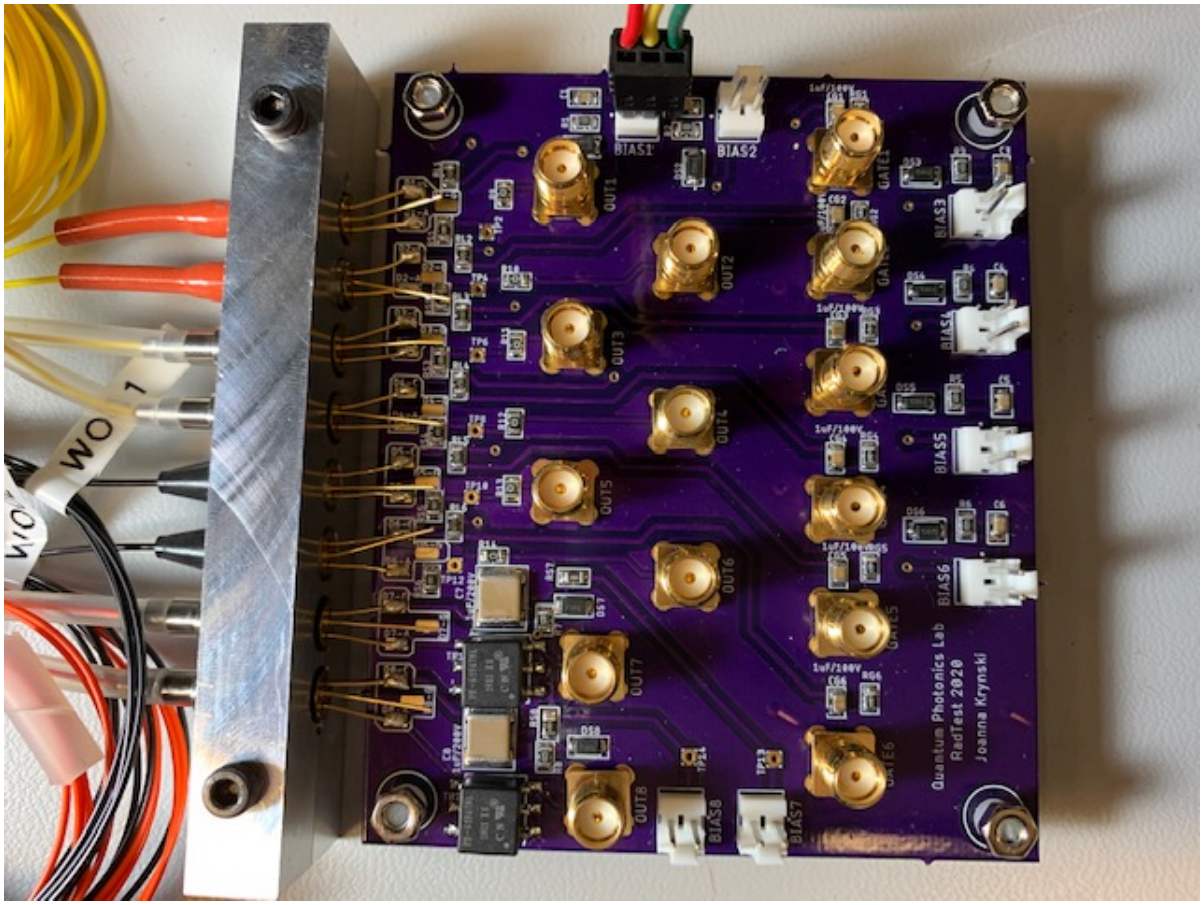

Figure 4.6: Final manufactured and populated PCB with attached SPADs in enclosure

The PCB width was dictated by the expected TRIUMF proton beam diameter of 8 cm. All eight of the planned SPADs had to fit within the 8 cm, though the SPAD leads could be deformed slightly. Six gated passive quenching circuits and two free-running NFAD circuits were necessary to readout the eight InGaAs/InP SPADs. It was important to minimize the length of the trace between the SPAD anode and R_S, since this particular trace section could pollute the readout signal. SMA connectors were used to carry the input gate pulse as well as to relay the readout signal. All in all, fourteen SMA cables

were necessary. As such, these connectors were placed strategically to ensure a compact yet manageable working distance of at least 14 mm (Figure 4.6). Refer to Appendix A for PCB schematic and board files.

4.3.3 SPAD Mounting and Cooling

Like the PCB, the SPAD mounting plate had several design constraints. The SPADs had to be housed within 8 cm to fit within the proton beam width and had to be narrow enough so that the detector leads could be easy soldered to the PCB. They whole detector housing had to be attached to a flat surface which would be the cold side of a thermoelectric cooler (TEC). Finally, the material had to be a good thermal conductor.

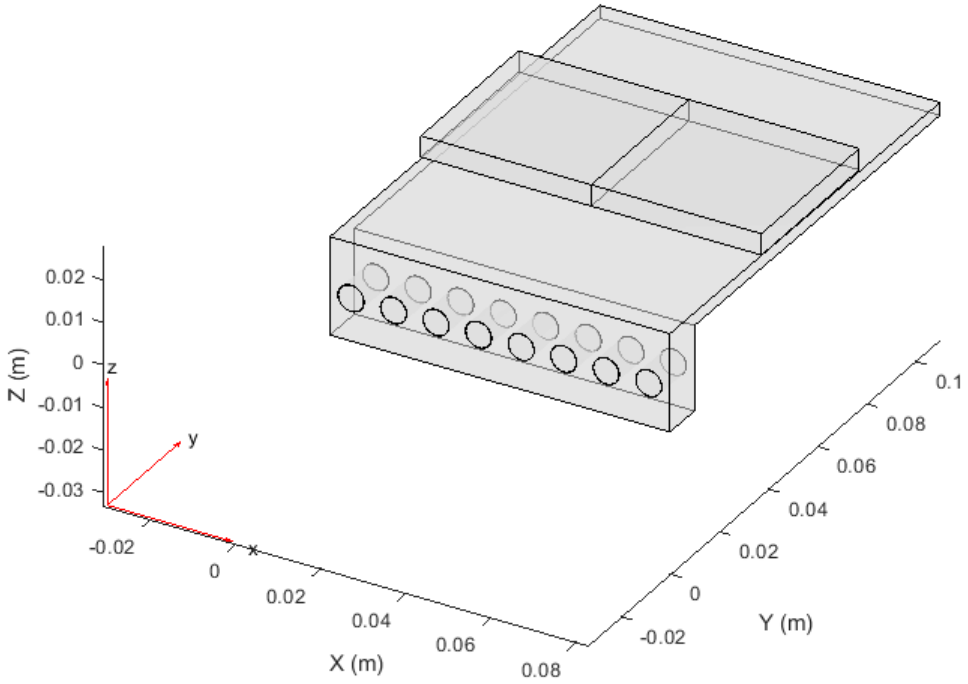

Figure 4.7: CAD design of SPAD enclosure and mounting plate with two TEC on top.

The dimensions of each of the SPADs were taken and a preliminary design for an enclosure was created in AutoCad software (Figure 4.7). The SPAD enclosure and mounting plate were chosen to be made out of aluminium, since it is a good thermal conductor, readily accessible and inexpensive. The dimensions of the enclosure and mounting plate can be found in Appendix A. In addition to the detector enclosure, a 3 mm aluminium plate was used to act as the TEC cold side contact with the SPAD enclosure, while the hot side was in contact with a large copper heat sink. The copper heat sink was previously machined; only four holes were necessary to add in.

Before assembling the machined parts, preparation of the thermoelectric coolers (TECs) was necessary. Thermoelectric coolers operate on the basis of the thermoelectric effect,

whereby a current passing through two dissimilar materials causes heat to be absorbed on one side of the junction while releasing heat on the other side of the junction. The two materials chosen are N- and P-type semiconductors, which are arranged in an alternating fashion between two thermally conductive plates. These semiconductors are arranged so that thermally they are parallel while electrically they are in series. In this way, the flow of charge carriers can induce heat absorption on one side and heat release on the other.

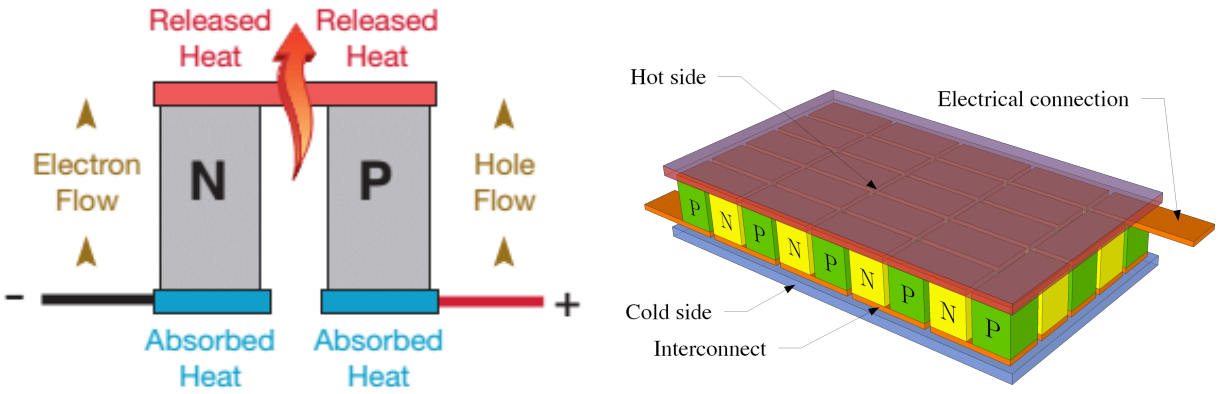

(a) Schematic of single semiconductor pair and thermoelectric effect [95].

(b) Illustration of thermoelectric cooler [64].

Figure 4.8: Thermoelectric cooler (TEC) operating principles

Heat is released on the "hot side" of the TEC, which is typically in contact with a heat sink at ambient temperature. Heat is absorbed on the "cold side", which is the side in contact with whatever needs to be cooled.

This experiment required that the SPADs were cooled much lower than room temperature and that their temperature is kept very stable between measurements. The stability is necessary because the breakdown voltage of the SPADs is temperature dependent, therefore an unstable temperature would affect the results of the SPAD characterization significantly. Dry ice ($CO_2(s)$) in contact with the larger back plate of the copper heat sink was used to provide the bulk of the cooling to $-50°C$; however, TECs were necessary to monitor and fine-tune the temperature of the SPADs in the enclosure. An important consideration for the choice of TEC model was that the TECs would be tightly situated

between the two aluminium plates (drafting details in Appendix A) which were expected to contract and expand with the temperature. The chosen TEC model from CUI devices (model: CP854345H with arcTEC structure) are designed to withstand dynamic thermal changes by using thermally conductive resin. Two TECs were used in order to cover the large width of the SPAD enclosure and cold side plate. The two TEC were connected in series (known as "daisy-chaining", Figure 4.9), so that they could be controlled together, then placed on the hot side aluminium plate using thermal paste as a thermally conductive adhesive. The cold side plate was placed on top, again with thermal paste on the TEC. A silicone thermal pad was placed between the aluminium hot side plate and the copper heat sink to ensure constant contact between the hot side and the heat sink. Finally, the two aluminium plates were screwed into the smaller front plate of the copper heat sink (Figure 4.10).

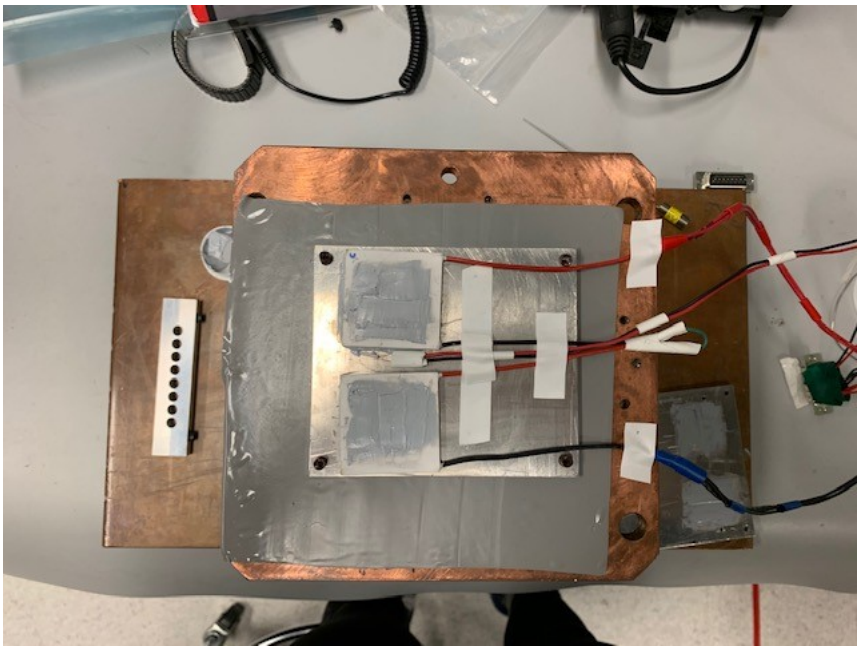

Figure 4.9: Daisy-chained TECs with thermal paste on top of aluminium hot side plate, silicone thermal pad and copper heat sink.

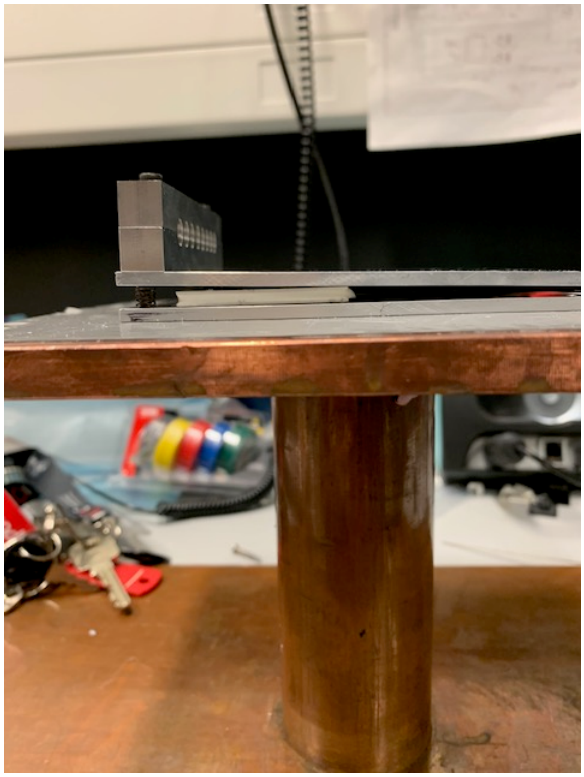

Figure 4.10: Side view of the TEC between aluminium plates on top of copper heat sink.

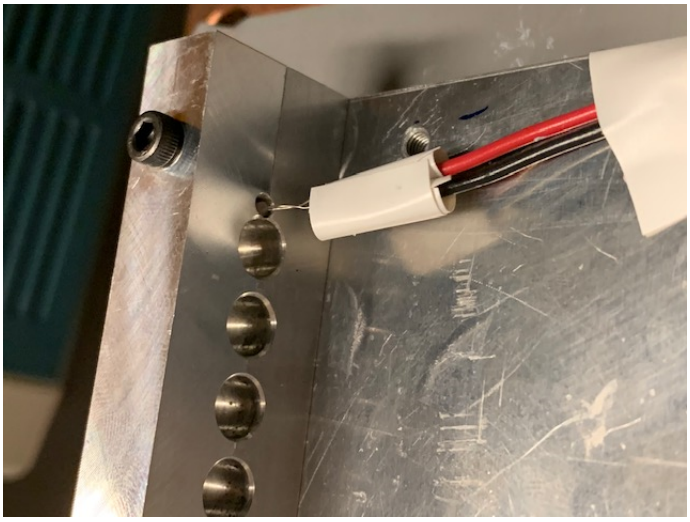

Figure 4.11: RTD temperature sensor in SPAD enclosure

The source of current for the TECs was the Arroyo 5300 TEC Source TEC controller. In order to modulate the current to the TECs, thereby heating or cooling the SPADs, the controller required a remote temperature sensor close to the SPADs. A PT-100 resistance temperature detector (RTD) was placed in the SPAD enclosure to detect the temperature (Figure 4.11). An RTD is used to detect temperature by sending an electrical current through it and measuring its resistance. The resistance of the RTD is related to the sensor's temperature. At 0°C, this type of RTD has a resistance of 100 Ω, and the resistance drops as the temperature decreases, following a well-defined relation [103]. The TEC controller uses the information from the RTD to provide positive current (to cool) or negative current (to heat) in order to reach the set temperature of −50°C. The feedback loop used to achieve and maintain this temperature was auto-generated by the TEC controller. To confirm the accuracy of the TEC controller temperature readout, a calibration with a second RTD was conducted (see Appendix A for details). It was found that the TEC controller reached each set temperature and its temperature read out was accurate as compared with the second RTD temperature measurement.

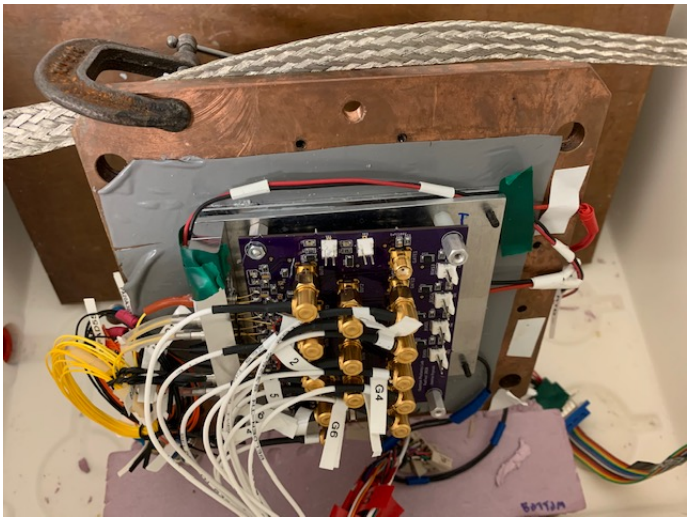

Figure 4.12: Final assembly of PCB, SPADs, TECs and copper heat sink, photographed during radiation testing experiment with appropriate readout and control cables.

4.3.4 Conclusion

Two types of readout circuits were designed: firstly, a gating circuit, to limit noise and afterpulsing by biasing SPADs above breakdown for a short gate width; secondly, a free-running circuit, designed for NFAD SPADs which limit noise by integrating the quenching resistor in the detector package. These circuits were reproduced several times to be printed on a PCB. A custom SPAD enclosure and cooling system was also designed and assembled. Together, the circuits and cooling makes it possible to readout the SPADs in the particularly constrained environment expected during the radiation testing experiment.

4.4 Experiment Organization and Methodology

4.4.1 Introduction

This section of the work lays out the methodology and results of an experiment to characterize any effects of radiation into InGaAs/InP SPADs. Information gathered from a

review of the literature related to this topic was used to determine the fluence endpoints which simulated various lengths of time at low-Earth orbit (see 4.2). The irradiation of the almost all samples presented in Table 4.2 took place at the TRIUMF facility in Vancouver, British Columbia; several devices (one Princeton Lightwave device and six Milano devices) suffered fatal failures at the University of Waterloo lab and were not characterized in Vancouver. All the previously discussed hardware as well as other equipment to be mentioned hereafter were transported from the University of Waterloo lab to TRIUMF, and the set-up in the radiation chamber, all measurements and troubleshooting were conducted by myself and two colleagues, with tele-correspondence to the team back in Ontario. The logistical and personnel constraints did not affect the experimental measurements as much as the time constraints of the experimental preparation and execution. Even so, the results presented in this section support the hypothesis that radiation effects do alter the single-photon detection ability of InGaAs/InP detectors and should be further investigated in a more refined and targeted approach.

4.4.2 Radiation campaign set-up

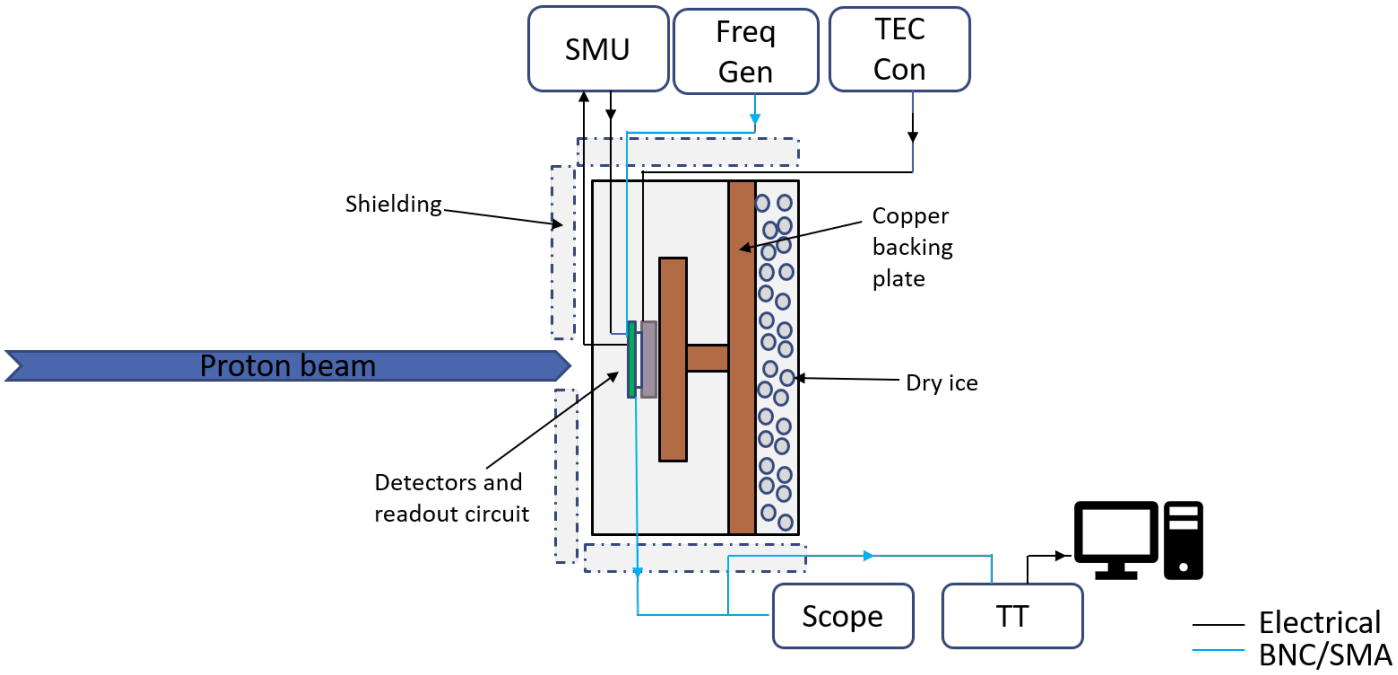

Figure 4.13: Schematic of experimental apparatus. The detectors, readout circuit and copper backing plate were placed in a cooling chamber filled partially with dry ice, facing the proton beam. Power and coaxial wires were routed through holes into the chamber so that it could remain closed for the experiment duration.

The organization of experimental apparatus was constrained by the radiation testing facilities at TRIUMF. Firstly, the SPAD placement had to be compact so that all the SPADS would be encompassed in the proton beam. Next, the detectors and the cooling apparatus, that is the TEC and the copper heat sink, had to be close together to ensure optimal cooling capabilities. All these elements also had to be in one enclosure which would be filled with dry ice for further cooling/heat sink. Figure 4.13 shows a schematic of the final experimental apparatus configuration. The proton beam impinged on the detectors at a 90°angle, with blocks of lead providing shielding to the readout circuit and surrounding areas. A previously drilled hole in the centre of the cooling chamber was used to pass

the optical and electrical wires without major contortion or strain. The cables were surrounded by anti-electrostatic foam, taped with black tape and the whole cooler chamber was covered in a black out curtain to minimize outside light sources from triggering the detectors (see Appendix A for photos). Electrical cables ran from the source measure unit (SMU) and the TEC controller, while coaxial BNC and SMA cables connected provided the gate signal from the frequency generator and relayed the output signal to oscilloscope and counting unit (Time Tagger, TT). The TEC controller was used to drive the TEC to fine tune the temperature of the detectors and detector bracket. The dry ice cooled the entire copper plate and cooler chamber to around -50°C and the TEC ensured the detectors' temperatures did not fluctuate much. Detectors counts were saved from the Time Tagger using the native software, TimeTag Explorer.

4.4.3 Measurement Methodology

Based on the radiation modelling, the endpoints of cumulative radiation presented in Table 4.1 were generated. At TRIUMF, the "beam on" time is calculated by multiplying the desired radiation step fluence (Table 4.1, 2nd column) by the beam's fluence calibration factor, as given by the beam operator. This was given to be $3.40\times10^4 p^+/cm^2/MC$, where MC stands for *Monitor Counts*, a unit of proton flux which the beam operation computer operates in. Once the number of MCs was calculated, it was input into the control computer and the beam block was removed automatically for the appropriate amount of time so that the desired MCs are reached. The actually achieved proton fluences were not exact due to the finite speed at which the beam block operates. The typical deviation from the target fluence was on average about 0.47%.

After each radiation exposure, several measurements were conducted. Firstly, a diode voltage vs current (IV) curve was conducted using the SMU, which can both source and measure voltage and current simultaneously. For each detector, the bias was increased slowly to a few V below breakdown then an automatic voltage sweep was programmed in the SMU. This allows the SMU to uniformly increase the bias towards and past breakdown, measure the diode current and immediately graph the IV curve. The breakdown voltage

(V_{Br}) was extracted from the IV curve as the point at which the increase in the current becomes nonlinear.

After V_{Br} was determined, the SMU was manually biased to 0.5 V below V_{Br}. The gating signal was activated such that the gate pulse height would bring the detector briefly above breakdown. The gate pulse width, rise and fall times were fixed at 20 ns, 5 ns and 5 ns, respectively. The gate pulse height was also fixed at 2.5 V; since the detectors were biased 0.5 V below V_{Br}, each pulse would bring the detectors briefly to 2V above V_{Br}, such that $V_{Ex} = 2V$. The gating frequency was set to the following frequencies: 1 kHz, 10 kHz, 25 kHz, 50 kHz, 75 kHz, 100 kHz, 500 kHz and 1 MHz. 30s of dark counts were collected for each detector at each gating frequency. The TimeTagger threshold was varied manually for each detector between 0.1 and 0.22V. The counting data was exported to a spreadsheet format for later analysis. Additionally, waveforms were saved using an oscilloscope (see Figure 4.14 for example screenshots of the waveforms. During these measurements, the detector temperature was monitored by the TEC controller. The temperature was fixed to $-50 \pm 2°$C.

As a final data point, IV curve, breakdown voltages and dark count rates were measured at IQC after five months after radiation exposure. The same procedures were followed as those in TRIUMF.

4.5 Results

Selected plots are published in the main body of the text. All plots for all tested devices may be found in Appendix B. Unless noted, no error bars were generated for the plots because single measurements were conducted for each exposure.

4.5.1 IV Curve

The current-voltage (IV) curve describes the relationship between the current of a device at a range of potential differences. The relationship may be linear, such as with resistors

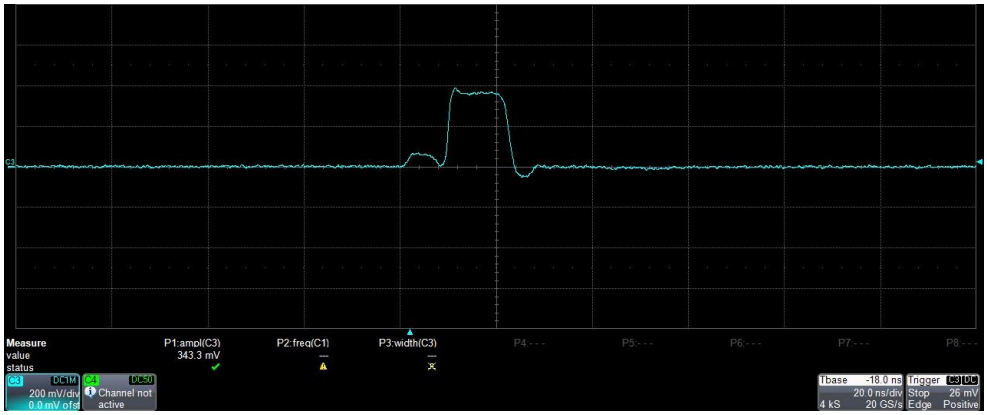

(a) Oscilloscope waveform of 1 MHz gated RMY 1 at 2 V excess bias. The smaller bumps prior to and after the large pulse are the gate on and off signals. The large pulse is from an avalanche. The avalanche pulse is quenched by the termination of the gate window.

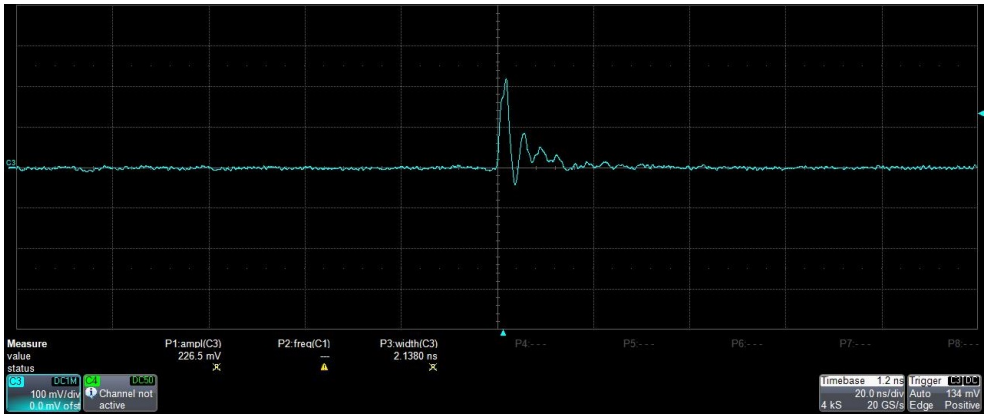

(b) Oscilloscope waveform of free-running NFAD 1 at 2 V excess bias. The variation in pulse shape between this waveform and the above is due to the NFADs not being gated and not possessing a means of external quenching.

Figure 4.14: Two typically oscilloscope waveforms of avalanche pulses in gated (top) and ungated (bottom) SPADs

and other Ohmic devices, or non-linear, such as with diodes. For avalanche diodes, the current rises linearly until the breakdown after which is rises non-linearly. The inverse of the slope of the linear region is equal to the resistance within the whole circuit, as per Ohm's law: $R = \frac{V}{I}$.

The IV curve was measured by slowly biasing the ungated detectors individually close to the expected breakdown voltage and then enabling an automatic voltage sweep in the SMU. This function allows the SMU to automatically increase the voltage by a specific step size while simultaneously measuring the current and graphing the curve. Typically, the IV curve was measured from about 5 - 10 V below breakdown. The variation in voltage range was due to human error, since the SMU must be set each time to perform the voltage sweep and the sweeping range varies from SPAD to SPAD. Figures 4.15 and 4.16 show two of the measured IV curves.

Most IV curves for the QPL provided SPADs did not change significantly with radiation exposure (see Appendix B). We see two regions for circuit behaviour before and after breakdown. For the QPL SPADs, the linear increase before breakdown is dictated by the use of a large value resistor (MΩ) and Schottky diode as a method of protecting the SPADs (see Section 4.3.2 for more details). Before breakdown, the current is increasing according to the load across this resistor and diode. After breakdown, the current rapidly spikes as the SPAD starts to conduct current in reverse bias.

The two Milano SPADs (hereafter called Polimi) displayed different IV curves from the QPL SPADs due to the differences in the readout circuit design. The slight increase in current before breakdown is believed to be the punchthrough voltage of the SPAD, which occurs when the entire multiplication region, charging and absorptive layer has depleted [45]. This voltage changed between radiation exposures, but there is no evidence to believe that it is due to the exposure since there is no clear trend that the radiation is altering the SPAD structure such that the punchthrough voltage shifted in a predicable manner. The behaviour of the SPADs below breakdown was not studied in this experiment, but it would be interesting to focus on the current in this area, known as the dark current, and how it changes with radiation exposure.

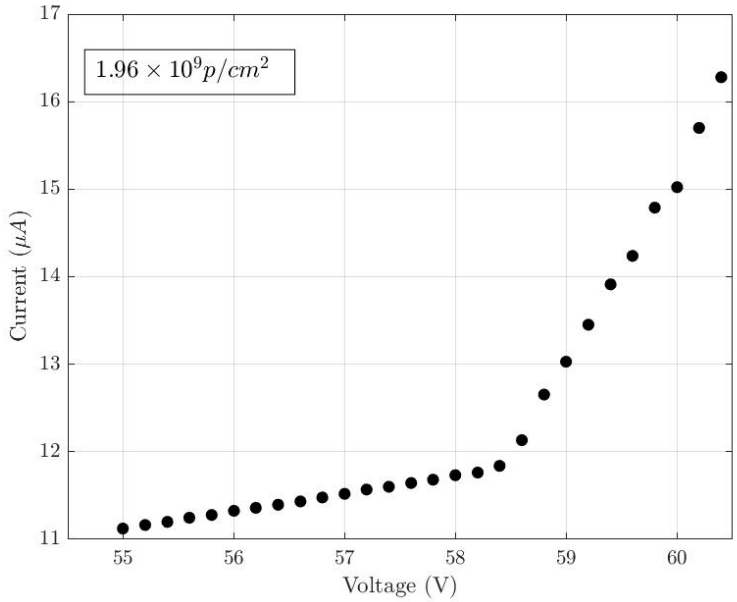

Figure 4.15: Example of RMY 1 IV curve. The linear behaviour below break down is due to the protective circuit with a 1 MΩ resistor parallel to the SPAD.

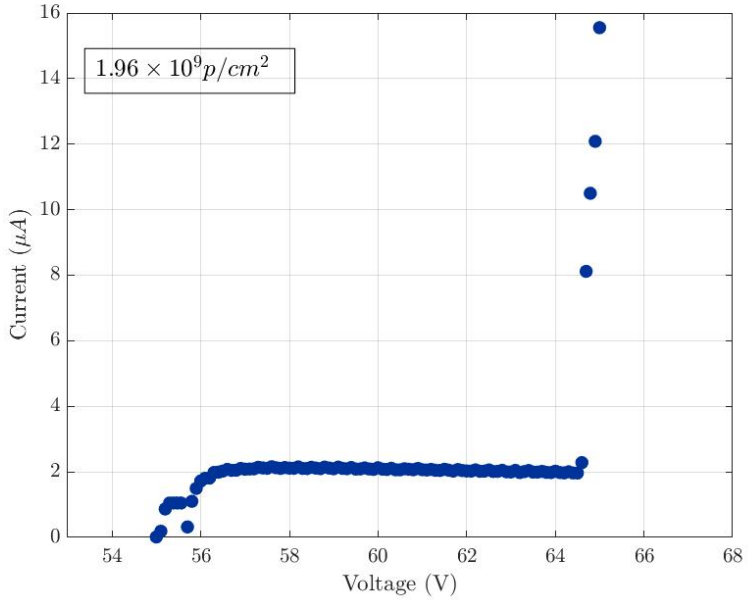

Figure 4.16: Example of Polimi 1 IV curve. The shoulder at about 56 V is believed to be manifestation of the *punchthrough voltage* phenomenon [45], while true breakdown occurs at the non-linear increase after 64 V.

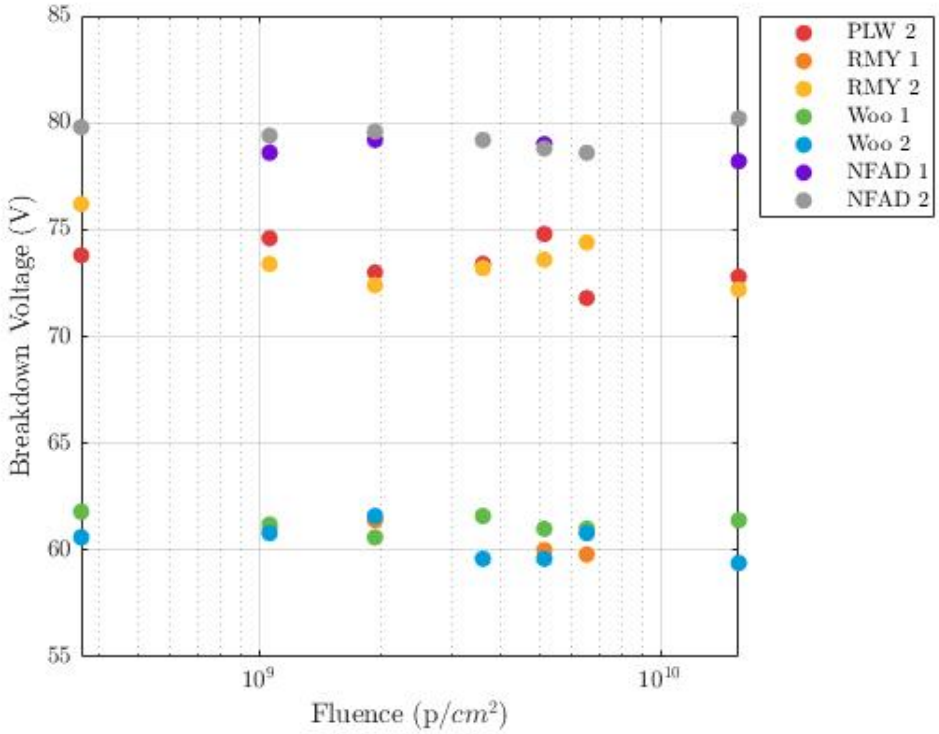

Figure 4.17: Breakdown voltages of tested SPADs after each exposure to proton radiation

Figure 4.17 shows the breakdown voltages (V_{Br}) extracted from the IV Curves for the QPL SPADs, by calculating the voltage at which the slope of current curve was greatest. V_{Br} remained fairly constant with each radiation exposure. Fluctuations could be due to slight temperature change and due to the program created for breakdown estimation.

4.5.2 Dark Count Rate

DCR with respect to cumulative proton fluence

The dark count rate (DCR) was measured after each radiation exposure by taking counts for 30 s without a light source. The detectors were biased 0.5 V below breakdown and

providing at 2.5V gate pulse, such that they were biased at 2V excess for 20 ns. This measurement was performed for each gating frequency. For the un-gated NFAD SPADs, one free-running mode measurement was conducted per radiation exposure.

In general, for the QPL SPADs, the DCR increases between the first exposure and the final longest exposure (see Figure 4.19 and Appendix B for all plots). However, the greatest increase in DCR does not occur after the highest exposure but varies between devices and the DCR does not appear to monotonically increase with each exposure. The reason the largest leap in DCR does not occur with the greatest exposure could be that at this point the devices are already so saturated from previous exposure that they are unable to register new dark counts. The Politechnico di Milano SPAD samples do not show much of a change in DCR with increasing cumulative fluence.

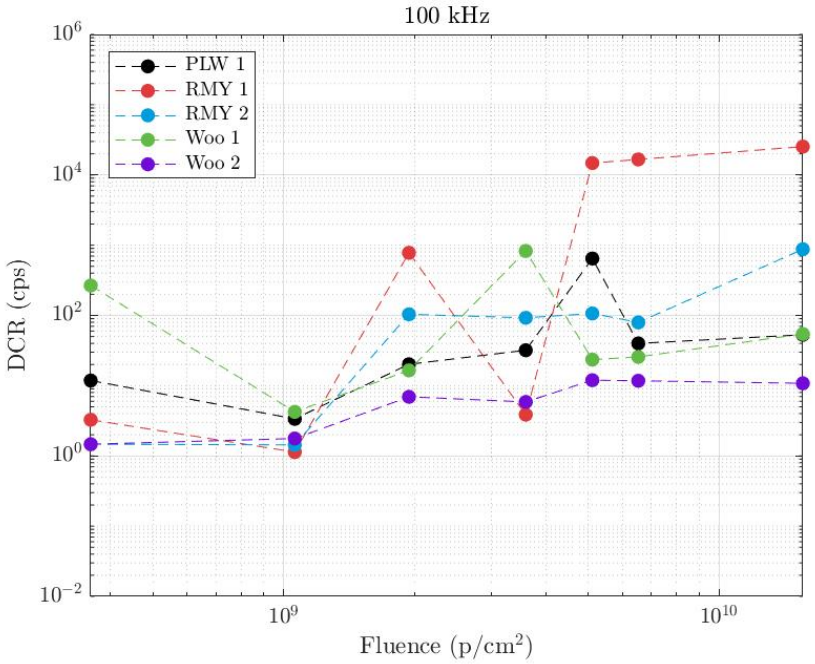

Figure 4.18: Dark count rate for 100 kHz gated QPL SPADs

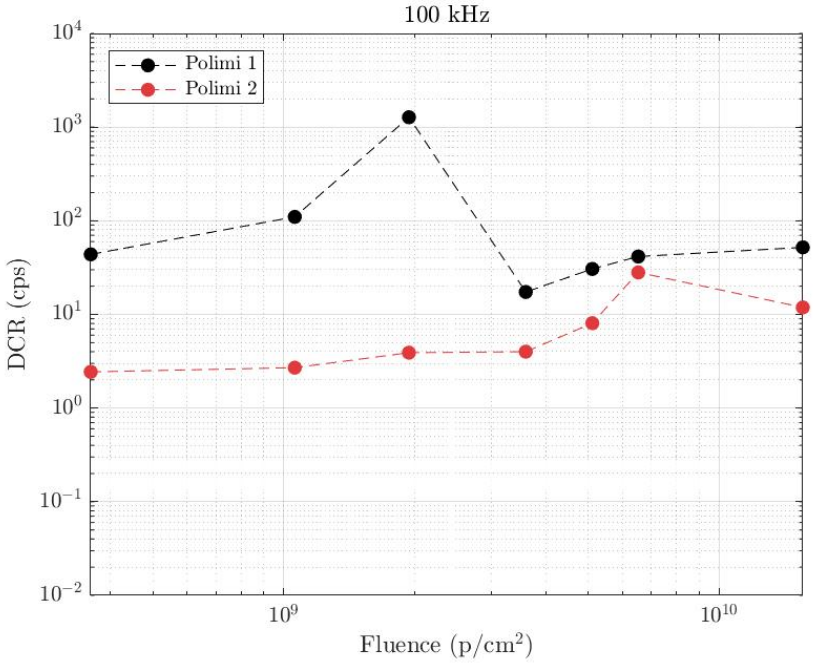

Figure 4.19: Dark count rate for 100 kHz gated Politechnico di Milano (Polimi) SPADs. Note the logarithmic scale on the y-axis.

Normalized DCR with respect to gating frequency

To see any effect of gating on the dark count rate, the DCRs were divided by the gating frequencies with which the SPADs were gated. This results in a *normalized DCR*. Plotting normalized dark count rate and gating frequency on a log-log plot would elucidate if gating frequency somehow contributes to DCR through an increase in afterpulsing (see Figure 4.20a and Appendix B for full set of plots).

$$DCR_{norm} = \frac{DCR_{gated}}{\omega_{gate}} \tag{4.1}$$

There does not appear to be a trend of increasing dark count rate with increasing gating frequency for most of the diodes. The normalized DCR remain relatively constant with gating frequency, indicating that higher gating frequencies do not contribute to dark count rate through increased afterpulsing effects. There also seems to be no effect of proton radiation on this behaviour. Indeed, the most variable normalized dark count rate occurs for the control (no radiation) measurement. One diode, RMY 1, exhibits interesting changes across the gating frequency spectrum (Figure 4.20a).

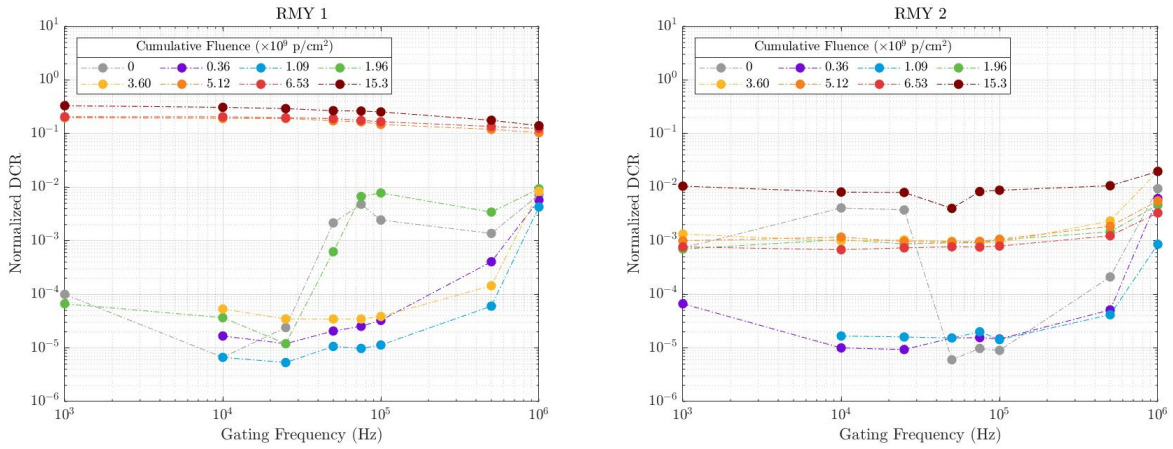

(a) (b)

Figure 4.20: Normalized DCR as function of gating frequency of RMY 1 (left) and RMY 2 (right) SPADs

Normalized DCR does indeed increase above 10kHz gating for the first five post-radiation measurements, while remaining constant for the last and highest post-radiation measurements. Also, the normalized DCR is orders of magnitude higher for these last two measurement even at low gating frequency. It is possible that the radiation damage increased the dark count rate so high that any trends in normalized DCR across the tested gating frequencies is drowned out by the thermal counts caused by the radiation. This normalized DCR flatness for the highest proton radiation fluences is exhibited in the other diodes, but the magnitude of the normalized DCR is not especially larger than that of the lower proton fluences. As such, it is difficult to draw conclusion of the behaviour of normalized DCR with respect to gating frequency and proton radiation exposure. However, there is evidence that these diodes can perhaps be gated to even higher frequencies before afterpulsing would become a problem. Future work could investigate such gating schemes.

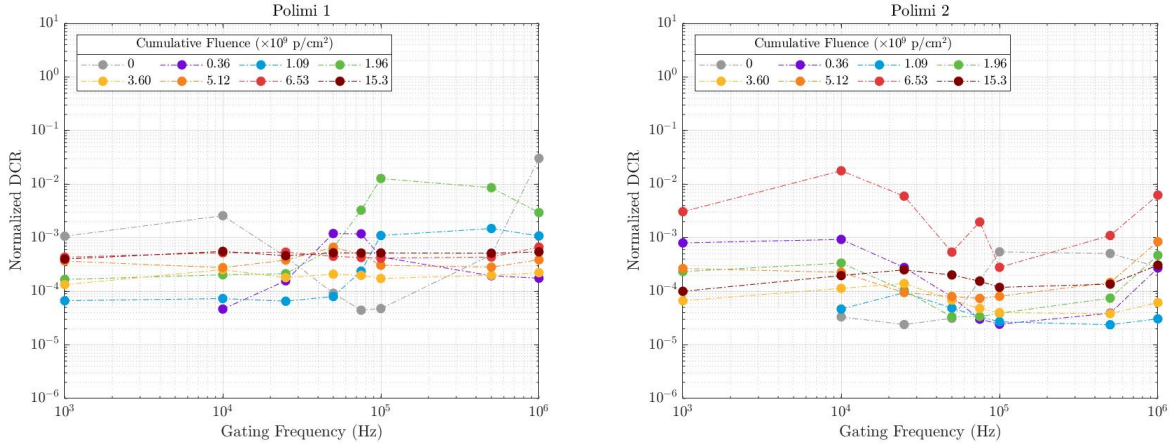

(a) (b)

Figure 4.21: Politecnico di Milano SPADs normalized DCR as function of gating frequency

Figures 4.21a and 4.21b show the relationship between normalized DCR and gating frequency for the Politecnico di Milano SPADs. There is a linear relationship on this log-log plot, meaning that an exponential increase in gating frequency resulted in an exponential increase in normalized DCR. This behaviour persists even at low gating frequencies, indicating perhaps that the count rates being measured were already dominated by afterpulsing due to the SPAD gating. Given this monotonic increase in normalized DCR, these SPADs would not likely be useful at much higher gating frequencies. Interestingly, the lowest normalized DCRs were achieved after the larger cumulative proton fluence, while the highest normalized DCRs were present for the control measurements. It is possible that these devices were already saturated from the initial measurements. Saturation could have been due to the low temperature inducing more afterpulsing or the excess voltage being too high and inducing more dark counts. The details of the readout circuit were not given, so it is difficult to know what the timing properties of the circuit were.

Normalized DCR with respect to cumulative proton fluence

Plotting the DCR as normalized by the SPAD gating frequency gives an advantage of being like a replication of a measurement. Figure 4.22a and 4.22b show the normalized DCR for each of the gating frequencies with respect to the cumulative proton fluence.

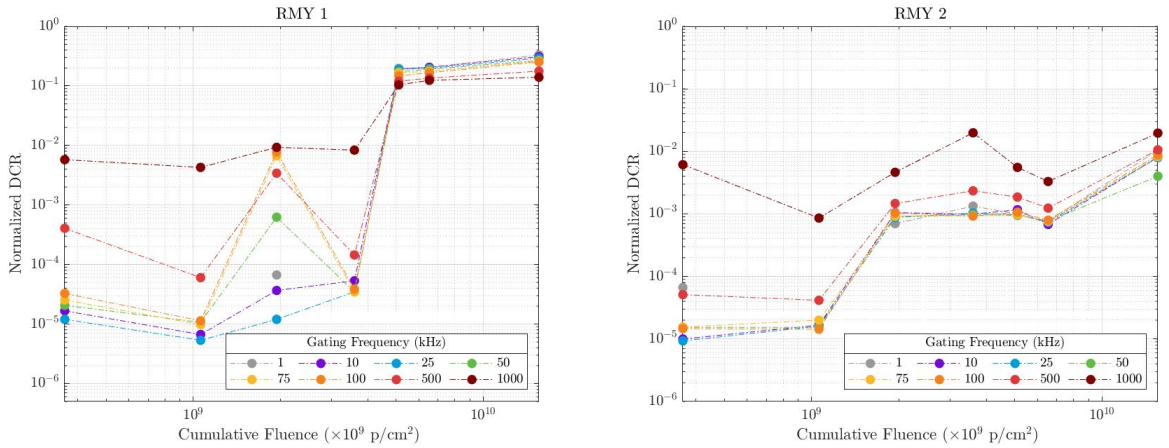

(a) (b)

Figure 4.22: RMY SPADs normalized DCRs as function of cumulative proton fluence for

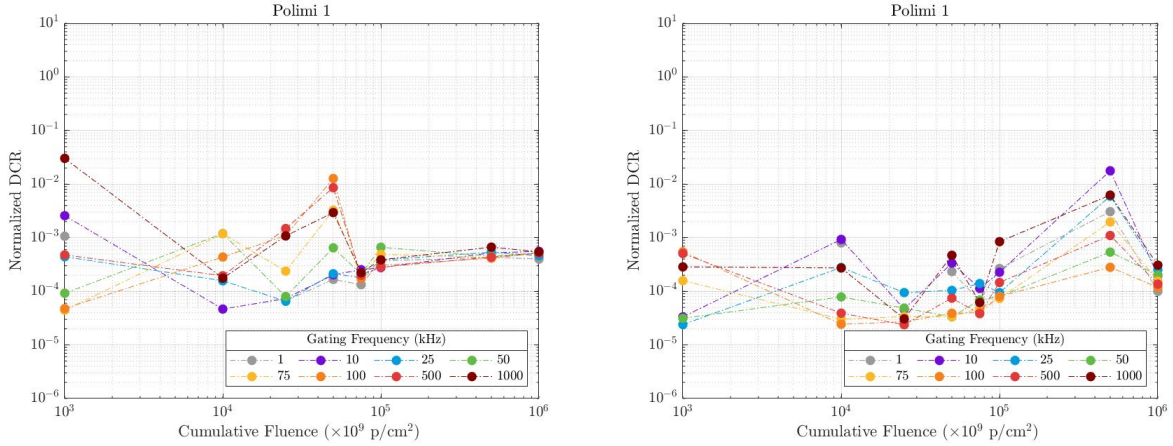

(a) (b)

Figure 4.23: Politecnico di Milano SPADs normalized DCR as function of cumulative proton fluence

The normalized DCR of the Politecnico di Milano SPADs was shown to decrease with increasing proton fluence (Figures 4.23a and 4.23b). This, as previously mentioned, could be due to the devices being saturated from the start of the measurements, such that increases in dark count rates from radiation damage were not sensed.

Free-running mode DCR

The final method of DCR comparison between SPAD samples was the so-called "free-running mode" DCR. Using a quick conversion equation, one can account for the frequency and duty cycle of the detector gating to estimate the DCR which would be exhibited if the SPAD were not gated ("free-running"). The conversion equation is:

$$DCR_{freerun} = \frac{-1}{T_{On}} log(1 - \frac{DCR_{gated}}{\omega_{gate}}) \tag{4.2}$$

where T_{On} is the length of the gate in seconds and DCR_{gated} is the DCR measured for a particular gating frequency, ω_{gate}. After the conversion of each gated DCR to free-running

DCR, the average of the free-running DCRs are used as representative DCR for each SPAD at each cumulative proton fluence. The advantage of converting the gated DCR data to free-running DCR is that we can compare the DCR behaviour of the gated SPADs to the ungated NFADs and to other data sets of irradiated SPADs which were also ungated.

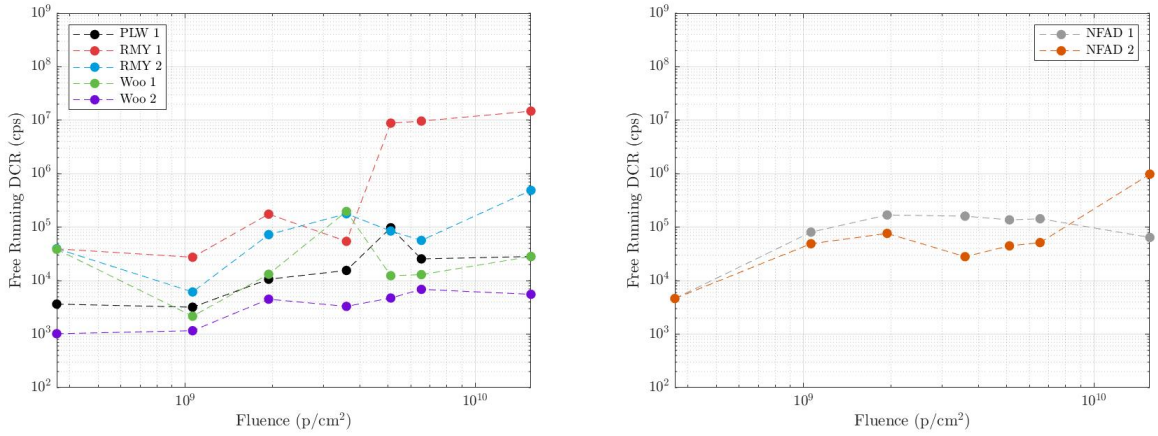

(a) (b)

Figure 4.24: Mean free-running dark count rates of SPADs as function of cumulative proton fluence. Error bars indicate one standard deviation, though they are so small that they are not visible at these scales.

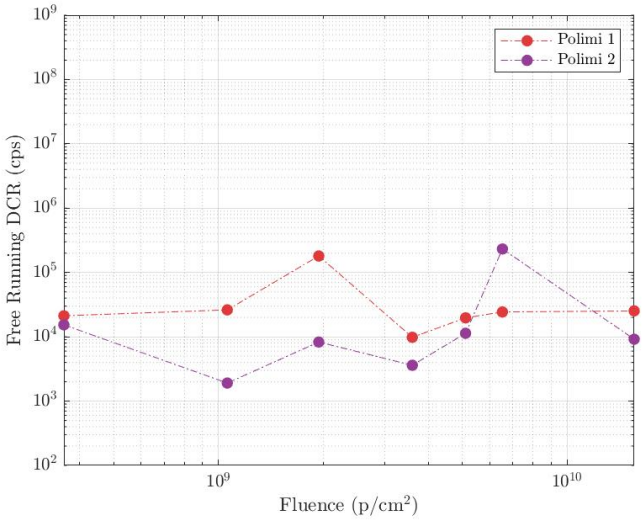

Figure 4.25: PoliMi SPADs free-running DCR as function of fluence.

The increase in DCR in the gated SPADS Figure 4.24a varies between SPAD models. The largest increases in DCR were measured in the RMY SPADs, with RMY 1 having a two-order of magnitude increase, and RMY 2 having a one-order of magnitude increase. The rest of the SPADs did not suffer such an increase in DCR, with Woo 1 actually exhibiting a lower DCR after radiation than before. While variation in post-radiation behaviour has been noted in the literature for silicon SPADs (3), there is a fairly consistent finding in literature that radiation will increase dark counts. The two InGaAs SPAD studies noted increases in DCR by two to three orders of magnitude, however their active area sizes were larger than the non-NFAD SPADs tested here (200 μm and 25 μm in the studies vs 16 μm) [47, 25]. Since displacement damage is expected to scale with active area volume, it is possible much less damage occurred in these smaller SPADs. Also, Harris et al., noted that there was high variability in the DCR increase between devices in their study [47]; this type of variability could also be at play in our experiment. Finally, the detectors which had little to no increase in dark count also happened to be situated on the edges of the proton beam width, so this could have further reduced displacement interactions in those edge SPADs.

NFAD 1 and NFAD 2 DCR increased by 1.5 and over 2 orders of magnitude, respectively. These SPADs had double the active diameter, leading to much larger active volume, however, they did not have a much larger increase in DCR. This could be due to the placement of the detectors in the proton beam width, since these were on the edge of the mounting bracket. The relatively modest increase in DCR could also indicate that the NFAD readout circuit type is better at handling the high noisiness of the InGaAs SPADs. Future work to compare against these results could involve gated NFAD SPADs to see if the fusion of the two readout schemes could contribute to better dark count rate management.

The overall trend for the Politecnico di Milano SPADs' free-running DCR (Figure 4.25) was decreasing with cumulative proton fluence. Again, it is possible that perhaps the devices were already saturated from the beginning of the experiment due to the temperature or excessive overbias, in which case they would have reduced sensitivity to increasing dark count rates due to radiation damage. Since the active area size of these SPADs is not known, it is difficult to compare these SPADs' results to the previous SPADs and results in literature.

4.5.3 Photon Detection Efficiency

Photon detection efficiency (PDE) is usually defined as the probability that photon will be detected, and can be estimated by the number of detected counts divided by the expected number of sent photons. Each component of the setup has an efficiency, since losses through optical elements, fibers and fiber coupling is inevitable. Additionally, there is an efficiency associated with the conversion of the photon detection to an electrical pulse. The increase in dark counts with cumulative proton radiation fluence is hypothesised to decrease the photon detection efficiency of SPADs. True single photon signals are not caught by the detectors which are overwhelmed with false counts comprising of thermal counts and afterpulses. Normally, one would calculate the efficiency of the detectors before irradiation and then after, but due to time constraints, we were only able to perform this calculation after irradiation. We are able to compare the calculated efficiencies to

those provided by the manufacturer. However, we attempted to the best of our abilities to recreate the measurement set-up which was utilized in TRIUMF, including cooling the detectors to -50°C.

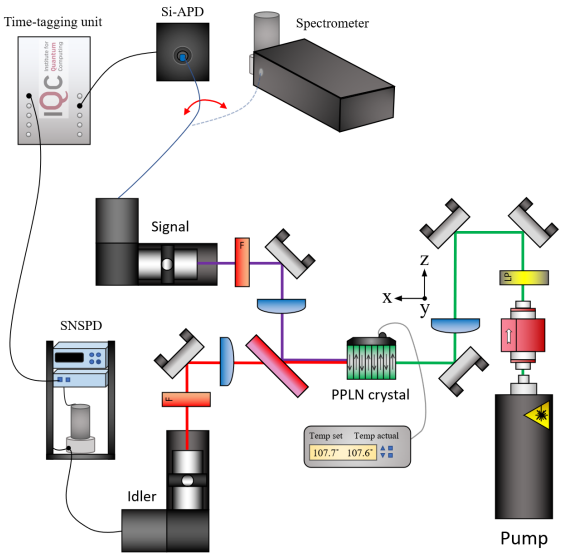

Figure 4.26: Schematic of correlated photon source set-up based on spontaneous parametric down conversion (SPDC), provided by Paul Oh. For the efficiency measurement described in this section, the superconducting nanowire photon detector (SNSPD) was interchanged with each irradiated InGaAs SPAD.

A correlated photon source was used as the signal source for the efficiency measurement (Figure 4.26). The source was built and optimized by my lab colleague Paul Oh for his own project. A 532 nm continuous wave laser pumps a periodically-poled lithium niobate (PPLN) non-linear waveguide, which has the property that it converts the pump light into two correlated single photons at 785 nm and 1550 nm (spontaneous down conversion, SPDC). The power of the laser was kept within 3 ±0.5 mW, as measured before the crystal. The 785 nm single photons are the signal photons and the 1550 nm are the idler photons. With each successful pump light conversion, a correlated single photon pair is created. The pair is divided into two arms via a dichroic beamsplitter which separates the photons by wavelength. After the beamsplitter, the photons are coupled in single-mode

fiber in their respective arms. The signal photons travel through fiber to be detected by a silicon-based SPAD (Excelitas SPCM), which is highly sensitive at the signal photon wavelength. Similarly, the idler photons travel through fiber to a detector sensitive to 1550 nm wavelength. In this experiment, two types of detectors were employed to detect the 1550 nm idler photons: the irradiated InGaAs/InP SPADs within the -50°C cooler and superconducting nanowire detectors (Quantum Opus model Opus One). After detecting the photons, the detectors send an electrical pulse to the TimeTagger counting unit.

An additional change with regard to the interchanging of the InGaAs SPADs and the SNSPD in the idler arm is that the SPADs were gated while the SNSPD was free-running. In previous measurements, the gating signal was triggered internally by function generator. In this experiment, the gate signal was triggered externally by the signal arm SPAD detection. This was possible by the use of BNC tee at the function generator with a 1kΩ impedance so that the TTL pulse from the silicon SPAD travelled to the function generator, triggered it, and then proceeded to the TimeTagger unit. Since the paths to the Si detector and the InGaAs detector were not equal, fiber and electronic delays were added so that the silicon and InGaAs detectors' detection would occur within a coincidence window. The gate pulse was delayed by approximately 930 μs in order to overlap the InGaAs SPAD detection window with the expected arrival of the correlated idler photon through the fiber which included a 250 m delay line.

Several measurements were taken for each detector in the idler arm, for up to four V_{Ex} values. First, counts were measured with both signal and idler beam paths unobstructed; this measurement would give the idler photon counts and dark counts. Next, the beam in the idler arm was obstructed so that the silicon APD would still be detecting signal photons and triggering the gate pulse but the InGaAs/InP APDs would only be detecting dark counts. This way we would measure the InGaAs/InP APD dark count rate. We measured the signal dark count rate by blocking the beam before the crystal, so that no 798nm signal photons would be created, nor would the InGaAs/InP SPADs be triggered. Finally, a correlation histogram was taken between the signal and idler channels, which measures the number of coincidences (counts of both signal and idler) within a small measurement window (2 ns in this case). This measurement required fine-tuning of the

delay between the two channels of the TimeTagger since the signal detection signal arrived much earlier than the idler detection signal. The correlation histogram collected 20 s of counts from each channel and constructed a histogram with the x-axis representing time of coincidence counts and bin height representing number of coincidence counts (see Figure 4.28 for example plot).

The construction of correlation histograms is noteworthy here as measure of the persistent sensitivity of the irradiated detectors to single photons. If such histograms show a clear correlations between the arrival of photons between the two arms, there is indeed still single-photon sensitivity in our irradiated devices. This would be confirmation, as well, of the successful function of the SPADs and readout circuit, which were not thoroughly tested prior to irradiation.

Heralding Efficiencies

The term *heralding photons* is related to having a single-photon source quasi on-demand. A PPLN waveguide will convert the pump light into photon pairs at some rate, R_p. Each photon travels down its respective arm of optical elements and fibers, and eventually, if it not scattered or absorbed, it may be detected by the single-photon detector at the terminus of the channel. Heralding efficiency is a good measure of the efficiency of the whole set-up because it gives an estimate to the question: what is the likelihood of a coincidence count, given that a single count has occurred? In other words, if a single photon has travelled through one channel, what is the likelihood its co-created photon also makes it through its channel and is detected within the measurement coincidence window.

Experimentally, heralding efficiency is the ratio of coincidence counts to one channel's single counts. A low heralding efficiency, which would occur if the coincidence counts are much lower than the single counts, indicates that despite high single counts in one channel, there are few single counts in the other channel. Therefore, there are few coincidence counts during the measurement window and little correlation between the photon arrival times. Conversely, a high heralding efficiency indicates many coincidence counts and a correlation between the arrival of the two photons. Low heralding efficiencies can be a result of poor

optical alignment or incorrect delays between the counter channels.

The heralding efficiencies were calculated for each InGaAs/InP SPAD for excess biases of 1 to 4 V. Table 4.3 summarizes the single and coincidence count rates as well as the calculated efficiencies.

Table 4.3: Net single and coincidence counts, as well as calculated heralding efficiencies for all tested SPADS after irradiation. Negative counts occur when photon count rate is lower than dark count rate, indicating detector saturation.

Detector	Excess Bias (V)	Signal Counts	Idler Counts	Coincidence Counts	Heralding Efficiency (%)
PLW 1	1	583 857	5285	2992	0.51
	2	584 833	299 060	10 681	1.83
	3	587 551	16 157	15 814	2.69
	4	589 584	20 722	19 582	3.37
RMY 1	1	589 734	6788	2065	0.35
	2	602 217	40 604	16 1813	2.69
	3	589 962	71 618	27 311	4.63
	4	588 785	92 757	35 067	5.96
RMY 2	1	611 245	7117	205	0.03
	2	608 010	40 478	16 183	2.66
	3	608 589	20 211	18 431	3.03
	4	609 768	25 913	22 636	3.71
Woo 1	1	518 595	3556	2051887	0.36
	2	516 289	14 851	13 662	2.65
	3	514 322	17 257	16 796	3.27
	4	513 365	22 446	21 435	4.18
Woo 2	1	642 585	2875	835	0.13
	2	684 642	11 052	10 552	1.63
	3	658 589	17 333	16 859	2.56
	4	665 925	23 453	22 360	3.36
NFAD 1	2	544 210	-7074	153	0.03
	3	544 981	-82 147	8116	1.5
	4	550 067	-17 840	5697	1.04
NFAD 2	2	673 374	-45 763	1784	0.26
	3	682 087	-117 856	51 963	7.62
	4	687498	-61 443	74 761	10.87

The heralding efficiencies of the idler channel increase with increasing SPAD excess voltage. We see, however, that this increase is short-lasting and even with an excess bias of 4V the efficiency trend is plateauing. The Figure 4.27 shows the trends for the gated

SPADs. The NFADs, which were not gated, suffered from very high levels of dark counts, such that more counts were registered when the idler beam was blocked, indicated that there were some saturation effects (resulting in negative count rates as seen in Table 4.3).

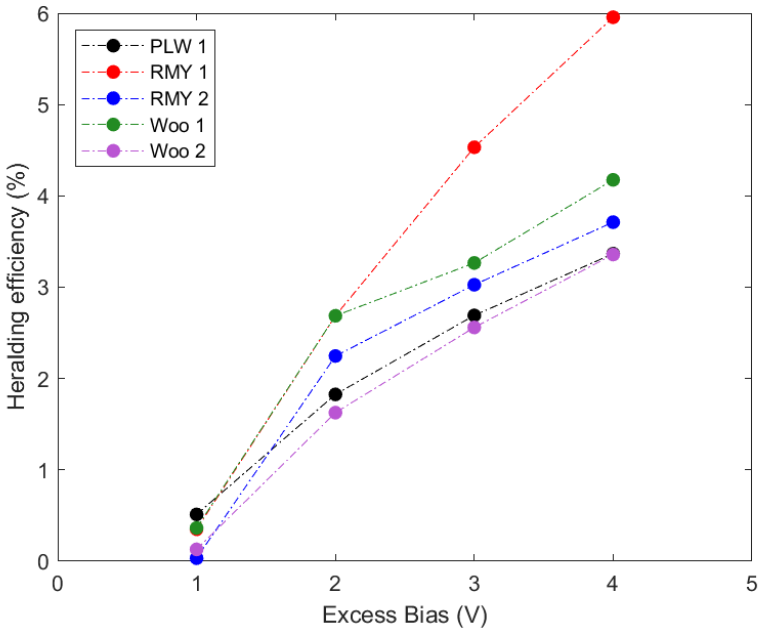

Figure 4.27: Heralding efficiency for idler channel for several gated InGaAs/InP SPAD excess biases.

Correlation Histograms

The collection of coincidences over 20 s and sorting the data by arrival time in a histogram allows to estimate a timing resolution of the whole entangled-photon source set-up. Coincidence peaks are clearly visible for most of the SPADs, denoting that a click from the signal detector and the idler detector coincided within the narrow 4 ns coincidence window. The flat area around these peaks are coincidence counts triggered by noise; their spread across the time bins indicates no correlation between the arrival times of the clicks.

Figures 4.28a and 4.28b show the correlation histograms for one gated and one NFAD

SPAD at various excess bias levels (all other correlation histograms may be found in Appendix B). We see that most of the gated SPADs have excellent signal-to-noise characteristics, with notable large peaks dominating the low noise levels for each of the excess bias levels. RMY 1, however, exhibited quite high noise levels which increased with increasing excess bias. Neither NFAD performed as well as the gated SPADs, with their maximum peak height at 4V excess bias less than half of the size of the SPADs' peak heights.

One thing to note is that the gated SPADs' peak shifts with change in excess bias. Larger excess bias shifted the peaks earlier in the histogram. This is related to the fact that with increase bias there is increased detection efficiency, so it is more likely that photons will be detected earlier in the gate window. This translates to an earlier arrival of coincidence counts. The behaviour is not visible in the NFAD correlation histograms, which is expected since they are not gated.

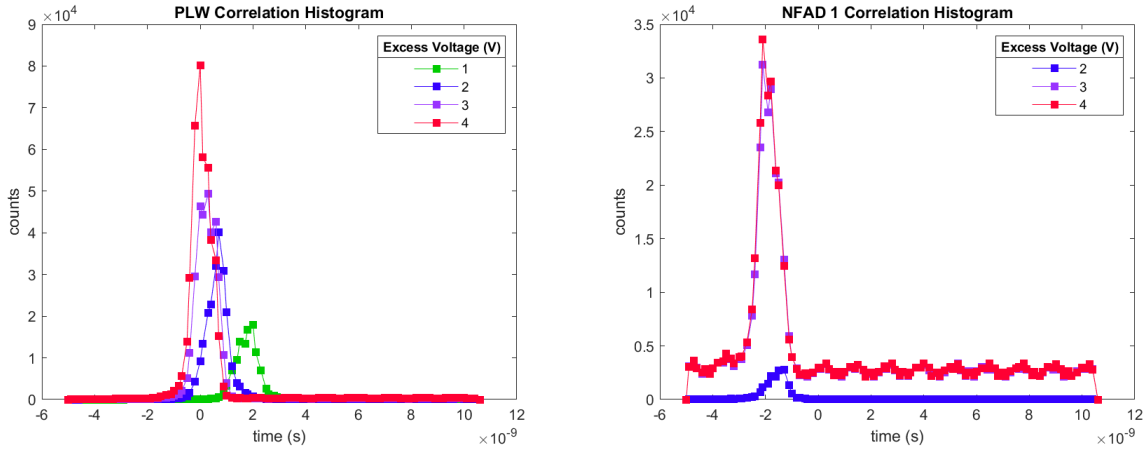

(a) PLW (b) RMY NFAD

Figure 4.28: Correlation histogram for two SPADs. Oscillatory behaviour outside the large peak is visible in all correlation histogram plots (Appendix B), and is believed to be an attribute of the software used to capture the time tag data.

Full-width-half-max (FWHM) was deduced for each of the SPADs from the correlation histogram plots by plotting in a logarithmic scale (see Figure 4.29 for an example plots as well as Appendix B for all other plots). One can see that the peak versus noise is much

easier to observe on a logarithmic scale than on a linear scale. To calculated the FWHM, one must first isolate the peak which resides on top of the base noise level. The base noise level was defined as the mean dark counts. Then the peak was defined as the peak maximum minus the base noise level. The half-max of the peak was found by dividing peak height by two and subtracting it from the peak maximum. Finally, interpolation was used to estimate the times at which the peak is at half-max. The FWHM is then the difference between the times that the peak is at half-max.

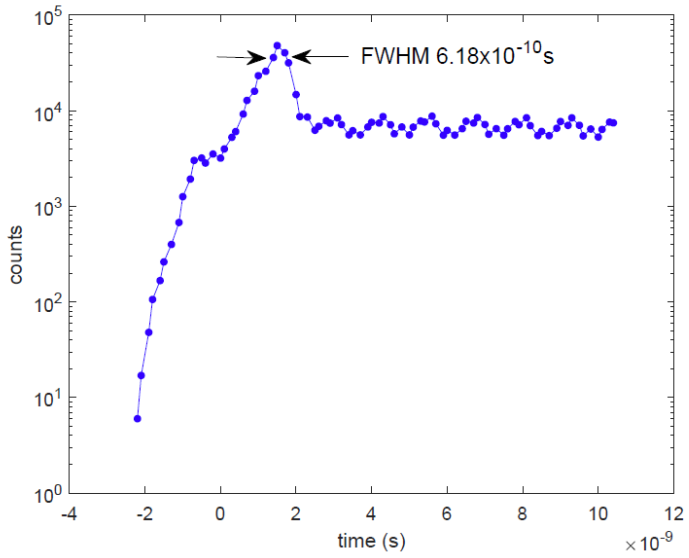

Figure 4.29: RMY 1 correlation histogram for excess bias of 2 V. The oscillation behaviour is seen in all correlation histograms and is believed to be an artifact of the software collecting the time tag data.

The use of a 1V excess bias led to a large variation in pulse widths, while higher excess bias settings resulted in more similar pulse widths (translating to less time jitter)(see Figure 4.30). Narrowing of pulse widths with excess bias is expected since the detector efficiency increases and the true signal is easier to distinguish from background noise. The FWHM values reported here are worse than typical values required for QKD purposes (which are on the order of tens of picoseconds). Without a comparison of the correlation histograms taken before irradiation (and lack of metric from the manufacturer data sheet),

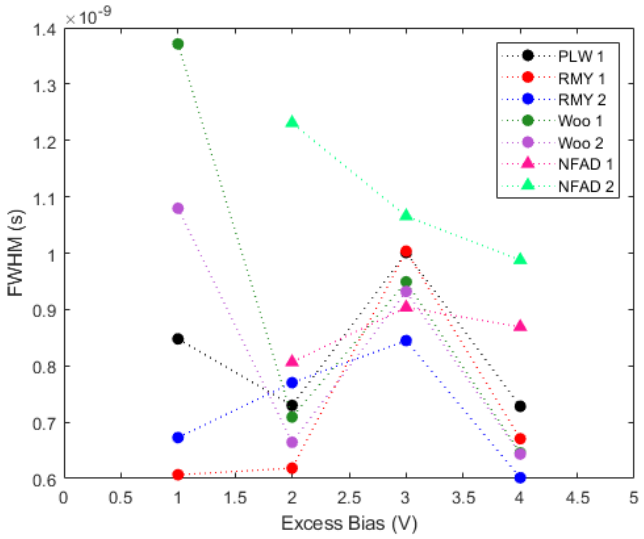

Figure 4.30: FWHM of correlation histograms as function of excess bias for all irradiated InGaAs SPADs.

it is difficult to conclude that the wide FWHM is solely due to the increase in noise from displacement damage effects, since the FWHM estimated here takes both the optical set-up and electronic jitter into consideration. However, it is likely that the increased noisiness of the SPADs after irradiation did not contribute with the overall poor timing resolution.

After calculation of the heralding efficiency, one can estimate the detector efficiency with further consideration of other efficiencies in the channel. Two methods were compared in the calculation of the irradiated detector efficiency. The first, called *Independent Detector Efficiency* requires only knowing the single and coincidence count registered from the InGaAs and silicon detectors, as well as the coupling efficiency of the whole optical channel. The second method estimated the efficiency by comparing the single and coincidence counts between the irradiation InGaAs detectors, whose detection efficiency we don't know, with the SNSPD, whose detection efficiecny is known. This method is called the *Inferred Detector Efficiency*.

Independent detector efficiency

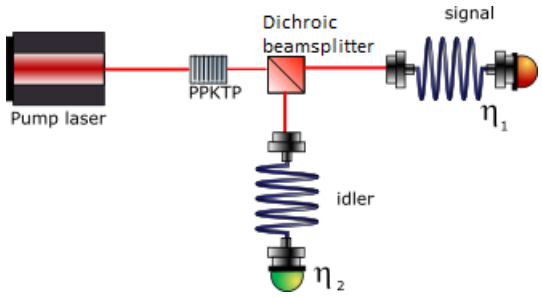

Figure 4.31: Schematic of SPDC sources and detectors for each single photon.

As labelled in Figure 4.31, we can describe the single counts from each arm as:

$$S_1 = R_p \eta_1 \tag{4.3a}$$

$$S_2 = R_p \eta_2 + DC \tag{4.3b}$$

where R_p is the pair rate of production of the PPKTP crystal and $\eta_{1,2}$ are the total efficiencies of the signal and idler arm, respectively. Dark counts (DC) are omitted for the signal single counts because they were much smaller (4000 counts) than the counts when the beam was not blocked (600 000 counts).

Coincidence counts are given by:

$$C = R_p \eta_1 \eta_2 + C_{acc} \tag{4.4}$$

where C_{acc} are the accidental coincidences, which are dark counts that happen to fall within the coincidence window and trigger a coincidence count.

If we divide the number of coincidence counts by the signal signal counts we get the *heralding efficiency*. For example, the heralding efficiency of the idler arm would be:

$$\frac{C}{S_1} = HE_2 \tag{4.5}$$

Using equation 4.3b, we can replace the C and simplify by dividing by the common denominator of $R_p\eta_1$:

$$\frac{C}{S_1} = \frac{R_p\eta_1\eta_2 + C_{acc}}{R_p\eta_1} \tag{4.6}$$

$$\frac{C}{S_1} = \eta_2 + \frac{C_{acc}}{R_p\eta_1} \tag{4.7}$$

Then we can find the idler arm efficiency by isolating for η_2.

$$\eta_2 = \frac{C}{S_1} - \frac{C_{acc}}{S_1} \tag{4.4}$$

This last equation came about from using the earlier definition of signal single counts (equation 4.3a). From there we can find the detector efficiency by noting that:

$$\eta_2 = \eta_{coupling}\eta_{D2} \tag{4.5}$$

where $\eta_{coupling}$ is the absolute efficiency of the optics, fibers, fiber couplings up until the detector. Therefore:

$$\eta_{D2} = \frac{\frac{C}{S_1} - \frac{C_{acc}}{S_1}}{\eta_{coupling}} \tag{4.6}$$

S_{signal}, C can be directly extracted from the single and coincidence counts from the TimeTagger, and C_{acc} can be estimated using two methods. $\eta_{coupling}$ was calculated by my colleague to be 45%.

One method of calculating C_{acc} was using the net single counts from the signal (channel 1) and idler (channel 2).

$$C_{acc} = S_1 S_2 CW \tag{4.7}$$

where CW denote the coincidence window, which in this case was 2 ns. As a reminder, S_1 and S_2 are the net single counts, so the single channel dark count rate is accounted for. This method of estimating the accidentals will be henceforth called the *direct method*.

Figure 4.32 demonstrates the second method for estimating accidental coincidence counts. The correlation histogram is plotted in logarithmic scale for ease of discerning

the coincidence peak from the noisy counts. As discussed previously in the estimation of FWHM, the base of the peak extends from the mean noise level up to the peak maximum and then return back towards the mean noise level. The width of the peak base is from t_1 to t_2. The true coincidence counts reside in the area of the peak that is *above* the mean noise level between t_1 and t_2 (unshaded area), while the accidental coincidence counts reside *under* the mean noise level, also within the same time range (shaded area). Therefore, to estimate the accidental coincidence counts, one must integrate the counts from 0 to the mean noise level for the time range of t_1 to t_2. The true number of coincidence counts can be estimated by subtracting this calculated number of accidentals from the measured number of coincidence counts. This method will be henceforth be called the *post-processed method* of estimating accidental counts.

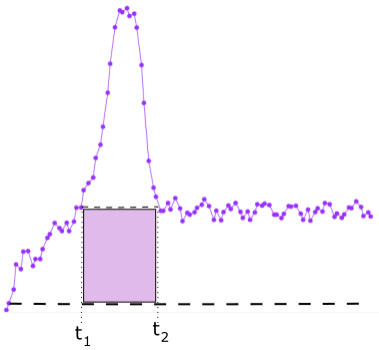

Figure 4.32: Sample coincidence histogram as it would look in logarithmic scale. The post-process method of estimating accidentals uses integration of the shaded area under mean noise level of pulse between pulse start and ends times.

We see that the two methods yield similar detector efficiencies (Table 4.5.3), therefore showing that integration of the correlation histogram peak is an accurate method of estimating the number of counts in a measurement period. The detector efficiencies, for the most part, increase linearly with excess bias at a rate of approximately 2.5% per voltage of bias. The SPADs with the more irregular behaviour, that is, RMY 1 and the two NFADs, are those which suffered the highest dark counts and most likely the most damage from the radiation. Data for SNSPD is also presented; with this state-of-the-art detector we see near 65% efficiency using this method. This is much lower than the manufacturer's

specification of 87.5%, however, their measurement set-up was probably much different, including a non-single photon source.

Table 4.4: Calculated photon detector efficiency (PDE) using two methods for estimating accidental coincidence counts

Detector	Excess Bias (V)	PDE (%) estimating C_{acc} with *direct method*	PDE (%) estimating C_{acc} with post-processed method
PLW 1	1	1.13	1.11
	2	3.79	4.01
	3	5.97	5.90
	4	10.5	7.36
RMY 1	1	0.77	0.12
	2	5.94	3.44
	3	10.22	1.25
	4	13.15	7.23
RMY 2	1	0.07	0.02
	2	5.88	5.78
	3	6.71	6.49
	4	8.23	7.87
Woo 1	1	0.81	0.79
	2	5.87	5.83
	3	7.24	7.15
	4	9.26	9.12
Woo 2	1	0.29	0.29
	2	3.61	3.57
	3	5.67	5.61
	4	7.44	7.34
NFAD 1	2	0.07	0.01
	3	3.40	2.07
	4	2.32	0.92
NFAD 2	2	0.63	0.55
	3	17.03	16.73
	4	24.22	20.22
SNSPD without delay		64.9	64.58
SNSPD with delay		62.1	62.01

Inferred detector efficiency

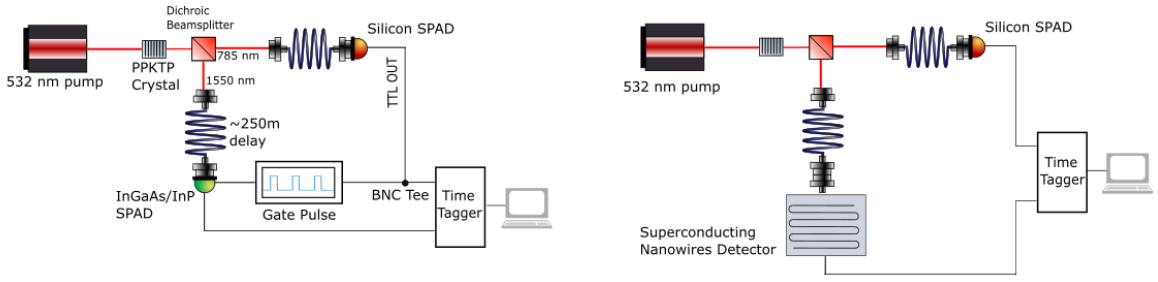

(a) (b)

Figure 4.33: Correlated photon source and detector set-up

We used two measurement configurations, one with the InGaAs/InP as the idler detector (Figure 4.33a) and the other with the SNSPD as the reference idler detector (Figure 4.33b). As described previously, the InGaAs/InP SPADs are gated using the signal silicon SPAD detector as a trigger, while the SNSPD is free-running. Using a constant pump power and near constant count rate from the signal detector, we can infer the detection efficiency of the InGaAs/InP SPAD. We show this by following the method from Yan et al.[97].

Much like the previous calculation, we describe the net single counts $S_{1,2}$ of channel 1 and channel 2:

$$signal : S_1 = R_p \eta_1 \eta_{d1} (1 + \kappa_1) \tag{4.8a}$$

$$idler : S_2 = R_p \eta_2 \eta_{d2} (1 + \kappa_2) \tag{4.8b}$$

$$coincidences : C = R_p \eta_1 \eta_2 \ \eta_{d1} \eta_{d2} \tag{4.8c}$$

Here $\eta_{1,2}$ are the coupling efficiencies of channels 1 and 2, $\eta_{d1,d2}$ are the efficiencies of each channels' detectors, and $\kappa_{1.2}$ are the afterpulsing constants for each detector. We find the following ratio which we recognize to be the signal heralding efficiency:

$$\chi_1 = \frac{\eta_2 \eta_{d2}^{InGaAs}}{1 + \kappa_1} = \frac{C}{S_1} \tag{4.9}$$

We can find a similar ratio for the second set-up, where the channel 2 detector is the SNSPD.

$$\chi_2 = \frac{\eta_2 \eta_{d2}^{SNSPD}}{1 + \kappa_1} = \frac{C'}{S_1'} \tag{4.10}$$

where C' and S_1' are the coincidences and single counts with the SNSPD as the channel 2 idler detector. Using these two ratios, we can isolate for our variable of interest:

$$\eta_{d2}^{InGaAs} = \eta_{d2}^{SNSPD} \frac{\chi_1}{\chi_2} \tag{4.11}$$

Therefore, through using coincidence and single counts from the two set-ups and knowing the efficiency of the SNSPD, one can infer the detection efficiency of the InGaAs/InP SPADs. Table 4.5 shows the results of this measurement.

Table 4.5: Detector efficiency as inferred by comparison to SNSPD discussed in Section 4.5.3

Detector	Excess Bias (V)	Inferred DE (%)
PLW 1	1	1.60
	2	5.70
	3	8.39
	4	10.50
RMY 1	1	1.09
	2	8.38
	3	14.44
	4	18.57
RMY 2	1	0.10
	2	8.30
	3	9.44
	4	11.58
Woo 1	1	1.14
	2	8.25
	3	10.18
	4	13.02
Woo 2	1	0.41
	2	5.07
	3	7.98
	4	10.47
NFAD 1	2	0.09
	3	4.67
	4	23.23
NFAD 2	2	0.82
	3	23.75
	4	33.91

As with the previous method, the detector efficiency increases with bias. This method estimates higher efficiencies for the same excess bias compared to the previous method. The differences in estimated efficiencies can be better seen the in Figure 4.34. Multiplication by the 87.5% SNSPD efficiency (η_{d2}^{SNSPD}) in equation (4.5.3) assumes that the efficiency specified by the manufacturer using their own testing procedure is accurately reproduced in

our test; however, the independent estimation method discussed previously (Section 4.5.3 capped the SNSPD efficiency at 65%. Therefore, the discrepancy between the estimated InGaAs/InP photon detection efficiencies could be associated with this decrease in SNSPD efficiency within our testing set-up.

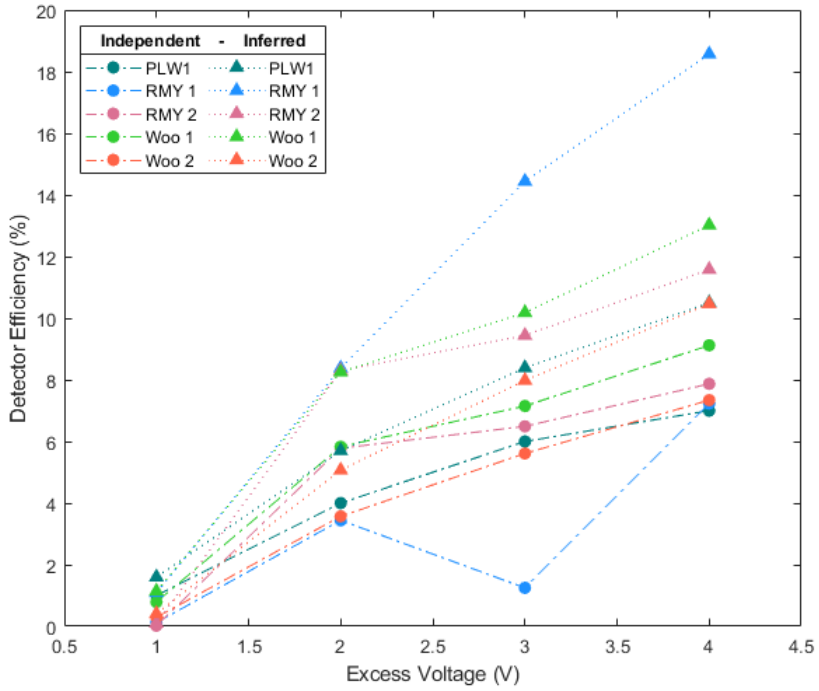

Figure 4.34: Detector efficiencies for five SPADs as estimated using the independent and inferred methods.

Comparison to pre-radiation photon detection efficiency

Table 4.6: Detector efficiencies prior to radiation, as specified by manufacturers, and after radiation, as estimated in this work. Unfortunately, due to limited lab access and timing we were not able to perform the PDE tests prior to irradiation. The post-radiation efficiencies presented are those estimated for 2V excess bias, as this is the typical operating excess bias.

Detector	Testing Condition			Pre-radiation Efficiency (%) from manufacturer	Post-radiation Efficiency (%)
	Temp(°C)	Gating parameters	DCR (kHz)		
PLW	-40	N/A	4.6	20	5.70
RMY	-40	N/A	100	20	8.38
Woo	-40	10 MHz, 2ns	0.5	20	8.25
NFAD	-33	N/A	75	10	4.67

Since detector efficiency measurements were not undertaken prior to irradiation, the best source for estimating the pre-radiation efficiency is the manufacturer specifications for the SPAD. These data can be found in Table 4.6, along with the testing conditions for the characterization. The data presented from this work is the inferred detector efficiency at 2V excess bias, which appears to be a good biasing point for these detectors with respect to the noise level.

The post-radiation efficiency is significantly lower than the pre-radiation efficiency. This comparison is not perfect, however. Since the testing conditions are not the same, it is hard to make a direct comparison between the manufacturer specified efficiency and the estimated efficiency in this work. The SPADs without gating parameters were tested in free-running mode (without gating). This mode allows for higher efficiency since the only limit to detecting the next photon is the detector's dead time, whereas in gated operation, you are limited by both the detector dead time as well as the gating duty cycle. Wooriro's gating scheme of 10 MHz frequency and 2 ns gate width is closer to our measurement conditions, with a duty cycle of 2% to our approximate 1.5%. At 2V excess, the Woo post-radiation efficiency is less than half of the pre-radiation efficiency and even at 4V excess

bias, the post-radiation efficiency only reaches 10%. In the case of the Woo SPADs, the dark count rate actually decreased after radiation, but the estimated detector efficiency was much lower than the manufacturer specified. Given that the noise level did not increase much with radiation exposure, the decrease in efficiency must be due to the readout circuit design and the lower gating frequency.

It is interesting to note that post-radiation efficiency exceeded the manufacturer specific efficiency for the two NFAD samples for the 3V and 4V excess bias. This can be explained by the very high dark count rate (>100 kHz) for each of the excess bias settings. The dark counts overwhelm the signal, so it is safe to assume that the coincidence counts measured were predominantly accidental counts and the efficiencies estimated for the NFADs are not accurate at all. This is bolstered by the fact that this post-radiation measurement took place at a much lower temperature which should have reduced dark counts past the manufacturer's maximum of 75 kHz. Clearly, radiation did increase the dark count rate so much that the signal is much lower than the noise level.

4.6 Conclusion

In this chapter, I presented the process of the experimental design, from choosing suitable SPADs, to designing the readout circuit and experimental apparata. The results reported in this chapter contribute the small number of studies on radiation effects in InGaAs SPADs; however, no clear conclusions can be drawn. Several devices exhibited a substantial increase in dark count rate (PLW 1, RMY 1 and 2, NFAD 1 and 2), while two devices showed a decrease in dark count rate after irradiation. Due to time constraints, complete characterization of the devices was not possible prior to irradiation; this perhaps would have elucidated other changes in the devices or the readout system. In comparison to previous studies discussed in Chapter 3, these SPADs did not exhibit as much dark count increase as was expected, but this could be due to their small active volumes. Future work could precisely model the estimated interactions in InGaAs substrate, accounting for the active area thickness and volume. Additionally, more effort could be spent into the design

of a higher frequency gating system which reflects the operating parameters necessary for QKD applications. Finally, the use of more devices and full characterization before and after radiation would allow for more conclusive analysis.

Chapter 5

Laser Annealing of Radiation-Damaged SPADs

5.1 Introduction

Radiation damage of single-photon detectors and electronics is inevitable in a space environment. The best way of mitigating the damage from radiation is to employ shielding: tools like SPENVIS can be used to model how thick satellite walls must be to block a portion of the harmful radiation spectrum. However, there are weight and cost limits to how much shielding can be used. Yin et al., reported that to reduce DCR increase to 1 cps per day, a 400 mm thick aluminium shielding, corresponding to 723 kg satellite, would be necessary. This was deemed unfeasible and the thickness was capped to 12 mm [98]. Inevitably this means more charged particles will be able to cross the thinner shielding and interact with the internal components, leading to higher displacement damage. As such, it would be useful to have additional methods of mitigating radiation damage. It has been shown both in our group and from others that heating and deep cooling of the detector active area is a method of reducing dark count rate in irradiated detectors [17, 41, 60]. While thermoelectric coolers have been most prevalent tool for localized heating and cooling, optical annealing via a high power laser incident on the active area has also been shown to be

a potent way of achieving very high local heating [59]. Following the lab tests by Lim et al., a space-borne experiment was conceived to test real-time laser annealing of silicon SPADs in LEO known as CAPSat; this experiment will be discussed in the first section of this chapter. In tandem to the release of CAPSat in orbit, ground laser annealing testing of a prototype of the satellite detector module was conducted to investigate the most effective annealing protocols; these tests will be laid out in the second part of the chapter.

5.2 CAPSat

5.2.1 Introduction

In a collaborative effort to observe in-orbit radiation damage of silicon-based SPADs, as well as healing of the radiation damage through cooling and laser annealing, the science teams at University of Illinois at Urbana-Champage and the University of Waterloo have designed, built and launched the **C**ool **A**nnealing **P**ayload **Sat**ellite into LEO. The satellite is housed in a 3U CubeSat bus (1U = 10 cm x 10 cm x 10 cm), with one level of the bus dedicated to the SPAD detector module (DM) and another level dedicated to the annealing laser controller module. The design of the satellite bus and annealing payload, as well as the integration of the DM and annealing payload, was conducted by University of Illinois at Urbana-Champaign, while then-PhD student Nigar Sultana designed the SPAD DM. My contributions include functional testing of the DM, so the DM design will be briefly summarized.

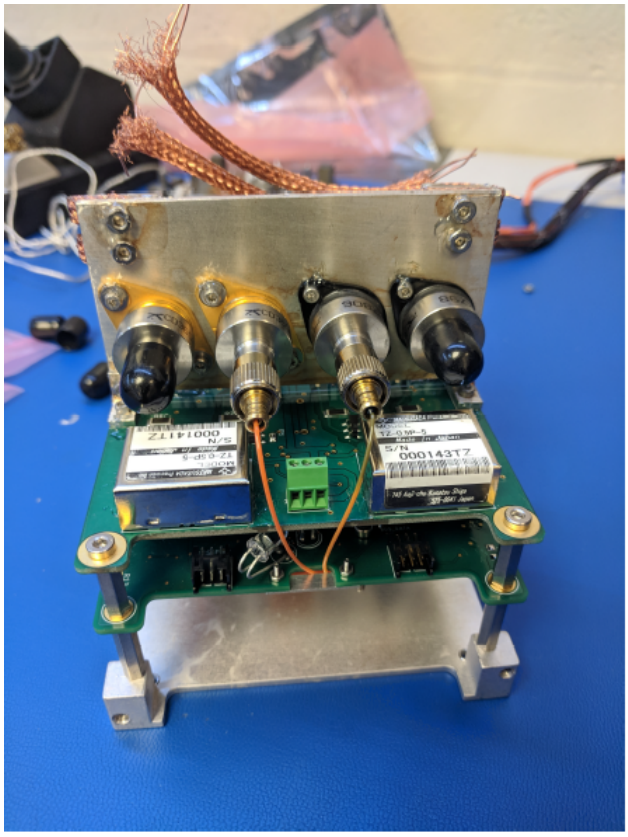

Figure 5.1: Flight version of SPAD DM (top) and annealing controller board (bottom). The four detectors are visible with black blacks and with fiber coupling. Image courtesy of University Illinois. Reprinted from [88].

The SPAD DM consists of four Si-SPADs from Excelitas Technologies (Figure 5.1). Two models were chosen for their difference in active area size: SLiKs (180 μm) and C30902H (500 μm). The hermetically-sealed metal housing contains the SPAD active area as well as a two-stay TEC and thermistor, so that the active area temperature can be precisely controlled in a range between -30°C and 100°C. The SPADs are connected to the annealing payload via a fiber-connector. The DM PCB is responsible for SPAD biasing, quenching, readout and TEC control. The circuit components were carefully chosen so to operate within the power budget of the satellite and to withstand the harsh conditions expected in space, notwithstanding radiation. The PCB was designed with limiting power

consumption and robustness in mind: only one detector is to be biased and read out at a time. The PCB can be viewed as two separate biasing circuits, each with a high voltage power supply, four separate passive quenching circuits for each detector, and a single thermal control circuit which can manage any one of the TECs within the SPAD package. Control of the detector bias and readout occurs through the controller board designed by the University of Illinois team. However, testing of SPAD DM prototype boards was possible at University of Waterloo via a PSoC3 development kit CY8CKIT-030A, where the PSOC creator integrated design environment (IDE) was used to configure PSOC3 hardware and firmware concurrently [7]. Firmware was written in C computing language to individually bias the detectors, readout the detector temperature (via thermistor), TEC current and count rate, as well control a proportional-integral-differntial (PID) thermal loop which instructed the TEC driver to control the SPAD TECs based on thermistor readout. All PCB design, firmware code writing, and early prototype testing was conducted by Nigar Sultana [88].

5.2.2 Impact of SPAD wire reinforcement on detection performance

During the pre-flight vibration tests, which simulate the expected vibration during launch to space, a weak, shaky joint between the CAPSat flight model SPAD cathodes and vertically placed quenching resistors was revealed. The vertical placement of quenching resistors was chosen to reduce the distance between the cathode, thereby reducing parasitic capacitance, and in turn reducing the recharge time of the detectors [88]. If the connection between the SPAD cathodes and the quenching resistor were to sever due to high vibration, the SPAD would be dysfunctional. As such, reinforcement of this joint was deemed necessary, with the two candidate reinforcing compounds being tape (3M DuPont Kapton Polyimide Film Tape 5413) or epoxy (Loctite EA 0151), both of which were pre-screened as space-compatible with respect to their out-gassing properties. However, it was possible that addition of tape or epoxy would change the dielectric properties near the SPAD wires, leading perhaps to degredation of the detector performance. We hypothesized that if there were significant changes in the detector performance then it would show up in the an in-

creased recharge time. To test this hypothesis, tape or epoxy was made by applying each to a prototype board (Figures 5.2a and 5.2b) and measuring changes in detector readout (Figure 5.4).

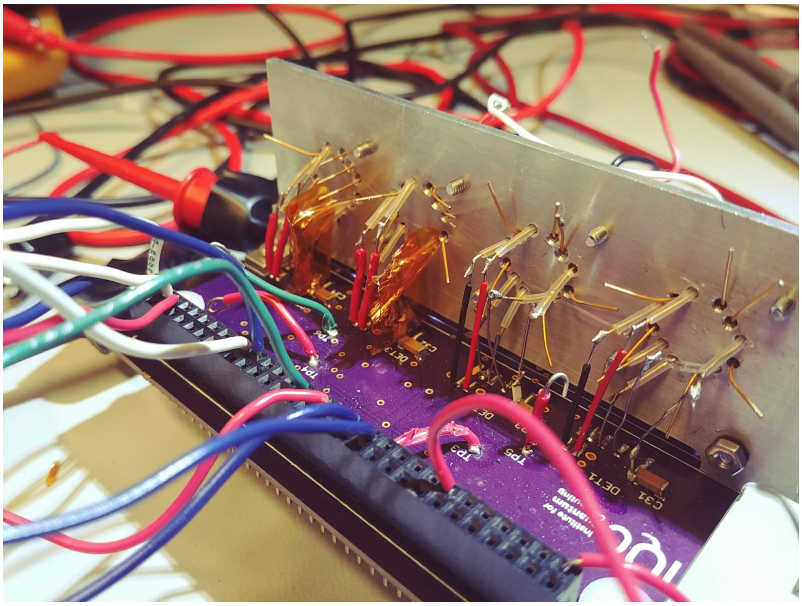

(a) CAPSat prototype board with cathod taped with Kapton tape (orange clear tape).

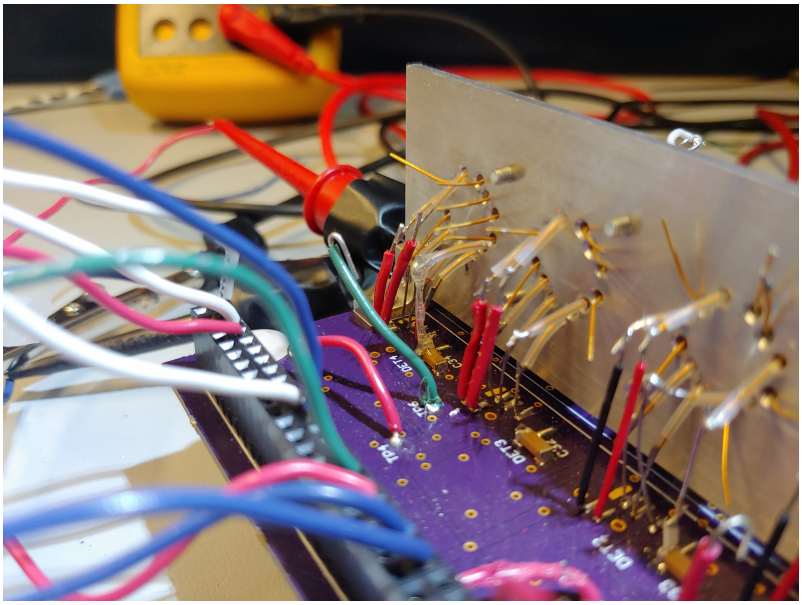

(b) CAPSat prototype board with cathode (furthest in background) covered in clear epoxy.

Figure 5.2: Two methods of reinforcing the SPAD wires. Photos courtesty of Nigar Sultana.

The detector bias and control voltages for the high-voltage supply (TZ-0.5Z) on the detector module (DM) were provided using a PSoC3 embedded system. The PSoC was programmed using PSoC Creator 4.2. The detector breakdown voltage V_{Br} and pulse characteristics were found using the oscilloscope (LeCroy Wave Pro 760Zi 6GHz, 40 GS/s with the PP00T-WR, 10:1, 500 MHz, 10M, 9.5 pF probe) connected at the output. Recharge time was measured with another oscilloscope (Agilent infiniium 1Ghz, 4Gs/s,1165A with the 10:1, 10M , 10.0 pF probe) by letting the pulses be recorded continuously for approximately 15 minutes. The recharge time (Figure 5.3) was calculated by noting the triggered pulse amplitude and then finding the time at which the subsequent pulses reached approximately 63% of the triggered pulse height. For one detector, signal and recharge time were characterized without tap and with tape applied, and for another detector, signal and recharge time were characterized without and with tape applied and, after removing tape, with epoxy applied.

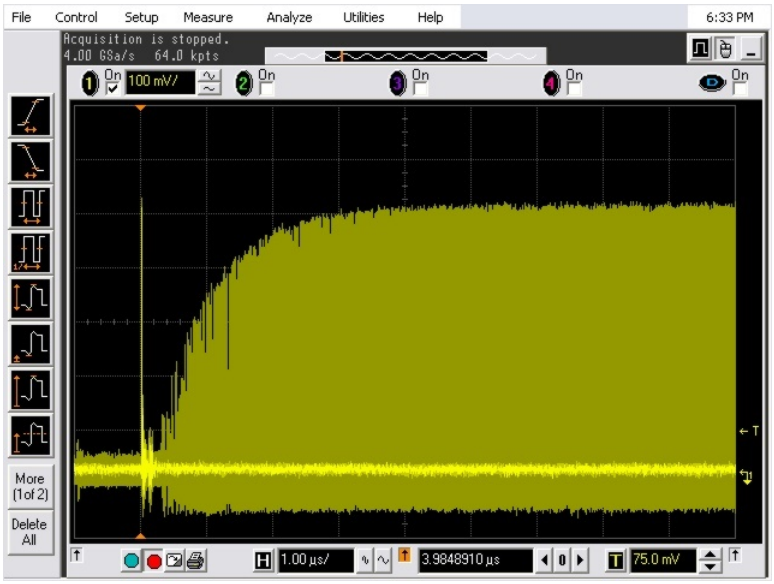

Figure 5.3: Oscilloscope screenshot of recharge time measurement.

Pulse characteristics were found to deviate minutely after tape was applied to the SPAD cathode. V_{Br} remained the same. Pulse width was slightly wider ($\sim$ 4-7 ns) after taping,

but that is expected with the increase in capacitance (Figure 5.5a). The trend of decreasing pulse width with increasing bias voltage persisted after taping as well. Pulse amplitude varied by maximum 10% between pre- and post-taping, corresponding to changes on order of tens of mV (Figure 5.5b). Temperature recorded between trials differed by about 1K and was relatively constant as voltage was increased. Recharge time did not change significantly (Figure 5.5d).

Similarly, no significant changes were found in detector characteristics when epoxied. The breakdown voltages were the same; the recharge times were very similar. Pulse amplitudes differed by less than 15%, and pulse width only varied greater than 10% for the V_{Br}. Temperature was constant within the range of one degree.

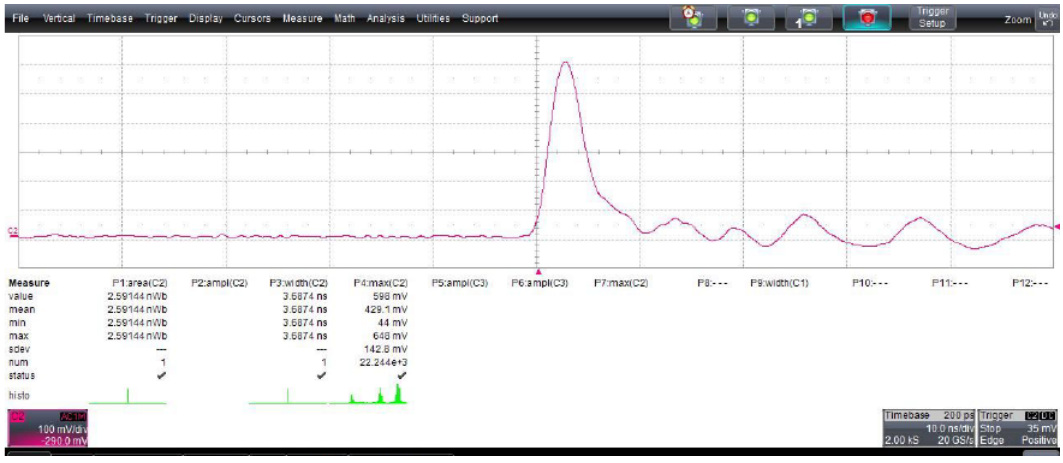

Figure 5.4: Readout pulse shape for $V_{ex} = 17V$ for detector with epoxy applied

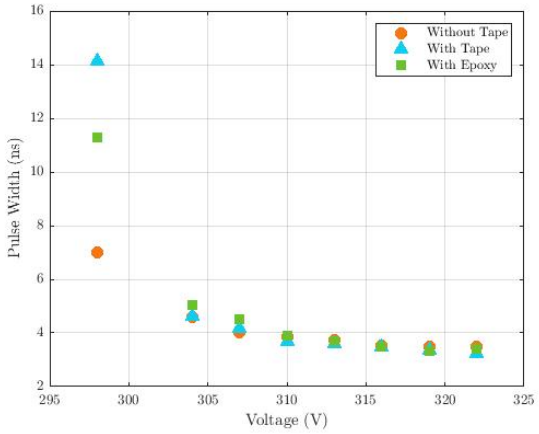

(a) Pulse width as function of bias voltage without or with tape, or with epoxy

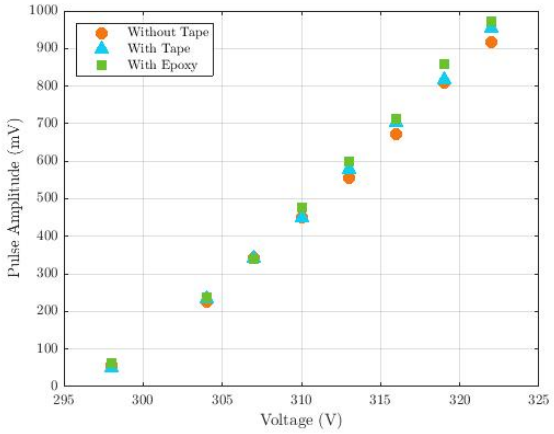

(b) Pulse amplitude as function of bias voltage without or with tape, or with epoxy

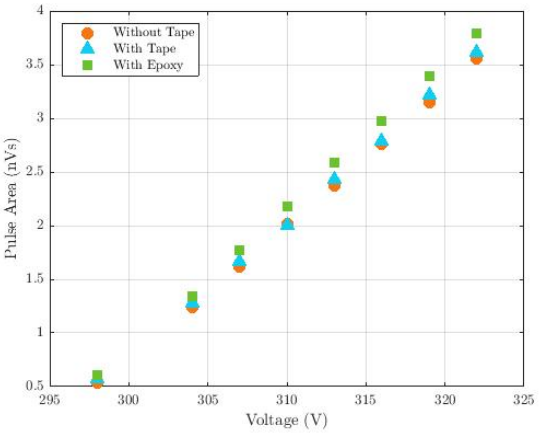

(c) Pulse area as function of bias voltage without or with tape, or with epoxy

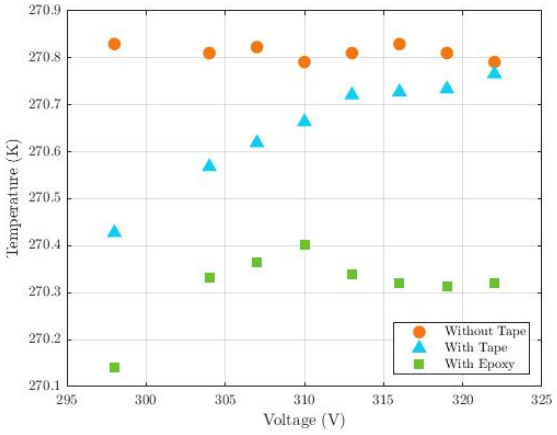

(d) SPAD temperature as function of bias voltage without or with tape, or with epoxy

Figure 5.5: SPAD characteristics with different cathode reinforcements

In summary, no significant changes in pulse width, amplitude or area were found after tape or epoxy was applied. The pulse width widened by a few ns; the pulse amplitude increased by tens of mV and the temperature differed by less than 1 K. Recharge times

were very similar, with the maximal change being 0.1 μs. Thus, supporting the shaky joint with tape or epoxy was deemed acceptable, with no major consequences to readout signal quality. Of the two tested methods for supporting the wires, Kapton tape appears to have less impact on the detector performance than epoxy.

5.2.3 Flight Board Functional Testing

The flight version of the CAPSat SPAD DM was tested in March 2021 to verify the function of the SPADs and other components. Figures 5.6 and 5.7 shows the testing set-up. A +3.3V and +5V power supply was hooked up to the board via alligator clip, and a common ground was made between the supplies to the PSOC and the DM. Jumper cables were used to directly connect the PSOC to the DM. Connection between the computer and the PSOC was made via a USB cable; this provided power to the PSOC as well as allowed for programming the PSOC. Serial data coming from the board (such as SPAD temperature, dark counts, etc.) were transmitted to the computer through a RS232 to USB A cable.

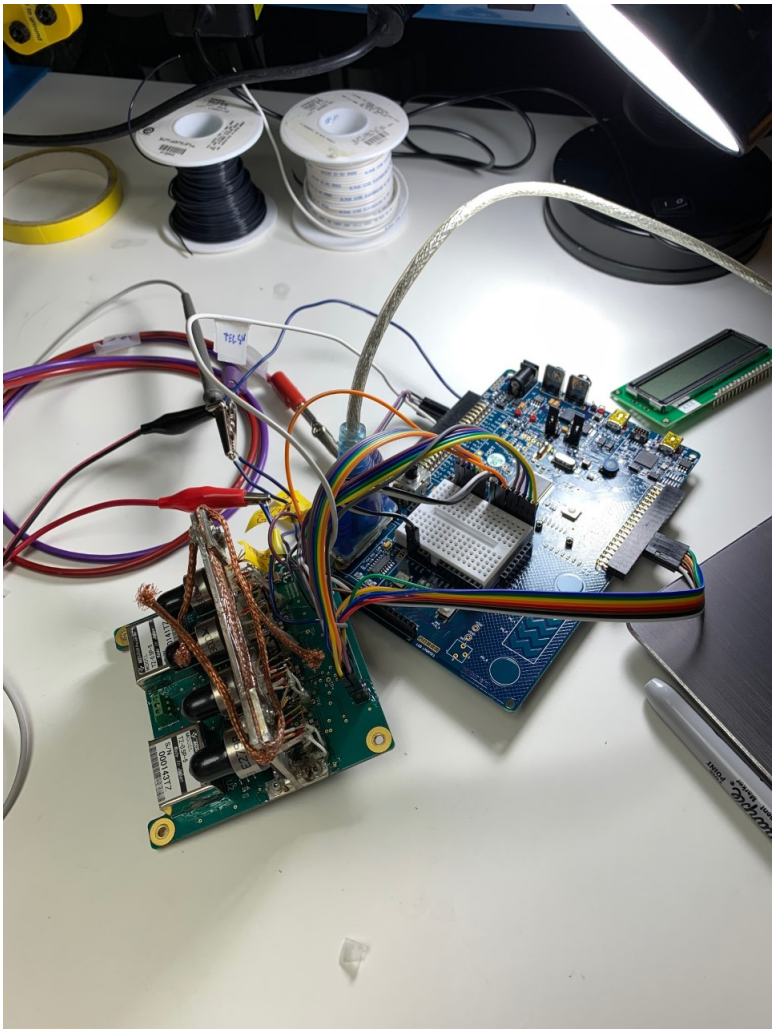

Figure 5.6: CAPSat DM (green PCB on left) rigged up to PSOC Development Kit (blue PCB on right) via jumper wires and to power supplies via alligator clips. Clear serial data cable is visible at the top going towards the computer

Thermal Loop Verification

Since detector efficiency is dependent on excess voltage, the breakdown voltage of the CAPSat detectors must be strictly known. V_{Br} varies proportionally to temperature, so it

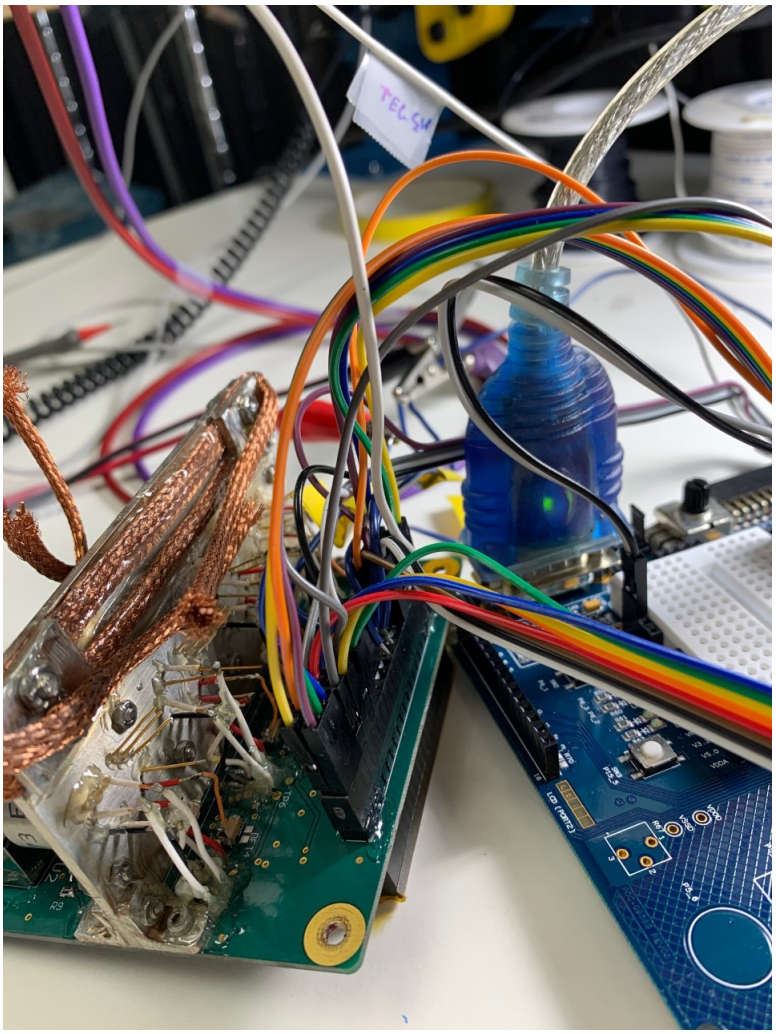

Figure 5.7: Closer angle of jumper wires directly placed into PCB connector. Placement of jumper was cross-checked with pinout of connector; likewise, this was done on the other side of jumper wires at the PSOC side.

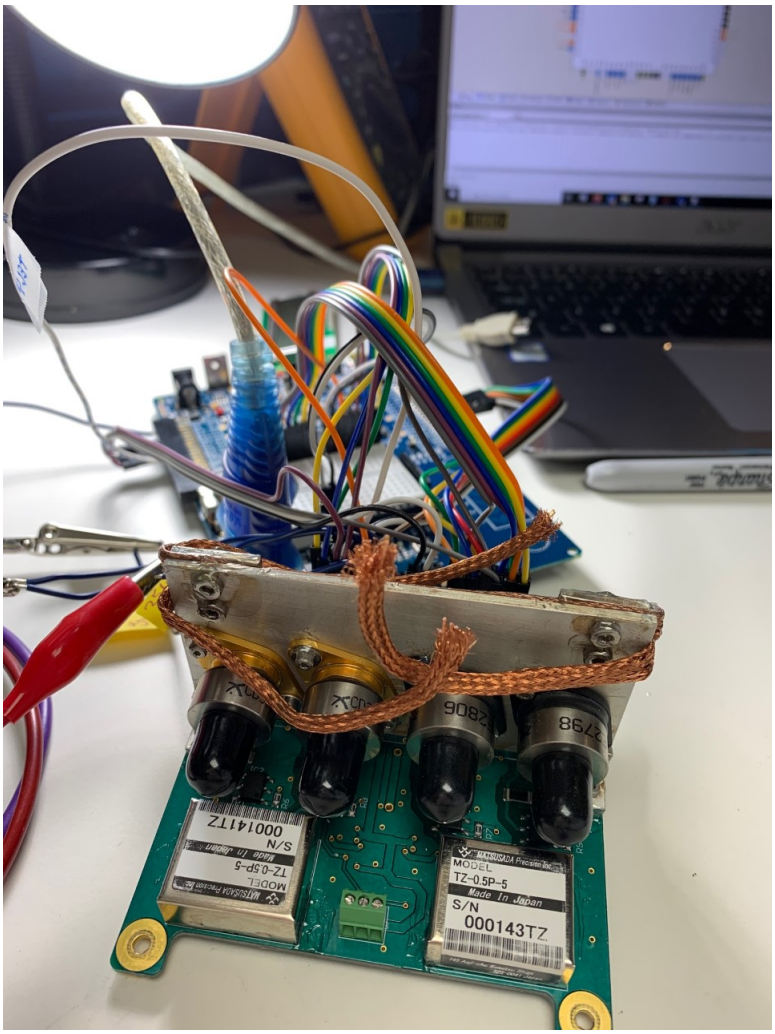

Figure 5.8: Front of CAPSat DM with four SPAD packages visible (black fiber caps on top).

is critical that the SPADs are kept at a fixed temperature; this is the function of the PID loop mentioned previously. Prior to launch, each SPAD thermal loop must be confirmed to be working properly.

The integrated TEC within the SPAD package is controlled by the TEC driver, which in turn is controlled by the PSOC. The integrated thermistor resistance (R_{Therm}) changes with SPAD temperature, and consequently the voltage drop across the resistor changes as well. This voltage, V_{Therm}, is read out by the PSOC ADC and compared to the set voltage. The PID loop enables the TEC driver to adjust how much current flows to the TEC, thereby nudging the SPAD temperature towards the desired temperature.

The PSOC Creator IDE was used to set the target V_{Therm} to the value which corresponds to the desired SPAD operating temperature. The PID loop is set to run for 90s to stabilize V_{Therm}; every second the PID loop reads the drop across the thermistor, compares the value to the set voltage and adjust the TEC current. V_{Therm} is reported through a serial communication terminal, along with the TEC Current, for every round of the thermal loop. Once V_{Therm} data was collected for several target values, the voltages were converted to thermistor resistance:

$$R_{Therm} = \frac{(V_{Therm} \times 10000)}{1.5 - V_{therm}} \tag{5.1}$$

Next, the temperature of SPAD in degrees Kelvin (K) can be found:

$$Temp(K) = \frac{3200}{ln(\frac{R_{Therm}}{0.1113})} \tag{5.2}$$

Finally, the temperature in degrees Celsius can be found:

$$Temp(^{\circ}C) = Temp(K) - 273.15 \tag{5.3}$$

The range of target temperature can be found in Table 5.1.

Thermal stabilization was found to occur within the first 60 s. Desired temperatures across the operation range were reached by each SPAD. Typical fluctuation of SPAD temperature was less than 0.2°C.

Table 5.1: Set values for voltage drop across thermistor (V_{Therm}) and corresponding SPAD temperature

V_{Therm} (V)	R_{Therm} (Ω)	Temp (K)	Temp (°C)
1.25	50000	245.86	-27.29
1.2	40000	250.15	-23.00
1.15	32857	254.06	-19.09
1.1	27500	257.70	-15.45
1.05	23333	261.16	-11.99
1	20000	264.48	-8.67
0.95	17272	267.73	-5.42
0.9	15000	270.93	-2.22
0.85	13076	274.11	0.96
0.8	11428	277.31	4.16
0.75	10000	280.56	7.41
0.7	8750	283.88	10.73
0.65	7647	287.31	14.16
0.6	6666	290.90	17.75

Breakdown voltage across whole operating temperature range

After thermal stabilization was found to be achieved for all desired SPAD temperatures, V_{Br} was determined at each of these temperature. A PSOC C code was written to "scan" across the SPAD bias voltage range for each set temperature and an oscilloscope was used to monitor when avalanche pulses appear before the discriminator (see Figure 5.9 for probe placement and Figure 5.10 for typical pulse size at breakdown). The pulse should be observed before the discriminator so as to not miss early small avalanches right at SPAD breakdown.

Figure 5.11 shows the V_{Br} as a function of SPAD temperature. A linear fit was used for the data set, since it is known that V_{Br} should vary linearly with temperature. The slope of the fit is known as the temperature coefficient of reverse bias. The extracted temperature coefficients for the C30902SH SPADs were 0.64V/°C and 0.70V/°C, and for the SliK SPADs were 0.31V/°C and 0.27V/°C. A typical coefficient value for the C30902SH SPADs is 0.7 V/°C and for the SLiK SPADs has previously been reported at 0.5 V/°C [4].

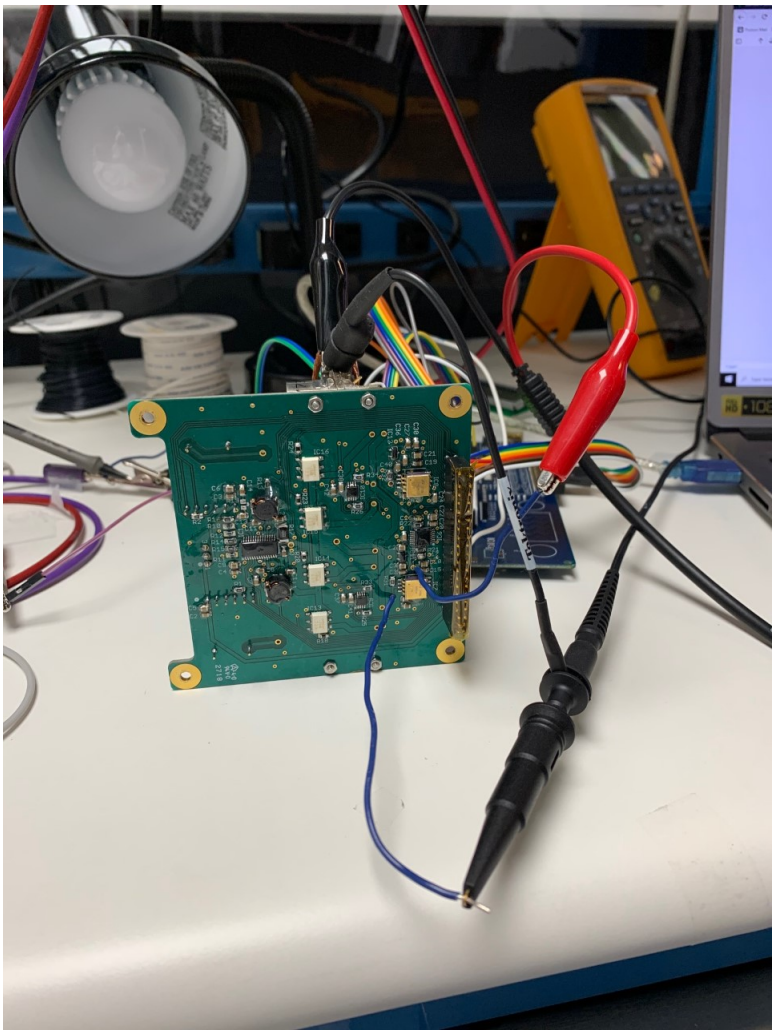

Figure 5.9: Bottom of CAPSat DM board with oscilloscope probe (black probe in forefront of photo) clamped to wire placed in testing point of PCB between the anode of SPAD and discriminator.

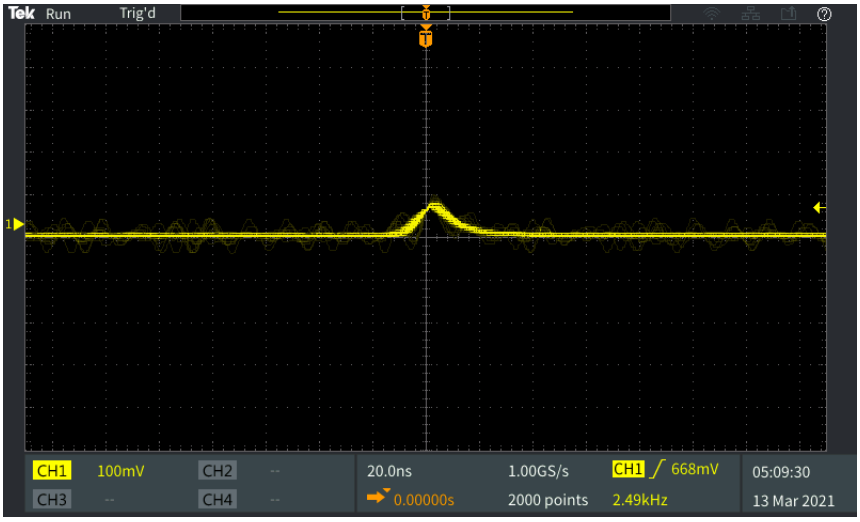

Figure 5.10: Oscilloscope screenshot of small avalanche pulse corresponding to breakdown.

As such, the coefficient extracted for the C30902SH is quite similar (< 0.6 V/°C difference), however, the SLiK coefficient is quite different. This is likely due to a worse linear fit for the SLiK data. The SLiKs' V_{Br}s (Figures 5.11c and 5.11d) can be seen to repeat for more than one temperature setting, implying that the breakdown voltages did not change with temperature in those cases. However, this is due to the fact that PSOC is only able to bias in 3V step size, so it is possible that for one data point avalanche pulses began to appear in the lower part of the 3V step and for the next data point the avalanche pulses began to appear in the higher part of the 3V step, but differentiating between these two breakdown voltages is not possible in the current biasing scheme. This lack of "resolution" makes it possible for the breakdown voltages to be the same for two temperature settings. A more rigorous way of determining breakdown is manually biasing the SPAD at various temperature (without digital intervention) and observing when SPAD current crosses a threshold value, usually 100 μA. However, since the CAPSat SPADs' breakdowns will be measured via a controller during the actual mission, this method of observing breakdown was sufficient.

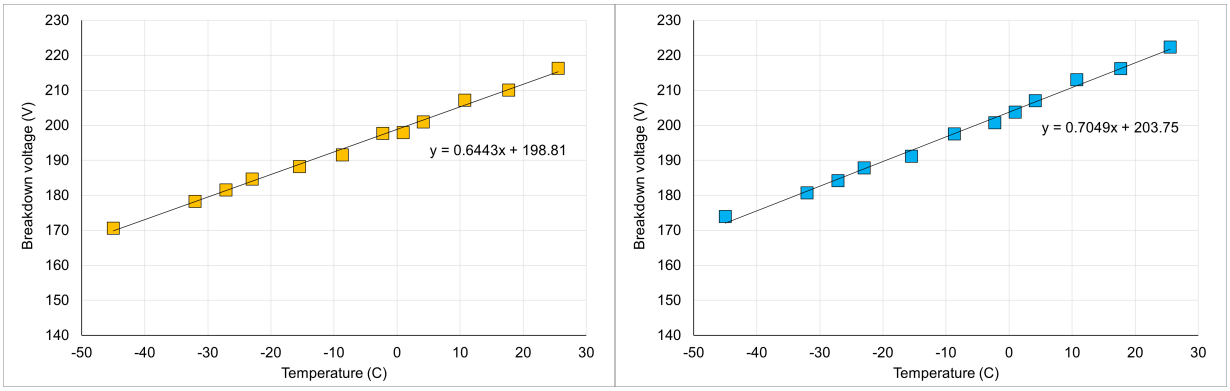

(a) C30902SH - 1

(b) C30902SH - 2

(c) SLiK - 1

(d) SLiK - 2

Figure 5.11: Breakdown voltages for CAPSat SPADs across temperature range. Fit is linear with slope indicating relationship between V_{Br} and T.

Another SPAD health check conducted was measuring the dark count rate at $V_{Ex} = 20V$ while changing the temperature (Figure 5.12. On average, DCR will double for every 7°C increase in temperature [52]. The behaviour of DCR with increasing temperature did indeed this expected exponential trend.

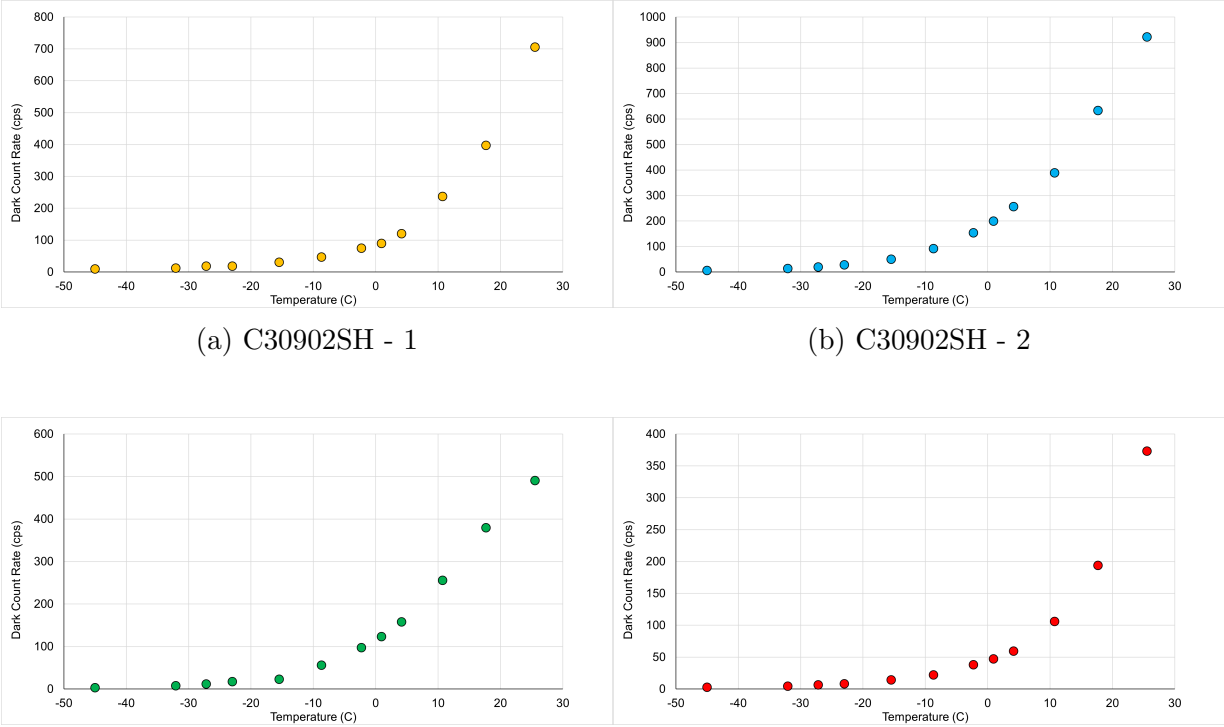

(a) C30902SH - 1

(b) C30902SH - 2

(c) SLiK - 1

(d) SLiK - 2

Figure 5.12: Dark count rate (cps) for CAPSat SPADs as function of operating temperature.

The thermally-dependent characteristics were successfully tested on all CAPSat detectors: breakdown voltage increased linearly with increasing temperature and dark count rate (from thermally generated carriers) increased exponentially with increasing temperature. These results are consistent with the manufacturer datasheets and with literature.

Discriminator Threshold

Once breakdown voltages were found to vary consistently with operating temperature, the next parameter to be investigated was the readout circuit discriminator threshold. The purpose of the discriminator is to only accept pulses above a certain amplitude. This is a method of reducing noise and ensuring true avalanches are being measured. The

discriminator on the CAPSat PCB receives two inputs, the first is a reference voltage which is set via PSOC code, and the second is the avalanche pulse (Figure 5.13). If the avalanche pulse is smaller than the reference voltage, then the discriminator produces a low output; conversely, if the avalanche pulse exceeds the reference voltage, then the output is high and the avalanche is counted. Due to the technical specification of the chosen discriminator (RHR801 from STMicroelectronics [11]), the avalanche pulse must be first shifted by 600 mV using a voltage reference (ISL21070 IC by Renesas [6]) [88]. This is notable because within the PSOC program, one must specify the discriminator voltage with the knowledge that the true pulses are really 600 mV smaller. For example, a discriminator setting of 700 mV will really be counting avalanches of 100 mV size. Finding the appropriate discriminator threshold range is critical so as to minimize noise but truly capture all detector avalanches.

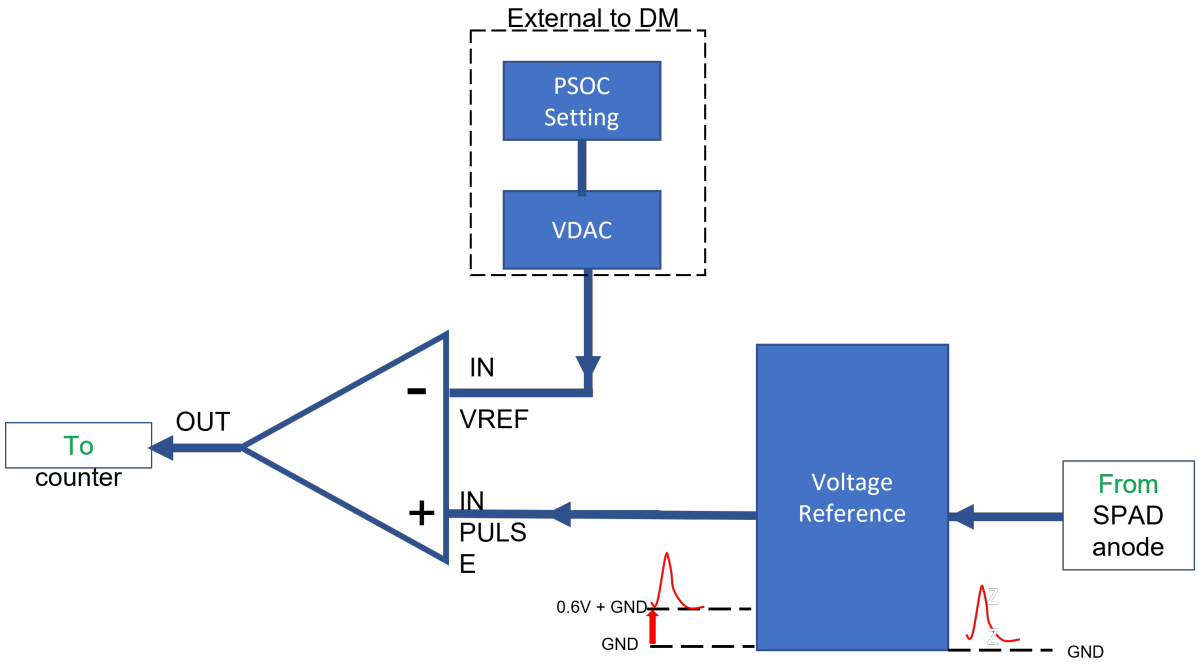

Figure 5.13: Schematic of inputs to discriminator. Avalanche pulse from SPAD anode is shifted 0.6 V in order for discriminator to recognize the input. The PSOC is programmed so the VDAC outputs a reference voltage to the discriminator which compares to the shifted avalanche pulse.

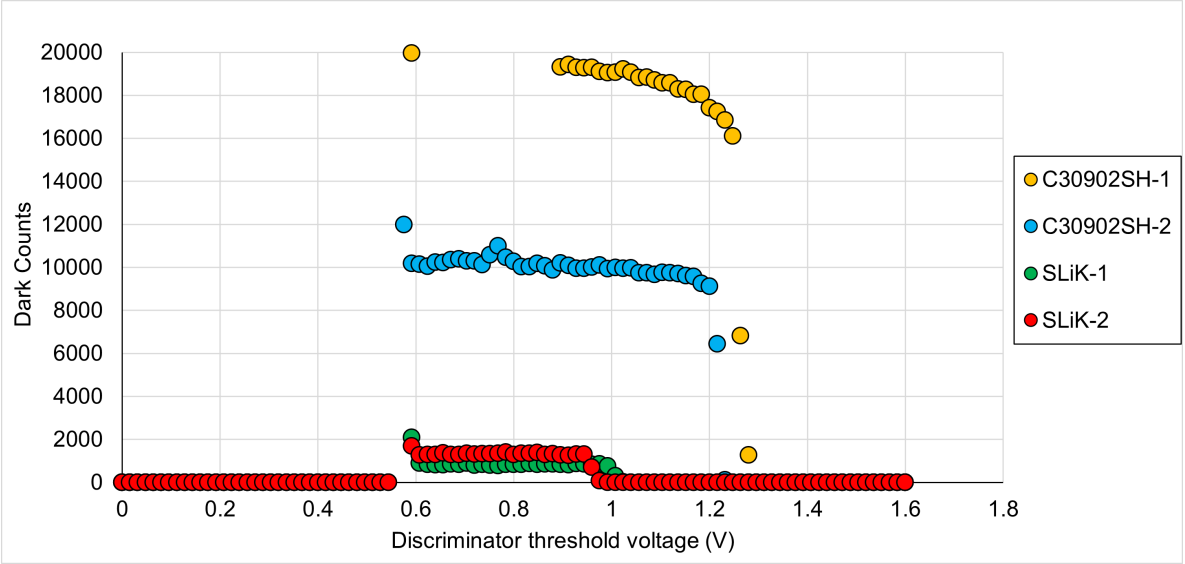

Figure 5.14: Dark counts as function of discriminator threshold voltage

Threshold increments were determined by the PSOC VDAC which provides the voltage to the reference voltage input pin of the discriminator. The PSOC3 VDAC is an 8-bit voltage digital to analog converter with two possible range of 0 to 1.020V or 0 to 4.080V [8]. The latter range was used. To get the output voltage of the VDAC (which is the input reference voltage to the discriminator) the whole 4.080 voltage range is subdivided 256 values such that:

$$V_{out} = \frac{value}{256} \times 4.096V \tag{5.4}$$

The PSOC program was written to cycle through the first 100 VDAC values (ergo discriminator threshold voltage) and measure the dark counts at a fixed bias of $V_{Ex} = 20$V for each threshold voltage.

As Figure 5.14 shows, the ideal range of discriminator threshold was found to be between 0.65V and 0.9V. This corresponds to an avalanche amplitude acceptance range of 0.05V to 0.3V.

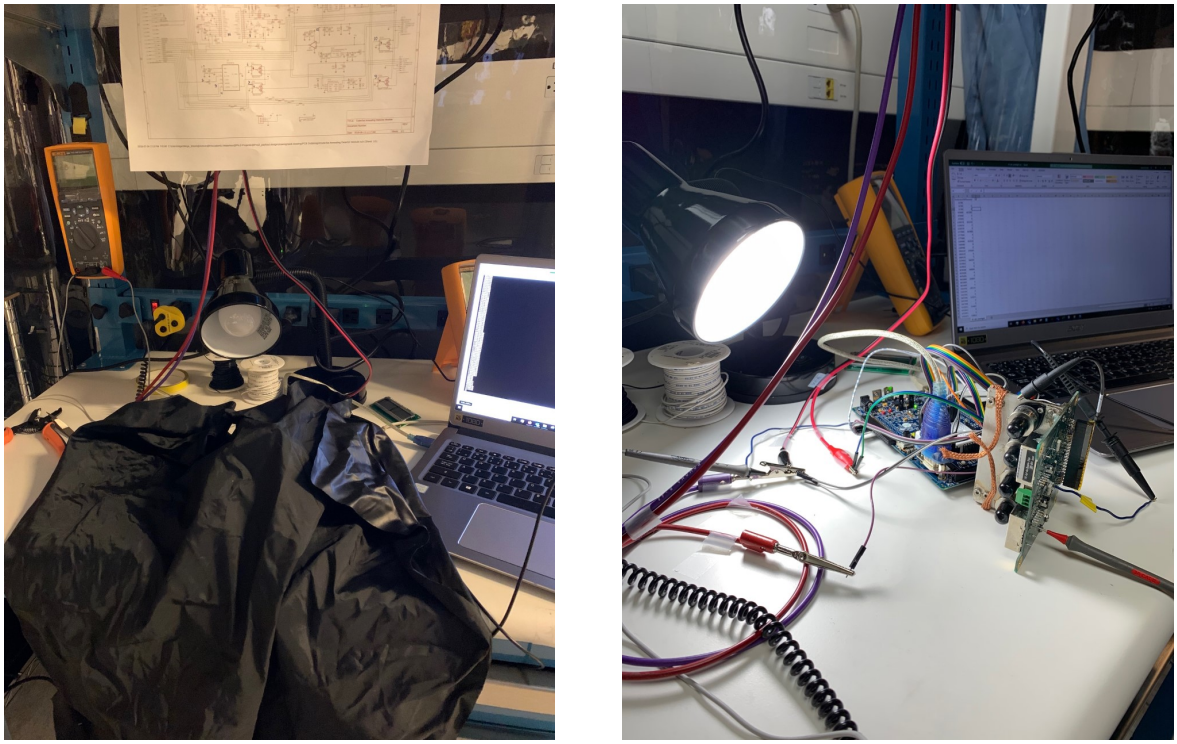

Figure 5.15: Diffuse light (left) and focused light testing conditions (right).

SPAD Sensitivity

In addition to observing dark count rate in-orbit, the CAPSat will also measure changes to the SPADs' sensitivity to light by shining an attenuated on-board LED at the active area of the detectors. A similar tests was undertaken during pre-launch checks. After fixing the discriminator threshold to 0.9 V and setting the SPAD target temperature to -22°C, the count rate was measured for dark, diffuse and focused light settings. The dark setting consisted of turning off the lab light and covering the PCB and detectors with a blackout curtain, the diffuse light setting consisted of keeping the blackout curtain and turning on distant lab lights and the focused light setting removed the curtain and added an LED lamp shining at the SPADs (Figure 5.15).

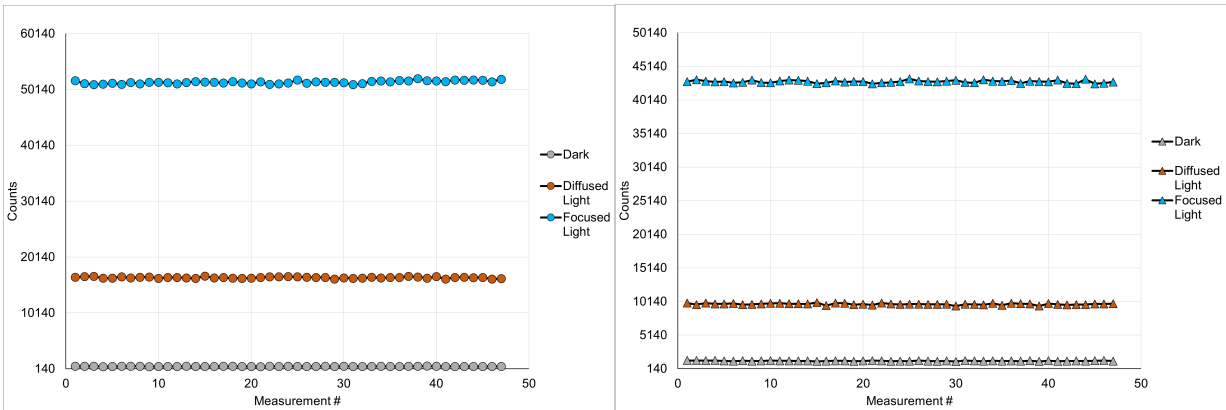

(a) C30902SH - 1

(b) C30902SH - 2

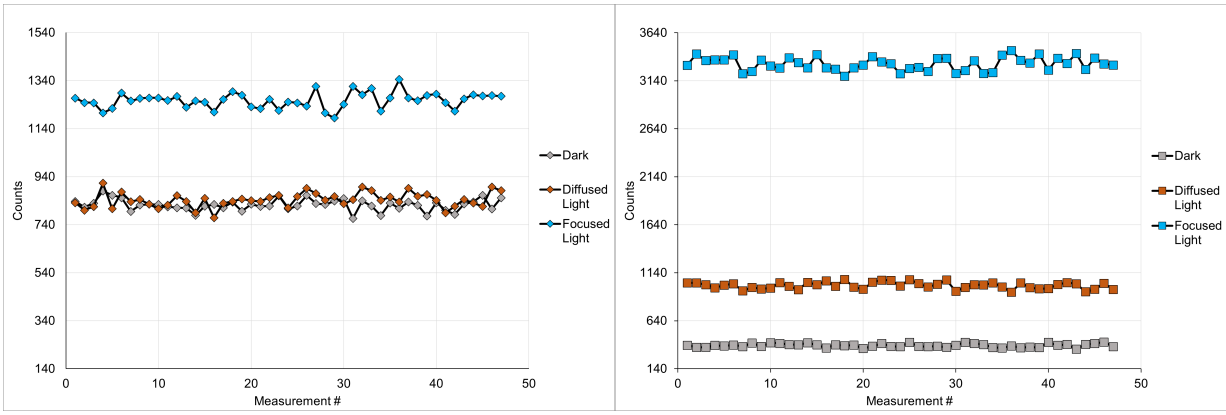

(c) SLiK - 1

(d) SLiK - 2

Figure 5.16: Light sensitivity of CAPSat SPADs to various light conditions

Both C30902SH and SLiK-2 show significant change in count rate between the dark and diffused light conditions (Figure 5.16). The measured counts between dark and diffused light conditions does not appear to be much different. The factors of measured counts in the brightest conditions to the measured counts in the darkest conditions were 97, 34, 1.5 and 9 for the two C30902SH and two SLiK SPADs, respectively. Again, SLiK-1 is the odd SPAD out – it appears to have a weaker sensitivity to light – however, both SLiKs have a much lower light sensitivity factor as compared with the C30902SH. This is not unexpected

since the C30902SH SPADs have an active area diameter of 500μm while the SLiKs have a diameter of 180μm, leading to a 7.7 times smaller active area for the SLiKs. That being said, this does not fully account for the difference in sensitivity factor. All SPADs except for SLiK-1 share a relatively common dark count level of 500 counts per measurement[1]. SLiK-1 had an unusually high dark count level and limited sensitivity in the focused light setting. While this variation is clear between the two SLiKs, further investigative steps were not taken since in-orbit SPAD sensitivity will be only compared with same-SPAD datasets rather than between SPADs. As such, it is mostly necessary to have a pre-launch baseline and observe any increase in dark counts and deterioration in sensitivity within the same SPAD throughout the mission lifetime.

5.2.4 Mission measurement objectives

Upon successful launch on August 29, 2021 and deployment from ISS on October 12, 2021, the next step for the CAPSat science team is deciding the first measurements to establish a post-launch baseline, as well as to sketch out a long-term schedule of measurements. Results from the pre-launch function testing as well as from a later laser annealing experiment (to be discussed in the next part of this Chapter) will shape the order and range of measurements.

Similar to the method of the functional testing, the first measurements should focus on controlling SPAD temperature and measuring the breakdown voltage. Table 5.2 shows a suggested range of bias voltages that the Controllers could use to check the SPAD breakdown voltage at various temperatures. This type of "voltage scan" should be an automated process and conducted before every measurement so that V_{Br} is known, since the detection efficiency and dark count rate depends on the excess voltage. These voltage ranges are not expected to have changed from before launch to after deployment. However, if counts are not observed in the suggested voltage range, it indicates that perhaps the SPAD temperature is being reported incorrectly and the breakdown is not achieved within the suggested

[1] Unfortunately, the length of the measurement was not accurately noted so a real count rate cannot be extracted.

Table 5.2: Suggested bias voltage ranges for determining breakdown voltage for each SPAD.

		C30902SH-1			C30902SH-2		
Thermistor Voltage (V)	Approximate Temperature (°C)	Start Voltage (V)	End Voltage (V)	Expected $V_{Br}(V)$	Start Voltage (V)	End Voltage (V)	Expected $V_{Br}(V)$
1.25	-27	179	185	182	181	187	184
1.2	-23	182	188	185	185	191	188
1.1	-15	185	191	188	188	194	191
1.0	-9	189	195	192	195	201	198
0.9	-2	195	201	198	198	204	201
0.85	1	195	201	198	201	207	204
0.8	4	198	204	201	204	210	207
0.7	11	204	210	207	210	216	213
0.6	18	207	213	210	213	219	216
		SLiK-1			SLiK-2		
Thermistor Voltage (V)	Approximate Temperature (°C)	Start Voltage (V)	End Voltage (V)	Expected $V_{Br}(V)$	Start Voltage (V)	End Voltage (V)	Expected $V_{Br}(V)$
1.25	-27	288	291	291	273	279	276
1.2	-23	288	291	291	273	279	276
1.1	-15	288	291	291	276	282	279
1.0	-9	291	294	294	276	282	279
0.9	-2	295	298	298	279	285	282
0.85	1	295	298	298	279	285	282
0.8	4	298	301	301	279	285	282
0.7	11	298	301	301	282	288	285
0.6	18	301	304	304	285	291	288

voltage range. In fact, breakdown voltages can be used as a good indicator of the SPAD temperature since it scales linearly with temperature. Given a V_{Br}, the temperature can be extracted using the linear fit generated in the plots in Figure 5.11.

After establishing approximate V_{Br}, it is highly suggested to check the functionality of the discriminator. Ensuring that the discriminator threshold is chosen appropriately will save time later during dark count measurements since it reduces the chance that counts are being missed due to a too high threshold setting. As mentioned previously, the suggested threshold is approximately 0.7V - 0.9V.

It is important to measure the dark count rate of the detectors as soon as possible once the CAPSat is deployed. Without the shielding provided by the ISS, the detectors are being exposed to much higher proton and galactic cosmic ray flux. Measuring dark count rate at several excess biases (such as $V_{ex} = 5$, 10 and 20 V) should be the next step

taken after establishing the breakdown voltage at the operating temperature. The point of taking measurements at several excess biases is to monitor SPAD saturation: if the radiation damage is so great that the dark count rate overwhelms the quenching circuitry, dark count rate will decrease with increasing bias once V_{ex} is greater than the saturation point. In congruence with the dark count rate measurement, the on-board LED will be used to monitor SPAD sensitivity like the test described in Section 5.2.3.

The aim of the mission is to observe changes in dark count rates due to radiation effects and then to heal the damage with on-board annealing lasers. A critical question to be answered is when to begin annealing. D'Souza et al. compared thermally annealing after every proton exposure to annealing after the dark count rate reached 2kcps [41]. The latter scheme was found to be slightly more effective at reducing dark count rate. Since the CAPSat will not be get a burst of monoenergetic radiation like in ground radiation testing, it is likely the increase in dark counts will be subtle and slow. Pro-active annealing is not yet shown to be useful, therefore, it is a better strategy to observe dark counts rise and anneal once a certain threshold is reached. This threshold could be that the dark count rate exceeds a level such as 2kcps, or that the sensitivity of the SPAD is shown to decrease. Sensitivity in this case could be defined as the difference between the count rate with LED on and the background dark count rate. The next critical question is what annealing power to use and for how long to anneal. As will be discussed later int the chapter, and as a previous study has suggested, a power of 1W is required to see a decrease in post-radiation dark count rate, and a maximum annealing time of 3 minutes (in the case of high radiation damage) should suffice [59].

It is recommended to hold off on biasing the detectors soon after annealing. Significant heating can occur with prolonged annealing in the detector package which would impact the V_{Br}. After annealing, the operating temperature should be chosen, temperature stabilization should be allowed to take place for at least 45 s, then V_{Br} can be confirmed again, and finally counting measurements can be made.

The satellite has an expected lifetime of less than a year [88]. Within this time, some example results that could generated are:

- dark count rate increase per day (in the spirit of [57]). This data would come from the two control SPADs that are not being annealed.
- dark count rate as function of cumulative annealing time (the time the annealing laser is on).
- SPAD sensitivity over mission length.

Additionally, telemetry on peripheral board function will be informative on the general health of the electronics as they traverse through increased space radiation flux.

5.2.5 Conclusion

The first in-orbit laser annealing of SPADs will surely contribute to our understanding of real-time methods of mitigating radiation damage. The results of this mission will be applicable to many fields which rely on highly sensitive detectors including the quickly developing global quantum internet network. Whilst shielding will always be the primary method of stopping hazardous particles in their tracks, it stands in the way of small, lightweight and cheap satellite launches. Laser annealing may be an answer to a less costly and more compact method of dealing with the ever-present issue of radiation-induced displacement damage in SPADs.

5.3 Laser annealing protocols for healing radiation damage in SPADs

As alluded to in the previous section, best-practice annealing protocols have not been established. Annealing power and duration is not yet established for the CAPSat mission; therefore, in an effort to set baselines parameters for these protocols, an earlier CAPSat prototype board with irradiated SPADs of the same type as those in CAPSat is laser annealed within a vacuum environment.

5.3.1 Experiment Methodology

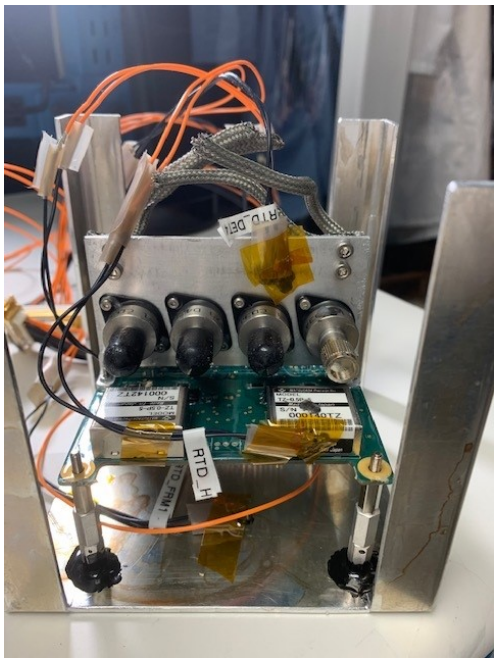

Figure 5.17: CAPSat DM prototype with four SLiK detectors mounted (with black and silver caps covering detector window). Resistance temperature detectors are placed to monitor SPAD and electronics' temperatures during operation and annealing in vacuum.

SPAD samples and readout electronics

The four samples to be annealed are silicon single-photon APDs (Excelitas SLiK, 180μm active area), custom-built with fiber connectors intended to focus the beam onto the active area. The SPADs were previously irradiated by 105 MeV protons, to a fluence equivalent to 10.5-years in low-Earth orbit (2×10^{10} protons/cm^2) and then repeatedly thermally annealed [41]. The samples were extracted from their previous detector module described in D'Souza *et al.* and integrated into a detector module (DM) of a space-qualified CubeSat (Figure 5.17). The four samples are mounted to an aluminium bracket in a side-by-side fashion, and the bracket is attached to the DM PCB. The DM PCB possesses circuitry

to bias, quench and readout the SPADs individually, as well control SPAD active area temperature. Control of the DM is conducted via the externally connected embedded programmable system-on-chip Cypress PSOC3 CY8CKIT-030A development kit. A thermal control loop in the PSOC program sets the target SPAD temperature (as measured by a thermistor close to the SPAD active area) and ensures that the SPAD temperature is steady during characterization via careful control of the TECs by the TEC driver. Detailed description of the CubeSat module can be found in [88] as well as in a forthcoming article.

Experimental setup

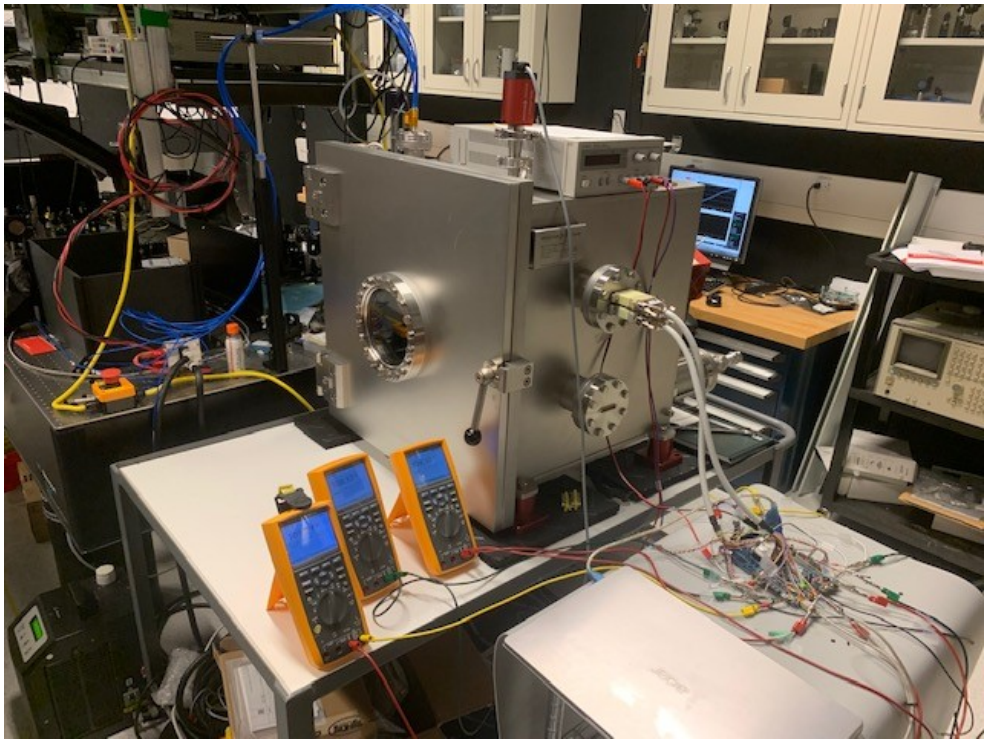

Figure 5.18: Photo of experimental setup. Optical components are covered by black panels on the left. Blue fibers are visible going through the feedthrough of thermal vacuum chamber (TVAC) top. Detectors in the CAPSat prototype DM are within the sealed TVAC. Three multimeters are used to readout resistance temperature diode sensor's resistances. Detector communication and power lines enter the TVAC via a DSUB adapter pictures on the right of the photo. The thick cable routes the power and communication lines to the PSOC microcontroller seen on the bottom right. A laptop is used to communicate and power the detectors; the high voltage supply rests on top of TVAC.

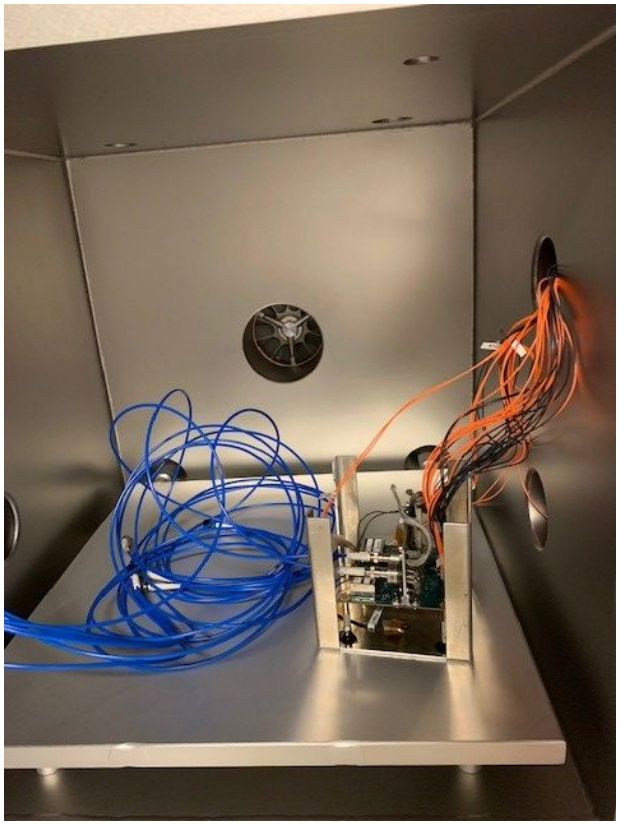

Figure 5.19: Photo of the CAPSat prototype DM inside the TVAC. The detectors are fiber coupled to the blue fibers which relay the optical annealing beam as well as a low-level light source used for characterization of the detector sensitivity. The orange and black wires extend from the CAPSat detectors module to the right of the TVAC where there is a DSUB connector to connect to the microcontroller and power supply outside of the TVAC.

Figures 5.18 and 5.19 show photos of the set-up while 5.20 demonstrates the a schematic of the experimental set-up.

The set-up is comprised of bench-top optics and the PSOC3 kit at room pressure, and the DM inside a thermal vacuum chamber (TVAC) at an average pressure of 10^{-6} torr (0.001 atm). On the optics side, a high power multimode 808 nm laser diode (Jenoptic JOLD-30-DC-12, capable of 30 W power) is used for annealing, while a tunable 780 nm laser diode (Toptica DL PRO 780 FD2) is used to test SPAD sensitivity (signal laser). The

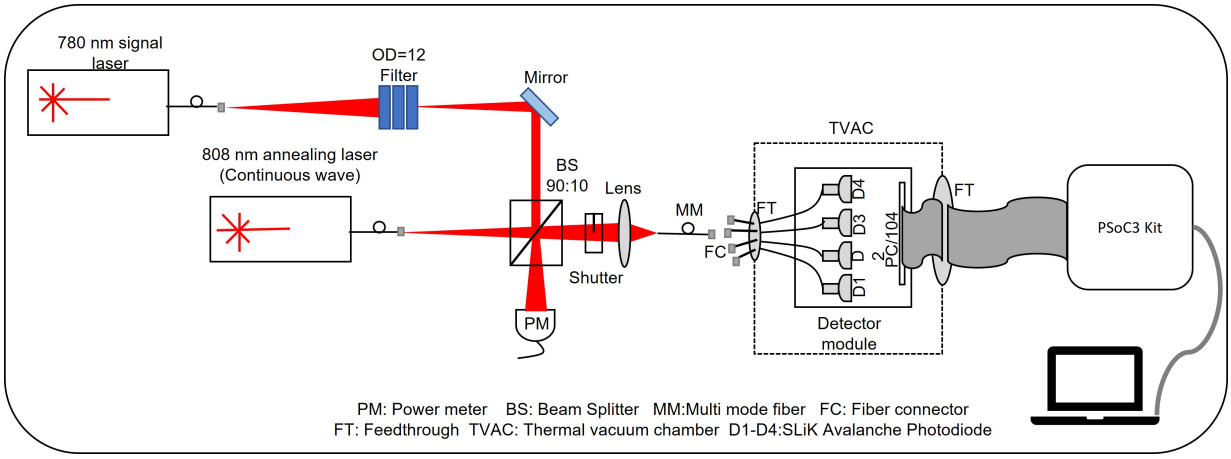

Figure 5.20: Schematic of the experimental set-up.

808 nm laser is chosen because of the affinity of the SLiK SPADs to absorb all photons at its central wavelength. The DL Pro was chosen because of its stability, ensuring that the signal photon rate was relatively constant during characterization. The annealing laser beam is collimated by a lens, after which it is incident on one port of a 90:10 beamsplitter; 10% of the beam transmits through to a power meter (Thorlabs PM1000D) and 90% of the beam reflects towards a fast electric-shutter where it is focused by a lens into a MM fiber (Coastal Connection CCU-850 Rev A, vacuum-suitable). The signal laser is coupled into SM fiber at the laser window and after some length in fiber, the beam continues in free space. It is attenuated to single-photon level using several neutral density filter (Optical density (OD) = 12). A mirror reflects the attenuated signal beam into the other port of the 90:10 beamsplitter, where is transmits and joins the annealing laser beam in the MM fiber. The MM fiber from the bench-top optics is joined via a fiber connector to another MM fiber to one of the SPADs in the TVAC via a fiber feedthrough at the top of the TVAC. The DM electrical wires are covered in vacuum-suitable jackets and are connected to the PSOC via another feedthrough. Three resistance temperature diodes (RTD-100 type) are placed on the aluminium mounting plate, on the SPAD high voltage supply and in the center of the PCB, to monitor the local heating of the respective areas. The RTDs' wires also exit the TVAC through the feedthrough and their resistance values

are measured using multimeters. Control of the DM is done using the PSOC3 integrated design environment *PSOC Creator* and data is read out in a terminal program (TeraTerm) via a serial connection to the PSOC. The data collected included those related to DM operational status (such as TEC current) as well as those related to SPADs (such as dark count rate)(See Appendix C Figure C.4 for example of such a data log).

Laser annealing protocols

Three laser annealing protocols were tested: (a) Variable annealing power with fixed 180s exposure time; (b) Variable, single exposure time and fixed annealing power; and (c) Variable, repeated exposure time and fixed annealing power. The difference between schemes (b) and (c) is that the former anneals the SPAD active area with a certain duration once, while the latter anneals the SPAD with a certain duration three times. SPAD characterization occurs after each annealing exposure. Table 5.3.1 summarizes the range of annealing powers and duration of exposures.

Table 5.3: Annealing exposure parameters

Protocol	SPAD	Annealing Power (W)	Max Annealing Time (mins)
Variable Power	1	0 - 2.3	3
Variable Time	2	1.5	14
	3	1.2	16
	4	1.8	16

The annealing power described in the table is the power measured at the end of the MM fiber which connects to the SPAD package. Because measurement of the power at the end of the MM fiber in the TVAC is impossible during TVAC operation, a portion of the annealing laser power is measured by the power meter at the 10% arm of the beamsplitter, and this allows for calculation of the power at the end of the MM fiber. A calibration curve was generated to allow for easy determination of annealing power at the TVAC based on

the power meter reading (details of this calibration process can be found in the Appendix C).

For each round of optical annealing, the annealing power is set by increasing the bias current of the 808 nm laser until the power meter reads the correct value (based on the calibration curve). The fast shutter is opened for a pre-determined exposure duration, allowing the SPAD active area to be annealed. The SPADs are not biased during annealing, therefore, the temperature of the active area is not known during the annealing exposure. However, the RTD resistance is measured for every minute of the exposure, giving an insight into the heating process of the area surrounding the annealed detector. Once the exposure time is reached, the fast shutter is closed and the annealing laser is turned off. The detectors are left unbiased for another several minutes to ensure that any local heating in the active area is cooled down.

Characterization

Characterization is conducted in complete darkness and with a blackout curtain covering the viewport of the TVAC to block out as much background light as possible. Before any measurements, the PSOC program is edited to choose which SPAD will be biased and at what temperature. Measurements are taken at three temperatures which are set in the PSOC3 program: $-22°C$, $-10°C$ and $0°C$. After approximately 60s of temperature stabilization, the previously chosen SPAD is biased to either 6V or 20V excess bias (breakdown voltage is determined before the annealing tests and is known to not be affected by laser annealing [59, 41]). An excess bias of 6V is unusually low for these SliK-type SPADs (20V is the typical operation bias) and means that the samples will have a small detection efficiency [39]. However, it was found prior to annealing that these particular samples have such high dark counts that they exhibit saturation effects at about 12V above breakdown. Therefore, detection efficiency is sacrificed for being below the saturation point. For each temperature, dark counts from the selected SPAD are logged once per second for 1 minute while the laser annealing beam is off and while the fast-shutter is closed. In a similar fashion, for each temperature, counts from the selected SPAD are logged while the fast-

shutter is open and the 780 nm signal laser is exposed to the SPAD active area. For the first SPAD sample, a 10 minute dark count measurement is also conducted to observe if the dark count rate behaves differently soon after annealing. A measurement of detector counts with respect to excess bias is also conducted as a method of observing any changes in the SPAD saturation point. Additional characterization of the SPADs, such as jitter or recharge time, is not possible due to inaccessibility of the DM within the TVAC.

5.3.2 Results and Discussion

Variable annealing power

Annealing with a power of less than 1W for a fixed 3 minute exposure with variable annealing power does not yield significant decrease in dark count rate (Figure 5.21a). DCR decreases noticeably after exposure to 1W beam and continues to decrease until 2W exposure. The pre-annealing DCR was 325 kcps and the lowest DCR achieved after annealing is 10.8 kcps, resulting in a dark count reduction factor (DCRF) of about 30 for a SPAD operation temperature of -22°C. All annealing exposure greater than 2W result in an increase in DCR, likely indicating that damage is being done to the SPAD active area.

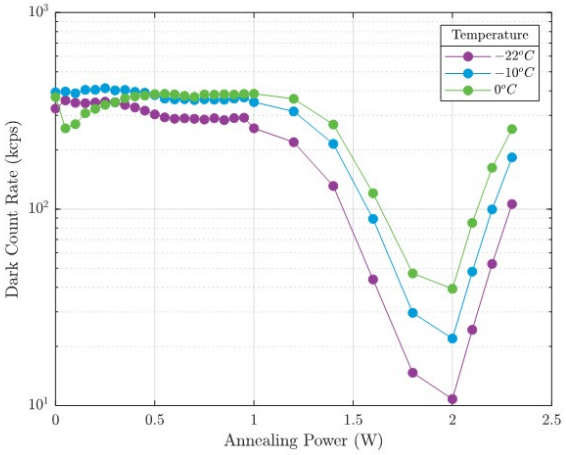

(a) DCR as function of annealing laser power

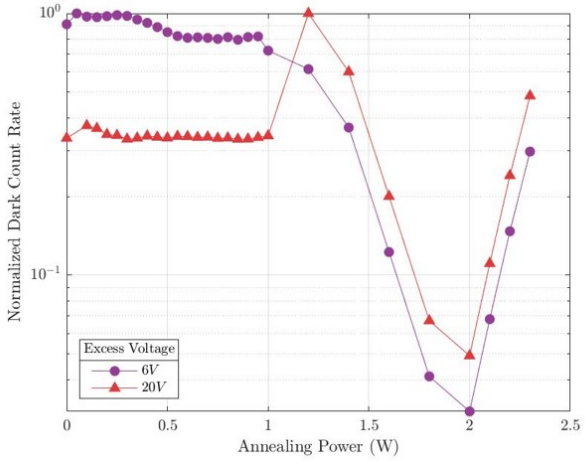

(b) DCR at two excess biases

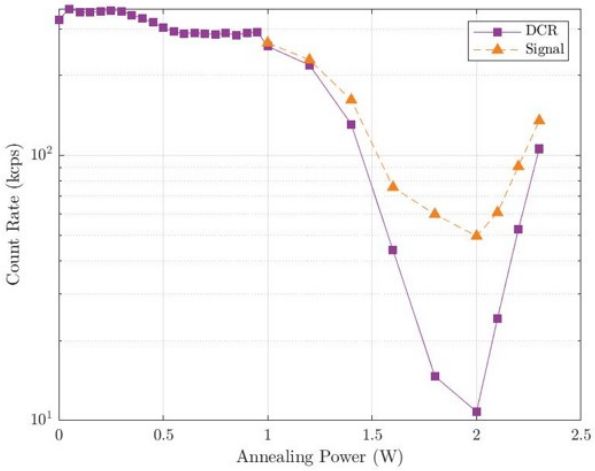

(c) Dark and signal count rate

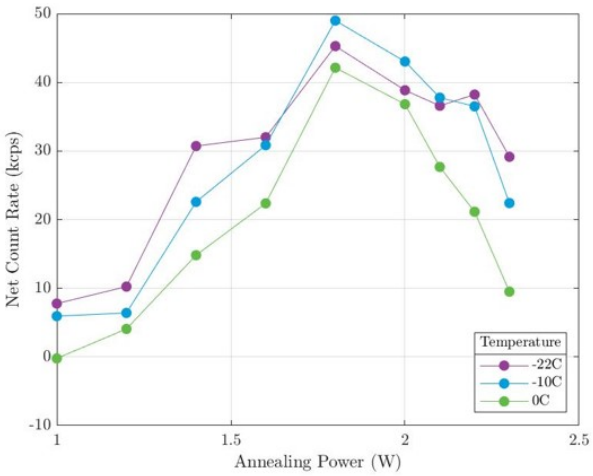

(d) Net count rate (signal minus dark count rate) as function of annealing power

Figure 5.21: SPAD 1 DCR, signal count rate and net count rates at -22°C at $V_{ex} = 6V$ unless indicated using the variable power annealing protocol.

Prior to annealing, operation at 20V excess bias results in lower dark counts than operation at 6V excess bias (Figure 5.21b). This is due to saturation of the SPAD from

radiation-induced damage. After 1W annealing, DCR at 20V excess bias operation exceeds DCR at 6V excess bias. This behaviour maintains for all subsequent annealing exposures.

Count rates with the signal laser turned on are very similar to when the signal laser is turned off (dark count rate) before annealing (Figure 5.21c). After 1W annealing, a divergence begins between the count rate with signal laser on versus off. The signal count rate follows the trend of the DCR with respect to the decrease in count rate until 2W annealing and then a rise in count rate afterward, however, the signal count rate does not drop as dramatically as the dark count rate. This is emphasized in Figure 5.21d, where the net count rate, or the difference between signal and dark count rates, is plotted.

Variable annealing time

The other three SPAD samples are annealed at various single powers: SPAD 3 at 1.2 W, SPAD 2 at 1.5 W and SPAD 4 at 1.8 W. There powers were chosen as they appear to yield a noticeable reduction in DCR and increase in SPAD sensitivity.

Larger annealing power yields a steeper decrease in DCR with the most drastic decrease in DCR after the first short exposures (Figure 5.22a). Longer exposure time does not appear to reduce DCR more than short exposure times. A plateau in the DCR is seen in all three cases of a fixed annealing power with very long exposure times. The DCRF for 1.2 W, 1.5 W and 1.8 W annealing tests is 2, 12 and 48, respectively. In the interest of confirming that this plateau is indeed the lowest achievable DCR for each annealing power, the SPADs are annealed with 2 W or more for 3 minutes. In the case of the SPADs annealed with 1.2 W and 1.5 W, an additional burst of 2 W annealing further reduced the DCR, while for the SPAD annealed at 1.8 W, the DCR actually rose after the 2 W exposure. Although on the whole the DCR decreased in the SPAD annealed at 1.8 W, the final spike in DCR after the higher annealing power burst, as well as the staggered descent of the DCR to the plateau level, indicates that an annealing power greater than 1.8 W is damaging the SPAD active area.

The NCR of each SPAD after annealing (Figure 5.22b) exhibits a trend of tending towards a count rate of around 30 kcps, despite an interesting discrepancy between the

two lower annealing powers and the highest annealing power. The sharp drop in NCR of the 1.8 W annealed SPAD after 3000s of cumulative annealing time coincides with a drop in a steep decrease in signal count rate (see Figure 5.22c for change in count rate between annealing measurements). While this is not the largest decrease in either signal or dark count rate that is observed throughout the measurements, it does mark a difference in the magnitude of decrease between the signal and dark count rates, which tend to change at the same rate before and after this one anomalous measurement. Since nothing changed in the characterization process or in the surrounding environment, this deviation is likely due to some reorganization of the defects in the semiconductor lattice such that the photoexcited carriers are more suppressed than the thermally excited carriers. After the last two rounds of 1.8 W annealing, both signal and dark count rates decrease similarly and NCR continues to tend towards 30 kcps, which indicates that annealing rearranged spurred permanent changes in the semiconductor.

The DCRF for operation at 20V bias is much smaller than for 6V bias (1-2 times reduction in DCR). The NCR, however, increases greatly as a result of prolonged, high power annealing. The initial NCR is on the order of 0 cps – the signal is indistinguishable from the dark counts – and the final NCR attained is over 9 kcps. Still, this is much lower than the NCR measured at 6V bias, so there is still significant saturation at the higher operating bias. Interestingly, the NCR at 6V bias does not follow the previous trend that higher annealing power results in higher NCR. Indeed, 1.2 W annealing results in a higher NCR than 1.5 W annealing. This could be attributed to the variability in the data collected at 20V bias operation.

Repeated annealing exposure

Figure 5.22d shows the change in dark count rate between subsequent measurements (i.e. $DCR(t_2) - DCR(t_1); t_2 > t_1$) for the three SPADs annealed with either a single or repeated exposure to the annealing beam. In both exposure schemes (single and triple) the change in dark count rate is largest for the earliest annealing rounds and then diminishes with later annealing exposures. However, the triple-exposed SPADs' DCRs exhibit higher fluctuations

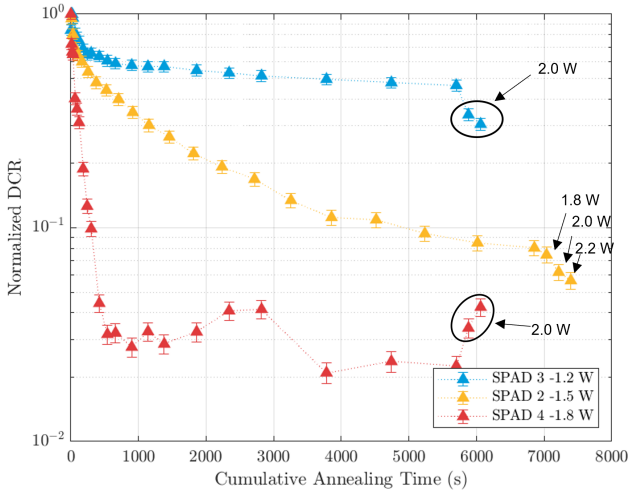

(a) Normalized DCR as function of cumulative annealing time (total time the annealing laser is shining on the SPAD active area.Annotated points indicate further annealing with higher laser power.)

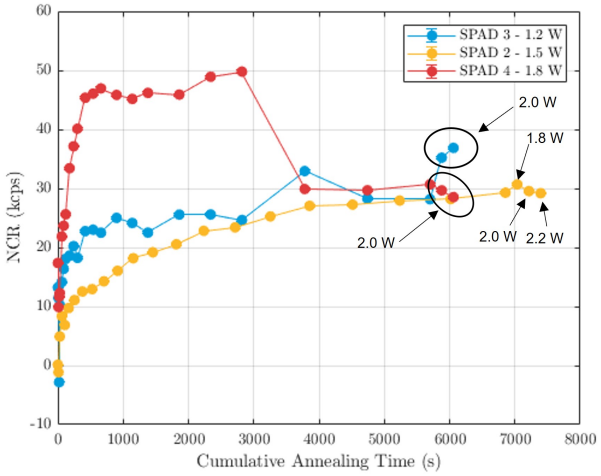

(b) Net count rate as function of cumulative annealing time. Annotated points indicate further annealing with higher laser power.

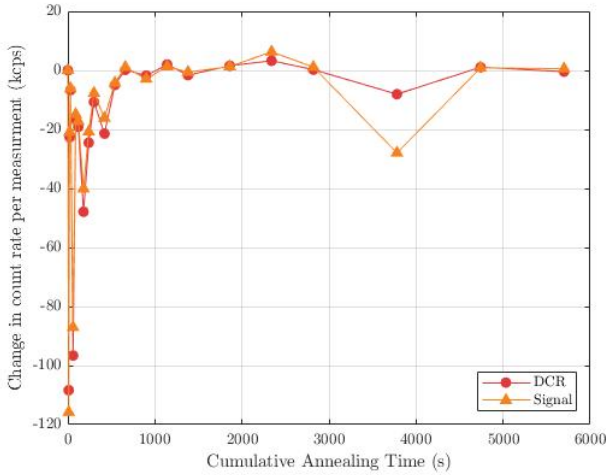

(c) Difference of count rates between two subsequent count rate measurements for 1.8 W annealed SPAD 4. The sharp decline of NCR in tile (*b*) coincides with a large decrease in signal count rate

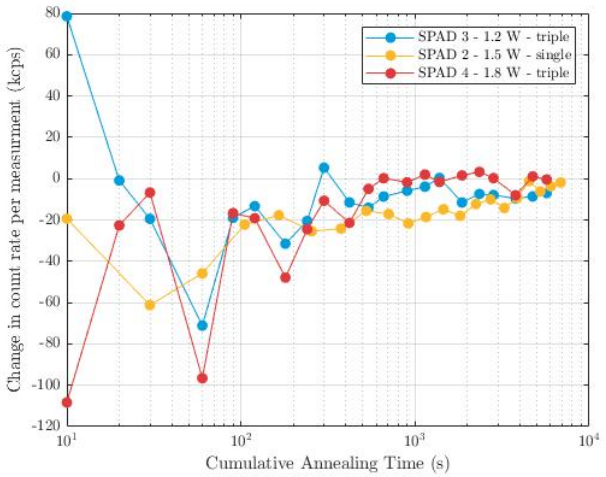

(d) Difference of count rates between subsequent measurements for SPADs annealed with single exposure or triple exposure of same duration.

Figure 5.22: Dark count rate, net count rate and changes in count rates between subsequent annealing exposure using the variable annealing duration protocol.

notably after every third exposure when the annealing time is extended. The greatest reductions in DCR occur after the first exposure at 10, 60, 180 and 480 s, and the reductions after the two subsequent exposures of the same duration are much smaller. The larger fluctuations cannot be attributed to a higher annealing power, since the effect is seen in the lowest annealed SPAD (1.2 W) as well as the highest annealed SPAD (1.8 W).

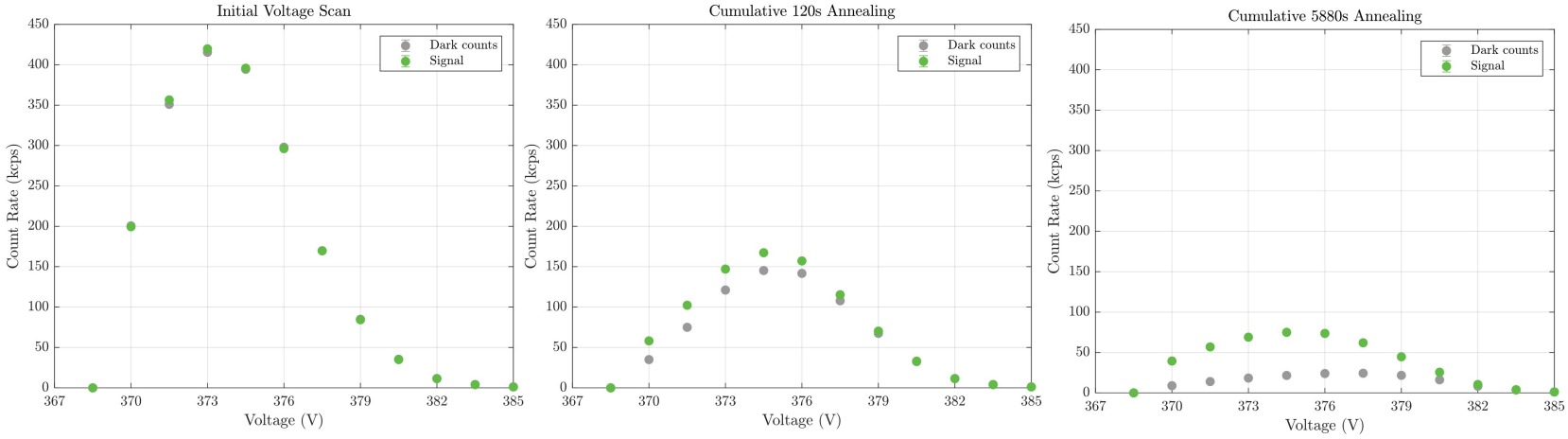

Figure 5.23: SPAD 4 (1.8 W annealed) dark and signal counts as function of bias voltage prior to annealing (left) and at a cumulative of 120s (center) and 5880s (right) of annealing. Breakdown voltage is defined as first voltage where there is non-zero count rate. Peak of count rate is the saturation point of the SPAD.

Alleviating saturation with annealing

Dark and signal count rates measured as a function of bias voltage gives an insight into the operational range of a SPAD(Figure 5.23). The heavily radiation-damaged SPADs in this set of tests exhibit a low saturation point occurring only approximately 12 V above breakdown, when typically a new device is operated with a 20V excess bias. Plotting the counts against detector bias on the same axis shows that not only is laser annealing reducing dark counts and producing better signal-to-noise-ratio in these damaged SPADs, but it may also be alleviating saturation. The saturation point, defined as the peak of the dark counts versus bias plot, appears to be shifting to a higher voltage as the SPAD is annealed(Figure 5.24). However, the count rate appears to drop again after 10 V above breakdown, which is lower than the expected 25 V excess bias with new, unirradiated SPADs. While it is tempting to attribute this shift solely to the annealing, there are two other possible explanations: firstly, the readout discriminator could be set too high and small avalanches are being missed, and secondly, the count rates are actually much higher after annealing and the passive quenching electronics are not able to register all the counts. However, there is a good argument that saturation effects are being reduced since the signal count rate becomes more differentiated from background dark counts as annealing progresses.

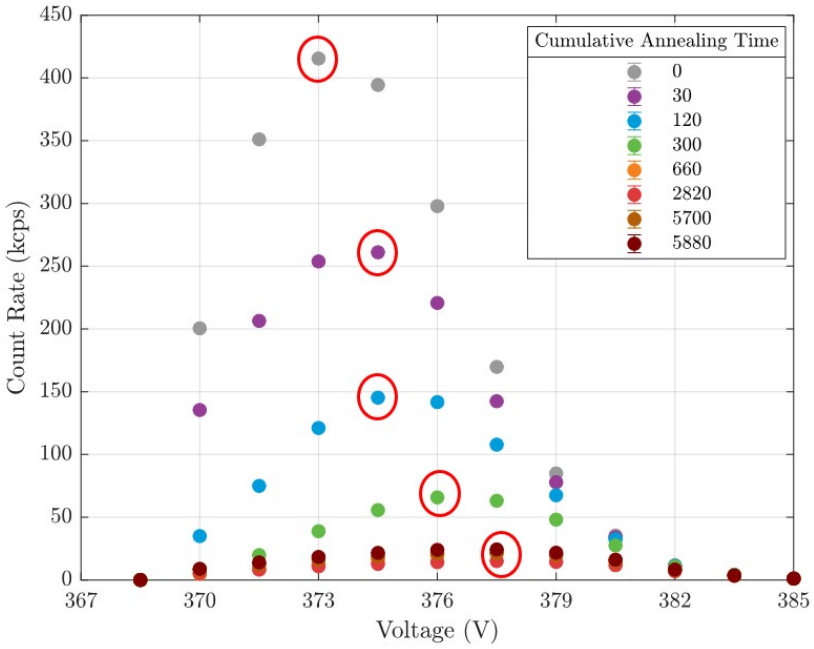

Figure 5.24: SPAD 4 dark counts as function of bias after 1.8 W annealing rounds. Circled points shows the highest count rate for the particular annealing rounds, which is defined to be the saturation point of the SPAD.

5.3.3 Conclusion

We show in this study that laser annealing can be a potent method of reducing dark counts in noisy detectors such that previously indistinguishable signal counts can be clearly resolved from background noise. It appears that annealing power is a more critical parameter than laser annealing time: much greater reduction of dark count rates was achieved with higher powers. We suggest that annealing also increases sensitivity of the detector at a fixed bias due to the diminishing of saturation effects. Our results agree with Lim et al. in that little change is seen for powers less than 1W, even though our study is fiber coupled. Annealing at such high powers has not yet been demonstrated before in a fiber-coupled system and shows that even long exposures of the SPAD active area can tolerate very high intensity stimulation. This result may come with the caveat that the SPADs must suffer

from a very high dark count rate, such as those seen after an extended period in space or after a particularly large radiation event such as after a solar flare. Repeated high power annealing can be reserved for cases of highly damaged detectors, while smaller bursts can be regularly applied to manage daily accumulation of dark count rate.

Chapter 6

Conclusion

This thesis focused on the two major projects in which I participated. In Chapter 3, I outlined the mechanisms of displacement damage and provided a summary of the literature that is available about radiation effects in SPADs. In particular, I found that there is limited knowledge on the effects of radiation on InGaAs/InP SPADs. This deficiency in understanding should be addressed before employing these types of SPADs in satellite-based QKD so as to understand the limits of these devices in space.

Chapter 4 presents work towards this goal of improving the general understanding of radiation effects in InGaAs SPADs. I modelled expected radiation fluence in LEO, GEO and greater altitude orbits during the solar cycle and with two SPAD substrate types. I found that om the absence of high solar activity, LEO orbits will incur the most radiation exposure. This is likely due to the ever-present Van Allen Belts. There was no large difference between the choice of material (Si or InGaAs). Since close examination of the differences in substrate were outside the scope of this thesis, it is recommended that further modelling be conducted, especially to account for substrate thickness, defect concentration and active area size. Despite not investigating the aforementioned parameters, a list of target radiation fluences was constructed for a future radiation ground test of InGaAs SPADs.

Later in Chapter 4, I summarized the procurement of several commercially available

InGaAs SPADs, the design of a gated and negative-feedback readout circut, and the integration of the detector testing set-up. I outlined the measurement protocol at the testing facility and presented the major results of the radiation testing campaign. We found that there is a general increase in the devices' dark count rates, although there are variations between SPAD models. These variations are attributed to differences in each SPAD substrate, which can differ even between two devices from the same manufacturer. We found that the increase in dark count rate in these InGaAs SPADs did not was not as large as the increase reported in literature or in Si-based SPADs. We believe this is linked to the small active-area of the devices tested. Again, it is likely the substrate characteristics also played a role in the smaller dark count rate elevation. We also measured the detection efficiency of the devices using two different methods. We found that the efficiency in all devices decreased as compared with the manufacturer specifications, though it is difficult to attribute this directly to radiation damage, since no pre-radiation measurement was conducted. While the results in this Chapter are not fully conclusive, they do point to more investigation being needed with particular emphasis on considering the SPAD active volume and substrate characteristics.

In the first half of Chapter 5, I outline my contributions to the pre-launch functional testing of the CAPSat CubeSat detector module, which is currently in low-Earth orbit. I characterized the detector break down voltages and observed detector behaviour in varying temperature and lighting conditions. I created a preliminary testing measurement schedule with suggested bias and discriminator ranges.

In the latter half of Chapter 5, I present novel results on laser annealing of highly radiation-damaged SPADs. We reuse the prototype CAPSat DM and integrated with a laser annealing set-up, with the DM placed inside a vacuum chamber to emulate a space-like environment. The experiment purpose was to determine annealing protocols that could be applied in the actual CAPSat mission. We found that annealing power is a more critical parameter than annealing time, with the greatest reduction in dark count rate occurring at $\sim$2W annealing power. We also investigated whether the number of exposures to the annealing laser is significant. We found that the number of exposures was not significantly different in the reduction of dark counts, however, there may be a slight

advantage to anneal with the same power several times. Finally, we monitored the CAPSat board functionality during the experiment to confirm the viability of the electronics in the space-like environment. Laser annealing is a powerful tool for combating radiation damage and should be studied further. One change to the protocols presented here is to anneal several times at the same power again, but conduct characterization after the multiple exposures rather than after each exposure. The several exposures could be done in a time frame similar to that of a satellite pass over the command center, since the annealing time is limited to how much duration of communication between the command center and satellite.

References

[1] Catalog of earth satellite orbits. https://earthobservatory.nasa.gov/features/OrbitsCatalog. Accessed: 2021-10-08.

[2] Characteristics and working of p-n junction diode. https://teknogenius.blogspot.com/2014/10/characteristics-and-working-of-p-n.html.

[3] Energy band gap eg of inxga1-xas alloys. https://batop.de/information/Eg_InGaAs.html.

[4] Excelitas c30902 datasheet. https://www.excelitas.com/product/c30902sh-si-apd-05mm-18-photon-counting.

[5] Google ngram of "quantum communication" from 1920 to 2019. https://books.google.com/ngrams/graphcontent=quantum+communication&year_start=1920&year_end=2019&corpus=26&smoothing=3#.

[6] Isl 21070 ic datasheet. https://www.renesas.com/us/en/document/dst/isl21070-datasheet.

[7] Psoc 3 data sheet. https://www.cypress.com/documentation/datasheets/datasheet-psoc-3-cy8c36-programmable-system-chip.

[8] Psoc3 vdac8 datasheet. https://www.cypress.com/file/97946/download.

[9] Real diode characteristics. https://learn.sparkfun.com/tutorials/diodes/real-diode-characteristics.

[10] Representation of the composite motion of charged particles trapped in the earth's magnetic field. https://www.spenvis.oma.be/help/background/traprad/traprad.html#TRENV.

[11] Rhr801 datasheet. https://www.st.com/en/space-products/rhr801.html.

[12] Screen relativistic (sr) nuclear and electronic stopping power calculator. http://www.sr-niel.org.

[13] South atlantic anomaly impact radiation. https://www.esa.int/ESA_Multimedia/Videos/2020/05/South_Atlantic_Anomaly_impact_radiation.

[14] Van allen radiation belt graphic. https://commons.wikimedia.org/wiki/File:Van_Allen_radiation_belt.svg.

[15] An evaluation of solar-proton event models for esa missions. *ESA Journal*, 16:275–297, 1992.

[16] Raichelle Aniceto, Randall Milanowski, Slaven Moro, Kerri Cahoy, and Garrett Schlenvogt. Proton radiation effects on hamamatsu ingaas pin photodiodes. In *2017 17th European Conference on Radiation and Its Effects on Components and Systems (RADECS)*, pages 1–6. IEEE, 2017.

[17] Elena Anisimova, Brendon L Higgins, Jean-Philippe Bourgoin, Miles Cranmer, Eric Choi, Danya Hudson, Louis P Piche, Alan Scott, Vadim Makarov, and Thomas Jennewein. Mitigating radiation damage of single photon detectors for space applications. *EPJ Quantum Technology*, 4:1–14, 2017.

[18] Pierre Arnolda, Christophe Inguimbert, Thierry Nuns, and Cesar Boatella-Polo. Niel scaling: comparison with measured defect introduction rate in silicon. *IEEE Transactions on Nuclear Science*, 58(3):756–763, 2011.

[19] Pierre Arnolda, Christophe Inguimbert, Thierry Nuns, and Cesar Boatella-Polo. Niel scaling: comparison with measured defect introduction rate in silicon. *IEEE Transactions on Nuclear Science*, 58(3):756–763, 2011.

[20] M. Aspelmeyer, T. Jennewein, M. Pfennigbauer, W.R. Leeb, and A. Zeilinger. Long-distance quantum communication with entangled photons using satellites. *IEEE Journal of Selected Topics in Quantum Electronics*, 9(6):1541–1551, 2003.

[21] M Avesani, L Calderaro, M Schiavon, A Stanco, C Agnesi, A Santamato, M Zahidy, A Scriminich, G Foletto, G Contestabile, et al. Full daylight quantum-key-distribution at 1550 nm enabled by integrated silicon photonics. *npj Quantum Information*, 7(1):1–8, 2021.

[22] Francis F Badavi. Exposure estimates for repair satellites at geosynchronous orbit. *Acta Astronautica*, 83:18–26, 2013.

[23] Gautam D Badhwar. Drift rate of the south atlantic anomaly. *Journal of Geophysical Research: Space Physics*, 102(A2):2343–2349, 1997.

[24] S Barde, R Ecoffet, J Costeraste, A Meygret, and X Hugon. Displacement damage effects in ingaas detectors: experimental results and semi-empirical model prediction. *IEEE Transactions on Nuclear Science*, 47(6):2466–2472, 2000.

[25] Heidi N Becker, William H Farr, and David Q Zhu. Radiation response of emerging high gain, low noise detectors. *IEEE Transactions on Nuclear Science*, 54(4):1129–1135, 2007.

[26] Heidi N Becker and Allan H Johnston. Dark current degradation of near infrared avalanche photodiodes from proton irradiation. *IEEE Transactions on Nuclear Science*, 51(6):3572–3578, 2004.

[27] Robert Bedington, Juan Miguel Arrazola, and Alexander Ling. Progress in satellite quantum key distribution. *npj Quantum Information*, 3(1):1–13, 2017.

[28] C.H. Bennett and G. Brassard. Quantum cryptography: Public key distribution and coin tossing. *Proceedings of the IEEE International Conference on Computers, Systems, and Signal Processing*, pages 175–179, 1984.

[29] Charles H Bennett, François Bessette, Gilles Brassard, Louis Salvail, and John Smolin. Experimental quantum cryptography. *Journal of cryptology*, 5(1):3–28, 1992.

[30] Charles H. Bennett, Gilles Brassard, and N. David Mermin. Quantum cryptography without bell's theorem. *Phys. Rev. Lett.*, 68:557–559, Feb 1992.

[31] Daniel J Bernstein and Tanja Lange. Post-quantum cryptography. *Nature*, 549(7671):188–194, 2017.

[32] Fabrice Boudot, Pierrick Gaudry, Aurore Guillevic, Nadia Heninger, Emmanuel Thomé, and Paul Zimmermann. Comparing the difficulty of factorization and discrete logarithm: a 240-digit experiment. In *Annual International Cryptology Conference*, pages 62–91. Springer, 2020.

[33] Sébastien Bourdarie and Michael Xapsos. The near-earth space radiation environment. *IEEE transactions on nuclear science*, 55(4):1810–1832, 2008.

[34] J-P Bourgoin, Evan Meyer-Scott, BL Higgins, B Helou, Chris Erven, Hannes Huebel, B Kumar, D Hudson, I D'Souza, R Girard, et al. A comprehensive design and performance analysis of leo satellite quantum communication. *arXiv preprint arXiv:1211.2733*, 2012.

[35] Jean-Philippe Bourgoin, Nikolay Gigov, Brendon L Higgins, Zhizhong Yan, Evan Meyer-Scott, Amir K Khandani, Norbert Lütkenhaus, and Thomas Jennewein. Experimental quantum key distribution with simulated ground-to-satellite photon losses and processing limitations. *Physical Review A*, 92(5):052339, 2015.

[36] Colin D Bruzewicz, John Chiaverini, Robert McConnell, and Jeremy M Sage. Trapped-ion quantum computing: Progress and challenges. *Applied Physics Reviews*, 6(2):021314, 2019.

[37] John Clarke and Frank K Wilhelm. Superconducting quantum bits. *Nature*, 453(7198):1031–1042, 2008.

[38] Lucian C Comandar, Bernd Fröhlich, James F Dynes, Andrew W Sharpe, Marco Lucamarini, Zhiliang Yuan, Richard V Penty, and Andrew J Shields. Ghz-gated ingaas/inp single-photon detector with detection efficiency exceeding 55% at 1550 nm. *arXiv preprint arXiv:1412.1586*, 2014.

[39] Sergio Cova, Massimo Ghioni, Andrea Lacaita, Carlo Samori, and Franco Zappa. Avalanche photodiodes and quenching circuits for single-photon detection. *Applied optics*, 35(12):1956–1976, 1996.

[40] Sergio Cova, A Longoni, and A Andreoni. Towards picosecond resolution with single-photon avalanche diodes. *Review of Scientific Instruments*, 52(3):408–412, 1981.

[41] Ian DSouza, Jean-Philippe Bourgoin, Brendon L Higgins, Jin Gyu Lim, Ramy Tannous, Sascha Agne, Brian Moffat, Vadim Makarov, and Thomas Jennewein. Repeated radiation damage and thermal annealing of avalanche photodiodes. *EPJ Quantum Technology*, 8(1):13, 2021.

[42] Artur K. Ekert. Quantum cryptography based on bell's theorem. *Phys. Rev. Lett.*, 67:661–663, Aug 1991.

[43] Richard P Feynman. Simulating physics with computers. In *Feynman and computation*, pages 133–153. CRC Press, 2018.

[44] Lov K Grover. A fast quantum mechanical algorithm for database search. In *Proceedings of the twenty-eighth annual ACM symposium on Theory of computing*, pages 212–219, 1996.

[45] Jianping Guo, Changjun Liao, Zhengjun Wei, and Jindong Wang. Punch-through characteristics of avalanche photodiodes under the geiger mode. *Modern Physics Letters B*, 24(03):357–362, 2010.

[46] Robert H Hadfield. Single-photon detectors for optical quantum information applications. *Nature photonics*, 3(12):696–705, 2009.

[47] Richard D Harris, William H Farr, and Heidi N Becker. Degradation of inp-based geiger-mode avalanche photodiodes due to proton irradiation. *Journal of Modern Optics*, 58(3-4):225–232, 2011.

[48] Chia-Lin Huang, Harlan E Spence, and Brian T Kress. Assessing access of galactic cosmic rays at moon's orbit. *Geophysical Research Letters*, 36(9), 2009.

[49] Mark A Itzler, Xudong Jiang, Mark Entwistle, Krystyna Slomkowski, Alberto Tosi, Fabio Acerbi, Franco Zappa, and Sergio Cova. Advances in ingaasp-based avalanche diode single photon detectors. *Journal of Modern Optics*, 58(3-4):174–200, 2011.

[50] AH Johnston. Radiation damage of electronic and optoelectronic devices in space. 2000.

[51] Ivan Kassal, James D Whitfield, Alejandro Perdomo-Ortiz, Man-Hong Yung, and Alán Aspuru-Guzik. Simulating chemistry using quantum computers. *Annual review of physical chemistry*, 62:185–207, 2011.

[52] Yong-Su Kim, Youn-Chang Jeong, Sebastien Sauge, Vadim Makarov, and Yoon-Ho Kim. Ultra-low noise single-photon detector based on si avalanche photodiode. *Review of scientific instruments*, 82(9):093110, 2011.

[53] C Kittel. Introduction to solid state physics, 6th edn., translated by y. *Uno, N. Tsuya, A. Morita and J. Yamashita,(Maruzen, Tokyo, 1986) pp*, pages 124–129, 1986.

[54] QL Kleipool, RT Jongma, AMS Gloudemans, H Schrijver, GF Lichtenberg, RM Van Hees, AN Maurellis, and RWM Hoogeveen. In-flight proton-induced radiation damage to sciamachy's extended-wavelength ingaas near-infrared detectors. *Infrared physics & technology*, 50(1):30–37, 2007.

[55] Emanuel Knill, Raymond Laflamme, and Gerald J Milburn. A scheme for efficient quantum computation with linear optics. *nature*, 409(6816):46–52, 2001.

[56] Jan Kodet, Ivan Prochazka, Josef Blazej, Xiaoli Sun, and John Cavanaugh. Single photon avalanche diode radiation tests. *Nuclear Instruments and Methods in Physics Research Section A: Accelerators, Spectrometers, Detectors and Associated Equipment*, 695:309–312, 2012.

[57] Michael A Krainak, W Yu Anthony, Guangning Yang, Steven X Li, and Xiaoli Sun. Photon-counting detectors for space-based laser receivers. In *Quantum Sensing and Nanophotonic Devices VII*, volume 7608, page 760827. International Society for Optics and Photonics, 2010.

[58] Michel Kruglanski, N. Messios, Erwin De Donder, E. Gamby, Stijn Calders, Laszlo Hetey, and Hugh Evans. Space environment information system (spenvis). pages 7457–, 04 2009.

[59] Jin Gyu Lim, Elena Anisimova, Brendon L Higgins, Jean-Philippe Bourgoin, Thomas Jennewein, and Vadim Makarov. Laser annealing heals radiation damage in avalanche photodiodes. *EPJ quantum technology*, 4:1–16, 2017.

[60] Vadim Makarov. Controlling passively quenched single photon detectors by bright light. *New Journal of Physics*, 11(6):065003, 2009.

[61] Martino Marisaldi, Piera Maccagnani, Francesco Moscatelli, Claudio Labanti, Fabio Fuschino, Michela Prest, Alessandro Berra, Davide Bolognini, Massimo Ghioni, Ivan Rech, et al. Single photon avalanche diodes for space applications. In *2011 IEEE Nuclear Science Symposium Conference Record*, pages 129–134. IEEE, 2011.

[62] Esteban A Martinez, Christine A Muschik, Philipp Schindler, Daniel Nigg, Alexander Erhard, Markus Heyl, Philipp Hauke, Marcello Dalmonte, Thomas Monz, Peter Zoller, et al. Real-time dynamics of lattice gauge theories with a few-qubit quantum computer. *Nature*, 534(7608):516–519, 2016.

[63] K. G. McKay. Avalanche breakdown in silicon. *Phys. Rev.*, 94:877–884, May 1954.

[64] michbich. *Peltier Element*. Jan 2010.

[65] Alan Migdall, Sergey V Polyakov, Jingyun Fan, and Joshua C Bienfang. *Single-photon generation and detection: physics and applications*. Academic Press, 2013.

[66] Francesco Moscatelli, Martino Marisaldi, Piera Maccagnani, Claudio Labanti, Fabio Fuschino, Michela Prest, Alessandro Berra, Davide Bolognini, Massimo Ghioni, Ivan Rech, et al. Radiation tests of single photon avalanche diode for space applications. *Nuclear Instruments and Methods in Physics Research Section A: Accelerators, Spectrometers, Detectors and Associated Equipment*, 711:65–72, 2013.

[67] N Namekata, S Sasamori, and Shuichiro Inoue. 800 mhz single-photon detection at 1550-nm using an ingaas/inp avalanche photodiode operated with a sine wave gating. *Optics Express*, 14(21):10043–10049, 2006.

[68] George T Nelson, Gildas Ouin, Stephen J Polly, Kevin B Wynne, Arthur W Haberl, William A Lanford, Robert A Lowell, and Seth M Hubbard. In situ deep-level transient spectroscopy and dark current measurements of proton-irradiated ingaas photodiodes. *IEEE Transactions on Nuclear Science*, 67(9):2051–2061, 2020.

[69] Jane E Nordholt, Richard J Hughes, George L Morgan, C Glen Peterson, and Christopher C Wipf. Present and future free-space quantum key distribution. In *Free-Space Laser Communication Technologies XIV*, volume 4635, pages 116–126. International Society for Optics and Photonics, 2002.

[70] Thierry Nuns, Christophe Inguimbert, Juan Barbero, Juan Moreno, Samuel Ducret, Alexandru Nedelcu, Bjorn Galnander, and Elke Passoth. Displacement damage effects in ingaas photodiodes due to electron, proton, and neutron irradiations. *IEEE Transactions on Nuclear Science*, 67(7):1263–1272, 2020.

[71] Stefano Pirandola, Ulrik L Andersen, Leonardo Banchi, Mario Berta, Darius Bunandar, Roger Colbeck, Dirk Englund, Tobias Gehring, Cosmo Lupo, Carlo Ottaviani, et al. Advances in quantum cryptography. *Advances in Optics and Photonics*, 12(4):1012–1236, 2020.

[72] John Preskill. Quantum computing and the entanglement frontier. *arXiv preprint arXiv:1203.5813*, 2012.

[73] John G Rarity, PR Tapster, PM Gorman, and Peter Knight. Ground to satellite secure key exchange using quantum cryptography. *New Journal of Physics*, 4(1):82, 2002.

[74] Gregoire Ribordy, Jean-Daniel Gautier, Hugo Zbinden, and Nicolas Gisin. Performance of ingaas/inp avalanche photodiodes as gated-mode photon counters. *Applied Optics*, 37(12):2272–2277, 1998.

[75] Vincent Rijmen and Joan Daemen. Advanced encryption standard. *Proceedings of Federal Information Processing Standards Publications, National Institute of Standards and Technology*, pages 19–22, 2001.

[76] Ronald L Rivest, Adi Shamir, and Leonard Adleman. A method for obtaining digital signatures and public-key cryptosystems. *Communications of the ACM*, 21(2):120–126, 1978.

[77] Susan W Samwel, Esraa A El-Aziz, Henry B Garrett, Ahmed A Hady, Makram Ibrahim, and Magdy Y Amin. Space radiation impact on smallsats during maximum and minimum solar activity. *Advances in Space Research*, 64(1):239–251, 2019.

[78] Valerio Scarani, Helle Bechmann-Pasquinucci, Nicolas J Cerf, Miloslav Dušek, Norbert Lütkenhaus, and Momtchil Peev. The security of practical quantum key distribution. *Reviews of modern physics*, 81(3):1301, 2009.

[79] Peter W Shor. Algorithms for quantum computation: discrete logarithms and factoring. In *Proceedings 35th annual symposium on foundations of computer science*, pages 124–134. Ieee, 1994.

[80] Fabio Signorelli, Fabio Telesca, Enrico Conca, Adriano Della Frera, Alessandro Ruggeri, Andrea Giudice, and Alberto Tosi. Low-noise ingaas/inp single-photon avalanche diodes for fiber-based and free-space applications. *IEEE Journal of Selected Topics in Quantum Electronics*, 28(2):1–10, 2021.

[81] Edward M Silverman. Space environmental effects on spacecraft: Leo materials selection guide, part 1. *Progress Report*, 1995.

[82] Harlan E Spence, Michael J Golightly, Colin J Joyce, Mark D Looper, Nathan A Schwadron, Sonya S Smith, Lawrence W Townsend, Jody Wilson, and Cary Zeitlin. Relative contributions of galactic cosmic rays and lunar proton "albedo" to dose and dose rates near the moon. *Space Weather*, 11(11):643–650, 2013.

[83] Helmuth Spieler. Introduction to radiation-resistant semiconductor devices and circuits. In *AIP Conference Proceedings*, volume 390, pages 23–49. American Institute of Physics, 1997.

[84] JR Srour, , and JW Palko. Displacement damage effects in irradiated semiconductor devices. *IEEE Transactions on Nuclear Science*, 60(3):1740–1766, 2013.

[85] JR Srour and DH Lo. Universal damage factor for radiation-induced dark current in silicon devices. *IEEE Transactions on Nuclear Science*, 47(6):2451–2459, 2000.

[86] JR Srour, Cheryl J Marshall, and Paul W Marshall. Review of displacement damage effects in silicon devices. *IEEE Transactions on nuclear science*, 50(3):653–670, 2003.

[87] E.G. Stassinopoulos and J.P. Raymond. The space radiation environment for electronics. *Proceedings of the IEEE*, 76(11):1423–1442, 1988.

[88] Nigar Sultana. *Single-photon detectors for satellite based quantum communications*. PhD thesis, University of Waterloo, 2020.

[89] Geoffrey P Summers, Edward A Burke, Philip Shapiro, Scott R Messenger, and Robert J Walters. Damage correlations in semiconductors exposed to gamma, electron and proton radiations. *IEEE Transactions on Nuclear Science*, 40(6):1372–1379, 1993.

[90] Xiaoli Sun and Henri Dautet. Proton radiation damage of si apd single photon counters. In *2001 IEEE Radiation Effects Data Workshop. NSREC 2001. Work-*

shop Record. Held in conjunction with IEEE Nuclear and Space Radiation Effects Conference (Cat. No. 01TH8588), pages 146–150. IEEE, 2001.

[91] Xiaoli Sun, Peggy L Jester, Stephen P Palm, James B Abshire, James D Spinhirne, and Michael A Krainak. In orbit performance of si avalanche photodiode single photon counting modules in the geoscience laser altimeter system on icesat. In *Advanced Photon Counting Techniques*, volume 6372, page 63720P. International Society for Optics and Photonics, 2006.

[92] Xiaoli Sun, Michael A Krainak, James B Abshire, James D Spinhirne, Claude Trottier, Murray Davies, Henri Dautet, Graham R Allan, Alan T Lukemire, and James C Vandiver. Space-qualified silicon avalanche-photodiode single-photon-counting modules. *journal of modern optics*, 51(9-10):1333–1350, 2004.

[93] Xiaoli Sun, Daniel Reusser, Henri Dautet, and James B Abshire. Measurement of proton radiation damage to si avalanche photodiodes. *IEEE transactions on Electron Devices*, 44(12):2160–2166, 1997.

[94] Yue Chuan Tan, Rakhitha Chandrasekara, Cliff Cheng, and Alexander Ling. Silicon avalanche photodiode operation and lifetime analysis for small satellites. *Optics express*, 21(14):16946–16954, 2013.

[95] Mayursinh Thakor, Sarman Hadia, and Ashok Kumar. Precise temperature control through thermoelectric cooler with pid controller. 04 2015.

[96] William K Wootters and Wojciech H Zurek. A single quantum cannot be cloned. *Nature*, 299(5886):802–803, 1982.

[97] Zhizhong Yan, Deny R Hamel, Aimee K Heinrichs, Xudong Jiang, Mark A Itzler, and Thomas Jennewein. An ultra low noise telecom wavelength free running single photon detector using negative feedback avalanche diode. *Review of Scientific Instruments*, 83(7):073105, 2012.

[98] Meng Yang, Feihu Xu, Ji-Gang Ren, Juan Yin, Yang Li, Yuan Cao, Qi Shen, Hai-Lin Yong, Liang Zhang, Sheng-Kai Liao, et al. Spaceborne, low-noise, single-photon

detection for satellite-based quantum communications. *Optics express*, 27(25):36114–36128, 2019.

[99] Lixing You, Jia Quan, Yong Wang, Yuexue Ma, Xiaoyan Yang, Yanjie Liu, Hao Li, Jianguo Li, Juan Wang, Jingtao Liang, et al. Superconducting nanowire single photon detection system for space applications. *Optics express*, 26(3):2965–2971, 2018.

[100] C Zeitlin, W Boynton, I Mitrofanov, D Hassler, W Atwell, TF Cleghorn, FA Cucinotta, M Dayeh, M Desai, SB Guetersloh, et al. Mars odyssey measurements of galactic cosmic rays and solar particles in mars orbit, 2002–2008. *Space Weather*, 8(11), 2010.

[101] Jun Zhang, Mark A Itzler, Hugo Zbinden, and Jian-Wei Pan. Advances in ingaas/inp single-photon detector systems for quantum communication. *Light: Science & Applications*, 4(5):e286–e286, 2015.

[102] Tao Zhang, Haizheng Dang, Rui Zha, Jun Tan, Jiaqi Li, Yongjiang Zhao, Bangjian Zhao, Renjun Xue, and Han Tan. Investigation of a 1.6 k space cryocooler for cooling the superconducting nanowire single photon detectors. *IEEE Transactions on Applied Superconductivity*, 31(5):1–5, 2021.

[103] Hank Zumbahlen. Chapter 3 - sensors. In Hank Zumbahlen, editor, *Linear Circuit Design Handbook*, pages 193–243. Newnes, Burlington, 2008.

Appendices

Appendix A

Technical Details and Experimental Photos

A.1 Electronics and mechanical designs

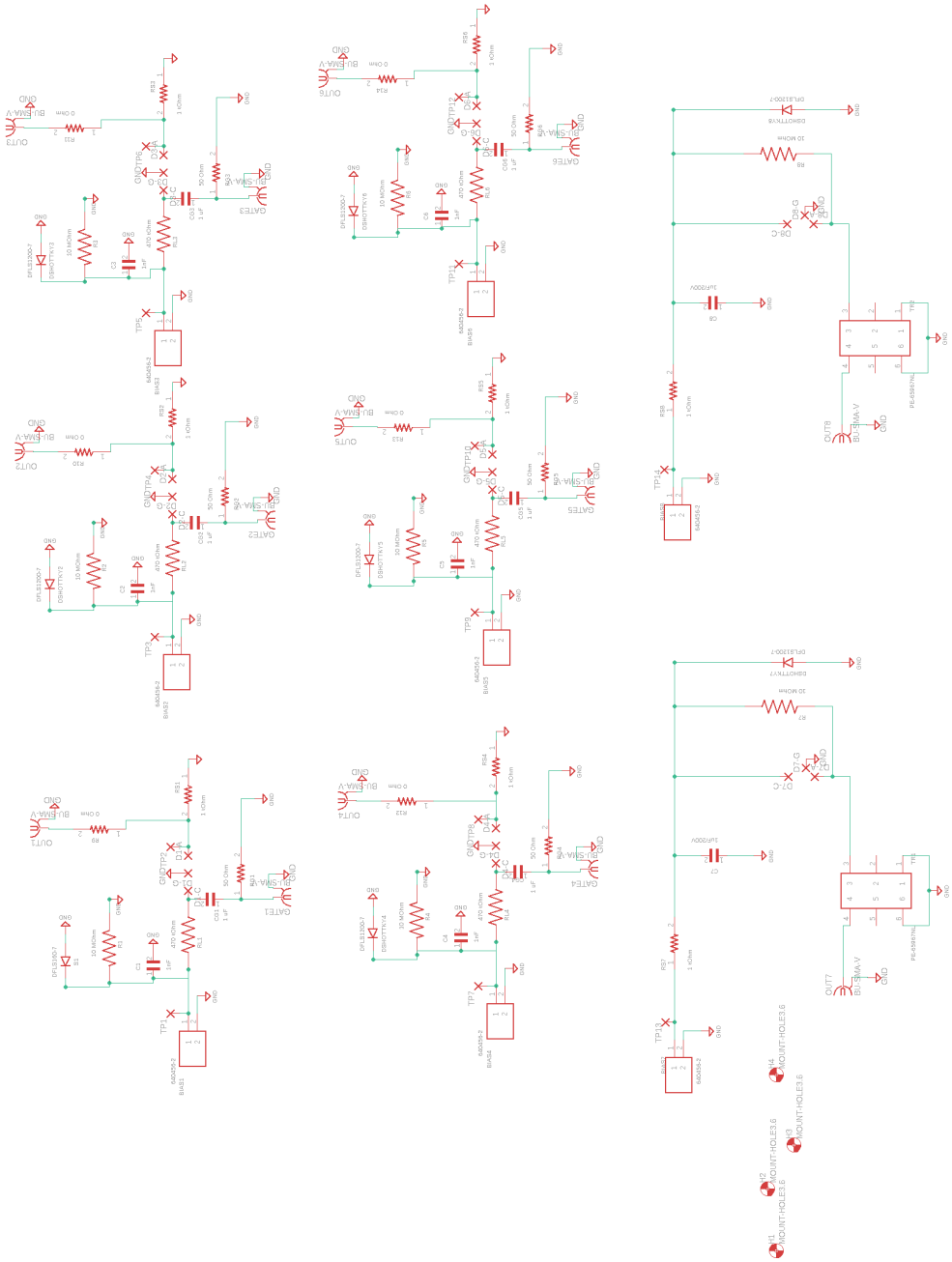

Figure A.1: Eagle schematic of all six gating circuits and two NFAD circuits.

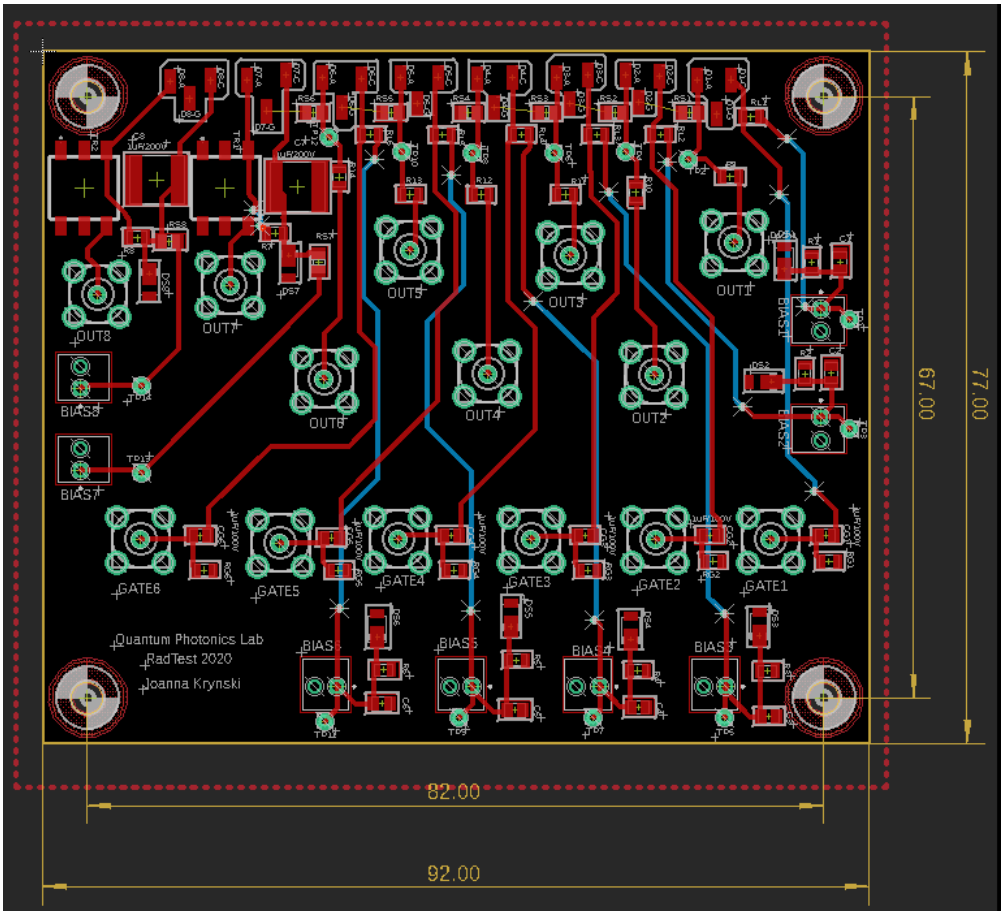

Figure A.2: Eagle PCB design. Red lines indicate top traces, blue indicate bottom traces. Drill holes for vias and connectors are green. The board dimensions are in millimetres.

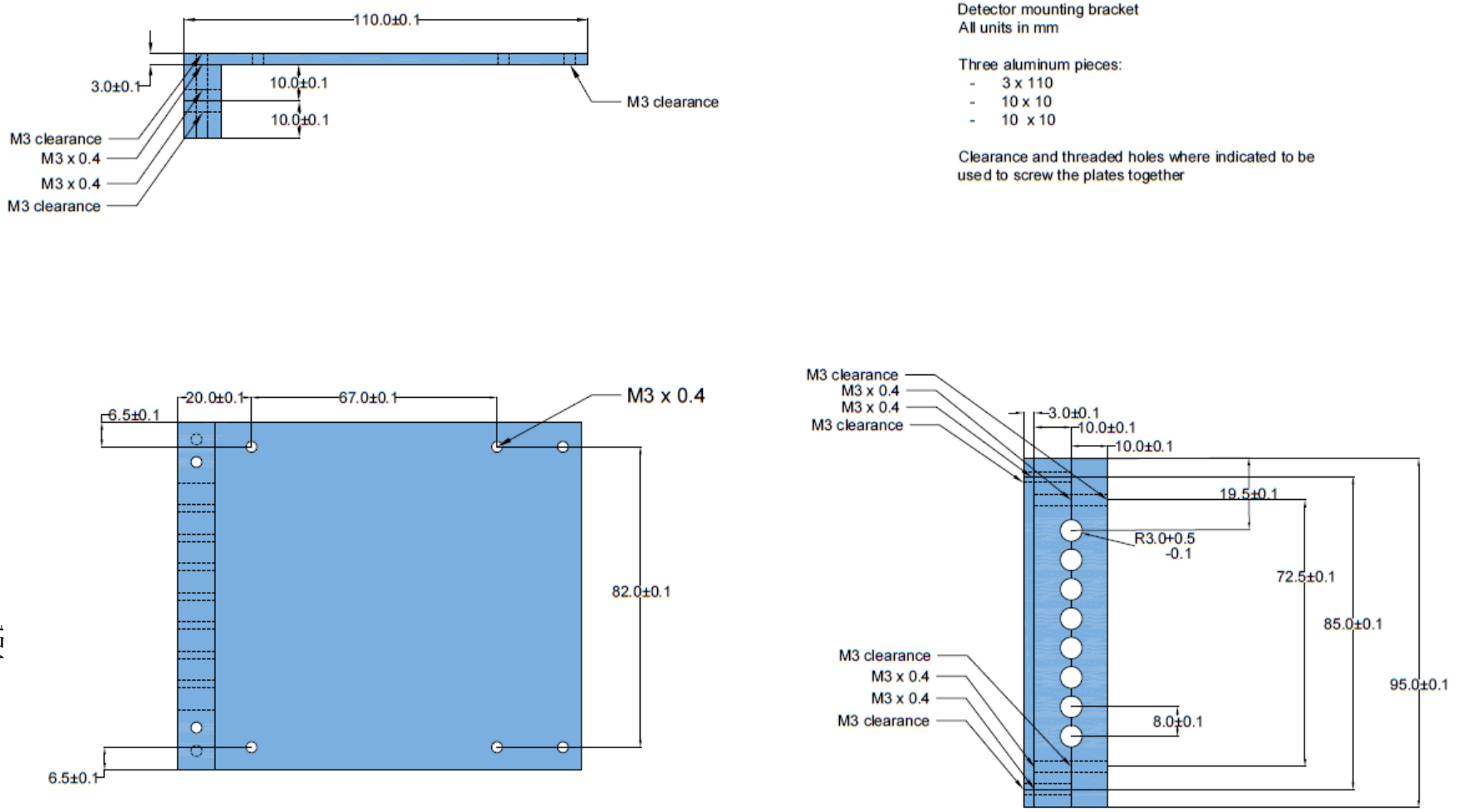

Figure A.3: SPAD enclosure and TEC cold side plate

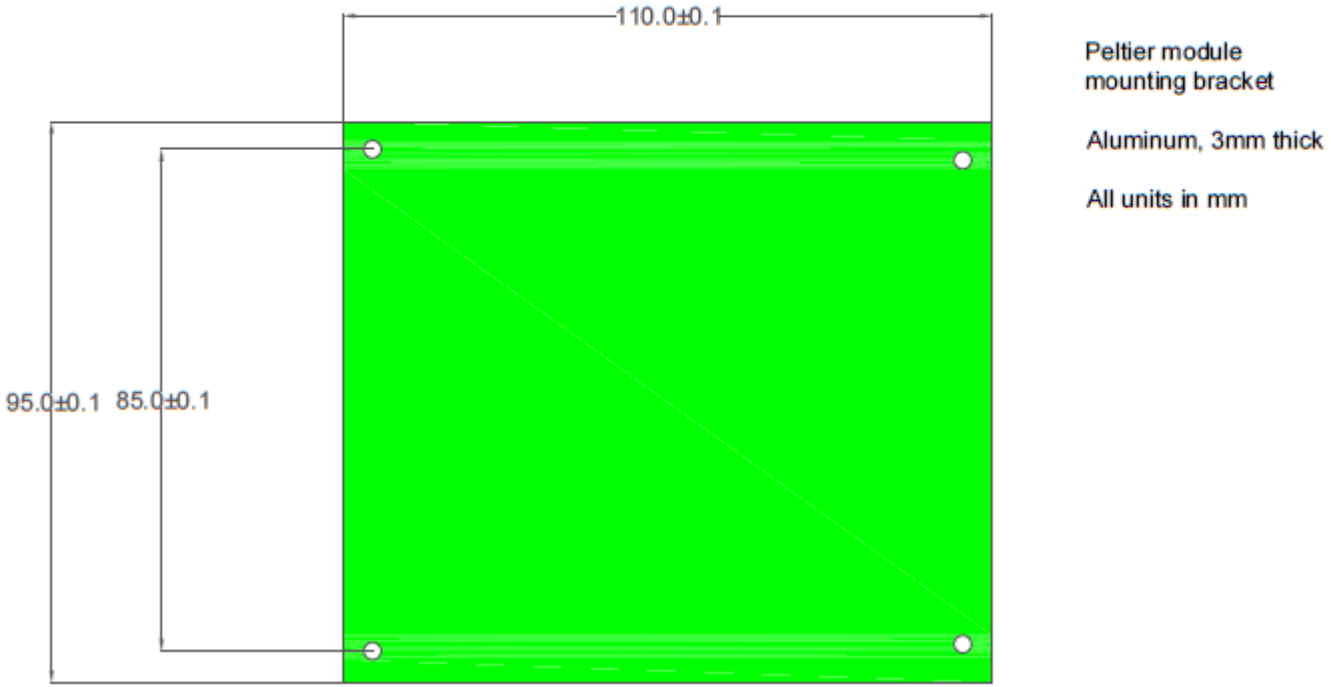

Figure A.4: Mounting bracket for hot side of TEC to copper heat sink

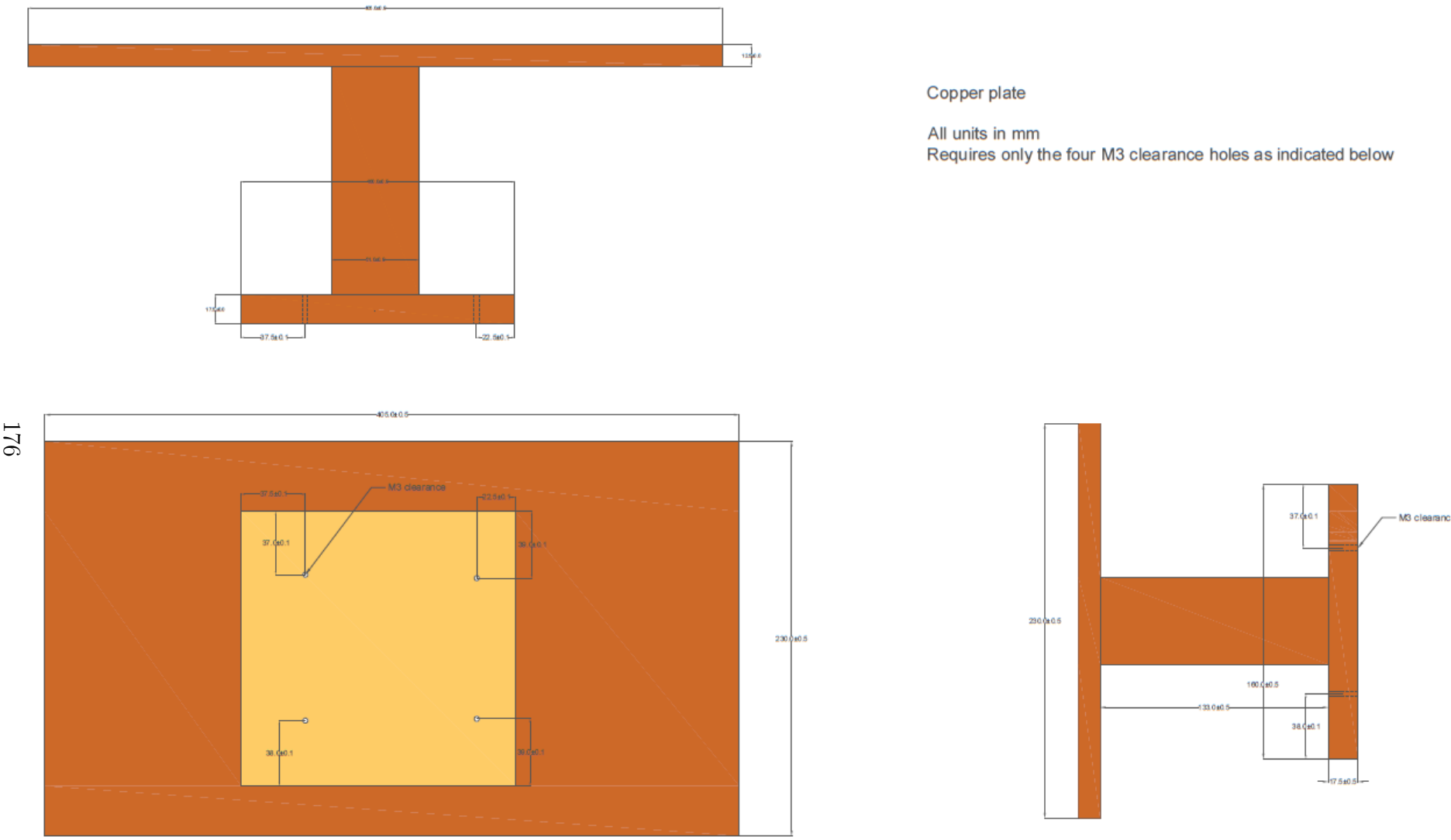

Figure A.5: Pre-machined copper heat sink with TEC mounting plate holes indicated

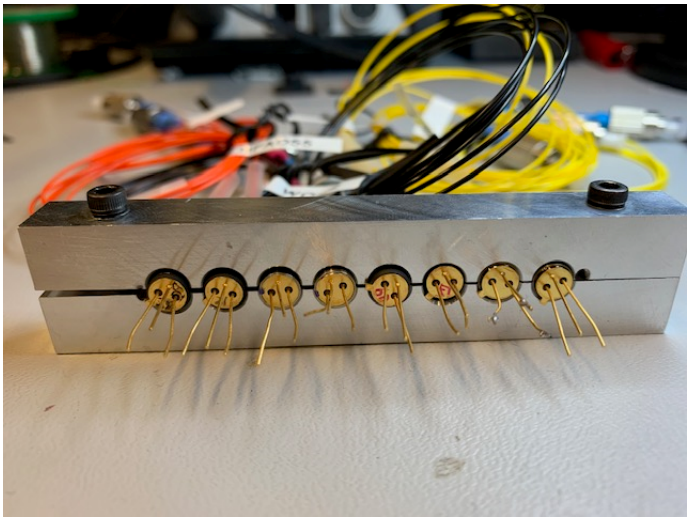

Figure A.6: SPADs in aluminium enclosure. Small gaps between the aluminium and the SPADs was inevitable due to machining limitations. RTD temperature sensor placement hole visible on the right.

A.2 TEC control calibration

The wired RTD (the one to be used for the experiment) was placed in the usual spot on the SPAD enclosure, while a second RTD was place on the opposite side of the SPAD enclosure. The TEC controller was set to six temperatures and allowed to heat or cool the SPAD ennclosure. The second RTD's resistance was then measured via a digital multimeter to estimate the SPAD enclosure temperature. The estimated temperature was compared to the TEC controller readout temperature. It was found that the TEC controller reached each set temperature and its temperature read out was accurate as compared with the second RTD temperature measurement.

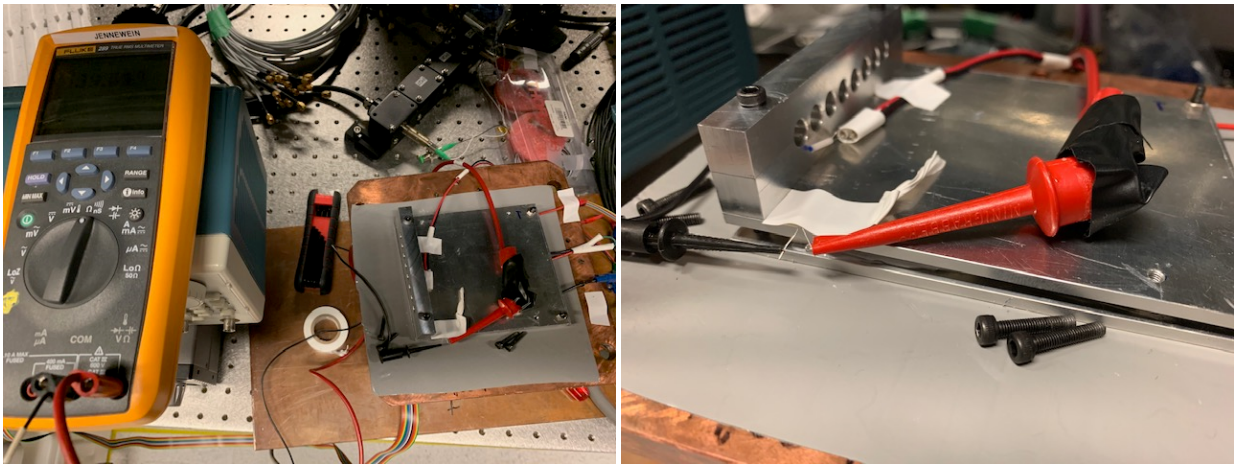

Figure A.7: Set-up for RTD calibration measurement (left). Multimeter was used to measure resistance of second RTD (shown on right), while primary RTD was used to drive TEC controller feedback loop.

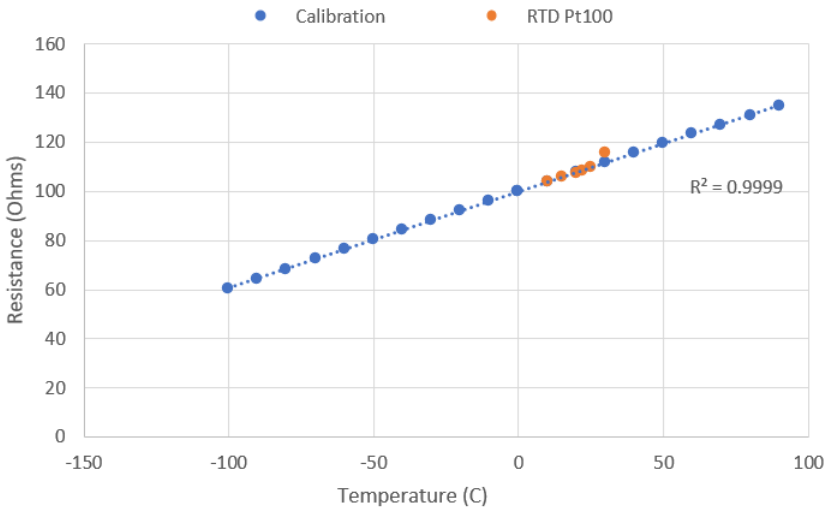

Figure A.8: Plot of Pt100 type RTD calibration curve (blue) and secondary RTD resistances measured with multimeter (orange). The linearity and proximity of the measured secondary RTD resistances to the blue calibration curve shows that the aluminium SPAD bracket was indeed being accurately heated and cooled to the set temperature by the TEC controller.

A.3 TRIUMF Set-up Photos

Figure A.9: Cooler containing detectors and electronics stands on height-adjustable platform. Proton beam port exit visible in the background. Oscilloscope, power supply and other control electronics were kept to the side of the radiation path.

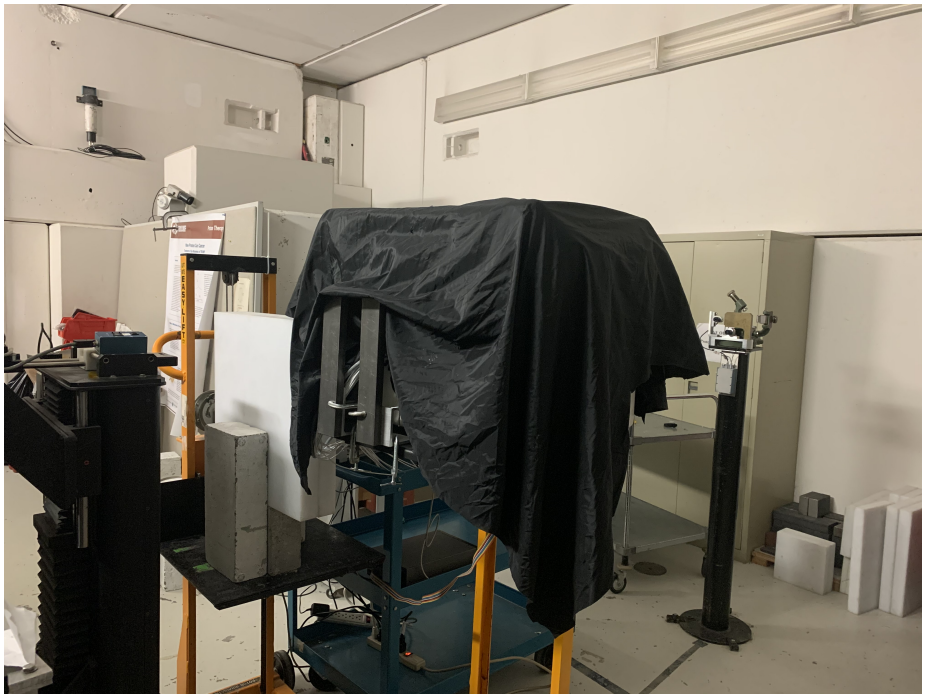

Figure A.10: Covered cooler prior to light dimming for measurement. Lead blocks and concrete shielding are visible as methods of reducing extra radiation damage to surrounding area (and experimentalists!)

Figure A.11: Top view of detectors in cooler were dry ice pellets. TEC driver cable (rainbow flat cable) goes through crack between cooler and lid, while all other cables go through hole previously drilled in middle of cooler

Figure A.12: Cooler cable hole stuffed with foam and tape to prevent leakage of cool air and moisture from entering the cooler. Power and signal cables are visible.

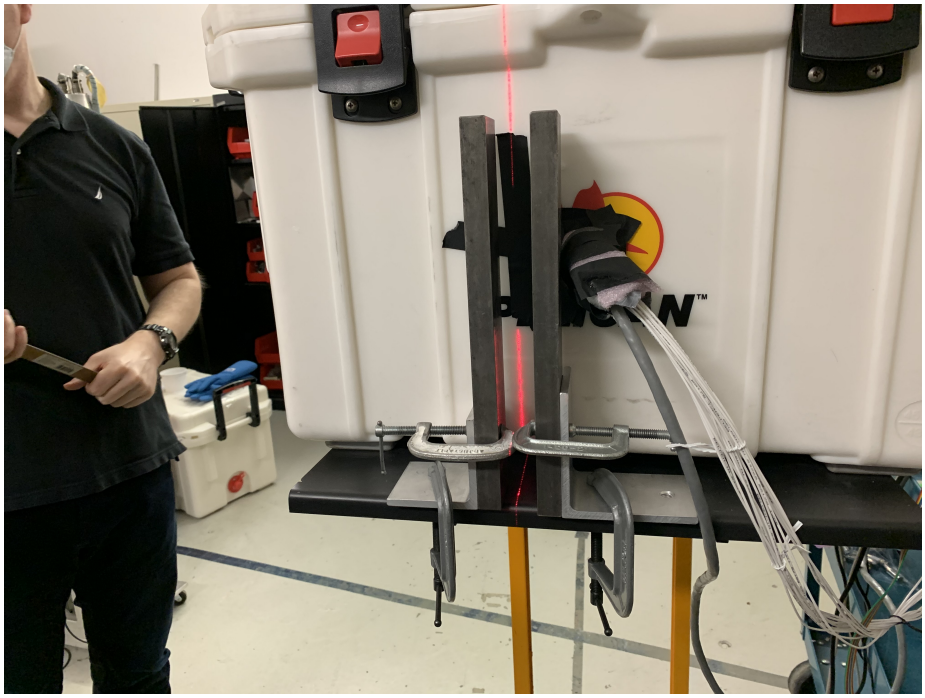

Figure A.13: Laser cross hair indicating proton beam position was used to align the detectors int he cooler on the platform to the beam line. Lead blocks are used to shield surrounding electronics.

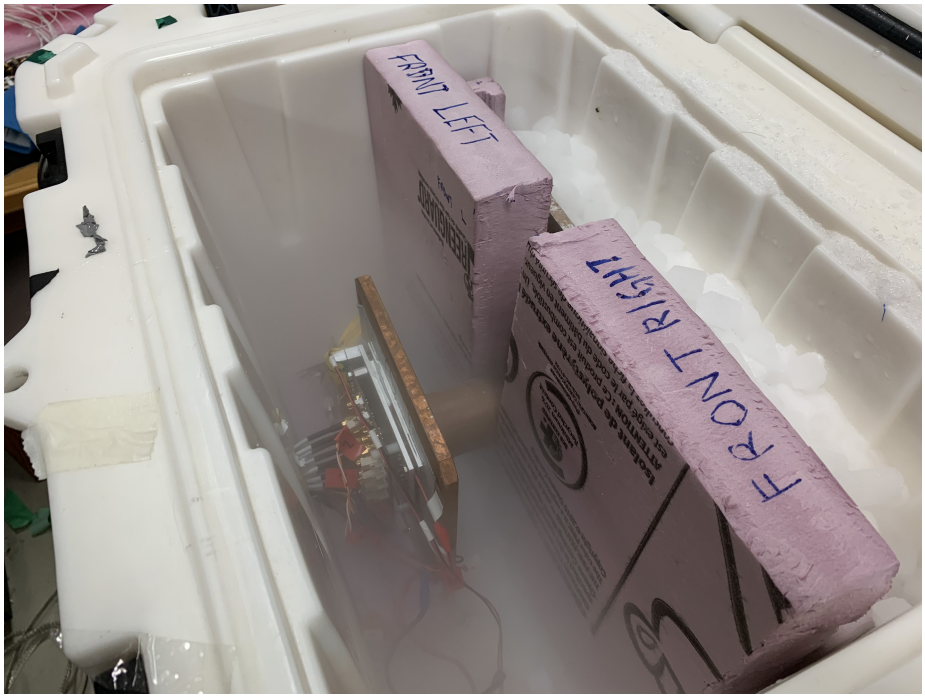

Figure A.14: Detector readout PCB mounted on copper heat sink abut to dry ice within the cooler. Foam was used to separate the ice from the front of the cooler where experimentalists work to make fine adjustments.

Figure A.15: Function generator (top left), source meter under function generator (left), NIM bin with time tagger (bottom) and oscilloscope (right) arranged as during measurement.

Figure A.16: Proton beam control room. Experimentalists called the cyclotron operator to provide the correct flux of protons, then used archaic computer system to set the exact dose needed. Before retirement, this system was used for radiation therapy of cancer patients.

Appendix B

Additional data from radiation testing

B.1 IV Curves

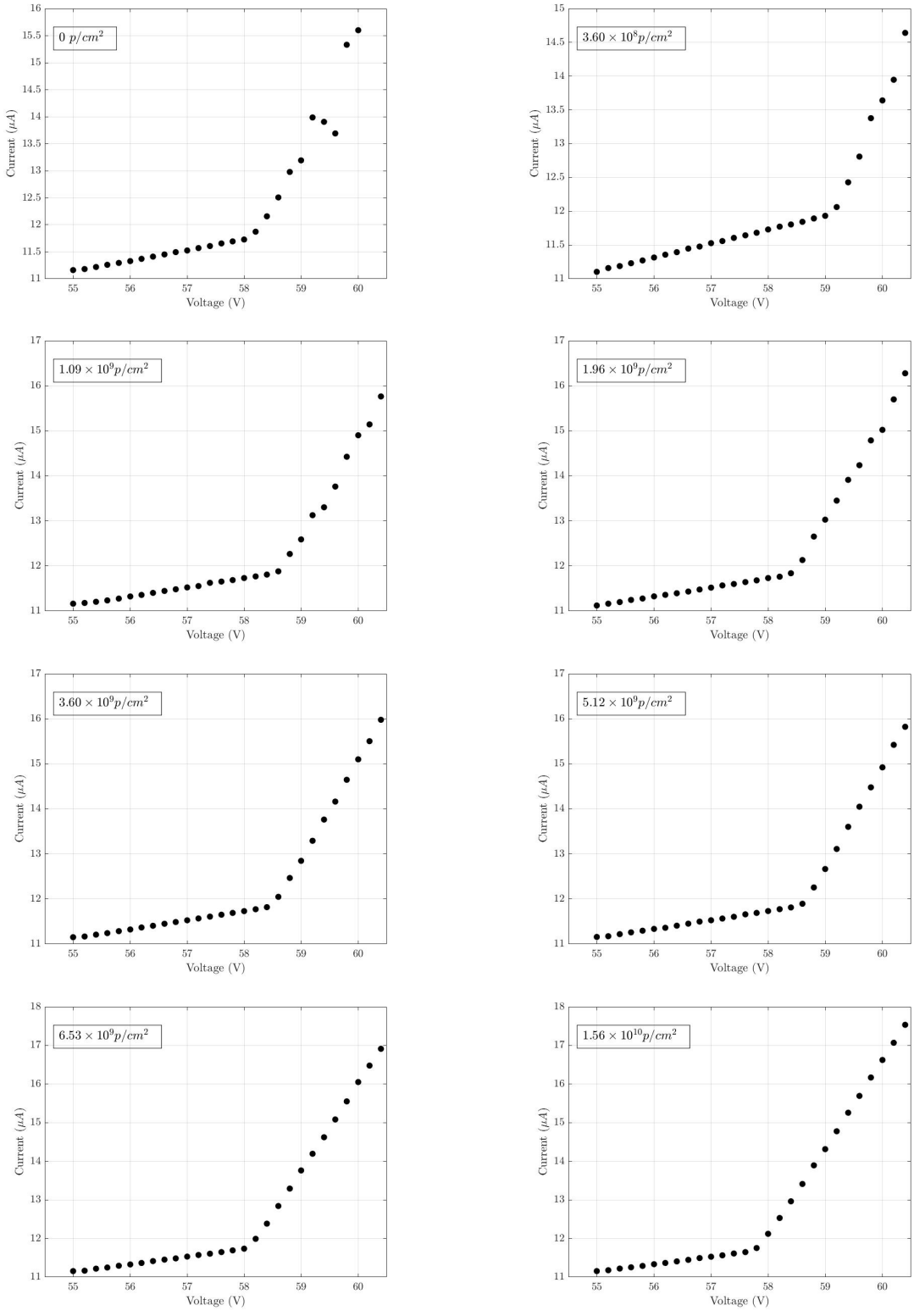

Figure B.1: Post-radiation IV curve for RMY-1

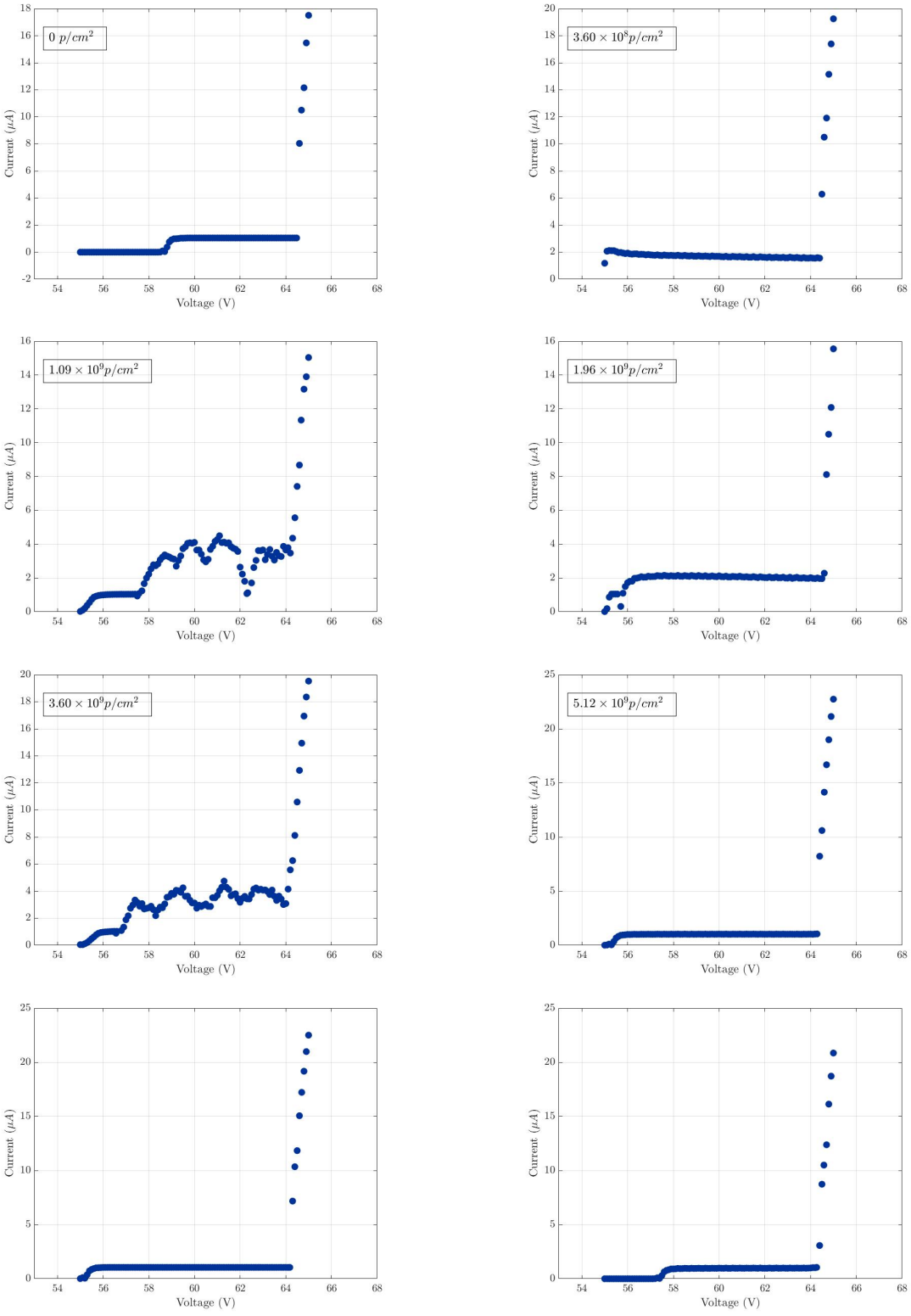

Figure B.2: Post-radiation IV Curve for Polimi 1

The fluctuating current in the IV curve for Polimi 1 in the third and fifth plots is believed to be due to issues with the automatic current measurement of the SMU. The Milano readout circuit required a few seconds to allow any capacitors to discharge and for current to stabilize. It is possible that for these measurements the SMU was measuring while the current was still unstable.

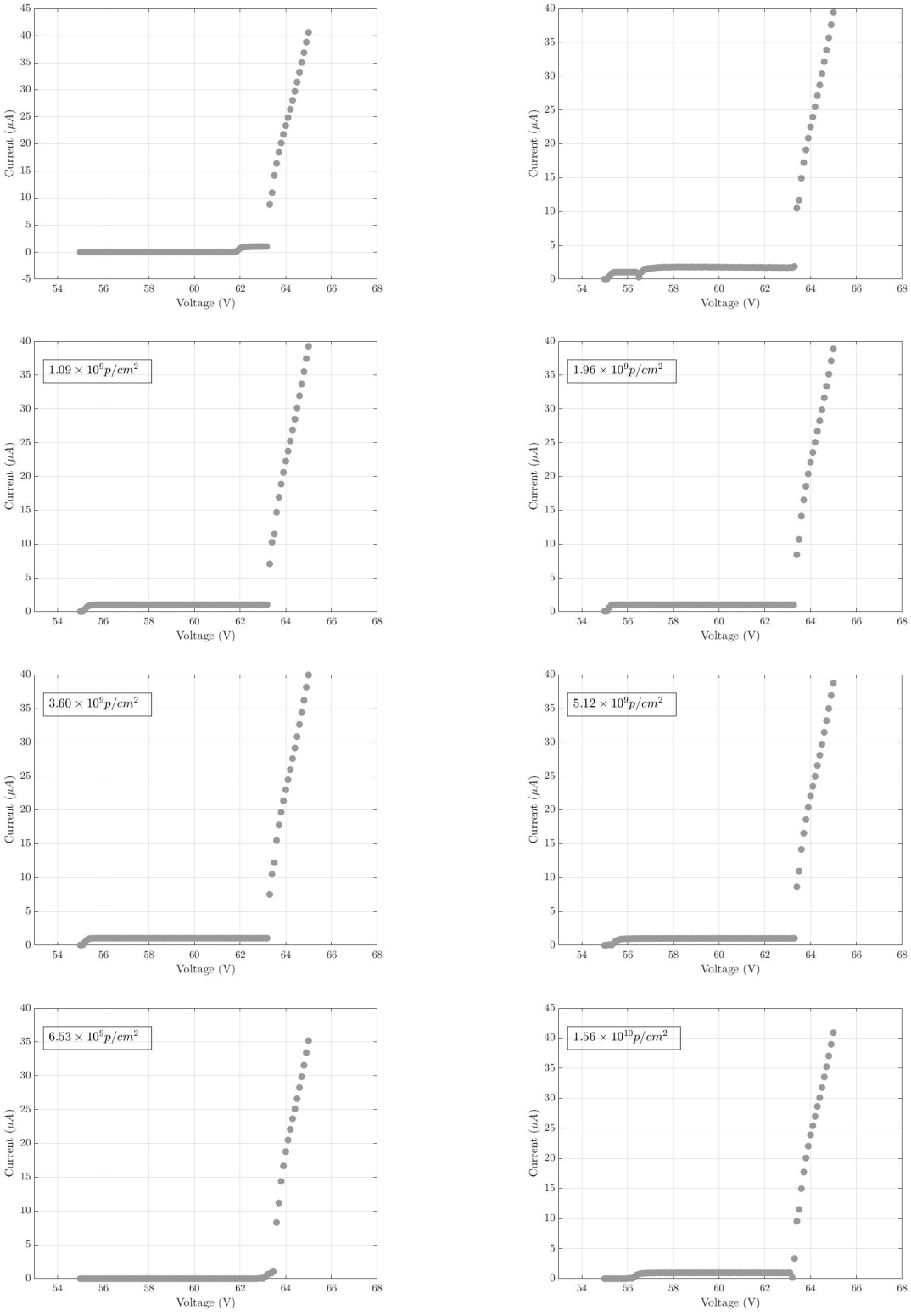

Figure B.3: Post-radiation IV Curve for Polimi 2

B.2 Dark Count Rate

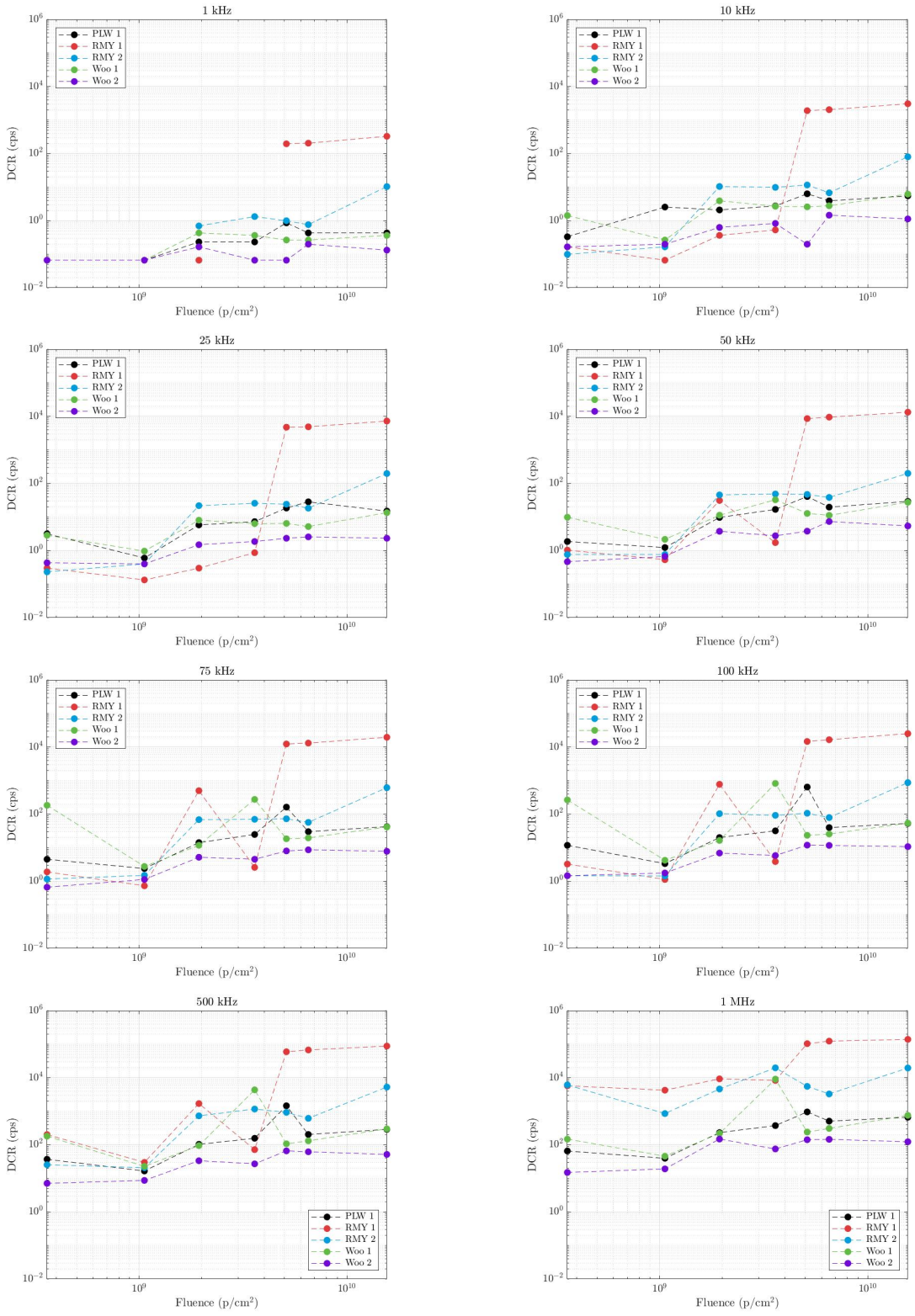

Figure B.4: QPL gated SPADs' DCR as function of cumulative proton fluence

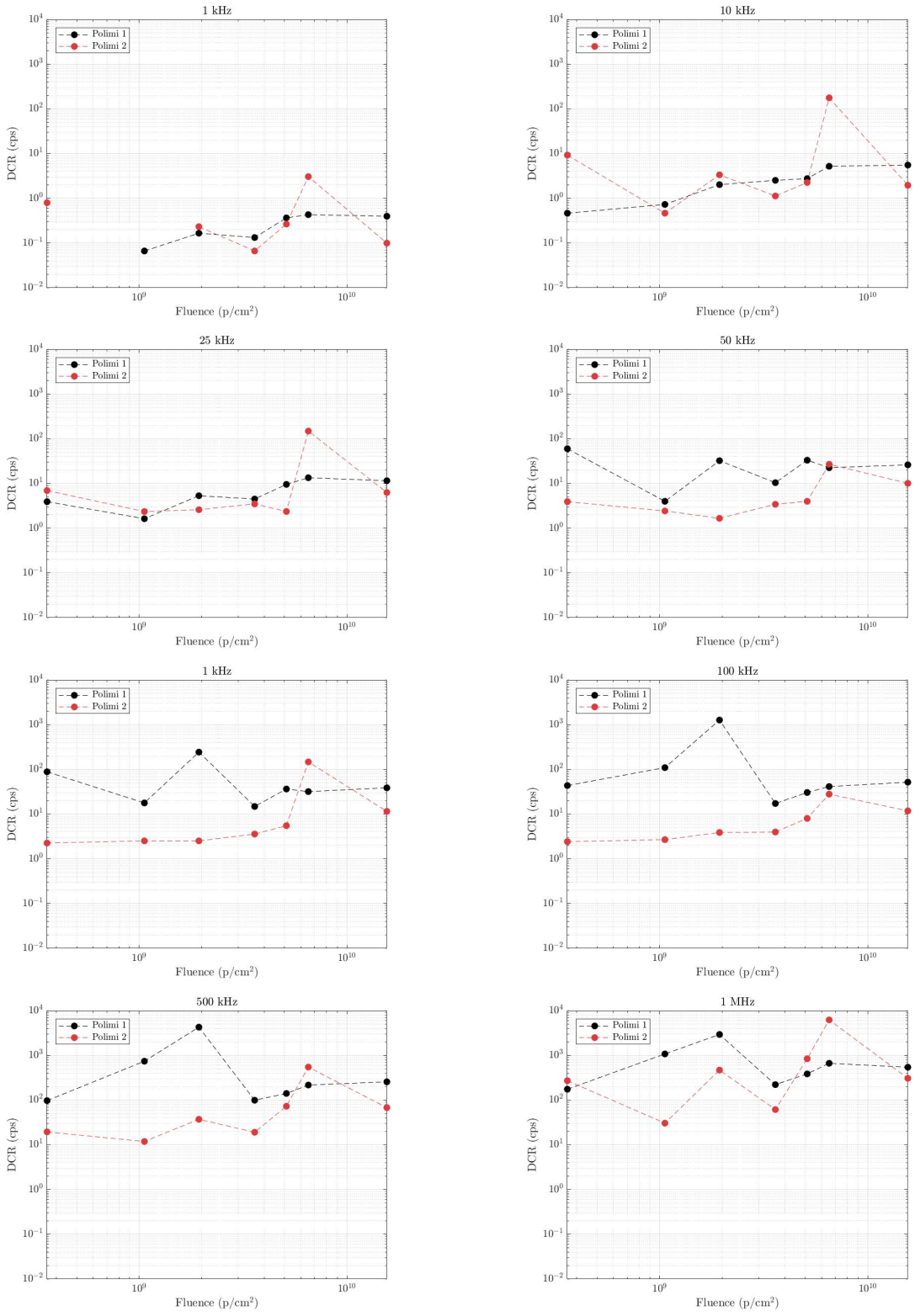

Figure B.5: Politechnico di Milano gated SPADs' DCR as function of cumulative proton fluence

B.3 Normalized Dark Count Rate

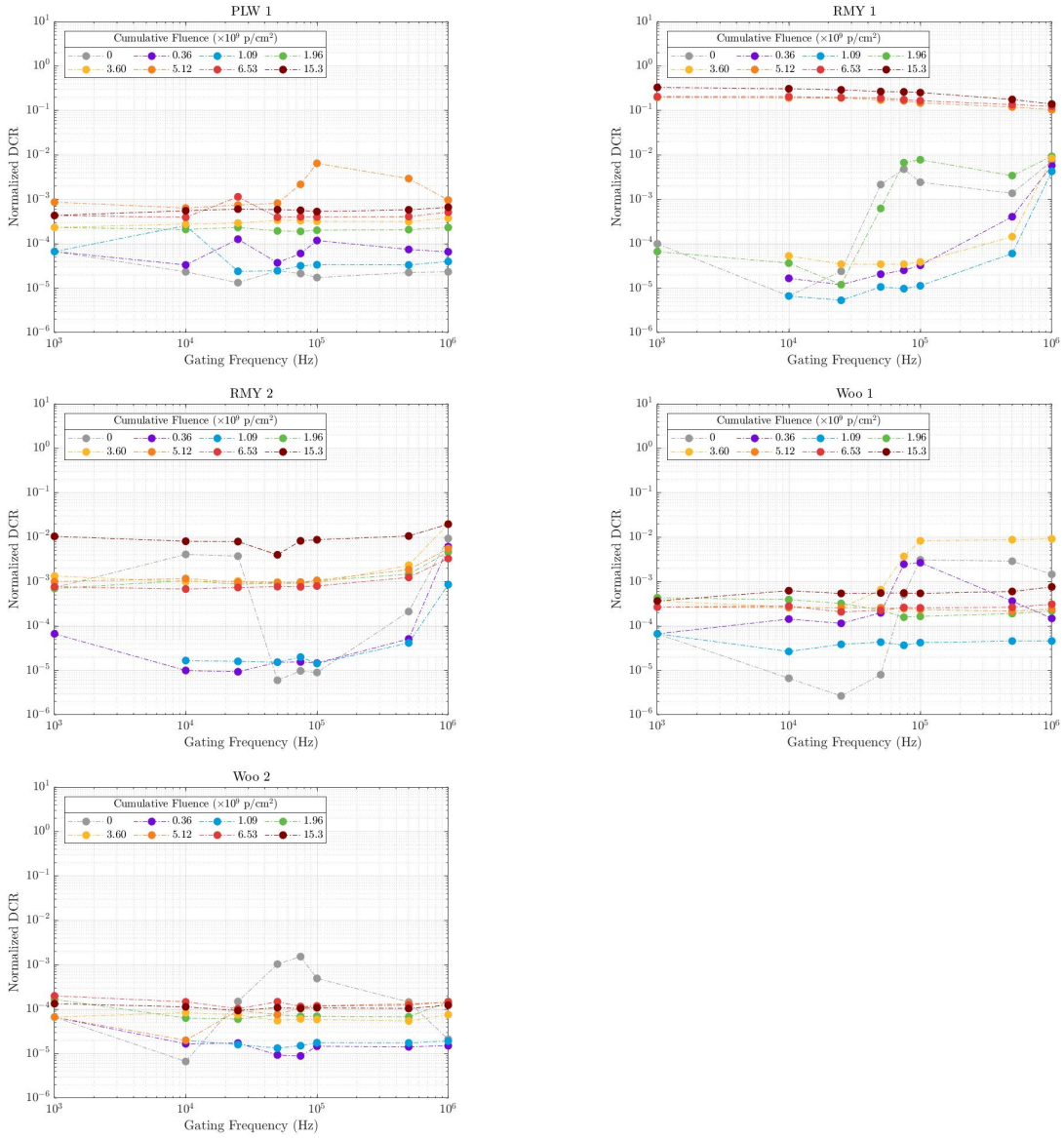

Figure B.6: Normalized DCR as function of gating frequency for gated QPL SPADs

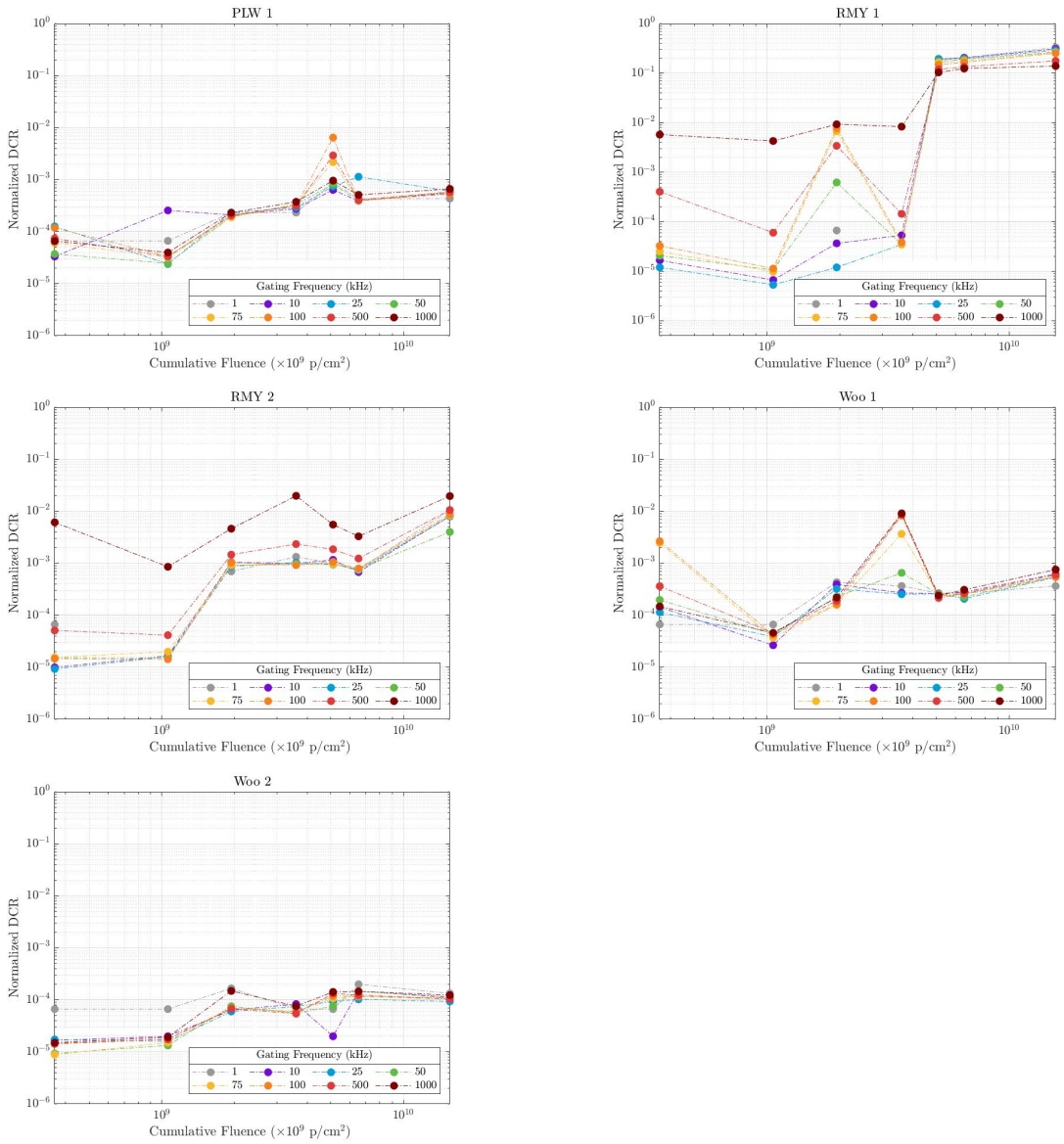

Figure B.7: Normalized DCR as function of cumulative proton fluence for gated QPL SPADs

B.4 Correlation Histograms

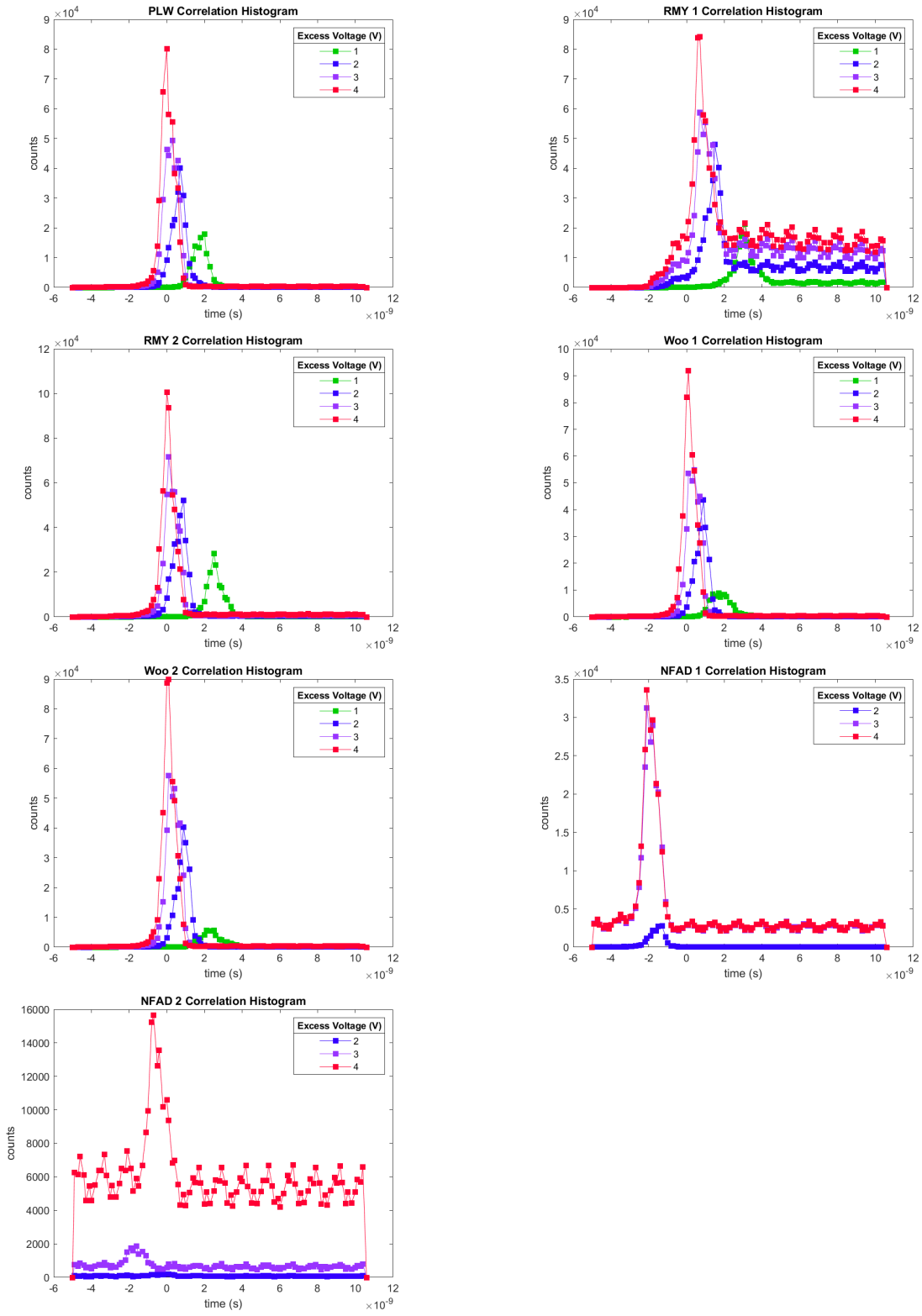

Figure B.8: correlation histograms for each SPAD at 1,2,3 or 4 excess bias

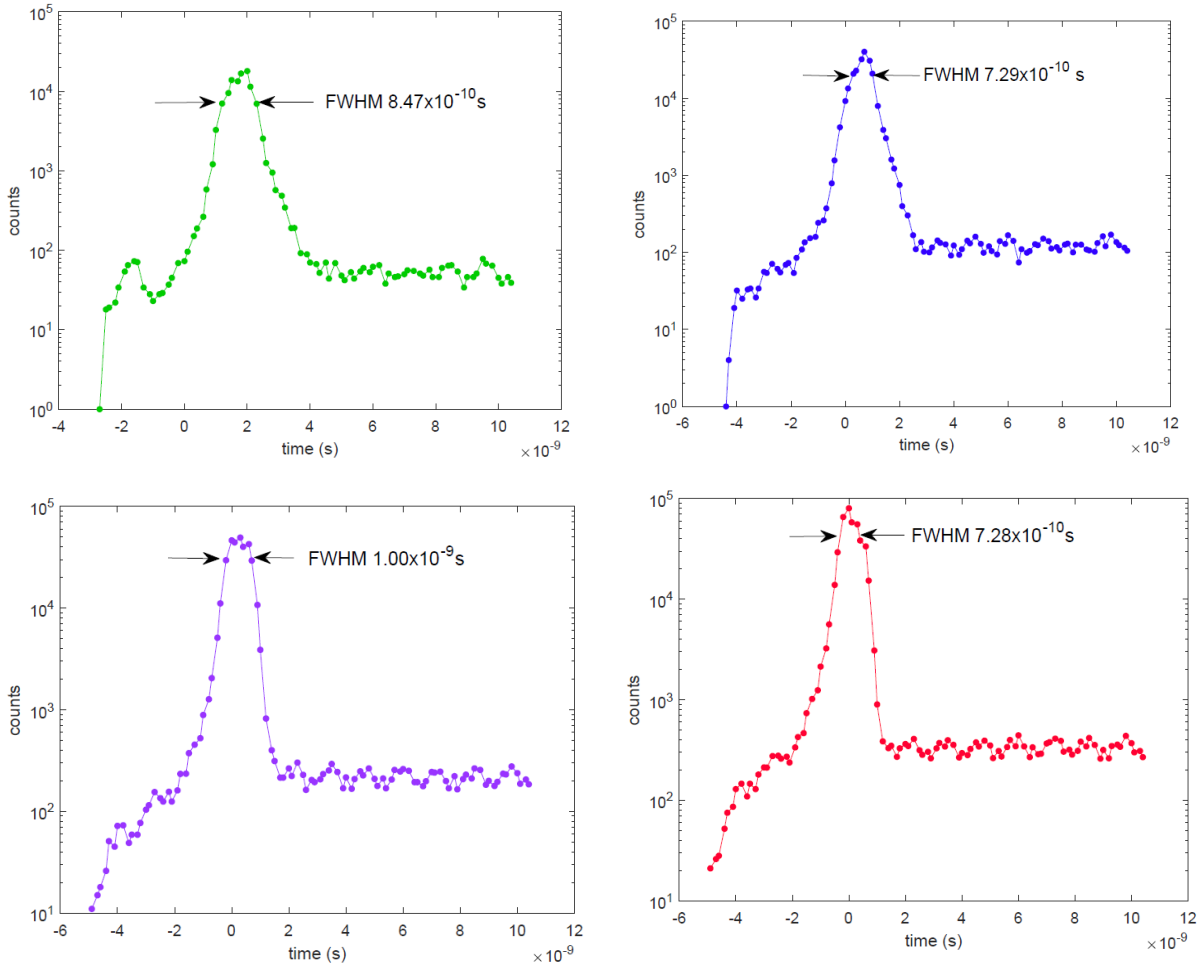

Figure B.9: PLW correlation histogram in logarithmic scale with calculated FWHM

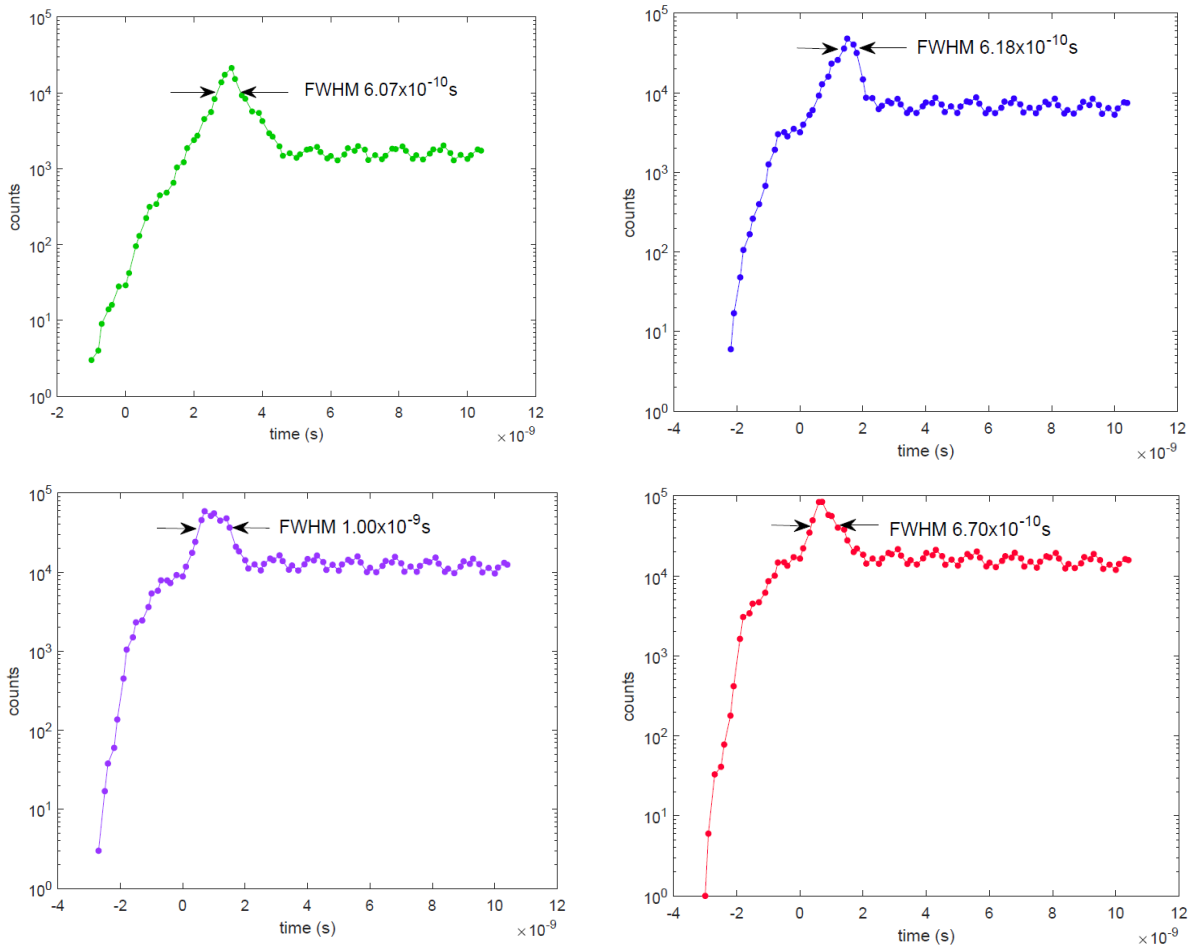

Figure B.10: RMY 1 correlation histogram in logarithmic scale with calculated FWHM

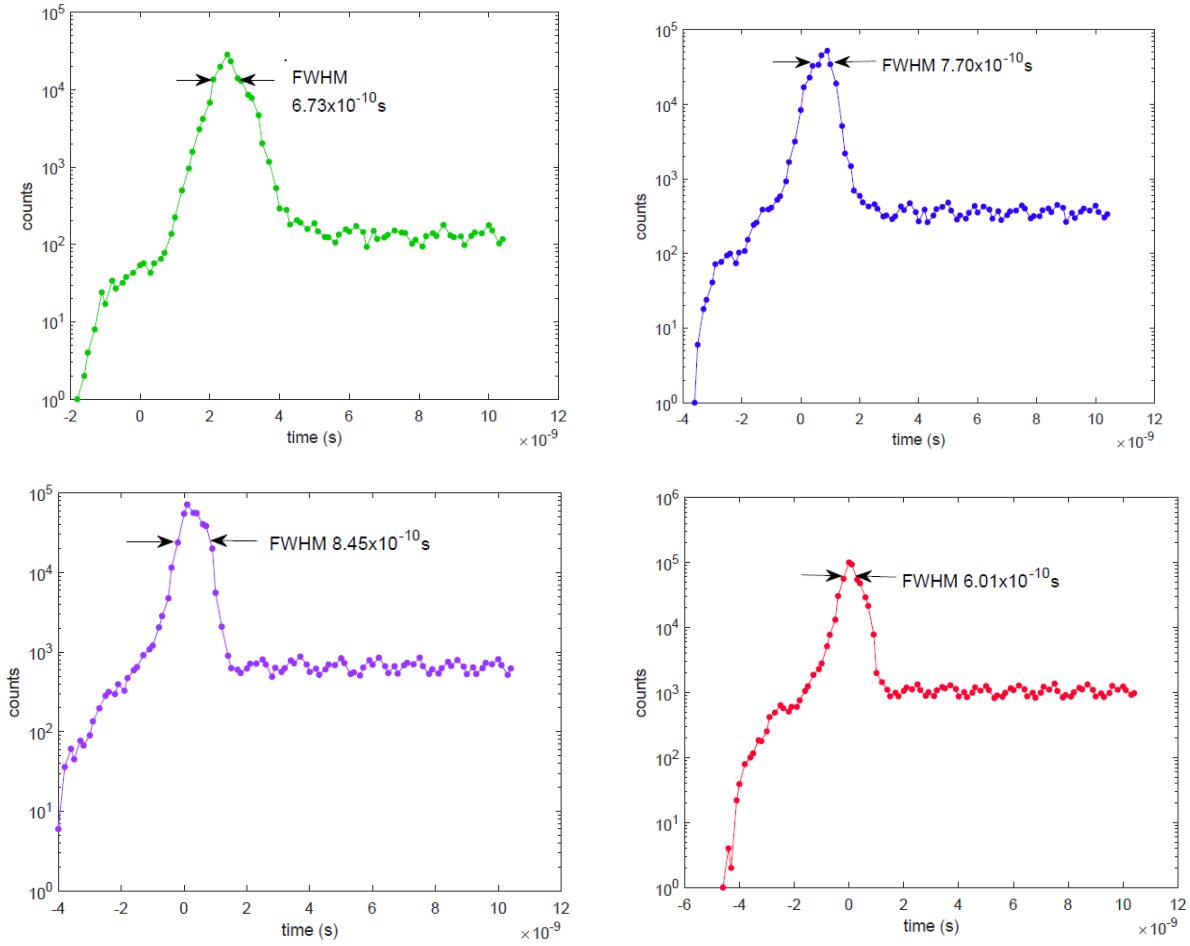

Figure B.11: RMY 2 correlation histogram in logarithmic scale with calculated FWHM

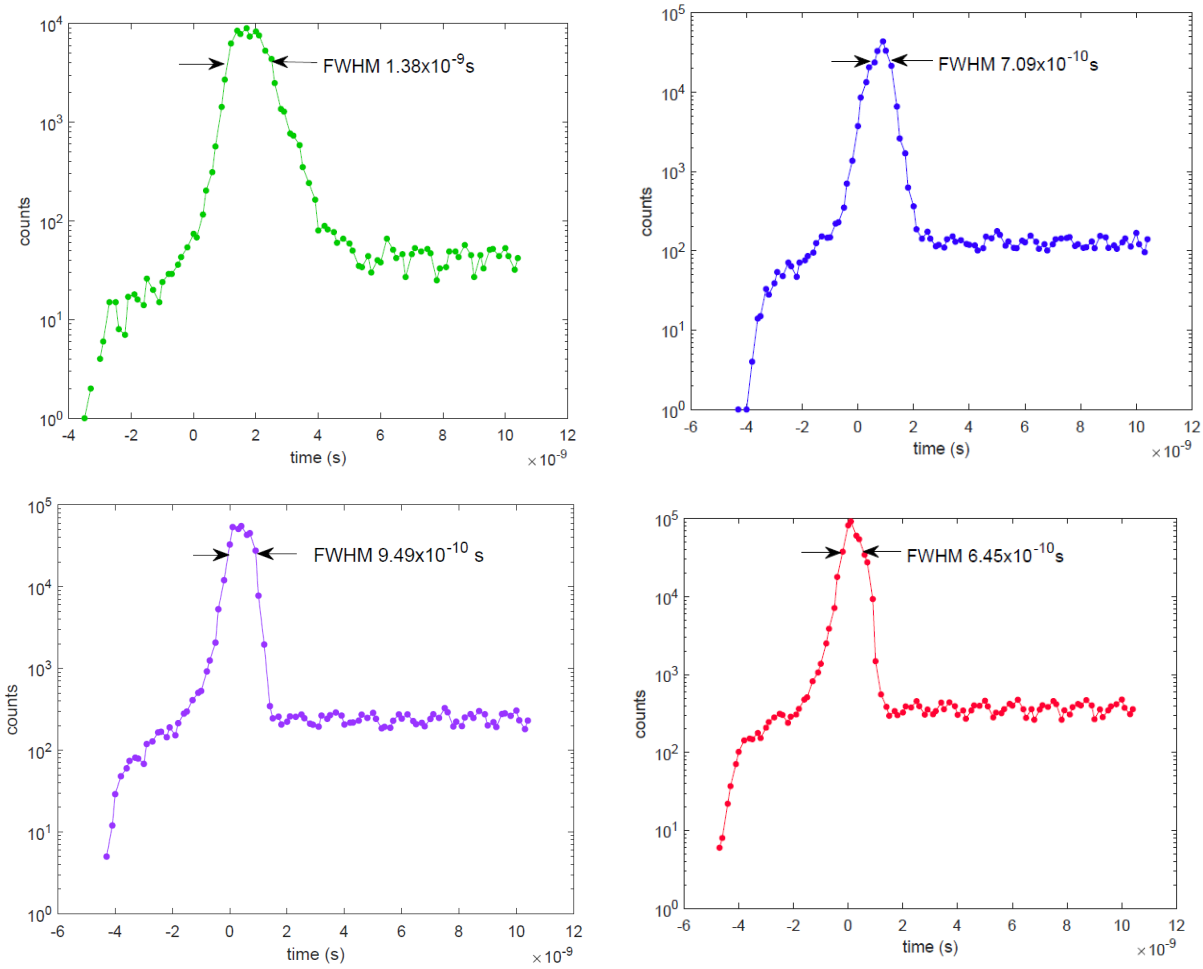

Figure B.12: Woo 1 correlation histogram in logarithmic scale with calculated FWHM

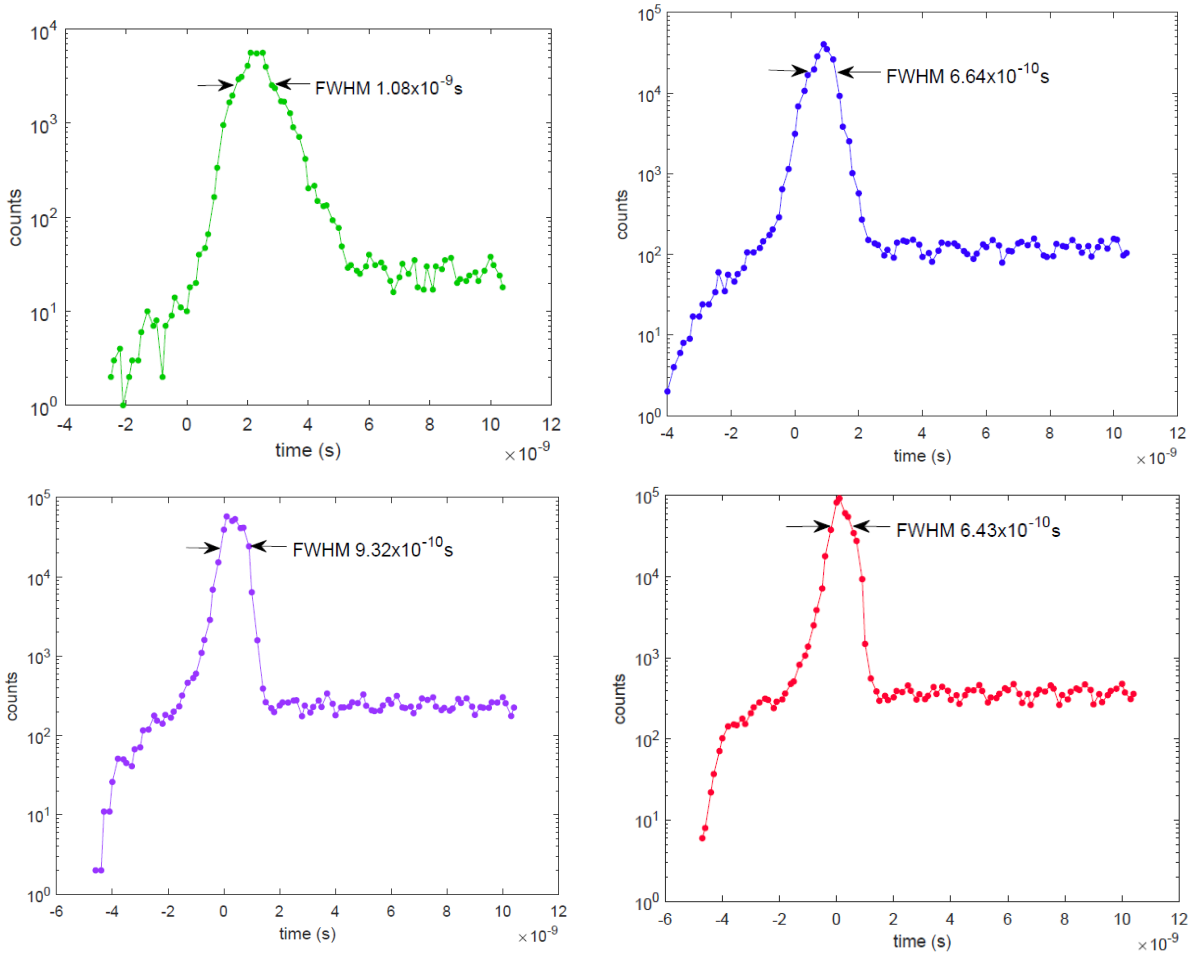

Figure B.13: Woo 2 correlation histogram in logarithmic scale with calculated FWHM

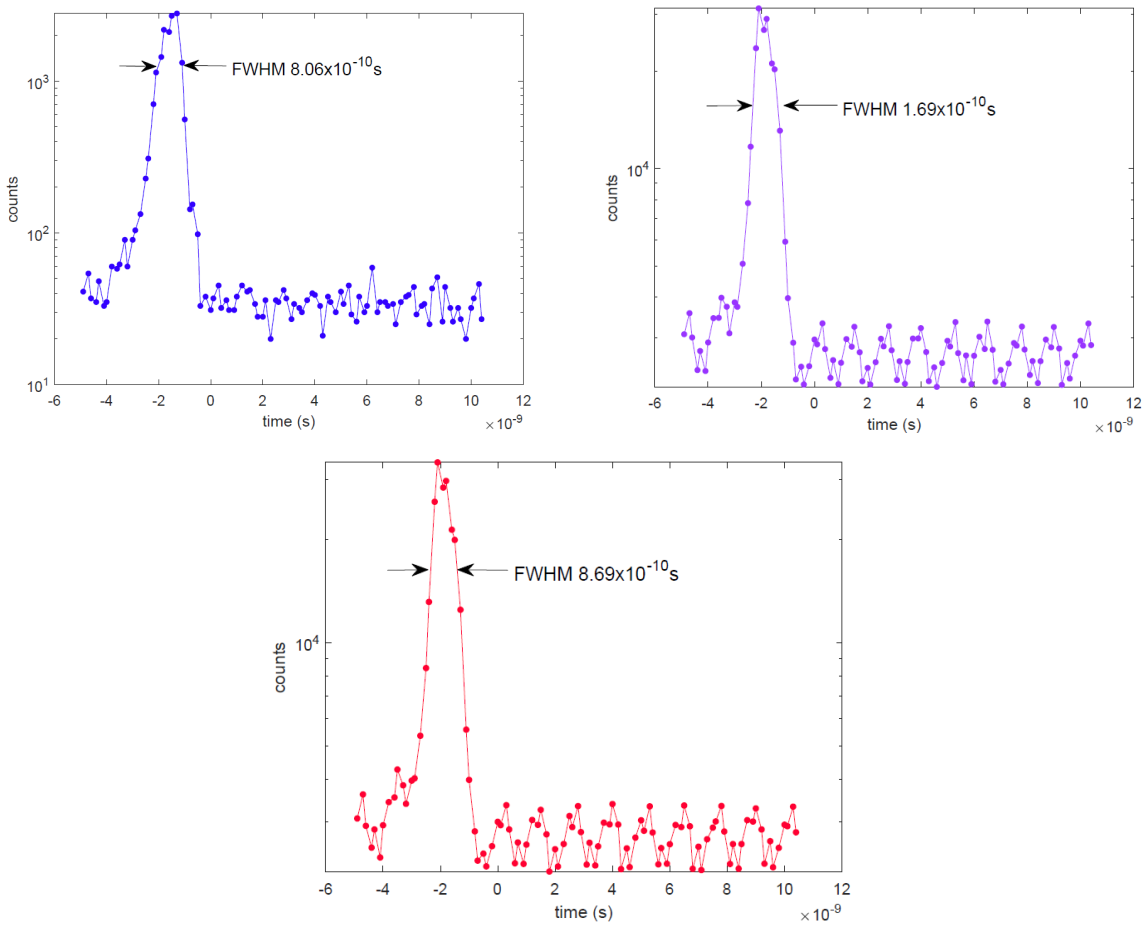

Figure B.14: NFAD 1 correlation histogram in logarithmic scale with calculated FWHM

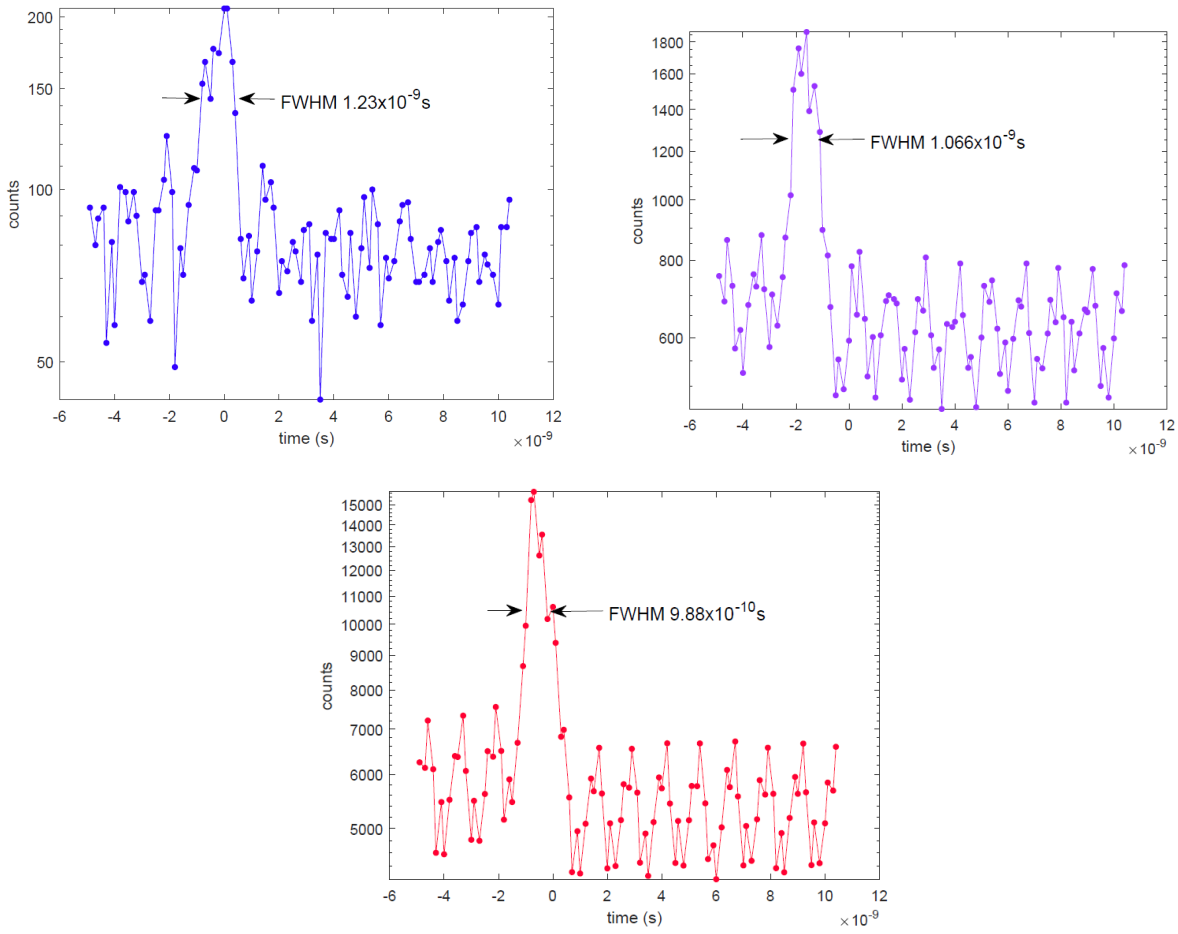

Figure B.15: NFAD 2 correlation histogram in logarithmic scale with calculated FWHM

Appendix C

Additional data for laser annealing experiment

C.1 Calibration

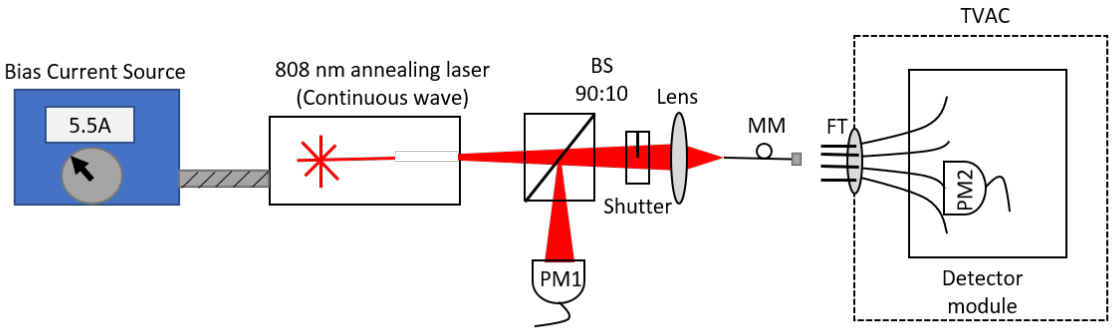

Figure C.1: Schematic of calibration measurement

The SPADs to be annealed by the high power laser were going to be inaccessible during TVAC operation. As such, the laser power actually making it through the fibers and

impinging on the SPAD active area would not be known during the experiment. However, the power at the SPAD could be estimated by comparing the power registered by a power meter at the 10% arm of the beam splitter with the the power registered by a power meter at the end of the fiber in the TVAC (in atmosphere pressure).

Figure C.1 shows a schematic of the calibration measurement. PM1 was situated at the output of the 10% arm of the beamsplitter, while PM2 was placed at the end of each fiber in the TVAC. The power after each fiber had to be measured since each fiber has a different attenuation level and coupling efficiency. Power through four fibers was measured since each fiber would be connected to one SPAD throughout the whole experiment. With the two PMs in place, the laser bias current was increased from 5A to 11.6A in steps of 0.3A. The starting current was chosen because this was the smallest current which registered a mW level reading from PM1; the final current was chosen when 1.5W was registered at PM2.

Figure C.3 shows laser power registered at PM2 (TVAC arm) as function of laser power registered at PM1 (10% arm of beamsplitter). These data were used to interpolate the laser power within the TVAC chamber based on the laser power read by PM1 by using the MATLAB command `interp1`. Once such interpolated powers were generated, the TVAC could be sealed and PM1 could be solely used to set the annealing laser bias current.

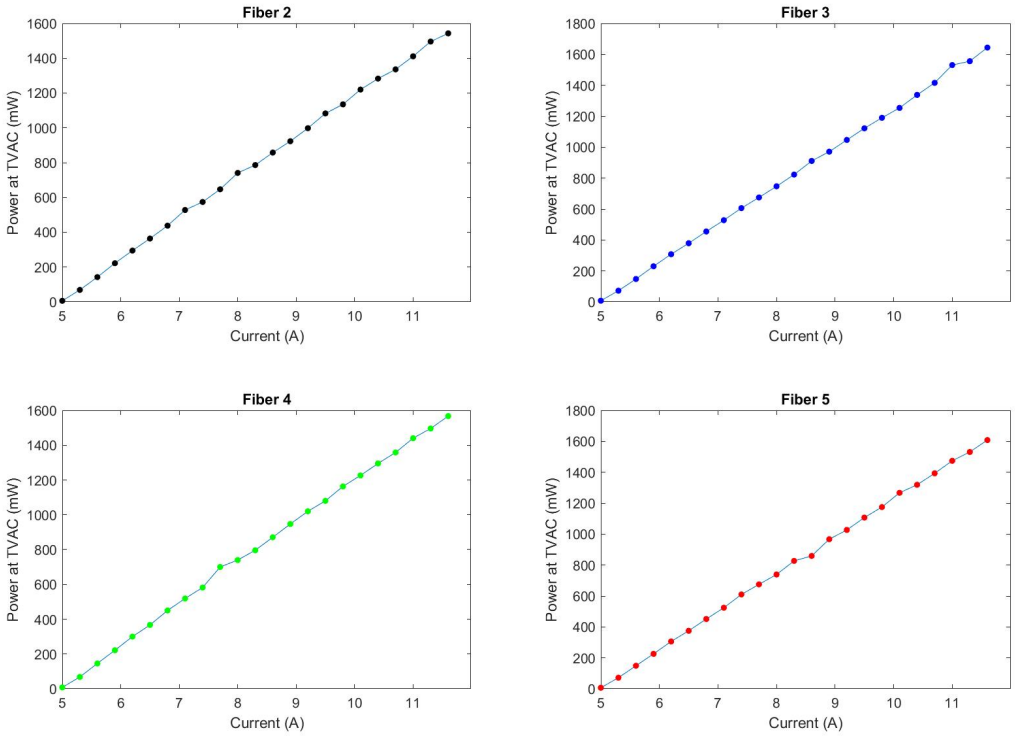

Figure C.2: Laser power registered by PM2 as function of bias current setting

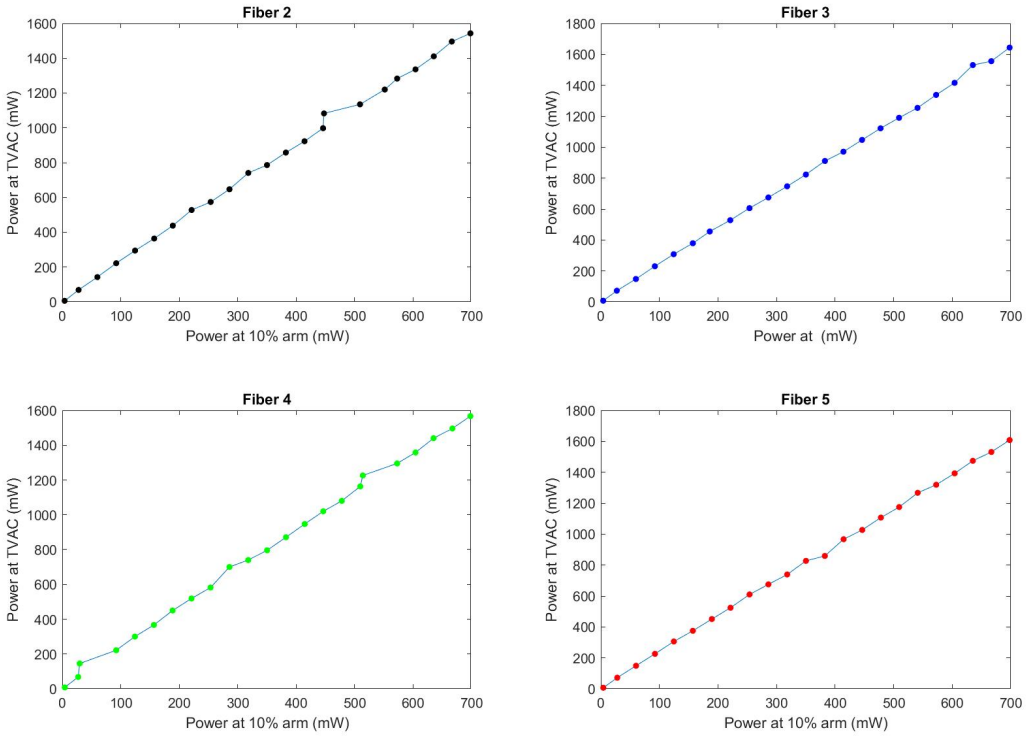

Figure C.3: Laser power registered by PM2 plotted against laser power registered by PM1 at one port of beamsplitter

Table C.1: Example interpolated data for power at the end of Fiber 2

Power at TVAC (mW)	Power at PM1 (mW)
50	20.76
100	41.55
150	63.12
200	83.25
250	104.56
300	126.95
350	150.58
400	172.67
450	193.29
500	211.18
550	236.79
600	265.23
650	286.92
700	304.05
750	324.50
800	356.38
850	378.81
900	403.01
950	425.71
1000	446.03

C.2 Data log

Figure C.4: Screenshot of terminal program (TeraTerm) log showing extracted data from PSOC microcontroller and detectors. `DET Thrs` is the discriminator threshold in units of ADC steps; `HV bias` is high voltage bias setting, in units of V; `Measurement` is the readout measurement number;`ThermVolt` is the readout of thermistor voltage in units of V; `ITEC` is a proxy measurement for thermoelectric cooler (TEC) current in units of V (had to be converted to current at latter time); `Cumulative Counts` is the number of counts accumulated in the counter buffer. In the upper half of the log, the detector is biased to 411 V and shows no accumulation of counts, indicating that at the temperature setting, the bias voltage is below the breakdown voltage. In the lower half of the log, the detector is biased to 414 V and there is an accumulation of counts, indicating that the detector is at or above breakdown voltage.

```
HVcon = 139

DET_Thrs = 56
HV_bias= 414.51
Measurement, ThermVolt, ITEC, Cumulative Counts,
0, 0.4974, 2.1469,1186,
1, 0.5000, 2.1464,2147,
2, 0.5032, 2.1271,2918,
3, 0.4991, 2.1276,3351,
4, 0.4949, 2.1471,3850,
5, 0.4971, 2.1475,4269,
6, 0.5000, 2.1467,4790,
7, 0.5026, 2.1458,5449,
8, 0.5051, 2.1279,5974,
9, 0.5011, 2.1282,6393,
10, 0.4969, 2.1279,6833,
11, 0.4929, 2.1463,7124,
12, 0.4956, 2.1462,7513,
13, 0.4980, 2.1473,8008,
14, 0.5005, 2.1473,8508,
15, 0.5030, 2.1468,9006,
16, 0.5061, 2.1276,9545,
17, 0.5020, 2.1284,10094,
18, 0.4974, 2.1286,10456,
19, 0.4928, 2.1468,10842,
20, 0.4954, 2.1468,11142,
21, 0.4975, 2.1471,11808,
22, 0.4999, 2.1475,12569,
23, 0.5020, 2.1472,13448,
24, 0.5053, 2.1277,13944,
25, 0.5006, 2.1279,14238,
26, 0.4961, 2.1474,14595,
27, 0.4980, 2.1475,15162,
28, 0.5003, 2.1470,15924,
29, 0.5025, 2.1468,16596,
30, 0.5048, 2.1281,17259,
```